Nd Lu CaF2 for high-energy lasers

Simone Normani

Normandie Université

THESE

Pour obtenir le diplôme de doctorat

Physique

Préparée au sein de l'Université de Caen Normandie

Nd:Lu:CaF_2 for High-Energy Lasers
Étude de Cristaux de CaF_2:Nd:Lu pour Lasers de Haute Énergie

Présentée et soutenue par
Simone NORMANI

Thèse soutenue publiquement le 19 octobre 2017 devant le jury composé de		
M. Patrice CAMY	Professeur, Université de Caen Normandie	Directeur de thèse
M. Alain BRAUD	MCF HDR, Université de Caen Normandie	Codirecteur de thèse
M. Jean-Luc ADAM	Directeur de Recherche, CNRS	Rapporteur
Mme. Patricia SEGONDS	Professeur, Université de Grenoble	Rapporteur
M. Jean-Paul GOOSSENS	Ingénieur, CEA	Examinateur
M. Maurizio FERRARI	Directeur de Recherche, CNR-IFN	Examinateur

Thèse dirigée par Patrice CAMY et Alain BRAUD, laboratoire CIMAP

UNIVERSITÉ CAEN NORMANDIE

ED PSIME

CiMap

Université de Caen Normandie

Nd:Lu:CaF_2 for High-Energy Lasers

Thesis for the Ph.D. title in
Physics

by candidate **Simone NORMANI**

Under the direction of **Patrice CAMY** and **Alain BRAUD**

Summary

Préface

Introduction et Programme Scientifique

Motivation et Problématiques

Les lasers d'haute énergie ont une variété d'applications grâce aux très intenses champs électriques. Cette caractéristique permette d'égaliser et de dépasser les forces pondéromotrices des particules subatomiques. Ces lasers permettent donc d'interagir avec les components des atomes, en particulier avec les noyaux. C'est donc possible utiliser lasers d'haute énergie pour applications en médecine (accélérateurs de particules pour hadronthérapie), physique des hautes énergies (validation des modèles théoriques), et physique subatomique (armements atomiques, fusion nucléaire).

Le travail présenté se déroule dans le cours du projet LASCAN, en collaboration avec le centre CEA-CESTA de Bordeaux pour la réalisation des lasers état solide pulsés de très haute énergie. La cible principale de l'étude est la caractérisation de nouveaux matériaux cristallins dopés néodyme pour l'amplification d'impulsions laser ultracourtes à haute énergie. L'objectif final du travail est la substitution des components actifs actuellement employés dans les amplificateurs laser du Laser Mégajoule.

Les sites de recherche qui emploient des lasers à haute énergie, comme le Lawrence Livermore National Laboratory (LLNL) en Californie, Gekko XII à Osaka, et naturellement le Laser MégaJoule (LMJ) dans le site CESTA en proximité de Bordeaux, utilisent multiple stades d'amplification pour obtenir des impulsions très courtes avec très haute puissance de sommet. Les matériaux amplificateurs utilisés pour les stades d'énergie de l'ordre du joule comprennent des verres phosphates dopés néodyme, en particulier les verres laser LHG-8 (Hoya) et LG-770 (Schott). Ces matériaux sont appropriés pour la génération d'impulsions laser ultracourtes en vertu de leurs bandes d'émission très larges. Dans la suite on se référera en particulier au LMJ pour ce qui concerne la description du système, ses applications et ses réquisits.

Le but du LMJ est l'obtention d'une efficiente fusion nucléaire à confinement inertiel (FCI). Le LMJ se compose de 4 stations laser, dont 1 dédiée au laser petawatt Petal, et une chambre sphérique pour les expérimentes de FCI. À l'intérieur de cette chambre, 176 faisceaux laser sont focalisés sur la position d'un échantillon, composé d'un cylindre d'or (*hohlraum*) contenant une mixture de deutérium et tritium. La fusion nucléaire est commencée par la radiation X du *hohlraum*, qui comprime le gaz des isotopes et augment la température du système. Pour commencer l'émission de rayons X, l'or qui compose l' *hohlraum* doit être excité par des photons à la longueur d'onde de 351 nm. Les faisceaux laser du LMJ focalisés sur l'échantillon donc doit avoir cette longueur d'onde. Pour obtenir cette propriété, la chaine laser du LMJ utilise un système de conversion d'énergie, pour tripler la fréquence des impulsions. La longueur d'onde originale des faisceaux laser doit être 1053 nm. Ça peut être obtenu d'une façon relativement facile par l'émission des ions trivalents du néodyme entre les niveaux $^4F_{3/2}$ et $^4I_{11/2}$. Les matériaux optiques dopés néodyme offrent donc une très bonne option, avec l'avantage que l'émission peut être obtenue en pompant le niveau excité à 800 nm avec des diodes laser commerciales.

Des cristaux fluorures dopés avec terres rares sont pris en considération pour prendre la place des verres dopés néodyme dans la chaîne amplificatrice du laser. En particulier, les cristaux ayants la structure de la fluorite présentent des propriétés très intéressantes pour cette application. Ces cristaux en fait ont des bandes spectrales très large, comparables à celles des verres lasers, et donc satisfont la requête principale pour obtenir des impulsions très courtes. En plus, les cristaux ont des conductivités thermiques généralement beaucoup plus hautes que les verres: ça les rend des matériaux très intéressants pour l'application aux lasers impulsés. Une haute conductivité thermique permet une plus efficace dispersion de la chaleur déposée en suite à l'absorption des photons d'excitation, et donc prévient l'endommagement du matériel active dû aux changements de température locaux à l'instant du pompage.

Les cristaux à structure de fluorite posent une difficulté particulière concernant le dopage pour applications optiques. C'est connu que les ions terres rares tendent à se rassembler facilement en clusters à l'intérieur de la matrice cristalline des fluorites, plutôt que suivre une distribution approximativement uniforme. Cet effet est particulièrement prononcé dans le cas du calcium fluorure, CaF_2 [1]. Les ions néodyme rassemblés de cette façon peuvent échanger énergie l'un avec l'autre par interaction dipôle-dipôle, dans un phénomène appelé relaxation croisée. En détail, les ions excités au niveau $^4F_{3/2}$, d'où la relaxation radiative pourrait avoir place, échangent énergie avec les ions dans l'état de base $^4I_{9/2}$, et les deux transite au niveau intermédiaire $^4I_{15/2}$

d'où ils se désexcitent de façon non-radiative. Pour cette raison, l'émission des terres rares est réduite avec l'introduction des ions au-delà d'un certain seuil.

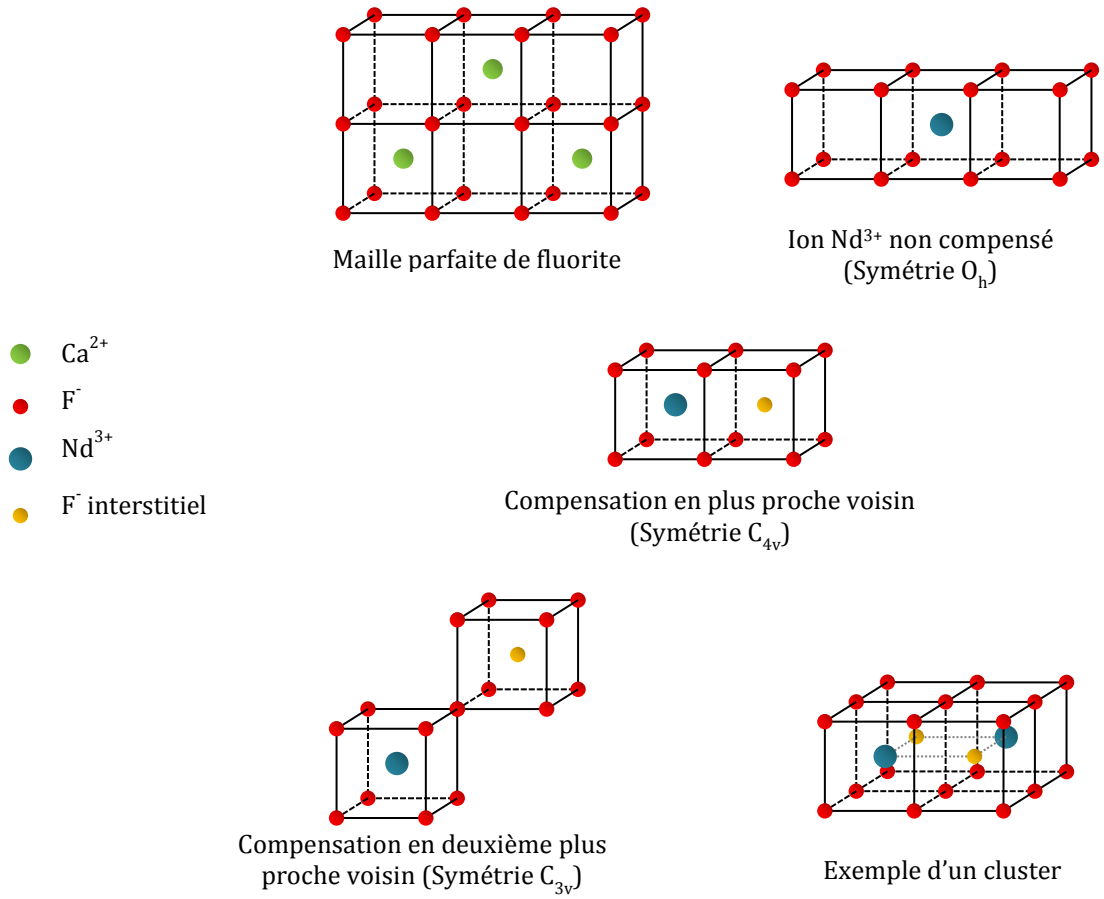

Fig. F1 Structure de la maille de la fluorite – maille parfaite du CaF_2, présence d'un ion Nd^{3+} non compensé qui substitue un cation Ca^{2+} de la matrice, compensation avec un ion fluorure interstitiel en position de plus proche voisin et de deuxième plus proche voisin, et un exemple de cluster d'ions Nd^{3+} (cf. Payne [1]).

Normalement, la quantité de dopage nécessaire pour obtenir des bonnes propriétés spectroscopiques est majeure de la valeur à laquelle le rassemblement (ou «clustering») du néodyme apparaitre. Pour contourner ce problème, il a été proposé d'employer un deuxième ion dopant qui n'interagit pas avec les ions actifs et qui puisse donc agir comme un «tampon». Cette contremesure permet d'obtenir des clusters des ions co-dopants autour des ions actifs solitaires, et donc isoler les ions de la terre rare utile à l'application. En le cas des matériaux dopés néodyme, le co-dopant choisi est le lutétium, car les niveaux d'énergie de cet ion ne se rapprochent pas à l'énergie des photons participants aux transitions du néodyme.

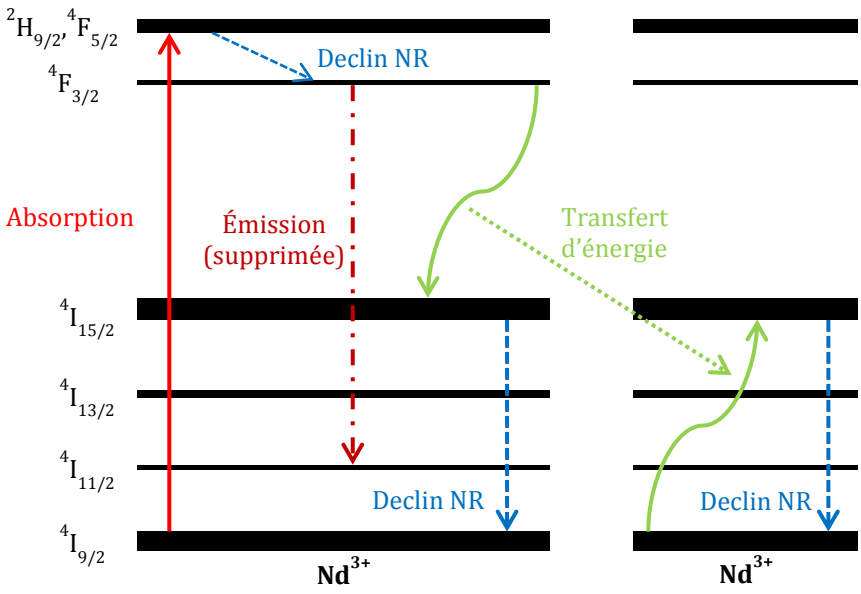

Fig. F2 Illustration du phénomène de relaxation croisée due au transfert d'énergie entre des ions néodyme communicants.

Contenu de la thèse

Le travail de thèse consiste en l'investigation des échantillons de cristaux fluorures dopés avec néodyme et lutétium, en comprenant leur spectroscopie, leurs propriétés thermomécaniques et d'amplification optique. L'intérêt de cette étude est l'obtention d'un ensemble le plus complète possible de quantités utiles pour la modélisation et la mise en œuvre des amplificateurs laser infrarouge à impulsions ultracourtes. La thèse se déroule sur cinq chapitres, distingués par sujet, qui incluent une introduction générale et une section des conclusions finales et perspectives futures sur les résultats du travail.

Le **premier chapitre** consiste en une introduction générale, et présente les motivations et intérêts scientifiques, technologiques et applicatifs de la recherche traitée dans la thèse. Dans ce chapitre, on présente le projet LASCAN et la littérature scientifique sur les cristaux fluorures dopés avec du néodyme. Les propriétés des cristaux dopés avec terres rares, la problématique de la suppression de la fluorescence due au rassemblement des ions terres rares (clustering) et la solution à cet inconvénient proposée sont discutées. L'état de l'art sur les propriétés des cristaux fluorures dopés avec néodyme est présenté.

La chaîne laser du LMJ est présentée (Fig. F3), en montrant les components amplificateurs qui emploient actuellement des verres phosphates comme milieu de gain. En particulier, le travail sur les cristaux fluorures dopés néodyme propose de remplacer les milieux actifs des amplificateurs d'entrée. L'objectif du projet est d'améliorer les prestations de cette section, en obtenant des impulsions très courtes (bien au-dessous de 1 ns), avec 1 J d'énergie par impulsion et une fréquence de récurrence de 10 Hz. Pour ce résultat, c'est très important avoir une vision complète du système et des matériaux, de façon de concevoir et optimiser le dispositif pour la fonction déjà introduite.

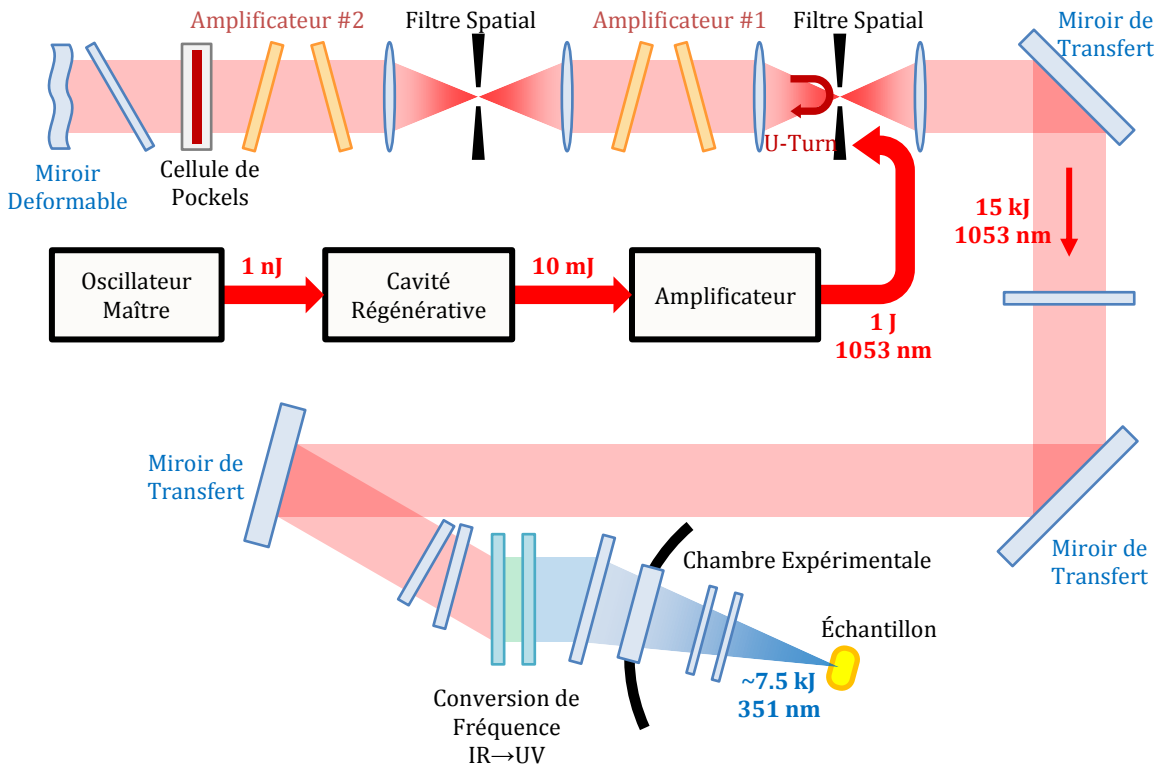

Fig. F3 Schéma de la chaîne amplificatrice, en montrant l'installation du faisceau laser du LMJ. L'oscillateur maître est une diode laser avec émission à 800 nm. Des verres phosphates dopés Nd^{3+} sont employés dans la cavité régénérative, l'amplificateur d'entrée, et les amplificateurs laser #1 and #2.

Spectroscopie

Le **deuxième chapitre** traite la spectroscopie des cristaux CaF_2 dopés avec une quantité fixe de néodyme et lutétium en quantités variables. Le travail de spectroscopie se focalise sur l'étude

des propriétés du matériel dans la zone infrarouge en absorption atour de 800 nm, et en émission atour de 1.05 µm.

Les échantillons sont fabriqués avec la technique de croissance cristalline de Bridgman-Stockbarger, et coupé en forme de disc de 6 mm de rayon et approximativement 4 mm d'épaisseur.

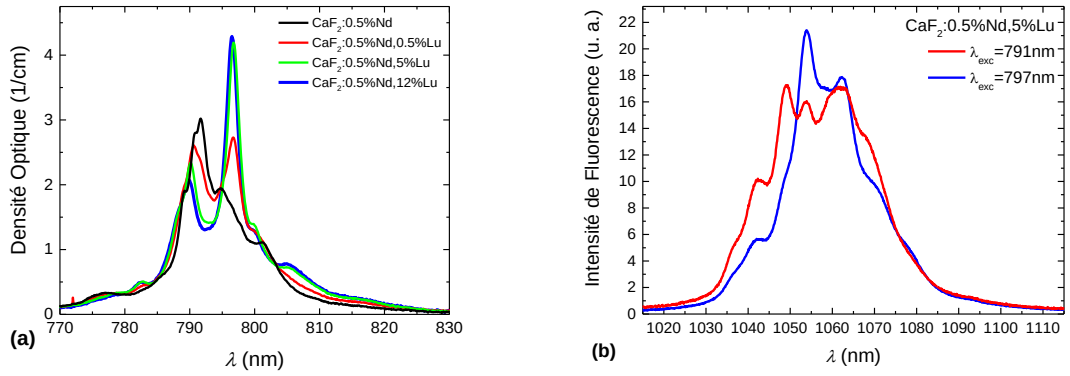

Fig. F4 (a) Spectres d'absorption CaF_2:Nd^{3+},Lu^{3+} qui montrent les changements de forme de la bande avec l'incrément de la concentration du Lu^{3+}. (b) Spectres d'émission de CaF_2:0.5% Nd,5% Lu à différentes longueur d'onde d'excitation normalisés par la valeur du coefficient d'absorption à la longueur d'onde d'excitation correspondante. Le spectre à 791 nm montre une valeur d'aire intégrée comparable à celle du spectre à 797 nm.

L'absorption des échantillons est mesurée. Le pic d'absorption pour l'échantillon CaF_2:0.5% Nd est positionné à la longueur d'onde de 791 nm. En ajoutant du lutétium, la forme de la bande d'absorption change graduellement. Le pic principal se déplace à 790 nm, et un deuxième pic apparait à 797 nm. À des concentrations de Lu^{3+} supérieures à 1 at% le pic à 797 nm dévient dominant. L'intégral de l'absorption ne change pas sensiblement, en signifiant que la force de l'oscillateur n'est pas modifiée par l'introduction du lutétium (Fig. F4(a)). Par contre, les changements des bandes d'absorption suggèrent la présence de deux ou plus types de centres actifs. La coexistence de différents sites a été notée en littérature pour CaF_2:Nd^{3+} [2-5], CaF_2:Nd^{3+},Y^{3+} [6,7] et SrF_2:Nd^{3+} [8].

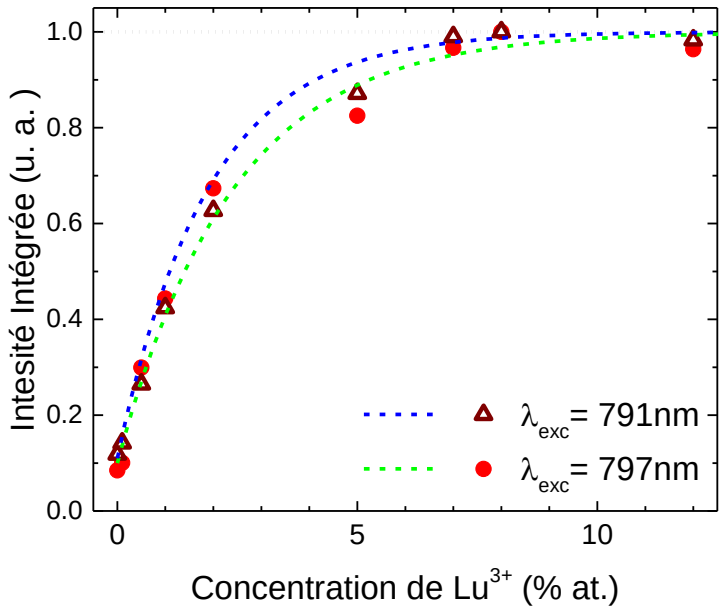

Fig. F5 Dépendance de l'intensité de fluorescence intégrée, normalisée à l'intensité du pic d'absorption, en fonction de la concentration du codopant. Les traits discontinus décrivent des comportements indicatifs de la croissance.

L'émission autour de 1.05 μm a été enregistrée en excitant les échantillons sur les deux longueurs d'ondes de sommet, 791 nm et 797 nm (Fig. F4(b)). La forme de la bande de fluorescence mesurée change avec la longueur d'onde d'excitation. En particulier, en excitant à 791 nm, la bande d'émission a trois pics, à 1049 nm, 1054 nm et 1062 nm, avec une largeur à mi-hauteur de 31 nm. En excitant à 797 nm, les pics principaux se trouvent à 1054 et 1062 nm, et la bande a une largeur de 18 nm. C'est possible voir la croissance de l'intensité d'émission pendant que du Lu^{3+} est introduit graduellement (Fig. F5). En fait, l'intensité de fluorescence intégrée augmente en fonction de la concentration d'ions Lu^{3+} avec une tendance vers une valeur asymptotique. Ce comportement démontre l'effet du codopage Lu^{3+}. Les clusters optiquement inactifs Nd^{3+}-Nd^{3+} sont remplacés par des clusters actifs Nd^{3+}-Lu^{3+}, qui séparent et isolent les ions néodyme l'un de l'autre, en prévenant la relaxation croisée.

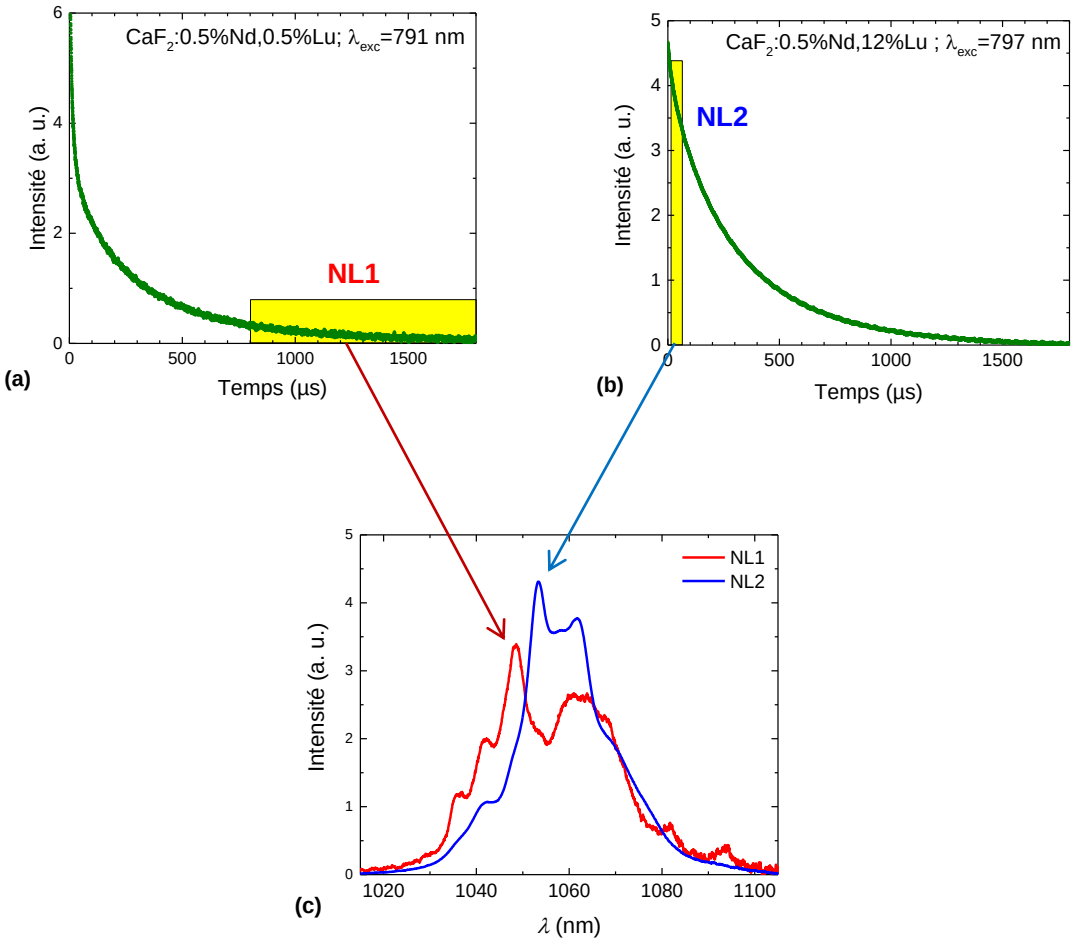

Fig. F6 (a-b) Mesures résolues en temps sur échantillons différents avec différentes longueurs d'onde d'excitation et d'émission; (c) spectres d'excitation obtenus par l'intégration dans les fenêtres temporelles soulignées ci-dessus, identifiés comme les spectres des deux centres actifs «purs».

Des spectres d'excitation ont été enregistrés sur les longueurs d'onde d'émission fixées 1049 nm et 1054 nm, en variant la longueur d'onde d'excitation. Ces mesures ont permis d'avoir une estimation qualitative de la concentration des différents sites actifs en fonction de la concentration de Lu^{3+}, et une approximation de leurs spectres d'excitation «purs». En comparant ces mesures aux spectres d'absorption, le premier type de centre actif, ayant émission principale à 1049 nm, a été associé aux échantillons avec basse concentration de Lu^{3+} et à la longueur d'onde d'excitation de 791 nm. Le deuxième centre, ayant émission principale à 1054 nm, a été associé aux échantillons avec haute concentration de Lu^{3+} et à la longueur d'onde d'excitation de 797 nm. Le centre identifié par le pair de longueur d'onde d'excitation-émission 791 nm-1049 nm a été appelé «NL1», et le centre identifié par le pair 797 nm-1054 nm a été appelé «NL2» (Fig. F6).

En considérant que tous les ions Nd^{3+} forment des clusters dans le cas du CaF_2 dopé uniquement avec du néodyme, le coefficient d'absorption de l'échantillon CaF_2:0.5% Nd, divisé par la concentration de ions Nd^{3+}, peut être considéré comme la section efficace d'absorption des clusters. En savant que à basses concentrations de lutétium, les centres NL2 sont négligeables, le recouvrement de la bande d'absorption de l'échantillon CaF_2:0.5% Nd,0.1% Lu par une combinaison linéaire du spectre des clusters et de le spectre d'excitation résolu en temps de NL1 permette d'estimer la section efficace d'absorption de ce site actif. De la même façon, une combinaison linéaire du spectre d'absorption de NL1 et du spectre d'excitation de NL2, comparée à l'absorption d'un échantillon avec haute concentration de Lu^{3+}, permette d'obtenir la section efficace d'absorption des centres NL2. Donc, les sections efficaces d'absorption des trois centres du néodyme du système ont été évaluées. En plus, en comparant des combinaisons linéaires des trois avec les spectres d'absorptions des échantillons avec diverses concentrations de lutétium, peut être utilisée pour estimer l'évolution de la concentration des différents sites en fonction du codopage Lu^{3+}. Le résultat démontre que les clusters Nd^{3+}-Nd^{3+} diminuent graduellement pendant que la concentration de lutétium augmente, et ils disparaissent presque totalement au-dessus de 5 at% Lu^{3+}. En plus, les centres NL2 deviennent dominants sur les NL1 à hautes concentrations du codopant (Fig. F7).

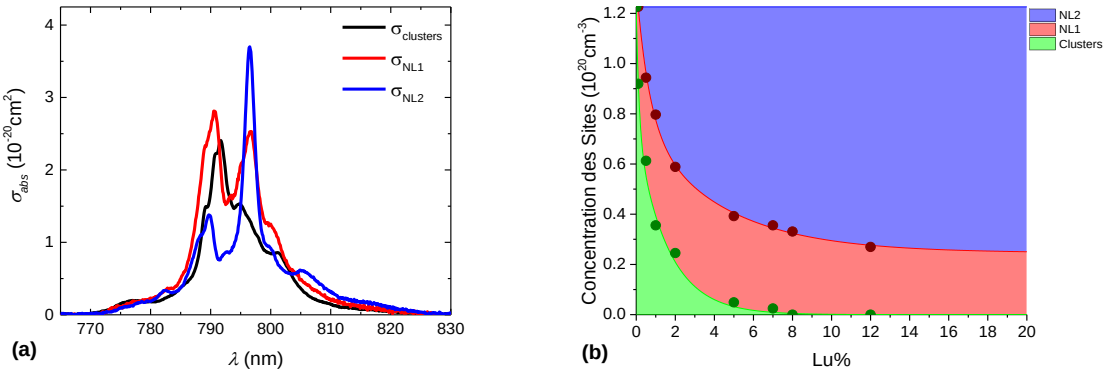

Fig. F7 (a) Spectres de section efficace d'absorption pour N1, NL2, and clusters Nd^{3+}-Nd^{3+} en CaF_2:Nd^{3+},Lu^{3+}; (b) évolution de la concentration des sites néodyme (NL1, NL2 and clusters Nd^{3+}-Nd^{3+}) en fonction de la concentration de Lu^{3+}.

Pour vérifier la validité des résultats obtenus pendant ces calculs, les valeurs de durée de vie et de concentration des sites actifs et les spectres d'émission résolus en temps ont été utilisés pour reconstruire les spectres de fluorescence et l'évolution de l'intensité d'émission en fonction de la concentration de lutétium. Les reconstructions sont en bon accord avec les résultats

expérimentaux de fluorescence, donc on peut conclure que les valeurs des sections efficaces d'absorption et de concentration des sites sont fiables.

Table F1 Longueurs d'onde de pic, sections efficaces d'absorption au pic, et sections efficaces intégrées pour le trois centres principaux du Nd^{3+} en CaF_2:Nd^{3+},Lu^{3+}.

		Clusters Nd-Nd	**NL1**	**NL2**
$\boldsymbol{\lambda_{max}}$	nm	792	791	797
$\boldsymbol{\sigma(\lambda_{max})}$	10^{-20} cm^2	2.4	2.8	3.7

Les sections efficaces d'émission pour les deux centres actifs NL1 et NL2 ont donc été calculées à partir des durées de vie radiatives et spectres de fluorescence, en appliquant l'équation de Füchtbauer-Ladenburg (Fig. F8).

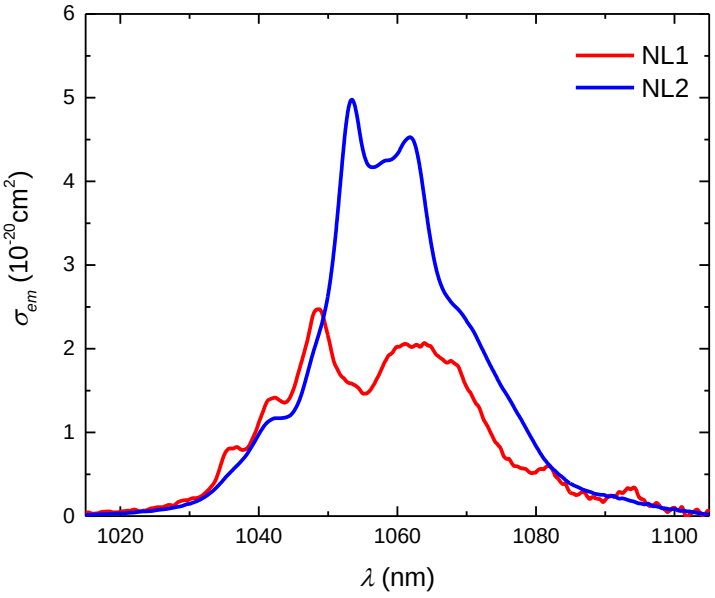

Fig. F8 Sections efficaces d'émission pour le centres NL1 et NL2, calculées avec l'équation de Füchtbauer-Ladenburg.

Enfin, des mesures de rendement quantique ont été effectuées avec l'aide d'une sphère intégratrice. Malheureusement, les mesures ne sont pas absolues, probablement pour des

raisons pas encore déterminées. En tout cas, les résultats sur le groupe d'échantillons de CaF_2:Nd^{3+},Lu^{3+} ont été comparés avec des mesures sur un échantillon de YAG:Nd^{3+}. La comparaison montre que la valeur du rendement quantique des fluorures, pour hautes concentrations de Lu^{3+} se rapproche à ce du YAG, qui est notoirement proche à 100%. En plus, l'évolution du rendement quantique suit en bonne approximation celle de l'intensité de fluorescence intégrée, en confirmant que, au moins, les résultats sont fiables en valeur relative.

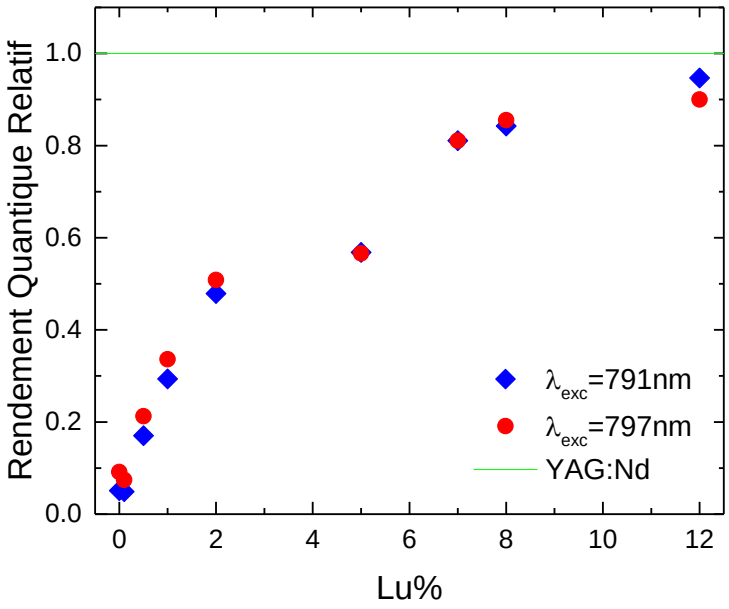

Fig. F9 Mesures relatives de rendement quantique pour les échantillons de CaF_2:Nd^{3+},Lu^{3+} normalisées et comparées aux valeur de rendement quantique d'un échantillon de YAG:Nd.

Les propriétés spectroscopiques d'autres cristaux fluorures ont été évaluées, en particulier celles de SrF_2 et BaF_2, avec les mêmes dopages de Nd^{3+} et Lu^{3+}. Une évolution imprévue de la densité optique a été observée, et on suspecte ça soit due à des défauts ou contaminations introduits pendant le procès de fabrication. Les spectres de fluorescence (Fig. F10) montrent l'élimination des clusters, et les mesures d'excitation et d'émission résolues en temps montrent qu'un seul type de site actif est présent en ces échantillons. En particulier, les spectres d'émission du SrF_2:Nd^{3+},Lu^{3+} ont des bandes très larges avec le pic principal à 1053 nm: ça rende le matériel particulièrement intéressant pour mes applications aux lasers impulsés.

On peut observer que le pic d'émission principal du BaF_2: Nd^{3+},Lu^{3+} corresponde au minimum local de la bande du SrF_2:Nd^{3+},Lu^{3+}. Pour cette raison, on peut prévoir qu'une combinaison des deux cristaux donne un spectre très large et plat autour de la longueur d'onde d'émission de

1053 nm. Pour obtenir une émission avec ces propriétés spectrales, des cristaux mixtes SrF_2-BaF_2:Nd^{3+},Lu^{3+} ont été fabriqués, avec différentes rapports des deux fluorures. Les meilleurs résultats spectraux ont été observés pour une mixture de 90% SrF_2 et 10% BaF_2 (Fig. F11).

Même en considérant la différence de forces d'oscillateur entre les deux cristaux, cette composition suggère que les ions des terres rares ont une plus forte tendance de former des clusters plus facilement dans un environnement cristallin BaF_2 que dans le SrF_2.

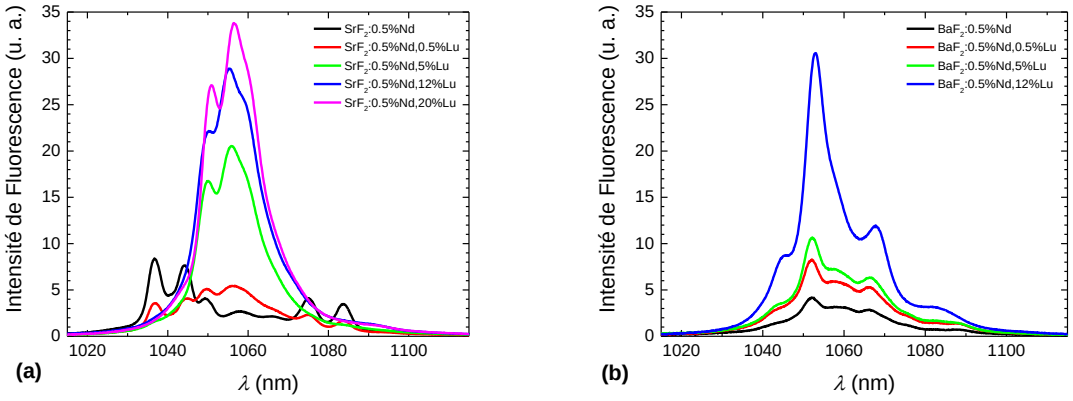

Fig. F10 Spectres d'émission des échantillons (a) SrF_2:Nd^{3+},Lu^{3+} excités à 795 nm et (b) BaF_2:Nd^{3+},Lu^{3+} excités à 799 nm.

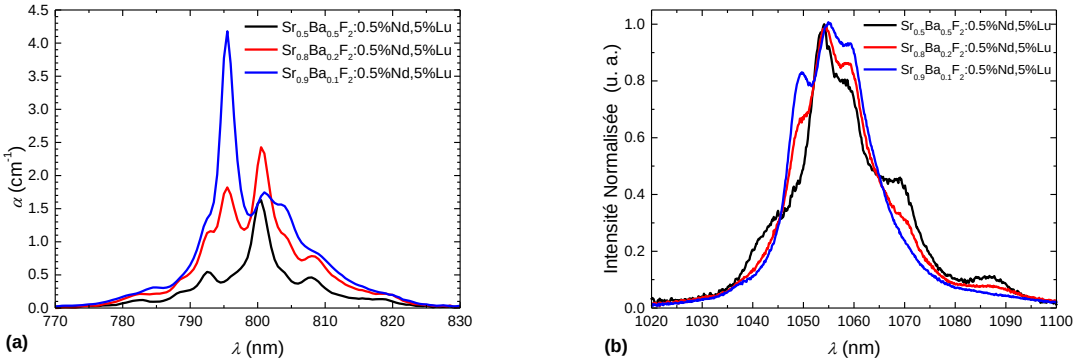

Fig. F11 Spectres d'absorption (a) et spectres d'émission normalisés (b) en excitant à 795 nm des cristaux mixtes SrF_2-BaF_2:Nd^{3+},Lu^{3+}. Les résultats montrent le changement de forme des bandes spectrales en fonction de la concentration relative des deux fluorures.

Propriétés Thermomécaniques

Le **troisième chapitre** prend en examen les propriétés thermiques des cristaux de fluorures dopés néodyme et lutétium: ces quantités sont cruciales pour la modélisation de l'amplificateur laser, car l'haute énergie des impulsions aux quelle les cristaux seraient exposées causent une accumulation de chaleur dans la matrice, laquelle doit être dissipée parmi une impulsion et la suivante, ou le stress thermique peut endommager le matériel. Différents techniques expérimentales ont été utilisées et comparées pour obtenir la conductivité thermique des échantillons.

L'effet du dopage sur la conductivité thermique des cristaux est discuté, en prenant en considération la théorie de Debye. Une modélisation théorique du comportement de la conductivité thermique des échantillons en fonction de la concentration du dopant est définie, basé sur la méthode de Klemens [9]. Le modèle est mis en pratique avec les paramètres des échantillons CaF_2:Nd^{3+},Lu^{3+}, en obtenant une estimation pour l'évolution de la conductivité en fonction de la concentration de lutétium.

Des mesures sur l'effet de lentille thermique ont été effectuées pour estimer les propriétés thermomécaniques des échantillons. La technique de lentille thermique consiste en mesurer la divergence d'un faisceau laser au-delà de l'échantillon, en passant à travers une section chauffée par l'absorption d'un faisceau laser de pompe. La lentille thermique est une combinaison de deux effets thermiques. Le premier effet est la lentille géométrique créée par le gonflement des facettes à cause du profil d'expansion thermique dû à l'absorption d'un faisceau gaussien. Cet effet cause la formation d'une lentille convexe, et donc toujours convergent. Le deuxième effet est la lentille de réfraction, qui est due au gradient d'indice de réfraction proportionnel au coefficient thermo-optique du matériel. Comme ce coefficient peut être positif ou négatif, l'effet peut être analogue soit à une lentille convergente, soit à une lentille divergente. La vitesse de l'effet total de la lentille thermique est définie par la diffusivité thermique du matériel, et donc la mesure de la divergence du faisceau de sonde résolue en temps permet d'estimer la conductivité thermique de l'échantillon. En plus, l'amplitude du signal enregistré peut être utilisée pour calculer la variation de chemin optique efficace à travers l'échantillon, et donc les valeurs d'expansion thermique et coefficient thermo-optique (Table F2).

La précision des mesures de lentille thermique a été discutée, en particulier en fonction des paramètres géométriques de la technique expérimentale. L'analyse des fonctionnes du signal en régime stationnaire et en régime transitoire permette de reconnaitre et isoler les paramètres les fluctuations des quelles ont l'influence la majeure sur les résultats des fit. Cette analyse a permis

de tenir sous contrôle les paramètres sensibles, et de cette façon obtenir une meilleure précision des mesures de lentille thermique.

Table F2 Valeurs des propriétés thermomécaniques des échantillons CaF_2:Nd^{3+},Lu^{3+} obtenues par les mesures de lentille thermique.

Échantillon	$\boldsymbol{D}$ **(cm²/s)**	$\boldsymbol{K}$ **(W/m/K)**	$\frac{\boldsymbol{ds}}{\boldsymbol{dT}}$ $(\mathbf{10^{-6}\ K^{-1}})$	$\frac{\boldsymbol{dn}}{\boldsymbol{dT}}$ $\left(\mathbf{10^{-6}\ K^{-1}}\right)$
CaF_2:0.5% Nd,0.5% Lu	0.024	6.7	--	--
CaF_2:0.5% Nd,1% Lu	0.017	4.9	-2.6	-11.6
CaF_2:0.5% Nd,2% Lu	0.017	4.9	-1.9	-11.0
CaF_2:0.5% Nd,5% Lu	0.013	3.6	-2.7	-11.8
CaF_2:0.5% Nd,7% Lu	0.009	2.4	-2.3	-11.3
CaF_2:0.5% Nd,8% Lu	0.010	2.8	-2.7	-11.8
CaF_2:0.5% Nd,12% Lu	0.008	2.2	-2.5	-11.5

La conductivité des échantillons a été évaluée aussi avec des mesures d'interférométrie transitoire (ou de Jamin-Lebedev). Pour la mesure, un faisceau laser de sonde est divisé sur deux bras avec polarisation mutuellement perpendiculaire par une lame de Savart. Les deux bras sont réfléchis à 180° par un miroir pour passer à travers l'échantillon deux fois sur le même axe, et sont donc recombiné par la lame de Savart. Un faisceau laser pulsé à la longueur d'onde absorbée est focalisé sur l'échantillon en correspondance d'un des deux bras de la sonde. La sonde recombinée est donc divisée par un *beam splitter* polariseur de polarisation à 45° par rapport à celle de la lame de Savart. La différence en intensité entre les deux faisceaux obtenus permet d'estimer la différence de phase entre les deux bras de sonde en fonction du temps. La différence de phase est due aux effets combinés, thermo-optique et d'expansion thermique, introduits ci-dessus.

Malheureusement, plusieurs résultats des mesures d'interférométrie n'étaient pas fiables à cause du très bas rapport signal sur bruit. La raison pour laquelle le bruit des mesures était si haut est la présence des effets de dépolarisation distribués dans le volume des échantillons, qui ont été observés avec des mesures qualitatives de lumière polarisée (Fig. F12).

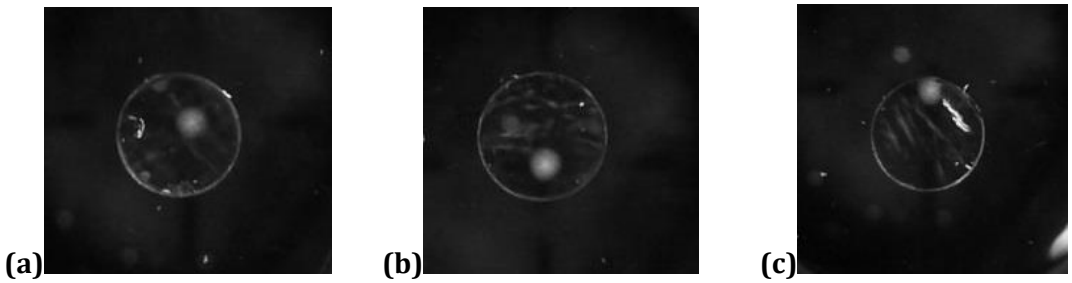

Fig. F12 Les images en lumière polarisée montrent les effets de dépolarisation des échantillons CaF_2:0.5% Nd,1% Lu (a), CaF_2:0.5% Nd,5% Lu (b), et CaF_2:0.5% Nd,12% Lu (c).

Les mesures d'interférométrie qui donnent des résultats précis ont été comparées aux valeurs obtenues avec les mesures de lentille thermique. On peut voir que les deux méthodes sont en bon accord l'une avec l'autre (Fig. F13). On observe que la conductivité thermique du CaF_2:Nd^{3+},Lu^{3+} diminue en augmentant la concentration de Lu^{3+}, en descendant vers 2 W/m/K. Cette valeur est beaucoup plus basse de la conductivité du cristal CaF_2 non dopé (9.7 W/m/K), mais elle est quand-même, pour toutes les valeurs de concentration du codopant, plusieurs fois plus haute de celle des verres phosphates, qui est de 0.57 W/m/K et 0.58 W/m/K pour les verres LG-770 et LHG-8, respectivement.

Les valeurs mesurées ont été comparé à l'évolution prévue par le model de Klemens. On retrouve que les valeurs de conductivité thermique mesurées sont consistent avec celles calculées à hautes concentrations de Lu^{3+}. Par contre, à basses concentrations, les calculs théoriques donnent des valeurs visiblement inférieures aux résultats des mesures. Le model de Klemens donc donne une bon approximation pour hauts dopages, mais n'est pas précis à basses concentration de dopant. On peut conclure que le model de Klemens est cohérent avec les mesures directes pour des cristaux fortement dopés, mais il échoue à faibles concentrations de dopants. Cette différence avec les résultats expérimentaux a été observée en littérature pour différents cristaux [10-12].

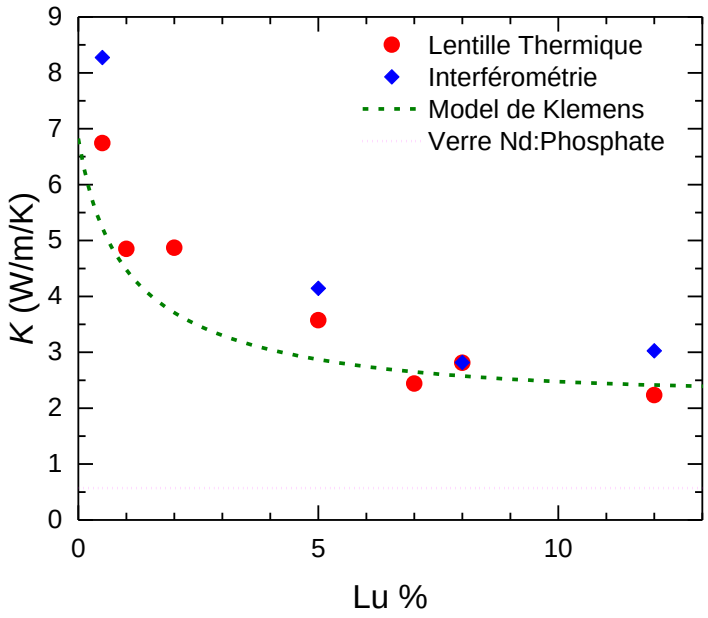

Fig. F13 Conductivité thermique des échantillons CaF_2:Nd^{3+},Lu^{3+} en fonction de la concentration de Lu^{3+}, en montrant la cohérence des résultats entre mesures de lentille thermique (points roux) et d'interférométrie (losanges bleues). On peut voir aussi la comparaison avec la conductivité thermique des verres phosphates (ligne pointillée magenta) et le avec les valeurs calculé par le model de Klemens (trait discontinu vert).

Amplification et Oscillation Laser

Dans le **quatrième chapitre**, les quantités d'intérêt pour l'application laser sont investiguées: les résultats des mesures de gain et de rendement quantique sont reportés, en comparant les propriétés des cristaux fluorures dopés avec néodyme et lutétium avec celles du YAG:Nd^{3+} et des verres laser dopés néodyme. Les résultats expérimentaux sont donc comparés avec des calculs, de façon de corroborer un modèle théorique prédictif pour l'amplification de la puissance laser.

La modélisation du système à 4 niveaux a été appliquée pour obtenir une méthode théorique pour l'estimation du gain optique et du profil du faisceau amplifié. Un programme de calcul basé sur ce modèle pour un expérimente de gain en setup à deux faisceaux laser co-propageants a été composé. Ce calcul devrait permette d'évaluer le fonctionnement d'un avec l'insertion des paramètres géométriques et spectroscopiques du système. Le code donne en sortie la valeur du gain, ainsi que la distribution du coefficient de gain dans le matériel, et le profil des faisceaux laser à travers l'échantillon.

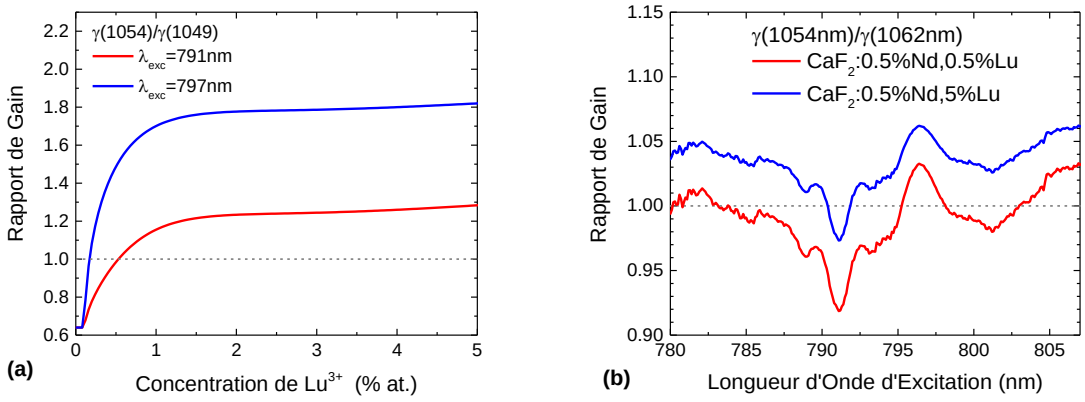

Fig. F14 (a) Rapport du gain entre l'intensité du pic d'émission à 1049 nm et à 1054 nm, démontrant l'incrément relatif en gain laser à 1054 nm avec la croissance de la concentration de lutétium. (b) Rapport du gain entre l'émission à 1054 nm and 1062 nm en fonction de la longueur d'onde d'excitation pour échantillons différents.

Les rapports du gain entre différentes longueurs d'onde d'émission et d'excitation et en fonction de la concentration du lutétium ont été évalués. Les calculs estiment que l'émission à 1054 nm dévient dominante sur celle à 1049 nm au-dessus de 0.1% Lu^{3+} pour l'excitation à 797 nm, et au-dessus de 0.5% Lu^{3+} pour l'excitation à 791 nm. En plus, en excitant à 791 nm, l'émission à 1062 nm est toujours dominante sur celle à 1054 nm, et vice versa pour l'excitation à 797 nm. Au même temps, largeur de la bande d'excitation pour l'oscillation à 1054 nm augmente avec la concentration de lutétium, et celle de l'oscillation laser à 1062 nm diminue. Cet effet est dû principalement à l'augment de concentration des sites NL2 en fonction de la concentration du codopant (Fig. F14).

Un apparat pour des mesures de gain a été préparé en utilisant une configuration pompe-sonde en régime continu. Le faisceau de pompe à la longueur d'onde d'absorption de l'échantillon est obtenu avec un laser accordable Ti:saphir. Pour le faisceau de sonde, une laser CaF_2:Yb^{3+} continu à la longueur d'onde d'émission du CaF_2:Nd^{3+},Lu^{3+} a été installé. Pour ça, un cristal CaF_2:Yb^{3+} a été placé dans une cavité laser en configuration alpha. Le cristal était excité par une diode laser, et un filtre de Lyot a été inséré en la cavité pour accorder la longueur d'onde de sortie. Les deux faisceaux de pompe et sonde ont donc été focalisés sur l'échantillon, en configuration colinéaire et co-propageante. La puissance du faisceau de sonde au-delà de l'échantillon est mesurée, en fonction de la puissance de pompe, avec une photodiode. Le rapport entre la puissance amplifiée et celle incidente est la valeur de gain de l'échantillon.

Les mesures de gain ont été réalisées sur des échantillons de CaF_2:Nd^{3+},Lu^{3+} et sur un échantillon de verre phosphate LG-770, et démontrent que le fluorure peut donner une amplification meilleure des phosphates utilisés actuellement par le LMJ (Fig. F15). En plus, la fluence de saturation de l'absorption pour les photons de pompe peut être estimée avec cette méthode. La saturation de l'absorption de pompe commence autour de 500 mW absorbés, donc la fluence de saturation a été estimée approximativement à 19 kW/cm² de pompe incidente.

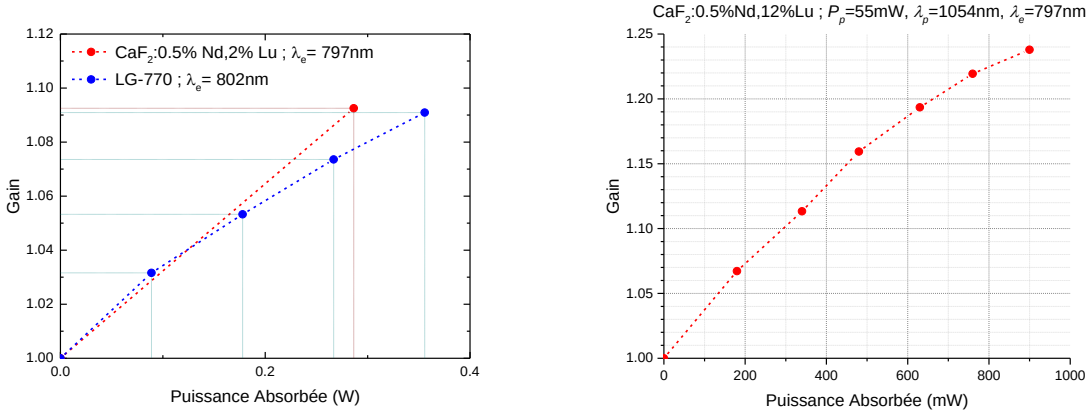

Fig. F15 (a) Comparaison entre le gain du verre phosphate LG-770 et l'échantillon CaF_2:0.5% Nd,2% Lu en fonction de la puissance de pompe absorbée avec un faisceau de pompe centré à 1054 nm. (b) Gain de l'échantillon CaF_2:0.5% Nd,12% Lu en fonction de la puissance de pompe absorbée. Les lignes discontinues sont une guide pour l'œil.

Des cristaux CaF_2:Nd^{3+},Lu^{3+} a été utilisé comme amplificateur dans une cavité plan-concave, en obtenant une émission laser à 1054 nm en régime continu. L'efficience de pente obtenue avec ces mesures est cohérente avec les résultats présents en littérature [13], et ces valeurs sont dans le même ordre de grandeur de celles obtenues avec des cristaux CaF_2:Nd^{3+},Y^{3+} dans le récent travail de Su *et al.* [14].

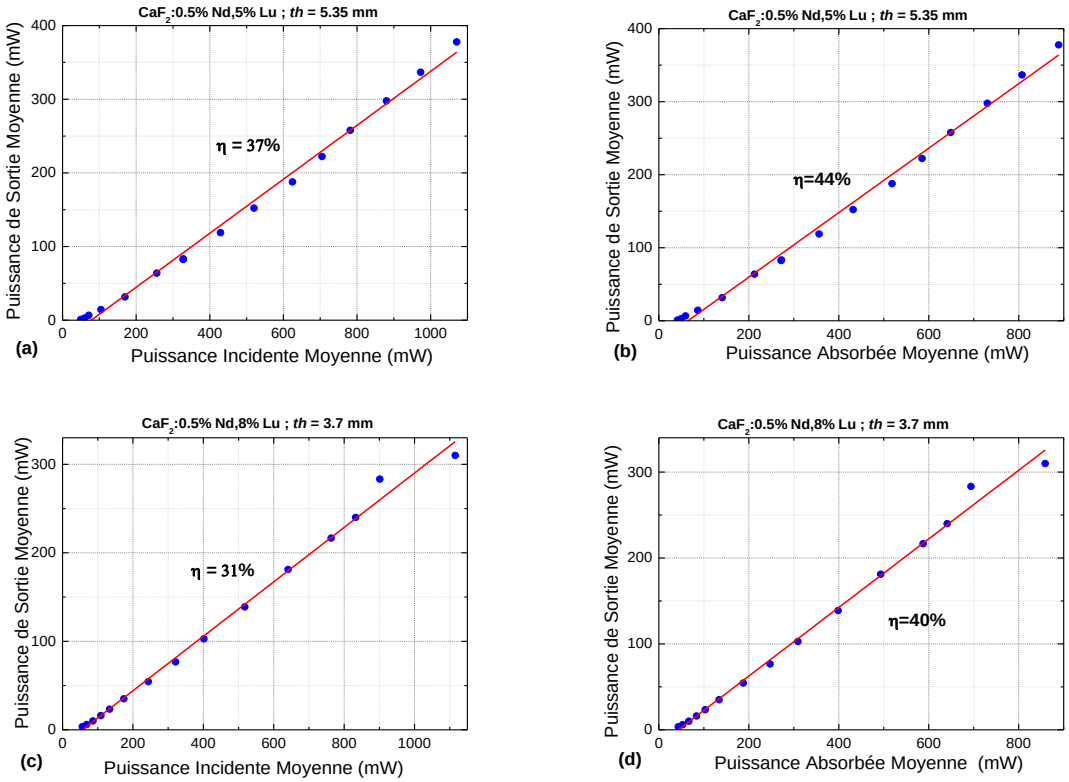

Fig. F16 Résultats des mesures laser pour les échantillons CaF_2:0.5% Nd, 5% Lu (a),(b) et CaF_2:0.5% Nd, 8% Lu (c),(d).

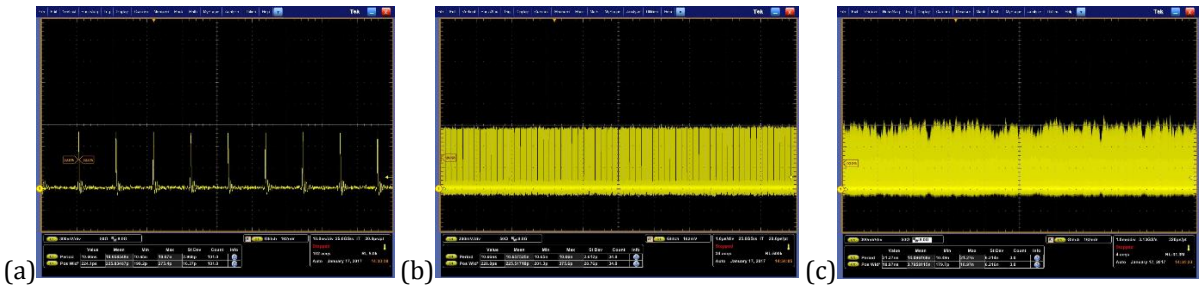

Fig. F17 Trains d'impulsions du laser mode-locked mesurés sur une échelle temporelle de 10 ns(a), 1 μs (b) and 1 ms (c), en montrant période et stabilité du laser impulsé.

L'opération laser pulsée a été obtenue pour un échantillon CaF_2:0.5% Nd,5% Lu en une cavité pliée, en pompant avec un laser continu accordable Ti:saphir. Le régime de mode-locking est obtenu avec l'emploi d'un absorbeur saturable à semi-conducteur (SESAM). Les résultats sont en bon accord avec les calculs des rapports de gain ci-dessus. Les spectres d'émission laser (Fig. F18) montrent un pic très haut à 1054 nm en excitant à 797, avec un deuxième pic plus bas autour de 1062 nm. En excitant à 791 nm, le pic principal est à 1049 nm, avec un deuxième à

1062 nm. Les mesures résolues en temps montrent les trains d'impulsions et permettent d'estimer leur durée.

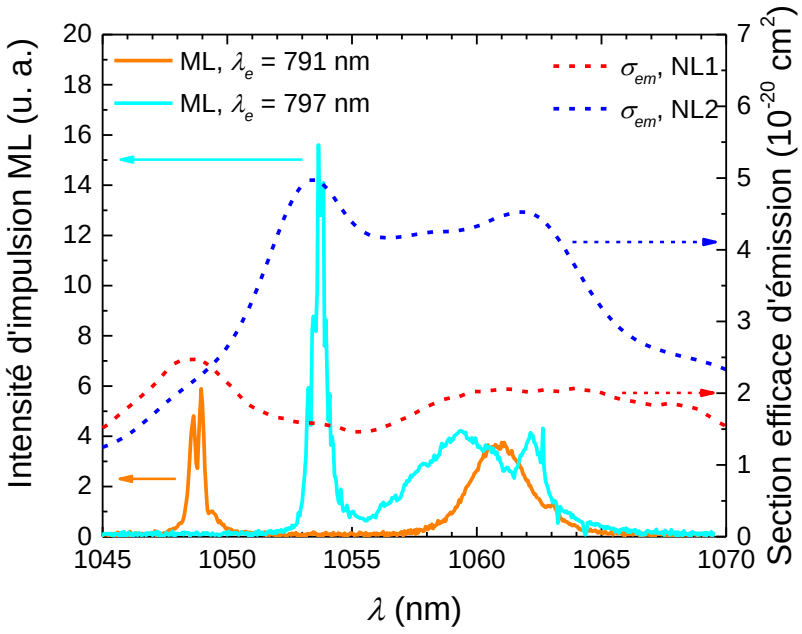

Fig. F18 Spectres d'émission du laser mode-locked avec un échantilloa CaF_2:0.5% Nd,5% Lu, comparés aux spectres d'émission des centres NL1 et NL2.

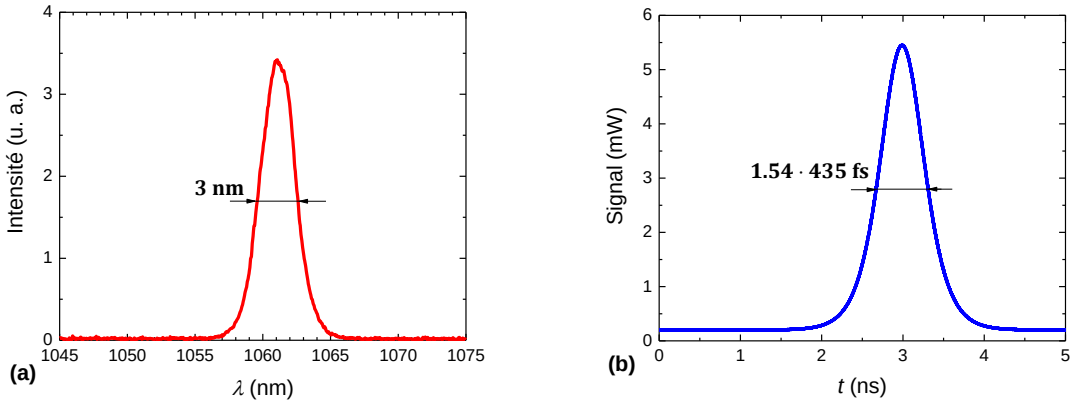

Fig. F19 (a) Spectre de l'impulsion laser mode-locked et (b) autocorrélation de l'émission filtrée à 1062 nm avec excitation à 797 nm.

En filtrant les émissions à différents longueurs d'ondes, on obtient pics spectraux pour les impulsions à 1062 nm avec une largeur d'environ 3 nm, et une durée des impulsions de 435 fs (Fig. F19). Cette mesures sont encore préliminaires, mais elles donnent des résultats très

encourageants, qui montrent la possibilité d'application de ces cristaux au cas des lasers pulsés femtoseconde autour de 1.05 μm.

Enfin, dans le **cinquième chapitre**, les conclusions sur les propriétés des cristaux fluorures dopés néodyme et lutétium sont enfin résumé, en discutant l'option d'une future application de ces matériaux et les études à suivre pour l'optimisation du fonctionnement et la mise en œuvre des amplificateurs basés sur ces systèmes.

Références

[1] S. A. Payne, J. A. Caird, L. L. Chase, L. K. Smith, N. D. Nielsen, and W. F. Krupke, J. Opt. Soc. Am. B 8 (4) pp 726-740 (1991)

[2] T. P. J. Han, G. D. Jones, and R. W. G. Syme, Phys. Rev. B 7, 22 (1993)

[3] V. V. Fedorov, W. Beck, T. T. Basiev, A. Ya. Karasik, and C. Flytzanis, Chem. Phys. 257 (2000) 275-281

[4] F. K. Ma, Q. Zhang, D. P. Jiang, L. B. Su, Y. J. Shao, J. Y. Wang, F. Tang, J. Xu, P. Solarz, W. Ryba-Romanowski, R. Lisiecki and B. Macalik, Laser Phys. 24 (2014) 105703 (7pp)

[5] Kh. S. Bagdasarov, Yu. K. Voron'ko, A. A. Kaminskii, L. V. Krotova, and V. V. Osiko, Phys. Status Solidi 12, 905 (1965)

[6] T. T. Basiev, Yu. K. Voron'ko, A. Ya. Karasik, V. V. Osiko, and I. A. Shcherbakov, Zh. Eksp. Teor. Fiz. 75, 66-74 (July 1978)

[7] T. T. Basiev, A. Ya. Karasik, R. L. Shubochkin, Journal of Luminescence 64 (1995) 259-265

[8] Yu. V. Orlovskii, T. T. Basiev, I. N. Vorob'ev, V. V. Osiko, A. G. Papashvili, and A. M. Prokhorov, Laser Phys. 6, 3 (1996) pp. 448-455

[9] P. G. Klemens, Phys. Rev. 119, 507 (1960)

[10] F. Druon, S. Ricaud, D. N. Papadopoulos, A. Pellegrina, P. Camy, J. L. Doualan, R. Moncorgé, A. Courjaud, E. Mottay, and P. Georges, Opt. Mater. Expr. 1, 3 (2011), 489-502

[11] R. Gaumé, B. Viana, D. Vivien, J. P. Roger, and D. Fournier, Appl. Phys. Lett. 83, 7 (2003) 1355-1357

[12] R. Gaumé, *Relations structures-propriétés dans les lasers solides de puissance à l'ytterbium. Elaboration et caractérisation de nouveaux matériaux et de cristaux composites soudés par diffusion*, PhD Dissertation, Université Pierre et Marie Curie – Paris VI (2006)

[13] J. L. Doualan, L. B. Su, G. Brasse, A. Benayad, V. Ménard, Y. Y. Zhan, A. Braud, P. Camy, J. Xu, and R. Moncorgé, J. Opt. Soc. Am. B 30, 11 (2013) 3018-3021

[14] L. B. Su, Q. G. Wang, H. J. Li, G. Brasse, P. Camy, J. L. Doualan, A. Braud, R. Moncorgé, Y. Y. Zhan, L. H. Zheng, X. B. Qian, and J Xu, Laser Phys. Lett. 10 (2013) 035804

INTRODUCTION

Principles and Problematics

Fluoride crystals doped with rare earth ions are good candidates as substitutes for rare earth-doped glasses in high-energy laser amplifiers, thanks to their broad spectral bands, high thermal conductivity and the possibility of large-scale production. In this work, the properties of fluorite-type crystals doped with neodymium for applications in high-energy lasers will be discussed. In particular, the issue of fluorescence quenching by Nd^{3+} ion clustering is tackled via codoping with lutetium, and the effects of such codoping are also investigated both from the thermomechanical and the light amplification points of view.

Rare earths, which are for the most part identified as the elements in the lanthanide group, have been employed for a long time as a dopant in transparent media because they allow tailoring their optical properties to fit specific needs. Rare earth-doped materials are employed for their luminescence properties, which can be exploited for a variety of applications, including light amplification and laser action [1].

Rare earth-doped crystals usually have characteristically tall and narrow spectral bands, as opposed to the broad, flatter bands of glass samples. This is a consequence of the crystal lattice local symmetries around the active centre positions. However, the spectral band width depends on the crystal composition and the type of doping, so that there are examples of broad-band rare earth-doped crystals. Such is the case of fluorite structures, in which charge compensation takes place and a degree of local disorder is introduced with doping [2]. While sharp spectral features usually allows for higher overall gain, having broad emission bands allows for a broader gain spectrum, and therefore shorter output pulse generation. In particular, these properties must be taken into account in the amplifier material choice for laser devices, as the tailoring of again medium optical features greatly influences the properties of the sample as an oscillator.

The optical properties of a material are not the only ones affected by the insertion of dopants: the doping ions act as phonon scattering centres within the material's structure, which leads to a change in the thermal properties as well. Namely, the thermal conductivity decreases as more and more impurities are introduced [3,4]. In the scope of laser amplifiers, a high thermal conductivity means faster heat dissipation, and therefore higher repetition rates, as well as a higher sustainable absorbed energy per pulse.

All these quantities and their dependence on the composition of the sample are very important to the end of obtaining a suitable material for the desired applications, and must be therefore described in detail in order to understand the phenomena that drive them and thus tailor the conditions under which such materials should be both fabricated and employed. Thus, in order to find the best efficiency as an amplifier material, one must identify the appropriate dopant concentrations for the optimal combination of both optical and thermomechanical properties.

A more detailed introduction on each of these topics will be presented at the start of each respective chapter.

As of today, crystalline materials doped with rare earths have been studied for a significant time, and indeed successfully employed as solid-state laser amplifiers, the most popular being the YAGs and sapphires, as well as the notorious ruby-based laser, which was employed in the making of the first working laser device in history. Because of their sharp spectral features, most crystals pose an additional challenge for very short-pulsed laser generation; on the other hand, many short-pulse lasers are based on rare earth-doped glasses, because of their wide spectral bands. In particular, several pulsed lasers at the 1.05 μm wavelength, employ neodymium-doped glasses as their material of choice [5,6].

Rare earth-doped fluoride crystals, however, offer the advantage of both broad spectral bands and a high thermal conductivity, which allows prolonged laser pulse amplification thanks to the higher heat dissipation and thermal shock resistance with respect to glasses. For this reason, fluoride crystals have been studied as possible pulsed-laser amplifier materials, as in principle they combine all the advantageous properties listed. In particular, CaF_2 crystals are most appealing for being relatively easy to grow, even in large size, and for their particularly high thermal conductivity, in addition to broad spectral bands, comparable to glasses.

In this thesis, an extensive study of neodymium and lutetium-codoped fluoride crystals for high-energy, short pulse laser amplification is presented. In particular, the samples investigated investigated were designed in the framework of the LASCAN project with the CEA – CESTA group, for the enhancement of the Laser MégaJoule front-end amplifiers performances by the replacement of its active components, which are currently Nd:phosphate glasses. The main purpose of this project is to increase the LMJ laser chain repetition rates from 10^{-3} Hz to 10 Hz. In this context, Nd^{3+},Lu^{3+}-doped samples of CaF_2, SrF_2 and BaF_2 with varying lutetium concentrations were grown and their spectroscopic, thermomechanical, and gain properties were characterised.

Spectroscopy

The first quantities to assess for the study of a short-pulse laser amplifier, are its optical and spectroscopic properties. In particular, knowledge of the position and width of the samples spectral bands, as well as their cross sections and lifetimes, is very important for the tailoring of the device. Thus, to identify the most viable composition for the desired application, an in-depth spectroscopic study of the prepared samples is necessary.

In CaF_2 crystals, or their isotypes, rare earths require a means of charge compensation as they are trivalent ions and therefore possess a charge unit in excess with respect to the Ca^{2+} ions in the lattice. Charge compensation takes place because of the appearance of interstitial fluorine ions in a vicinity of each dopant centre: this in turn causes a tendency of other doping ions to occupy nearby cells, leading to the formation of rare earth clusters [2,7]. This may cause undesired phenomena, including up- and down-conversion, as well as fluorescence quenching. Such is the case of Nd^{3+}-doped CaF_2, where clustering takes place at extremely low dopant concentrations, and is particularly inconvenient for the 1.05 μm transition, which is completely quenched. To avoid this drawback, Nd^{3+}-Nd^{3+} clusters have to be broken up so that the single Nd^{3+} ions be separated and do not exchange energy. To do so, codoping with an optically-inactive ion species has been proposed. This has been shown to work, enhancing the spectroscopic properties of the samples, in different occasions, as seen in the case of Pr^{3+}-doped fluorides using Y^{3+} and Lu^{3+} as buffer ion [8,9], and even in Nd^{3+}-doped CaF_2 and SrF_2 codoped with Y^{3+} with encouraging results [10-14]. CaF_2:Nd^{3+},Sc^{3+} crystals have also been investigated [15], which showed the possibility of tailoring the sample emission band shape as well as the emission lifetime, in particular for the 1.06 μm emission peak, via the insertion of inactive ions. Stimulated emission was observed for both the 1.05 μm and 1.06 μm lines in CaF_2:Sc^{3+},Nd^{3+}. The

1.06 μm stimulated emission line however, becomes dominant as the relative scandium concentration increases.

Other possible laser crystal candidates for this project are strontium fluoride (SrF_2) and barium fluoride (BaF_2). These materials share very similar properties with CaF_2, as they all possess very similar cubic fluorite-type lattice structures. All three crystals, doped with neodymium, have been investigated in Payne's work [2]. The Nd^{3+}-doped fluorides spectroscopic properties and clustering tendency of Nd^{3+} ions within the different crystal hosts were compared. Payne concludes his work stating that CaF_2:Nd^{3+} is virtually useless as a laser crystal, due to the early Nd^{3+} ions clustering. Instead, he proposes doubly-doped CaF_2:Nd^{3+},La^{3+} or CaF_2:Nd^{3+},Y^{3+} as viable candidates, and discusses the coexistence of different active centres in the codoped crystals. Payne also identifies SrF_2:Nd^{3+} as a viable laser material, for dopant concentrations of 0.5 at% and lower.

SrF_2:Nd^{3+} is now well known as a laser amplifier material for infrared emission [16-18]. In particular, the different kinds of emitting centres L and M were identified in SrF_2:Nd^{3+}, and their absorption and emission properties were characterised, both in ceramic and crystalline samples. The formation of either cubic or hexagonal active centre geometries was observed in SrF_2:Nd^{3+},La^{3+} [18], and its dependence on the sample composition was assessed, showing the transition from ordered cubic to ordered hexagonal structure as the LaF_2 fraction increases in the composition.

On the other hand, at present times there is little to no information about BaF_2:Nd^{3+} as a laser gain medium, possibly due to the fact that its quantum yield was estimated to be lower than the other fluorite-type crystals [2], making it less appealing for laser applications.

Composite CaF_2-SrF_2:Nd^{3+} crystals were also investigated [19,20]. In particular, Basiev's work demonstrated the tendency of Nd^{3+} ions to cluster in a CaF_2 environment more than within SrF_2, showing the increase in clustered Nd^{3+} centres as the Ca^{2+} concentration increases for samples with the same Nd^{3+} concentration.

To assess the optical and spectroscopic properties of these crystals, standard spectroscopy techniques were employed, and the evolution of the spectroscopic features as a function of codoping concentration was observed. Time-resolved spectroscopy was then used to discern and evaluate the spectroscopic properties, concentration and cross sections of different optically active centres, as well as to assess the removal of inactive Nd^{3+}-Nd^{3+} clusters from

the crystals by lutetium codoping. Doubly-doped SrF_2-BaF_2 crystals were also studied in the search for the optimal spectral band width and shape.

Thermal Conductivity

The thermomechanical properties of the optically active medium are also crucial to the design of a laser amplifier, as they determine the heat dissipation times, resistance to thermal shock, and thermal lensing effects. A study on the samples thermomechanical properties and their dependence on doping concentration is therefore needed for a complete description of the crystals as active components for laser applications.

Crystals, and especially fluorite, are usually known for their high thermal conductivity [21-24]. For this reason in particular, the replacement of neodymium-doped glasses with neodymium-doped fluoride crystals in high-energy laser amplifiers should, in principle, lead to better performances, allowing for the generation of more energetic beams and higher repetition rates. However, it is known that the insertion of structural defects in the lattice gradually reduces the host thermal conductivity. This is a consequence of the introduced ions acting as phonon scattering centres, which limit the heat transmission throughout the lattice.

The decrease in the thermomechanical properties of rare earth-doped calcium fluoride as a function of the dopant was observed by Popov *et al.* in CaF_2:Yb^{3+} at room temperature [23], leading to a drop from nearly 10 $W \cdot m^{-1} \cdot K^{-1}$ to about 2 $W \cdot m^{-1} \cdot K^{-1}$ at high Yb^{3+} concentrations. While the thermal conductivity reduction is significant as the impurity content increases, the value remains several times higher than that of laser glasses, which still makes fluoride crystal an appealing alternative for the improvement of an amplifier thermomechanical properties.

In order to assess the thermomechanical properties of a sample, an appropriate experimental technique has to be implemented. The thermal lens technique in particular is a favourite for the study of optical materials. Thermal lens spectrometry (TLS) is a very popular thermo-optic technique for the investigation of a transparent sample thermal conductivity and thermo-optic path variations, and has been used to assess the properties of many different crystals [25-28]. The advantage of this technique is its reliability, and the possibility to obtain both thermal conductivity and thermo-optic path variation for a sample within the span of a single measurement.

Another interesting technique for the study of the thermomechanical properties of transparent media is transient-state interferometry (or Jamin-Lebedev interferometry), in addition to the thermal conductivity, allows to separately evaluate the population and thermal components of a sample thermo-optic coefficient. It is regarded as a very useful technique in the estimation of the thermo-optic properties of crystals such as YAG [29,30].

Both thermal lens and transient-state interferometry were used to estimate the CaF_2:Nd^{3+},Lu^{3+} samples thermomechanical properties. The evolution of thermal conductivity and thermal diffusivity as a function of codopant concentration was investigated, and the thermo-optic path variation and thermo-optic coefficient were evaluated.

Optical Amplification and Laser Operation

Finally, the light amplification and laser oscillation properties of the samples need to be assessed as well, in order to verify the crystals viability as effective laser amplifier media, and their limitations. The results must then be compared to the phosphate glasses properties, and the differences between the two systems will define the adjustments to the amplifier devices setup and laser chain, in order to optimise their performances.

Rare earth-doped fluorites have already been employed successfully in oscillators, obtaining laser operation. One of the most successful fluorite-based laser materials is CaF_2:Yb^{3+}. CW tuneable laser operation with a CaF_2:1.7% Yb crystal was demonstrated by Petit *et al.* [31] in a plano-concave cavity, with 920 nm pump and a 1% transmission output coupler. They obtained a 50% slope efficiency versus absorbed power and a 72 nm bandwidth about the 1.05 μm emission line. After this first demonstration, a lot of results were reported, especially in the mode-locked regime. Among these results, CaF_2:Yb^{3+}-based multipass laser amplifiers have been studied, obtaining high repetition rate pulsed laser operation [32]. Laser oscillation at both 20 Hz and 100 Hz repetition rate was demonstrated, with no noticeable gain narrowing effects and less-than-500 fs pulses. Friebel *et al.* [33] employed a diode-pumped folded cavity setup with a semiconductor saturable absorber mirror (SESAM), obtaining CW mode-locked laser operation at 1053 nm. The resulting pulses were as short as 99 fs, with a 13.2 nm wide autocorrelation spectrum. The same paper also observed the system oscillation between mode-locked and *Q*-switched emission. Ytterbium-doped CaF_2 crystals have recently played an important role in the design of laser amplifiers for ultrashort, high-power pulse generation, in particular the

PEnELOPE and POLARIS projects in Germany [34,35], and the APOLLON 10 PW project in France [36].

Diode-pumped CW mode-locked laser oscillation and laser pulse amplification was obtained in a folded-cavity setup for $CaF_2:Yb^{3+}$, as well as for $SrF_2:Yb^{3+}$ [24]. Measurements on CaF_2 samples oscillation yielded broader spectra and shorter pulses in comparison to SrF_2 measurements. $SrF_2:Yb^{3+}$ laser output, on the other hand, showed a higher average power. Mode-locked laser operation using a SESAM with $CaF_2:Yb^{3+},Y^{3+}$ crystals [37], obtaining 330 fs-long pulses at 1049 nm.

Neodymium-doped fluorides have also been employed successfully as active material for laser oscillators in recent years. In particular, $CaF_2:Nd^{3+},Y^{3+}$ and $SrF_2:Nd^{3+},Y^{3+}$ have been extensively studied as the active medium. $CaF_2:Nd^{3+},Y^{3+}$ flash lamp-pumped laser was obtained, with laser emission lines at 1054 nm and 1063 nm. The effects of two different active neodymium centres were observed [14,38]. Diode-pumped CW laser operation at 1064 nm with a CaF_2:0.5% Nd,10% Y sample was demonstrated, exciting the 790 nm absorption [10]. Even more recently, CW mode-locking experiments with a CaF_2:0.5% Nd,10% Y sample demonstrated the possibility of obtaining pulses as short as 103 fs, with 12 nm wide emission peaks centred at 1064 nm and 100 MHz repetition rate[39].

The Y^{3+} and Lu^{3+}-codoped $CaF_2:Nd^{3+}$ crystals laser properties have been investigated and compared in the work by Doualan *et al.* [8], exciting the sample at 796 nm and collecting the 1054 nm laser emission. CaF_2:0.5% Nd,5% Lu showed better laser properties than CaF_2:1% Nd,5% Y, possibly as a consequence of lesser Nd^{3+}-Nd^{3+} clustering at lower neodymium concentrations, thanks to the lower overall neodymium concentration. This result makes Nd^{3+},Lu^{3+}-doped CaF_2 a very promising material for NIR laser oscillation, in particular for ICF applications which require 1.05 μm emission, thus leading to the demand for further investigation of the crystal properties and its eventual application to high-power laser facilities.

Laser oscillation with doubly-doped fluoride was also demonstrated using $SrF_2:Nd^{3+},Y^{3+}$. Jelinek*et al*. [11] showed both the CW and pulsed operation with 2 ms pulses and 10 Hz repetition rate. These measurements yielded a wavelength tuneability ranging from 1048 nm to 1070 nm and a 51% maximum slope efficiency in the pulsed regime. Mode-locked $SrF_2:Nd^{3+},Y^{3+}$ laser emission was recently obtained [40], leading to 97 fs long pulses at 1061 nm. Doubly-doped SrF_2 is therefore a very interesting material in the field of research for improvement of high-power laser performances, as a novel option for short-pulse oscillation.

In the research for novel and efficient active media, doubly-doped mixed crystal laser properties have been investigated as well. CW laser oscillation upon 1057 nm has been achieved with CaF_2-SrF_2:0.65% Nd,10% Y crystals pumped on the 796 nm absorption line [41]. The same material was successfully used to achieve CW *Q*-switched laser pulses using a YAG:Cr^{3+} crystal saturable absorber, with repetition rates in the order of several kHz, and pulse durations in the order of 100 ns. The possibility of using mixed crystals in order to enhance laser performances was thus proven, opening the way to further research on these systems as possible high-power laser amplifier media. In particular, the great interest of these materials is the study and tailoring of their spectroscopic properties via appropriate combinations of different crystals.

In the framework of the LASCAN project, the doubly-doped CaF_2 crystals optical amplification was investigated via gain measurements, and the results were compared between the fluoride crystals and the LMJ Nd:phosphate glasses. The CaF_2:Nd^{3+},Lu^{3+} laser oscillation ability was also assessed, both in the CW and mode-locked regime, with preliminary in-cavity experiments.

Chapters Overview

All the properties discussed above need to be determined to understand the behaviour of Nd^{3+},Lu^{3+}-doped fluorite-type crystals as active media, identify the optimal composition and optimise their properties for the desired application. During the work presented in this manuscript, the doubly-doped fluoride crystals properties were studied, assessing their viability for the replacement of the LMJ neodymium-doped glasses and the improvement of the amplifiers performances. This document will therefore present the methods adopted during the investigation and its results, leading to an extensive description of these materials.

The first chapter contains an overview of the most important aspects of lanthanide doping, which serve as a base for the spectroscopy of rare earth-doped crystals, and adiscussion on the state of the art concerning the samples, experimental techniques and applications which are employed in the course of this work.

The second chapter of this work introduces the samples spectral properties. In particular, the distinct absorption and emission spectra, fluorescence and radiative lifetimes as well as the respective concentrations for the two main emitting centres in CaF_2:Nd^{3+},Lu^{3+} are

presented. In this chapter the correspondence between the observed active sites and the known local symmetries will be discussed. One can then see that one site most likely correspondsto the L^* centre, and the other to the M' and N' centres on the other hand as reported in the literature for $CaF_2:Nd^{3+},Y^{3+}$.

In the third chapter, the thermal conductivity and thermal expansion coefficient of $CaF_2:Nd^{3+}$ samples codoped with various amounts of Lu^{3+} are investigated by means of thermal lens spectrometry and transient-state interferometry measurements. The techniques accuracy and the critical parameters at play are discussed. The results are then compared with the theoretical model proposed by Klemens [42] and the model validity is discussed.

In the fourth chapter, the $CaF_2:Nd^{3+},Lu^{3+}$ samples optical gain and viability as a laser medium are introduced. Gain measurements are performed, comparing the results to the values for neodymium-doped phosphate glasses and the pump power values at which absorption saturation takes place. A theoretical model for the samples gain is also introduced for comparisonwith the measurement results. Finally, the $CaF_2:Nd^{3+},Lu^{3+}$ crystals laser emission properties are investigated, both in the CW regime in a plano-concave cavity, and in the mode-locked pulsed regime in a folded cavity setup.

The last chapter sums up the results and traces the final conclusions for the entire work. Finally, the perspectives for further investigation are discussed, with the purpose of leading to the sample properties optimisation and their application as high-energy ultrashort pulsed laser amplifiers.

CHAPTER 1

"One can never produce anything as terrible and impressive as one can awesomely hint about."

Rare Earth-Doped Crystals for High-Energy Lasers

High-power or high-intensity lasers have been developed – and several are currently under development – all around the globe, and have known widespread success in the scientific community thanks to the large number of application they provide. In fact, high-energy laser sources provide a great variety of valuable applications for research in different fields of physics, as they are able to generate and deliver high amounts of energies with very high spatial and temporal accuracy. Therefore, high-power lasers are regarded as the ideal energy source for a large number of both academic and practical applications.

For instance, the use of high-power laser beams made possible performing high-energy physics, plasma physics, and even astrophysics. Coherent XUV rays and X-rays can also be generated with the use of appropriate high-intensity laser beams. Moreover, the intense electric fields provided by high-power laser beam are particularly interesting for subatomic physics, since they allow overcoming even the intra-atomic bond forces. Particle acceleration is another very important option for the employment of high-power lasers, as it is currently applied for novel medical applications.

Thanks to the interest in all these applications, high-power laser research and development has increased greatly in recent years, achieving kilowatt-level CW beams, pulsed lasers with petawatt peak powers, and single-pulse energies up to the order of the megajoule.

This work is concerned mainly with the investigation on crystalline materials for the improvement of the Laser MégaJoule (LMJ) and PETAL high-energy laser facilities front-end amplifying stages, which drive the pulse energy, wavefront shape and repetition rate. LMJ and PETAL currently employ neodymium-doped glasses as amplifier media, allowing for high-energy and high-peak power pulse generation. However, in their current state, their output is constrained by the limitations of the amplifier glass. In particular, their repetition rate and operating time are limited by the low thermal diffusivity – and therefore long heat dissipation times – of the phosphates they employ.

The use of neodymium-doped calcium fluoride crystals is therefore taken into consideration to replace the active materials in the LMJ/PETAL front-end amplifiers, in order to obtain higher output pulse energy, a higher system repetition rate, and a longer laser operating time. Moreover, the implementation of neodymium-doped fluorides also allows using diode pumping for the master oscillator. The final goal of this research is to obtain 1 J laser pulses with 10 Hz repetition rate at the front-end output.

In this chapter, the state of the art on high-intensity laser research and facilities will be presented. In particular, a more detailed view of LMJ and PETAL will be introduced, discussing the aim of the research on novel active materials for the improvement of their performances. Finally, the concepts at the base of an eventual implementation of neodymium-doped fluorides as an amplifier medium for the LMJ/PETAL front-end amplifiers will be discussed.

1.1 Context and tendencies of high-power lasers

As introduced, high-intensity lasers come in many forms, and have an accordingly extensive variety of applications. One of the most widespread uses for high-intensity lasers is material processing in the industrial sector. Many other options, however, stem from the possibility of surpassing the average oscillation energy of free electrons (ponderomotive energy or quiver energy). Since the development of the first pulsed lasers, research has increased single-pulse energies, surpassing the quiver energy range, and therefore allowing for the use of lasers in relativistic and ultra-relativistic optics (Fig. 1.1). Experimental high-energy physics and particle physics tests can therefore be performed via the use of high-intensity lasers. Recent years have witnessed an increase in high-power laser research and in the development of high-power laser facilities, spurred by the possibility of using these facilities for both research and industrial,

medical, or military applications. This has brought forth an improvement of high-power laser performances, allowing an exponential growth of these facilities output powers with time.

The possibility of generating very high power densities and electric fields allows performing experiments in high-energy physics, relativistic optics and subatomic physic. This makes high-power lasers very appealing to the scientific community as means of probing theoretical models, and performing nuclear reaction experiments, as well as for other academic applications, for instance in astrophysics, for the investigation of exoplanetary environmental conditions.

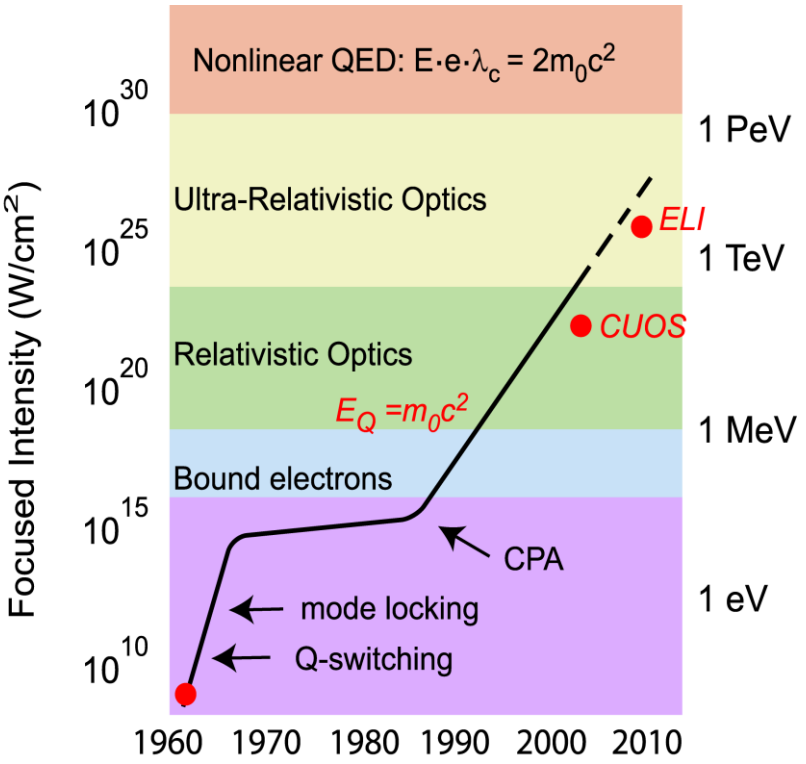

Fig. 1.1 Evolution of laser pulse intensity through the years.

Health science also has a very strong interest in high-power lasers, in particular as far as particle acceleration applications are concerned. In fact, the development of relatively small-scale high-power lasers (such as so-called table-top petawatt lasers) opens a path for novel cancer treatment techniques. Such systems may indeed be employed as accelerator mechanisms for protons and other subatomic particles, which may be used for hadron therapy.

High-energy and high-power lasers are also interesting for military applications. For instance, aerial defence systems based on kW lasers have been proposed in the last decade.

These systems (such as HELLADS) are designed to employ high-power laser beams to destroy offensive artillery in mid-air by direct laser exposition. High-energy lasers may also be used for nuclear fusion ignition – meaning the achievement of a nuclear fusion chain reaction releasing large amounts of energy – as the mechanism for compression and heating of nuclear fuel. This of course provides applications both in the military context, allowing for the realisation of novel nuclear weaponry – and therefore nuclear deterrents, and in the energy production field, providing clean energy production controlled and efficient nuclear fusion.

Finally, high-power lasers have several applications that make them appealing for industrial use, primarily as material processing tools. In particular, the development of performant, affordable and compact high-intensity lasers is therefore of course one of the main interests in this field.

The increasing concern with these laser systems calls for extensive research on laser amplifier architectures, materials and geometries to tackle the issues and limitations arising from the extremely high energies involved in the operations of such devices and facilities.

One of the main issues in high-power and high-energy lasers is thermal damage. Very high pulse peak powers and repeated pulses can damage or deteriorate the materials and components, which limits the system's performances. This, of course, calls for in-depth research on materials for the amplifier stages, as well as for other components, in order to raise the chain components damage threshold.

In addition, other solutions have also been proposed and put into practice. Chirped-pulse amplification (CPA) is one such solution. In short, the technique consists in stretching out in time the optical pulse, amplify the stretched signal, and re-compress it into the final amplified pulse. By stretching the pulse, the peak power is greatly reduced, and this allows for the achievement of much more energetic output pulses while avoiding thermal damage to the amplifier material. The combination of CPA with OPAs into optical parametric chirped-pulse amplification (OPCPA) has been extremely successful, allowing active pump amplification of short, high-power pulses. OPCPA is nowadays the state-of-the-art architecture for short-pulse high-power laser amplification, since not only does it tackle the damage issue, but it also reduces the beam distortion due to thermal lens phenomena and power losses by amplified spontaneous emission. Moreover, it allows amplification by many decibels with a single pass, and therefore the construction of more compact amplifiers.

Another method for limiting detrimental thermal effects and ensuring higher amplification consists in branching the laser light into numerous beamlines, which are then fired simultaneously and converged on the same spot in the target chamber. In this way, the total laser power is divided among the different beamlines, and recombined upon the target for the experiment. Furthermore, beam-shaping techniques are used for optimising amplification. In particular, the beams are usually shaped into square sections, with flat profiles, which help avoiding uneven gain, saturation effects and thermal damage, which can take place in the case of a narrower, peak-function profile.

In order to enhance pumping efficiencies, diode arrays have replaced flash lamps as the most common pumping mechanism for high-power laser drives. The diode emission wavelength can be tuned via temperature control, which allows more efficient pumping and therefore more efficient amplification, as well as more responsive output, thanks to the diodes being directly controlled by current, and higher, more concentrated brilliance at the desired wavelength.

However, diode pumping requires the active material to have broad absorption bands for maximum efficiency, which is one of the main defining requirements for the amplifier material choice. This choice in turn determines the spectroscopic properties of an amplifier, but it also affects the system's thermal limitation. A material with a higher damage threshold can amplify laser beams to higher powers without suffering permanent degradation, which is extremely important for the optimisation of output intensity. Secondly, the material choice determines the laser chain working characteristics. In particular, a high thermal conductivity allows for faster dissipation of the heat deposited during the amplification, and therefore defines the cooling mechanism specifics. This is particularly important for pulsed lasers, since the heat dissipation time is a limiting factor for the laser repetition rate. In addition, a more efficient heat dissipation also allows the system operating for longer periods before it must be shut off to avoid thermal damage to the active materials. Materials with high thermal conductivity are therefore very valuable for pulsed high-intensity lasers. However, in order to obtain very short, sharp pulses, the material must also possess very broad emission bands. All these requirements make research on novel gain materials very important for the improvement of high-power pulsed lasers. In particular, favourable thermal properties are most important in materials for front-end amplifiers, which drive the whole laser chains and thus strongly influence their operating parameters.

Glasses are widely used for ultrashort laser operation because of their broad spectral bands, however their low thermal conductivity is a detrimental factor for their operating

times and repetition rates. On the other hand, crystals are more common for high-energy and high-average power applications, because of their narrow but very intense spectral features.

In order to minimise losses, most high-power laser amplifiers operate in the infrared range, where most materials are transparent, and reach the correct wavelength for their application by means of frequency conversion at the output. For this reason, neodymium- and ytterbium-doped amplifier materials are most common because of their favourable spectroscopy. In general, Yb^{3+}-doped materials are a worldwide favourite for high-intensity laser amplifiers, because of the simplicity of their level structure, the low quantum defect, their long emission lifetimes and the possibility of diode pumping. Ytterbium-doped glasses, as well as crystals such as Yb:YAG and CaF_2:Yb^{3+} have been successfully implemented as active materials for high-intensity applications.

1.2 High-Power Lasers: Different Kinds for Different Applications

High-intensity lasers, which may benefit from the implementation of rare earth-doped fluoride crystals, are divided into three main categories. The distinction among these categories is made based on the carried energy, length and repetition rate of their output pulses. The first category is high-energy lasers, whose output consists of short single pulses (nanoseconds or shorter) carrying very high energies. Another category is petawatt lasers, including ultrashort pulsed lasers (with pulse duration the fs range), which have very high peak power, reaching the order of 1 PW – hence the denomination. The third is the high-average power category, which can be anywhere between continuous or short-pulse, and carry high average output power (in the order of kW).

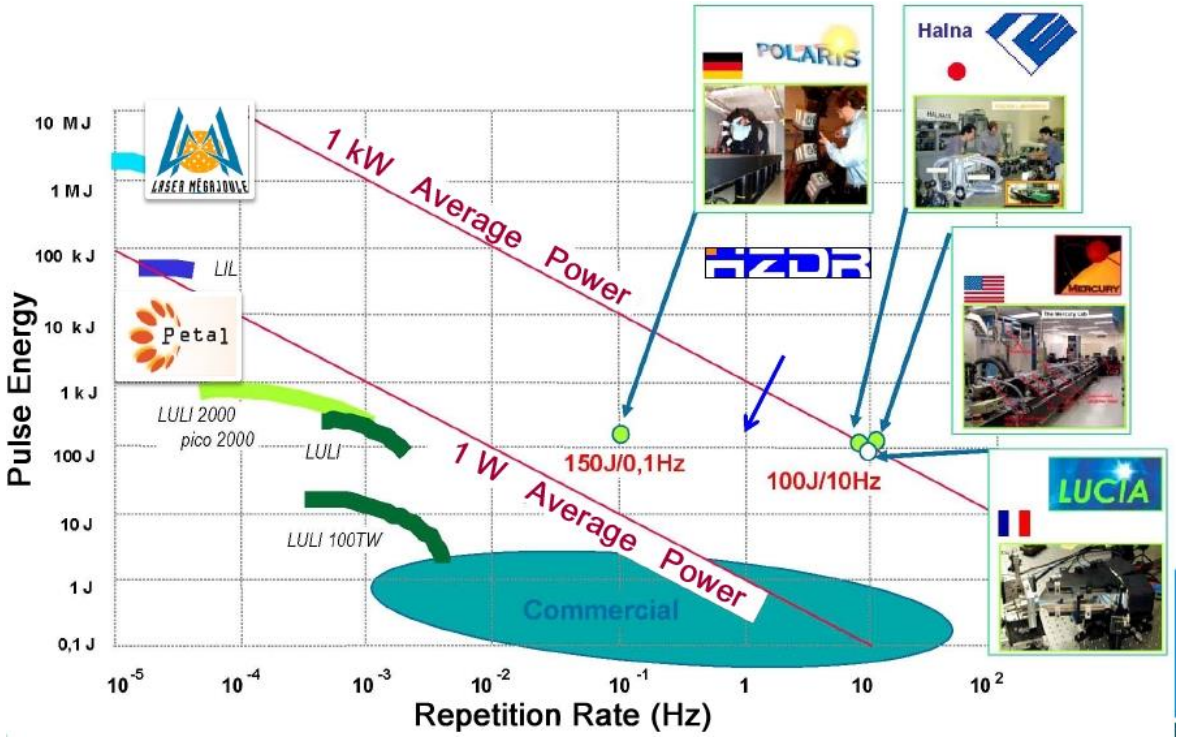

Fig. 1.2 High-intensity laser facilities in the world.

Over the years, several high-intensity laser facilities have been built all over the world, ranging from high-energy lasers to high-repetition rate systems (Fig. 1.2).

In the next paragraphs, the state of the art of high-intensity laser facilities – albeit non-exhaustive – will be presented, to provide the context in which the contents of this manuscript are framed, as well as some details on laser chain design, architectures and materials. The entirety of high-intensity lasers hereby discussed will be organised by the three categories previously defined, starting with the high-energy lasers, followed by the high-peak power lasers, and concluding with the high-average power lasers.

1.2.a High-Energy Lasers

As, introduced, so-called high-energy lasers are pulsed laser devices which deliver large amounts of energy with each pulse (kJ-level or higher). This category includes lasers with generally low repetition rate, due to the large energy values per pulse involved, which generate equally large amounts of heat to dissipate by the amplifier materials. High-energy pulsed lasers are especially interesting for their use in nuclear and plasma physics, thanks to the very high electric fields they are able to generate, which can be used for the production of

coherent extreme ultraviolet (XUV), X-rays and plasmas. Particularly, they may be employed as the trigger mechanism for the process of inertial confinement fusion (ICF), and therefore play a key role in the advancement of research on sustainable energy production, as well as military weaponry. Other high-energy laser applications include, of course, high-energy physics and laser-matter interaction experiments that can be set up for the testing of theoretical models.

For the purpose of ICF, a very specific design is required. To achieve efficient nuclear fusion, it is necessary to obtain very high-energy pulses at the wavelength absorbed by an X-ray source, generally consisting of a heavy metal pellet (*hohlraum*), which also acts as the fusion fuel container, holding a mixture of hydrogen isotopes deuterium and tritium. The X radiation in turn excites the deuterium and tritium nuclei that compose the fuel to very high temperatures, and the radiation pressure condenses them to very high densities at the centre of the pellet. This application requires very specific parameters, and therefore calls for an in-depth study of novel laser materials, and for the tailoring of their properties to suit the purpose of the laser amplifiers.

High-energy solid-state laser (SSL) projects for the demonstration of ICF are underway all around the globe [43]. For instance, the High Power laser Energy Research (HiPER) project in Europe [44-46], the Laser Ignition Fusion Engine (LIFE) project in the United States [47], and the GEKKO XII project in Japan [48] are working towards the achievement of efficient nuclear fusion. In addition, several high-energy SSLs are currently used as coherent XUV and X-radiation sources, and experimental verification of theoretical models. In this context, research on the implementation of rare earth-doped fluorides is predicted to allow for enhanced laser performances. However, to devise these improvements, one must first have a general knowledge on state-of-the-art designs.

Currently, one of the most important high-energy SSLs facilities is the American Lawrence Livermore National Laboratory (LLNL), home of the National Ignition Facility (NIF), which housed several lasers, ultimately leading to its current installation. Three of the largest and most prominent of such lasers are Janus, Argus and Shiva [49].

Janus, a kJ-class laser with 200 ps to 10 ns long pulses, with energy per pulse ranging from 200 J to 1 kJ, was originally set up for ICF experiments. It was later repurposed for studies on the equations of state (EOS), operating as an ultra-high pressure shockwave generator. Janus was able to obtain shockwaves up to 1 TPa of pressure on an aluminium target.

The second laser chain, Argus, reached output energies of 2 kJ per pulse, with 0.1-1 ns pulse durations. Argus was used mainly for laser-matter interaction studies, converting the fundamental beam wavelength (1053 nm) to the second (532 nm) and third harmonic (351 nm).

Finally, Shiva, which reached a total of 10 kJ per pulse, with durations between 100 ps and 30 ns, was dedicated to the ICF experiments. Shiva consisted of 20 amplifier chains, driven by a Nd:YAG oscillator, each carrying about 500 J of energy to the target. Frequency tripling was used to convert the IR beams to the UV (351 nm), which is the necessary wavelength to obtain the plasma temperature and compression in the experimental chamber for the start of nuclear fusion in a deuterium and tritium-filled target. The full-power frequency conversion mechanism was first achieved within the now-dismissed Novette laser in 1983-1984, and the same system has been used in every ICF laser thereafter.

The Nova laser, for which Novette was a test bed, was the first chain built for the express purpose of obtaining ICF ignition. Nova was a Nd:glass-based, Xe lamp-pumped laser, consisting of 20 beamlines capable of delivering a combined energy of approximately 100 kJ in the IR, or about 40 kJ after conversion to the UV, with a single 2-4 ns pulse. The Nova laser was dismantled in 1999, failing to obtain ignition, but providing a better understanding of the instability issues remaining to tackle. These results led to the design of the NIF.

The current NIF laser chains (Fig. 1.3) use neodymium-doped phosphate glasses as the active material, amplifying the Nd^{3+} 1.05 μm emission wavelength by pumping at 0.8 μm. The system employed in the facility is based on the laser chain of Mercury, a high-average-power laser able to deliver 50 J of energy per pulse with a 10 Hz repetition rate. The main difference between NIF and Mercury is the pumping method. While NIF uses xenon flash lamp excitation as a pump, Mercury is a diode-pumped solid-state laser (DPSSL).

Fig. 1.3 National Ignition Facility (NIF) laser bay at the LLNL.

The aim of the NIF is to obtain a 500 TW peak-power, picosecond-long flash for the ignition of ICF in a nuclear fuel pellet. The apparatus consists of 192 combined beamlines, each including Nd:phosphate-based amplifiers [5], driven by an ytterbium-doped low-power optical fibre laser, called the master oscillator [50]. The amplified beam, at 1053 nm, is frequency-tripled to 351 nm before entering the experimental chamber, and nominally delivers a single 1.8 MJ pulse upon the nuclear fuel (deuterium-tritium) target. Due to the high energies involved and the subsequent heating and deformation of the laser glass slabs within the chain, the facility cannot fire more than one shot per day. As anticipated at the start of the chapter, current research is working towards faster cooling processes, leading to shorter recover times, which would allow firing the pulses more often.

The most direct competitor of the NIF is the Laser MégaJoule (LMJ), housed at the CESTA facility near Bordeaux, in France. Similar to the NIF, the LMJ employs Nd:phosphate laser glasses for the amplification of its pulses, and is designed to deliver single-pulse energies of 1.8 MJ at 351 nm with a 176-beam setup for ICF research. The work presented in this manuscript takes place in the framework of the LASCAN project for the enhancement of the LMJ performances. Therefore, a more detailed description of this facility and the aforementioned LASCAN project will have a dedicated section further on within this chapter.

Currently, the NIF and LMJ installations are by far the leading facilities for high-energy laser research and development worldwide. However, while extremely important both historically and from the technological point of view, the two alone do not give an exhaustive overview of

the advances in the field. Other interesting examples of performant high-energy laser facilities, for instance, are found in Asia, and in particular in Japan. The most prominent is the GEKKO XII laser, housed in the Institute for Laser Engineering (ILE) in Osaka. GEKKO XII is a 12-beam DPSSL intended for ICF experiments. As for other ICF facilities, it uses Nd:glass as the amplifier material, obtaining 1.05 μm laser beams. However, unlike other high-energy lasers used for ICF, GEKKO XII does not employ frequency tripling, but only frequency doubling at its output, achieving 532 nm pulses. Compared to facilities such as the NIF or LMJ, GEKKO XII is very small, with 10 m long beamlines. In turn, of course, it has lower output energies, delivering about 10 kJ pulses with duration of 1-2 ns.

Another project for a high-energy laser has been started in the ILE, named GENBU [51,52], with the aim of eventually reaching 10 ps long output pulses at 1.05 μm, with 1-10 kJ pulse energy and a 16 Hz repetition rate. In its first stage, GENBU is designed as an Yb:YAG-based DPSSL to be employed as a nuclear reactor drive, pumped by an Yb:fibre laser as a master oscillator. A joule-class laser, GENBU-Kid, is currently under construction to test the chain design. This is particularly interesting as it uses diode-pumped rare earth-doped crystals as the front-end amplifier materials, giving a frame of reference for the work on the improvement of these stages in high-energy laser chains. Its high-energy output end will be operated as a neutron source for the production of inertial fusion energy (IFE), but a femtosecond petawatt output end, which will used for medical applications, is also included in the design.

There are several high-energy laser facilities currently operating, under construction or in the design process in Europe as well. The European Union is currently working on the so-called High Power laser Energy Research facility (HiPER), a project aimed to obtain high-gain ICF while reducing the facility construction and maintenance costs by using lower-energy laser beams (70 kJ) than other facilities such as the NIF. In order to do so, HiPER intends to use an approach called “shock ignition” [53], which provides better fusion efficiency. Shock ignition is a two-step process, which differs from standard ICF ignition in that the DT fuel compression and ignition are decoupled. For this purpose, a lower-power, longer pulse is used to induce a relatively slow compression, after which a second, very short and very powerful shock pulse deposits the heat and starts the ignition, thus triggering the chain reaction at the time when the fuel density is highest [54]. The project is, of course, very important for advances in ICF engineering, which is what makes it particularly interesting and worth keeping up-to-date with.

Other currently working high-energy laser facilities in the European continent include DiPOLE, Orion and Vulcan in the United Kingdom, and Asterix IV (or PALS) in Czech Republic.

The Orion laser, housed at the British Atomic Weapons Establishment (AWE), is a good example of a Nd:glass-based system. It is able to provide 5 kJ, nanosecond-long pulses, as the result of 10 combined beamlines, tripling the 1054 nm fundamental wavelength to 351 nm at the output [55]. These beams are used for ICF experiments, while two additional beamlines provide femtosecond, petawatt pulses that are employed in combination with the ten longer pulses for plasma physics studies.

A similar system is Vulcan, housed at the Rutherford Appleton Laboratory in Oxford, also employed mainly for ICF research. The Nd:glass-based Vulcan laser delivers 2.6 kJ nanosecond-long pulses. Similar to Orion, two of the 8 Vulcan beamlines are dedicated to ultrashort PW laser pulses.

The DiPOLE and Asterix IV lasers share a similar purpose, that is, high-brightness X-ray flash generation. However, the two systems differ in active material and chain composition. In particular, DiPOLE (Diode Pumped Optical Laser for Experiments) is interesting as a DPSSL. It is based on Yb:YAG amplifiers and delivers 100 J pulse with 10 Hz repetition rate. DiPOLE was the first DPSSL to break the 1 kW "limit" at its full design performance in 2016, and it is used for studies on matter under extreme pressure and temperature conditions, simulating exoplanet environments. This makes DiPOLE a good example to take into consideration as a reference for high-energy DPSSL design.

On the other hand, Asterix IV (or PALS, Prague Asterix Laser System) is a single-beam, photolytically pumped terawatt iodine laser, and it uses a UV flash lamp as the pump for the master oscillator. It is able to reach output pulse energies of 1 kJ at 438 nm after the tripling of its fundamental line, and with pulse duration between 300 and 500 ps. The system is also used for laser-plasma interaction experiments [56].

1.2.b Ultrashort High-Peak Power Lasers

The lasers of the second category, the ultrashort, high-peak power systems, have been developed in order to deliver high amounts of energy in the shortest time possible and reach the highest peak powers achievable. In fact, this category of lasers is able to reach petawatt–level power at the peak of each output pulse, and very short pulse durations, in the order of 100 fs,

hence the name femtosecond lasers or petawatt lasers. Since they also work in single-pulse regime, they may be considered a sub-category of high-energy lasers, the main difference from the latter being the pulse duration and peak power ranges.

In particular, the invention of CPA, has allowed the power of laser pulses to increase greatly (see figure 1.1), providing a valuable tool that allowed for the birth of the ultrashort high-peak power laser, leading to the recent achievement of petawatt-class lasers. In fact, the application of CPA – initially designed for radar signals – to lasers has led to greater amplifications than those possible with other techniques, as it contours some of the limitations of standard direct amplification, thus allowing much more intense output signals with very short duration after the compression.

These laser systems are able to generate extreme conditions and can be used to investigate previously unobtainable states of matter, which makes them highly valuable for fundamental research and applications in high-energy and plasma physics [57]. For instance, in the framework of ICF, femtosecond laser pulses are commonly used in conjunction with high-energy laser beams, and can also be used to obtain so-called "fast" ignition [58] thanks to their very fast insertion of heat. In this approach, the heat deposition is decoupled from the compression, provided by a high-energy laser beam that triggers the *hohlraum* X-ray emission. The decoupling allows having a more uniform and symmetrical fuel distribution the at the instant of heat insertion, and the ultrashort pulse then triggers the nuclear burn beginning from a peripheral spot, rather than at the centre of the pellet, which leads to the chain reaction spread throughout the compressed gas (Fig. 1.4). Alternatively, a hollow cone may be used to allow the ultrashort laser pulse to reach the pellet centre and trigger the burn from its core. While this approach to ignition is less reliable and harder to achieve– with current technology and expertise – than the conventional "central hot spot" mechanism, it allows for much higher efficiencies. Fast ignition follows a very similar concept to shock ignition, with the difference that it uses two different laser beams rather than a sudden, short increase of the same beam's intensity.

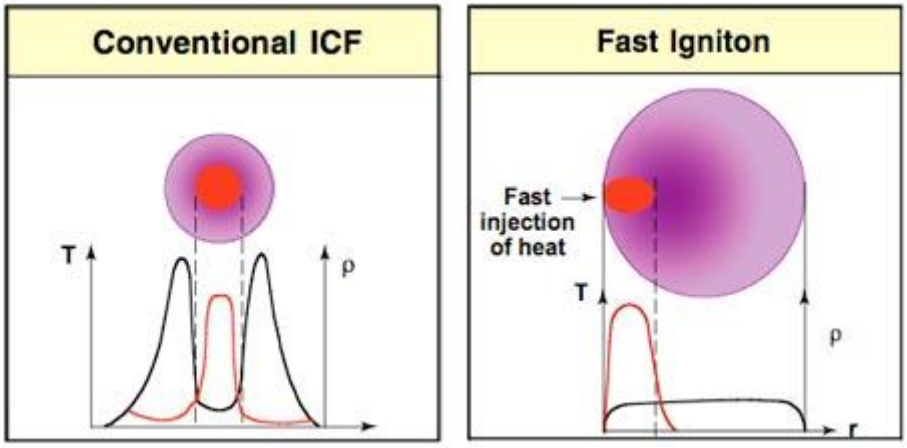

Fig. 1.4 Density and temperature profiles of a conventional central hot spot inertial confinement fusion target and a fast ignition target (from the LNLL website).

Another prominent interest of petawatt laser research is obtaining compact particle accelerators. In particular, the possibility of designing and realising table-top particle accelerators driven by compact high-power lasers is very appealing, for both research and medical centres. The feasibility of such a system has already been demonstrated [59], opening the way for the production of these devices and spurring further research in the field.

Currently, two of the most powerful femtosecond beams in the world are those of AWE's Orion laser, which also operates as a high-energy one-shot laser, as explained before. The two ultrashort beams of Orion carry 500 J nominal energy each, with less-than-500 fs duration at 1054 nm [60]. This allows Orion to achieve about 1 PW peak power per pulse.

The Vulcan laser at the Rutherford Appleton Laboratory also includes two femtosecond beamlines, as introduced before, and has a similar architecture to Orion. Moreover, both Orion and Vulcan are Nd:glass-based lasers Like Orion, Vulcan is able to deliver 500 J pulses with durations under 500 fs [61].

The Rutherford Appleton Laboratory also houses Astra-Gemini, a Ti:sapphire crystal ultrashort laser, able to provide 15 J output pulses at 800 nm, with durations as short as 30 fs, thus reaching 0.5 PW peak power. Astra-Gemini is used for the generation of coherent X-rays, as well as energetic electron or proton beams. Ti:sapphire amplifiers have become an increasing successful component for ultrashort-pulse lasers, thanks to their commercial distribution that makes them available even to smaller groups, thus allowing a large diffusion of Ti:sapphire-based ultrashort devices in recent years.

Other rare earth-doped crystals have also been implemented for ultrashort pulse generation in high-power lasers. In particular, fluoride crystals were successfully employed. These crystals are very appealing material for fs pulse amplification, because they are able provide short-pulse emission like glasses, and at the same time sustain more frequent and more intense power spikes and greater thermal stress.

Indeed, two main projects employ CaF_2:Yb^{3+} as their amplifier material of choice, both situated in Germany: the Petawatt Optical Laser Amplifier for Radiation Intensive ExperimentS (POLARIS) at the Helmoltz Institute in Jena, and the Petawatt Energy-Efficient Laser for Optical Plasma Experiments (PEnELOPE) at the HZDR.

POLARIS employs both ytterbium-doped glasses and CaF_2:Yb^{3+} crystals in its amplifier chain, and is currently the only fully DPSSL with output pulse peak power reaching 0.2 PW. The system is pumped at 940 nm, and it generates pulses centred at 1030 nm with a FWHM of 19 nm and a 0.02 Hz repetition rate. The ultrashort output pulses of POLARIS are obtained via CPA, they are under 100 fs long, and carry about 17 J of energy each.

PEnELOPE, on the other hand, is a facility currently under construction that will house a laser system designed to deliver 150 J pulses with a 120 fs duration and a 1 Hz repetition rate. The PEnELOPE laser employs CaF_2:Yb^{3+} slabs and will be fully diode-pumped. The seed pulses are generated via an Yb:KGW oscillator at 978 nm and the output will be centred at 1035 nm, with a FWHM of 20 nm, and amplified via CPA [34]. PEnELOPE is designed for proton acceleration, in the interest of proton therapy applications, however a second laser target chamber in the same facility, called DRACO (DResden laser ACceleration sOurce), will be dedicated to electron acceleration, ideally delivering 25 fs long, 30 J pulses.

Investigation and implementation of novel laser materials is therefore extremely important to this kind of lasers, as it affects sensibly their performance. In particular, in the interest of ICF applications, research on neodymium-doped materials for ultrafast lasers is already underway, as it allows delivering pulses at the ideal wavelength for ignition. In this framework, neodymium-doped crystals, and in particular Nd:fluorides are the object of increasing interest, as they are predicted to push further the laser amplifiers limitations.

Another petawatt-class laser program currently underway is ELI, the Extreme Light Infrastructure, which is part of a European effort. ELI is based on four sites, three of which are situated respectively in Czech Republic (ELI-Beamlines), Hungary (ELI-ALPS, Attosecond Light Pulse Source), and Romania (ELI-NP, Nuclear Physics). The fourth site (ultra-high

intensity) has yet to be decided. ELI is designed for fundamental physics research, providing access to novel, high-performance technologies for the study of plasma physics, XUV, X- and γ-radiation, hadrontherapy and radiography to the scientific community worldwide.

In Japan, a high-peak power line was added during an upgrade to GEKKO XII. This line uses CPA to deliver 0.5 PW peak-power pulses carrying a total energy of 0.4 kJ. Kodama *et al.* [62] proved the function of this beamline as an efficient system for ICF performance improvement. The PW beam was successfully used in 2002 in combination with the kJ-class beamlines, decoupling heating and compression effects. This allowed obtaining fast ignition, and a 3 order of magnitude fusion yield enhancement.

1.2.c High-Average Power Lasers

High-average power lasers take a different path with respect to both high-energy and ultrashort lasers, in that they provide lower-energy output pulses with much higher repetition rates, or even CW. High-average power lasers have the advantage of being operational for an extended period, during which they can deliver a steady power flow to the target. Cryogenic cooling of the amplifier materials allows for prolonged system operations, preventing high thermal deformations and damage. The main characteristic of these lasers is their ability to deposit high amounts of energy on their target by delivering numerous pulses, each with relatively low energy – compared to other high-power lasers. Therefore, unlike the ultrashort lasers case, the most crucial parameter for these laser devices is their repetition rate, rather than their single-pulse peak power. This makes this category particularly interesting for light-matter interaction studies, coherent XUV or X-ray generation, and, of course, material processing.

High-average power lasers have known a very fast grow in recent times (Fig. 1.5), spurred by the increasing research on high-power laser architecture and amplifier materials. A variety of different active media is currently employed in these systems, as the material choice depends on the intended function, and thus changes based on each chain design and applications.

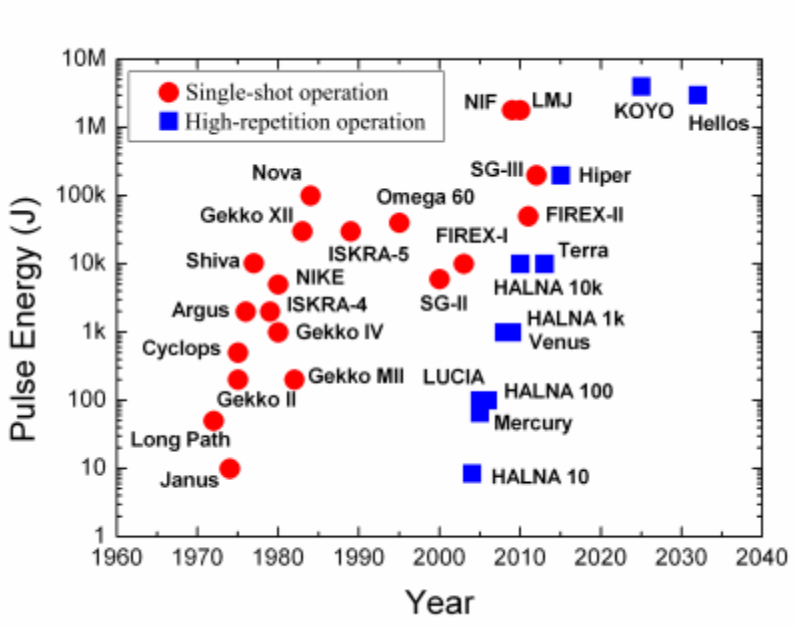

Fig. 1.5 Evolution over the years of the pulse energy achieved for single-pulse and high-repetition rate laser facilities, and prediction of future facilities.

A prominent high-average power laser project is being developed by the Laboratoire pour l'Utilisation des Lasers Intenses (LULI) in France. The LULI is interested in laser-matter studies, in particular hot plasma physics and laser shock peening. For this purpose, a laser chain named Lucia is currently under construction [63]. The Lucia facility is designed as an Yb:YAG-based DPSSL with 1.03 μm output wavelength. The program has the aim of delivering 10 ns long, 100 J pulses with a 10 Hz repetition rate. In this case, Yb:YAG was chosen over other crystals because of its very high thermal conductivity, despite an optical efficiency lower than other popular laser crystals such as Yb:$Ca_8La_2(PO_4)_6O_2$, Yb:$Sr_5(VO_4)_3$ and Yb:$Sr_5(PO_4)_3$. [63] A higher thermal conductivity allows for a faster cooling, which in turn means the system repetition rate can be increased with the appropriate active material choice in regards to its thermal properties. Moreover, the wide Yb:YAG absorption bands are more convenient for pumping via an array of laser diodes, which might have slight differences in wavelength one from the other. Lucia's amplifiers are helium gas-cooled.

A high-average power laser program is also being pursued in the Czech Republic, under the name HiLASE. The main goal of this project is to investigate the optimisation of laser amplifier efficiency, laser diode pumping and cooling methods in order to surpass current output limitations. HiLASE is currently employed in material processing, light-matter interaction experiments, and X-ray generation. The project consists of multiple research

programs, in particular for the achievement of both a 1-2 J output at 1 kHz, and a 100 J output at 10 Hz, intended to be eventually scaled up to 1-10 kJ for IFE generation [64].

Because of the achievement and the many applications of HiLASE, it is a project worth following even in the interest of other systems than high-average power systems. In particular, the data that HiLASE can provide to the scientific community concerning on laser chain component engineering and system performances can prove relevant also to the case of other high-power facilities and ICF applications.

A different means of obtaining high-average power laser emission is a free electron laser (FEL), such as the one housed at the Helmholtz-Zentrum Dresden-Rossendorf (HZDR), at the Electron Linear accelerator with high Brilliance and low Emittance (ELBE), named FELBE. The FELBE laser produces a mid- to far-infrared beam with pulse energy up to 2 μJ, and a repetition rate of 13 MHz. The system can be operated either at its 13 MHz repetition rate with 1-to-25 ps long pulses, or in macropulses 100 μs long with repetition rate up to 25 Hz, and is used for light-matter interaction and material studies.

The use of high-average power lasers for an alternative ICF ignition mechanism was also proposed. The so-called High Average Power Laser program (HAPL) is a currently undergoing project aimed to obtaining IFE production using a sample injection mechanism rather than a stationary target, and a high-power pulsed laser array to ignite the chain reaction. In particular, it is expected to achieve effective nuclear fusion with the combination of several beamlines from two laser outputs, from the so-called Mercury and Electra lasers, which already make up the HAPL experimental system prototype. The array is predicted to deliver a combined energy of 10 to 100 kJ per shot onto the target. This project is supposed to provide a more affordable and more compact alternative to large facilities like NIF or LMJ for ICF reactors, able to operate for longer periods.

Mercury [65] is a DPSSL using ytterbium-doped $Sr_5(PO_4)_3$ crystals (Yb:S-FAP) as the amplifier material. Yb:S-FAP has a very high optical efficiency, which is why it was chosen as the ideal material for high-power DPSSL amplifiers. Mercury's beamlines deliver 15 ns long, 50 J pulses, and the chain is able to run at 10 Hz for several hours (3 10^5 shots fired). The amplifier crystals are cooled with a high-speed helium gas cooling system.

Electra [66] is a KrF gas laser which yields 100 ns long flat-top pulses, with 5 Hz repetition rate and single-shot energy higher than 400 J. Electra is pumped by 500 kV, 110 kA electron beams, and has been demonstrated to run continuously for over 30 thousand shots.

Another DPSSL system for ICF applications similar to Mercury was developed in Japan, with the aim of reaching 100 J pulses at 10 Hz. This project is called the High Average-power Laser for Nuclear Fusion Application (HALNA). Its front end consists of an ytterbium-doped fibre as master oscillator, and a Nd:YLF front-end ring amplifier. HALNA successfully delivered 20 J pulses, 10 ns long and with a 10 Hz repetition rate at 1053 nm, employing a zigzag amplifier geometry with Nd:glass slab active mirrors [67].

1.3 *LMJ and PETAL programs*

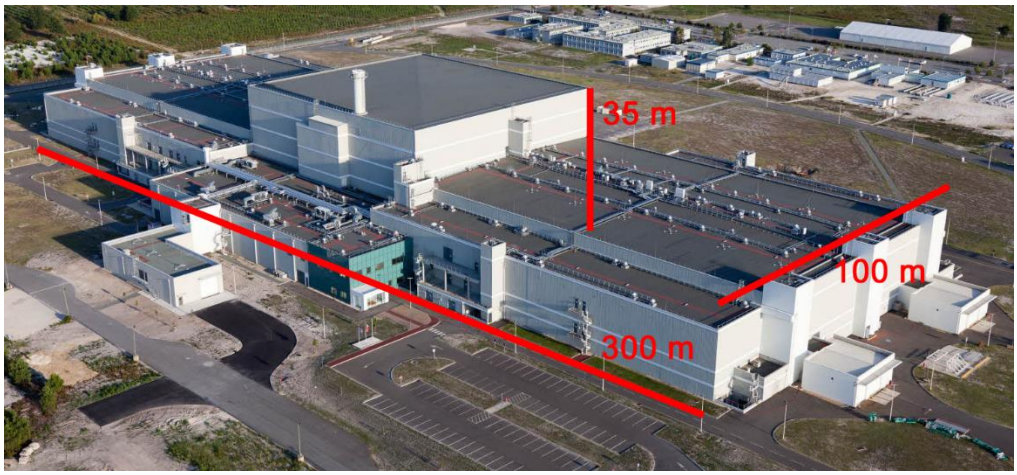

Fig. 1.6 Aerial view of the LMJ facility at CESTA, and measurements of the building.

As introduced before, the work presented in this document was performed in collaboration with CEA-CESTA in Bordeaux, with the aim of improving one of the Laser MégaJoule amplifier stages in order to obtain overall higher laser performances. The purpose of Laser MégaJoule is to obtain the most energetic laser worldwide, aiming to picosecond laser pulses, each carrying an energy amount equal to, or higher than 1.8 MJ [68].

In its current configuration, the laser chain is composed of multiple amplifying stages, starting with a flashlamp-pumped master oscillator with nanojoule-level output pulse energy. The facility hosts four 125 m long laser bays – one of which dedicated to the PETAL petawatt laser – and a spherical reaction chamber, at the centre of which 176 laser beamlines are collimated upon a nuclear fuel target, contained in a gold *hohlraum*, which acts as the X-ray source. To excite the X-radiation emission, the laser beams have a wavelength of 351 nm, obtained by the energy conversion of lower-energy beams by frequency tripling. For this purpose, it is possible to obtain the fundamental wavelength at 1053 nm via the emission

from the well-known $^4F_{3/2} \rightarrow {}^4I_{11/2}$ transition of trivalent neodymium. This emission can be achieved by pumping on the 800 nm Nd^{3+} absorption band, thus one can see how Nd^{3+}-doped materials are most appealing for this particular kind of laser amplifiers. Neodymium-doped glasses are used in the first amplifier stages, which increase the front-end pulse energy up to 500 mJ, with a 3 mHz repetition rate with the aid of a regenerative cavity, as well as in the multipass amplifiers. In particular, LMJ and PETAL make use of neodymium-doped phosphates designed for high-power laser amplification, such as LG-770 (Schott) and LHG-8 (Hoya), the same used in the NIF. These glasses are used in both the front-end components and the main amplifier stages. With these specifics, the current LMJ setup allows delivering UV pulses with 1.5 MJ energy and duration between 0.3 and 25 ns. A rendition of the LMJ amplifying chain is shown in figure 1.7.

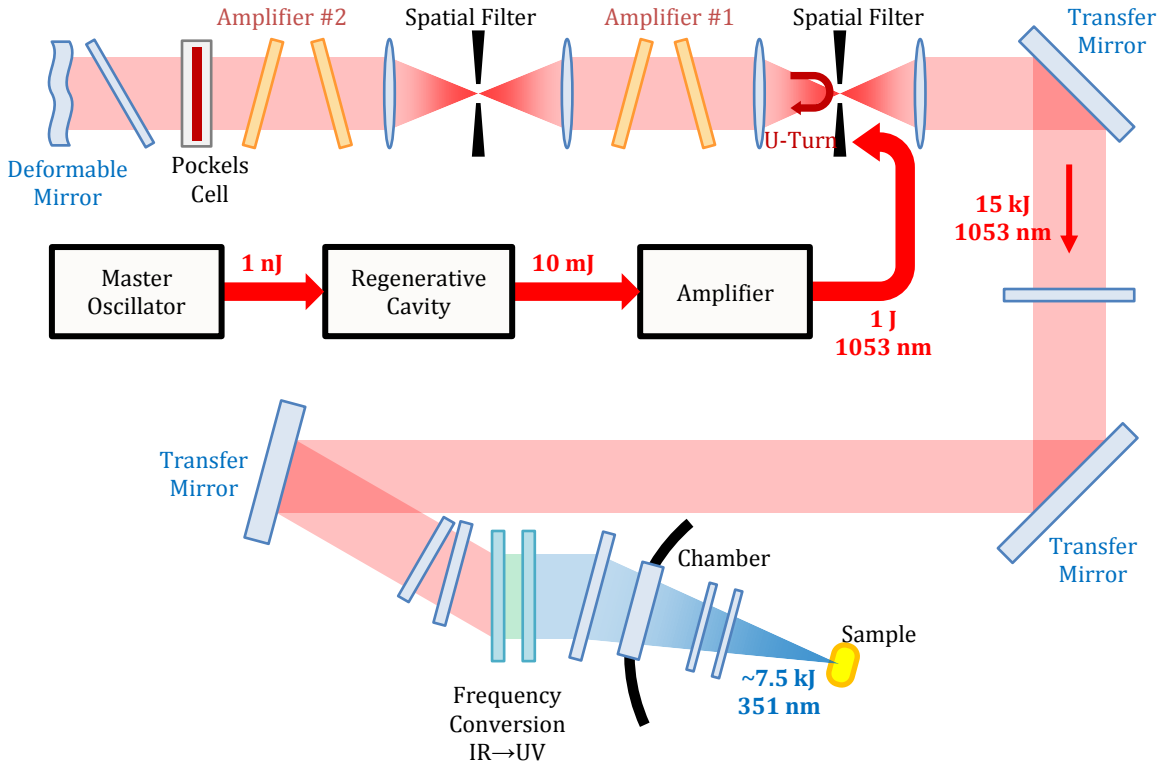

Fig. 1.7 Amplifying chain schematic, illustrating the LMJ laser beam setup. The master oscillator is a laser diode emitting at 800 nm. Nd^{3+}-doped phosphate glasses are employed in the regenerative cavity, the front-end amplifier, and the laser amplifiers #1 and #2. Fluoride crystals are supposed to replace glasses in the regenerative cavity and front-end amplifier.

The LMJ predecessor and prototype, the Laser Integration Line (LIL), was operating and open to the scientific community for 9 years, from 2005 to 2014. Laser MégaJoule was officially

commissioned on October 23, 2014, with the performance of its first series of experiments. The LMJ was since then employed for experiments in high energy density physics (HEDP) simulations, in particular radiation transport, fundamental data for EOS, implosion hydrodynamics and hydrodynamic instabilities. Nowadays, the LMJ facility annual schedule (Fig. 1.8) consists of three main activities: mounting of a new bundle, activation and qualification of the previously mounted bundles, and plasma experiments. LMJ is working in two shifts; the first one is dedicated to the mounting of new bundles all-year long, the second one to either activation and qualification or plasma experiments. This two-shift schedule allows for 1 shot per day during 4 months, however, the LMJ has been able to provide 2 shots per day with both shifts dedicated to experiments. All experiments were performed with the first 8 LMJ beams. The implementation of a larger number of beams is planned for the next years, and the facility is then expected to focus its research on ICF once full functionality of the 176 beamlines has been reached [69].

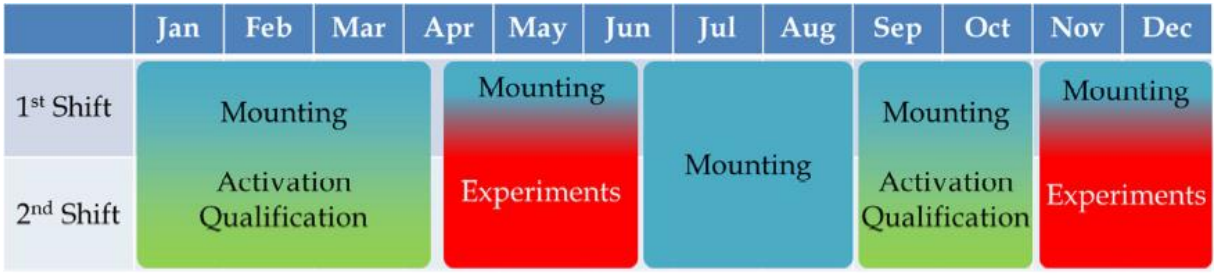

Fig. 1.8 Annual schedule of the LMJ activities [69].

The improvement of the LMJ front-end amplifiers with the implementation of neodymium-doped fluoride crystals in the place of Nd:phosphate glasses is predicted to improve the front-end output to 1 J pulses with 10 Hz repetition rate at 1053 nm. These specifics are required in order to improve the laser chain performances, reaching the desired 1.8 MJ single-pulse output in the experimental chamber, and ideally more frequent shots of the LMJ laser beams.

The CEA femtosecond laser, PETAL (PETawatt Aquitaine Laser) is housed at the CESTA facility in Bordeaux, along with the LMJ, as introduced previously. PETAL too currently uses Nd:glass slabs as amplifier media, in particular laser phosphates, and it is designed to deliver 500 fs long pulses with up to 3.5 kJ energy per pulse at 1053 nm with 16 nm spectral FWHM, and then tripled to 351 nm [68,70]. PETAL's short pulses are intended to be coupled with the picosecond-long output from LMJ in order to obtain an efficient ICF via shock ignition. PETAL has a similar architecture to LMJ, but works on a combination of CPA and OPCPA to obtain ultrashort pulses. The master oscillator is a mode-locked Ti:sapphire laser.

Both LMJ and PETAL performances are predicted to benefit from the implementation of fluoride crystal amplifiers, thanks to their spectroscopic and thermomechanical properties. Calcium fluoride in particular is regarded as a viable candidate for the enhancement of the facility performances because of its very high thermal conductivity.

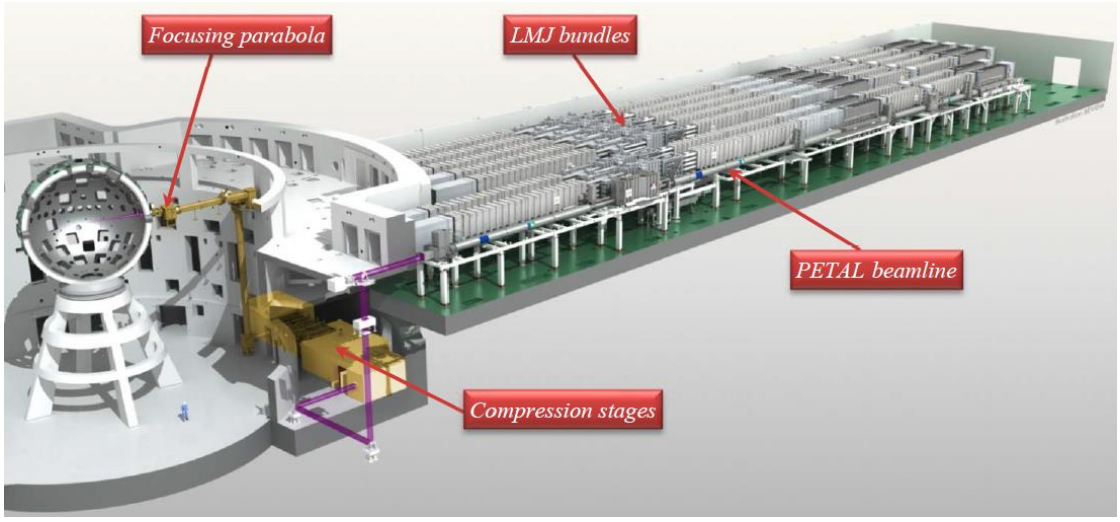

Fig. 1.9 Implementation of the PETAL laser bay in the LMJ facility. The PETAL beam is focussed along the target chamber equatorial plane via an off-axis parabola.

The PETAL front-end oscillator is a Ti:sapphire mode-locked laser that provides 3 nJ, 100 fs long pulses with 16 nm wide spectra at 153 nm, and 77.76 MHz repetition rate. Each pulse is stretched out to 9 ns, and sent to the pre-amplifier module, consisting of several OPA stages and a pump laser. With this setup, 150 mJ front-end output pulses were demonstrated on the LIL facility. PETAL employs the same multipass amplifier as chain as LMJ, with 16 amplifying slabs divided into 2 sets, delivering up to 6 kJ per pulse. At this point, the pulse duration is reduced to 1.7 ns due to gain narrowing. The pulse is then compressed via a two-stage system, which reduces the pulse duration to 350 ps first, then divides the beam into four sub-apertures which are independently compressed, reaching the final pulse duration, which is tuneable from 500 fs to 10 ps.

PETAL has been shown to output up to 1.05 kJ pulses with 1 ps duration in 2015. On May 29th, 2015, PETAL obtained 846 J, 700 fs long pulses, corresponding to a 1.2 PW peak power. This made it the most powerful laser worldwide within the high-energy lasers category.

Five 700 fs long PETAL laser beams with 0.9 PW peak power were first led into the LMJ experimental chamber in December 2015. In the same occasion, a combined PETAL and LMJ pulse was shot into the chamber for the first time. In 2016, the pulse compression was further

improved, reaching durations as short as 570 fs for 220 J shots, corresponding to a potential 1.85 PW peak power.

It was observed that PETAL's pulse energy is limited by the damage threshold of the chain optics, which makes research aimed at improving the components performances extremely important for future enhancements of the system. The laser repetition rate may also be improved by enhancing the front-end amplifier performances. In particular, as in the case of LMJ, the use of neodymium-doped fluorides for the replacement of the front-end active components has been taken into consideration. This is the main concern of the recent LASCAN project, which encases the work presented in this thesis.

1.4 LASCAN Project: CaF_2:Nd^{3+} as a Novel Host for High-Power Lasers

LASCAN is the project aimed at the improvement of the LMJ and PETAL output by upgrading the front-end amplifier section of the laser chains. In particular, the project aims at increasing the output pulse energies, the laser repetition rate and the facility operating time, as a part of the system enhancement leading to full LMJ operation. To do so, it is necessary to overcome the front-end amplifier limitations, by replacing the currently used active material with a more favourable one from the spectroscopic and the thermomechanical points of view.

As discussed before, the LMJ/PETAL facility currently makes use of neodymium-doped phosphate glasses specifically made for high-energy laser applications (namely, LG-770 and LHG-8). Rare earth-doped phosphate glasses are commonly employed for the amplification of ultrashort lasers, because they possess very low phonon energies and wide transparency windows in the NIR range, as well as very broad emission bands that allow reaching very short pulse durations. However, glasses have very low thermal conductivity and a low thermal damage threshold.

In order to address these drawbacks, neodymium-doped fluorides, in particular fluorite-type crystals, have been proposed as a possible replacement for the front-end amplifiers phosphate glasses. Fluorites are very interesting materials for their applications in laser physics, since their wide transparency window makes them suitable for applications in the visible and infrared range. In addition, these crystals have quite broad and intense absorption peaks, which are ideal for efficient diode pumping. Moreover, rare earth-doped CaF_2 crystals are known to possess very wide emission bands, as broad as those of rare earth-doped

glasses. This peculiarity makes these materials extremely appealing for applications in ultrashort laser pulse generation.

Most importantly, using a crystal-based amplifier over a glass-based one leads to an improvement from the thermomechanical point of view. In fact, rare earth-doped glasses are susceptible to thermal damage as a consequence of high amounts of heat deposited in short times, which poses a limit to the beam power they can sustain without suffering harmful effects. Moreover, the repetition rate of laser pulse amplification is limited by the low thermal diffusivity of glasses, which extends the heat dissipation time and thus the cooling time needed between pulses. Crystals, on the other hand, have a crucial advantage over glasses as laser amplifier materials, in that they generally possess a high thermal conductivity. This allows a better thermal shock resistance and a faster dissipation of the heat deposited with each pulse, in turn making it possible to sustain higher pulse energies and higher repetition rates than rare earth-doped glasses. Because of these properties, neodymium-doped crystals have also become particularly interesting for high-energy laser facilities, such as the NIF, that currently employ neodymium-doped phosphate glasses for the generation of high-power short pulses.

Fluorite-type crystals like CaF_2, SrF_2 and BaF_2 are particularly appealing, since they have similar spectroscopic qualities to glasses, but much better thermomechanical properties. Another favourable property of these fluorides is that rather large single crystals can be grown relatively easily, which is important when crafting large-scale devices, as is the case of high-power facilities.

In the particular case of LMJ, improving the front-end amplifiers performances means that it would be possible not only to obtain more efficient nuclear fusion reactions, but also to conduct more measurements, for a longer period, thus collecting more – and more comprehensive – data.

Ytterbium-doped calcium fluoride crystals have known success in recent times for their implementation in ultrashort petawatt lasers. In fact, CaF_2:Yb^{3+} has large spectral bands and a near-unitary quantum defect as a result of its simple two-energy level structure. These properties make it suitable for short-pulse laser oscillation. Moreover, this crystal thermomechanical properties make it ideal for prolonged, high-power and high-repetition rate operation at the wavelength of 1 μm. Ultrashort laser operation with CaF_2:Yb^{3+} has indeed been proven, obtaining pulses as short as 99 fs [33], and its implementation as a high-power laser amplifier medium is an integral part of the POLARIS and PEnELOPE projects.

In the case of LMJ and PETAL, however, the ideal wavelength for the application is about 1053 nm, which does not correspond the Yb^{3+} emission. However, broadband laser emission around 1.05 μm has been achieved in recent years, taking advantage of the $^4F_{3/2} \rightarrow {}^4I_{11/2}$ transition of Nd^{3+} in rare earth-doped doped fluorite crystals by codoping the host with optically inactive ions, such as Y^{3+} and Lu^{3+} [8,10,11]. In particular, the doping of calcium fluoride and strontium fluoride single crystals was investigated because of their very low phonon energies. For this reason, they provide very broad Nd^{3+} absorption and emission bands. Consequently, as mentioned before, Nd^{3+}-doped CaF_2, SrF_2 and BaF_2 offer attractive spectroscopic glass-like features while maintaining several advantages of crystals [71], which makes them appealing for the LASCAN project.

The 1.05 μm Nd^{3+} emission in of CaF_2 is well-known to be completely quenched because of the clustering of Nd^{3+} ions in CaF_2 which starts at relatively low dopant concentration (0.1 at%) [2,7]. This ion clustering is driven by the early appearance of interstitial fluorine ions coming into play to ensure the necessary charge compensation following the substitution of divalent calcium ions by trivalent neodymium ions. This clustering effect hinders the Nd^{3+} emission because of cross-relaxation processes between neighbouring Nd^{3+} ions, which quench the $^4F_{3/2}$ emitting level [72].

To address this drawback, it has been proposed to co-dope the crystals with optically inactive ions in order to form clusters around single Nd^{3+} ions, thus isolating them from one another. Among possible buffer ions in CaF_2, the codoping with Y^{3+} ions has been studied and ultra-short laser operation has already been demonstrated, with 103 fs laser pulses at 1054 nm [39]. Another promising candidate is Lu^{3+}, which was also observed to break up both Nd^{3+} and Pr^{3+} ion clusters [8,9]. The local symmetry of Nd^{3+}-Nd^{3+} clusters and Nd^{3+}-Ln^{3+} clusters (Ln^{3+} representing either Y^{3+} or Lu^{3+}) has been discussed in literature, but their respective absorption, emission cross-section spectra or concentrations have not. Three main local geometries in Nd^{3+}-doped CaF_2 and SrF_2:Nd^{3+}have been identified, one quasi-tetragonal and two quasi-rhombic [18,73-76]. However, the quasi-rhombic centres have very similar geometries and can only be observed separately by low-temperature spectroscopy [74,76]. Thus, in spectroscopic investigations at room temperature these two centres may be treated as a single one [12,77].

1.5 Conclusions

High-power laser facilities have become more and more important in the scientific world during the past few years, thanks to the many possibilities they offer to research, particularly in high-energy physics, astrophysics and plasma science, as well as their many applications, ranging from medical to energy production, to military use. A significant number of high-power laser programs have been commissioned in recent years, or are planned for commissioning in the near future. This prominence of high-intensity laser facilities in the current academic world has led to increasing efforts in the research and development for efficient laser materials, architectures, geometries and components. This research is pushing the high-power laser limitations further and further, allowing for higher powers or energies delivered per beam, shorter, highly energetic pulses, and higher repetition rates.

The LASCAN project has been commenced as an effort to enhance the performances of the high-energy Laser MégaJoule and the ultrashort, high-peak power PETAL, two of most intense lasers in the world, both housed in the CEA-CESTA facility near Bordeaux, and intended for simultaneous use in ICF experiments.

The main aim of the LASCAN project is to improve the LMJ output energy and repetition rate. For this purpose, it is necessary to find a way to surpass the system limitations. In particular, one factor that limits pulse energy and repetition rates is the thermal damage threshold of the chain amplifier materials, especially in the front-end amplifiers that feed the drive signal to the rest of the chain. To this end, the proposed solution is the replacement of currently employed active material within the front-end amplifier stages with a different kind of active medium having a higher damage threshold. In particular, a material with higher thermal conductivity, and thus a faster heat dissipation, a more responsive reaction to heat absorption and higher resistance to thermomechanical stress may provide the solution to the issue. However, it is important that the new material have appropriate spectroscopic properties, i.e. similar or better than those of the replaced medium. In the case of pulsed lasers, and particularly so for ultrashort lasers, this means broad emission bands and high emission cross sections.

Because of the width of their spectral bands, glasses have long been considered the best candidate for short-pulse lasers, in particular phosphate glasses for their low phonon energies and optical losses. Neodymium being the ideal rare earth for ICF applications thanks to its emission at 1.05 μm, Nd^{3+}-doped phosphate glasses have been implemented in the LMJ chain as the amplifier medium of choice. However, due to their low thermal conductivity, these glasses are also a primary source of the system limitations. Crystals, on the other hand, are known to

possess generally higher thermal conductivities than glasses, but much sharper, narrower spectral features, which makes most of them unsuitable for very short pulse generation.

Fluoride crystals are known for possessing a high thermal conductivity – as high as 9.7 $W \cdot m^{-1} \cdot K^{-1}$, which makes them a very interesting candidate for application requiring materials with good heat dissipation and thermal shock resistance. However, while the optical properties of neodymium-doped fluorides are improved by the insertion of Lu^{3+} inactive ions, the thermal conductivity is known to drop with higher levels of dopants. Therefore, a thorough investigation of the thermal properties of doubly-doped fluoride crystals is needed in order to determine the best doping concentrations suitable for high-energy laser pulse amplification.

To perform properly, the incident UV beamlines must be aligned at the *hohlraum* position with 50-μm accuracy. This, in practice, means that the laser beam profile and wavefront must be meticulously controlled, and corrected throughout the cavity passes. It is therefore important to evaluate properly the active material characteristics that may lead to the beam profile deformation, such as thermo-optic properties, nonlinearities and so forth.

One of the requirements for an efficient broadband high-power laser is a relatively flat beam profile around the laser emission wavelength. Finding the appropriate host requires more than the investigation of a single material. This study, however, must always take into consideration that a rather large number of variables is at play, and bandwidth is just one of them. In this work, the spectroscopy of two other host materials than CaF_2 is investigated, namely SrF_2 and BaF_2, which share a similar lattice structure to calcium fluoride. Their spectral features are then mutually compared to define the most suitable material for high-energy pulsed laser applications. Other possible candidates for maximising the emission bandwidth are composite crystal, combining the spectral properties of two or more fluorides. Known their respective spectroscopic properties, in principle, a composite of the different crystals may be designed with the optimal composition in order to obtain the flattest profile possible.

CHAPTER 2

"The appeal of the spectrally macabre is generally narrow because it demands from the reader a certain degree of imagination and a capacity for detachment from everyday life."

CaF_2:Nd^{3+},Lu^{3+} spectroscopy

2.1 *Introduction*

To understand the changes that come with lutetium codoping within neodymium-doped calcium fluoride crystals, a detailed spectroscopic investigation was undertaken. In particular, the critical parameters for the optimisation of the laser operation were studied, namely the spectroscopic signatures (absorption and emission cross-sections, radiative and fluorescence lifetimes) of the different Nd^{3+} active centres and their respective concentrations in relation to the buffer ion concentration. These characteristics of CaF_2:Nd^{3+},Lu^{3+} crystals were then compared to those of the current amplifier materials. Finally, a similar study was performed on other types of fluoride crystals within the fluorite type family – namely, SrF_2 and BaF_2 with similar Nd^{3+} and Lu^{3+} doping levels.

Principles of Rare Earth Spectroscopy

Rare-earth spectroscopy is concerned with the properties of lanthanide-doped materials, which have unique features depending on both the doping ion embedded within them, and the local lattice structure surrounding the dopant. To understand these properties, one must first of all understand the underlying processes, which are the result of the interaction of a lanthanide free ion with the surrounding crystal field. Knowing the electronic configuration of xenon [Xe] having all electronic shells filled up including the 5p subshell, most lanthanide's electronic

configurations can be written as [Xe] $4f^n$ $5d^1$ $6s^2$, with n ranging from 0 to 14. When bonding with other elements, the trivalent oxidation state of rare-earth ions is the most stable. The electronic configuration of lanthanide ions Ln^{3+} is therefore [Xe] $4f^n$. The energy levels scheme of this ground-state configuration is well distinct from that of the first excited configuration, [Xe] $4f^{n-1}$ $5d^1$.

It is noteworthy that, since the 4f shell is more internal than the 5p and 5s shells, it is partially shielded from the surrounding crystal field. Because of this, the crystal field interaction is generally much smaller than the spin-orbit interaction. This causes each lanthanide to preserve a set of specific energy levels, which is characteristic of the rare earth ion regardless of the surrounding crystal field. This energy level "ladder" therefore allows for the selection of very specific absorption and emission features in rare earth-doped materials, depending on the dopant ion.

While a rare earth ion's spectral band positions depend first of all on the ion itself, the precise spectral value, shape and width of these bands depend on the coupling of the 4f electron orbitals with the local crystal field in which the ion is immersed. The static electric field due to the surrounding host ligands cause the splitting of the free ion energy levels in what is known as Stark sublevels [78].

Properties of Rare Earth-Doped Fluorides

In the case of crystalline hosts, where the crystal field tends to have well-defined incorporation site symmetry, the spectral bands are generally narrow, with sharp peaks, while disordered structures like glasses, due to the coexistence of different local geometries enclosing the dopant ions, have much broader, smooth bands. This rule of thumb of course has its exceptions, such as in the case of rare earth-doped fluorite structures: in fact, the spectral bandwidth of rare-earth ions in these crystals is comparable to what can be observed in doped glasses.

Fluoride crystals of the fluorite group, such as calcium fluoride, strontium fluoride and barium fluoride, are known to be interesting and useful materials for optical purposes. First off, the crystals belonging to this group are optically transparent over a very large spectral range, running approximately from 0.2 μm to 9 μm. Moreover, they exhibit low dispersion compared to glasses which provides a lesser degree of chromatic aberration (having Abbe numbers V_D

greater than 60). These properties make them especially versatile for applications in a wide section of the light spectrum, from the ultraviolet to the infrared. For this, they are currently employed in the fabrication of a wide variety of both passive and active optical devices. Another very important property of the fluorite structure crystals is that they share the face-centred cubic lattice structure: this cubic geometry presents several advantages from the optical point of view. Possibly the most important of these features is that cubic lattices are isotropic, in virtue of their symmetry. This renders the optical properties of the crystals independent of the orientation, making in turn the study and investigation of these samples easier, and reducing the number of constraints on the orientation of the crystals in their practical usage.

The optical applications of fluorite-like crystals are numerous, and they are especially useful in the field of academic and industrial research. Some of the more relevant devices built out of these materials are transparent windows for spectroscopy, UV-, visible-, and IR-range lenses and prisms (making them appealing options for high-performance camera and telescope elements), as well as coatings for optical elements, and even scintillators for X-ray detection. The possibility of generating colour centres within fluoride crystals by introducing fluoride ion F^- vacancies has been demonstrated [79-82], allowing to tailor the spectroscopic properties of the materials by means of X-ray irradiation, or pressure. Other applications arise from the doping of these materials. As far as doped fluoride crystals are concerned, alkali ion-doped fluorite structures have been investigated for the purpose of holography [83], while lanthanide ion-doped fluorides have been studied as possible laser materials – though with less than encouraging results, until recently.

Challenges of Neodymium-Doped Fluorides

The main difficulty in obtaining a viable fluorite-based laser medium comes from the issue of the clustering of the dopant ions. This clustering occurs spontaneously due to the valence difference between the dopant and the substituted ion in the crystal structure. Trivalent rare earth ions RE^{3+} introduced as dopants during the crystal fabrication take the place of interstitial divalent calcium ions Ca^{2+} within the lattice: the excess positive charge introduced with the dopant induces an extra fluorine ion F^- to take a place in an adjacent cell interstitial site as a means of charge compensation. This in turn, as more and more rare earth ions are added to the material, causes other positively charged dopant ions to take up a space in another adjacent cell during the crystal growth. This process is the cause of the dopant ion clusters, wherein trivalent rare earth ions sit close enough to one another, so that they are no longer isolated from each

other, and strong dipole-dipole interaction can take place. This means that non-radiative energy transfer processes may take place between ions in a cluster, thus leading to nonradiative relaxation, and therefore the quenching of radiative emission. Unfortunately, dopant ion clustering in fluorites takes place at very low doping concentrations, much lower than the quantities needed for efficient laser applications.

Nevertheless, neodymium-doped fluorides have been regarded as possible materials for laser applications in the near infrared. In particular, the cubic fluorite structure provides very broad spectral bands, with comparable width to those of neodymium-doped glasses [8,84,85]. These broad bands make the material suitable for short-pulse laser applications, as a larger spectral width allows for the generation of shorter pulses. Moreover, crystals have in general the advantage of a higher thermal conductivity than glasses, which is very important for high-energy pulse generation, as it allows for efficient heat dissipation, preventing thermal damage. Among these, calcium fluoride is one of the most interesting thanks to its especially high thermal conductivity and its well mastered crystal growth. However, the effect of energy transfer due to the dopant ion clustering severely hinders the efficiency of the materials, so much so that neodymium-doped fluoride crystals have been dismissed as viable laser materials altogether for a long time. This drawback is particularly critical in CaF_2 crystals, in which the clustering of the rare earth dopants takes place at very low ion concentrations, below 0.1 at% [2,72], preventing any significant photon emission around the main neodymium transition at 1.05 μm. Excited neodymium ions exchange energy with Nd^{3+} ions in the ground state, leading both ions to the $4I_{15/2}$ energy level from which only nonradiative decay occurs, as illustrated in figure 2.1.

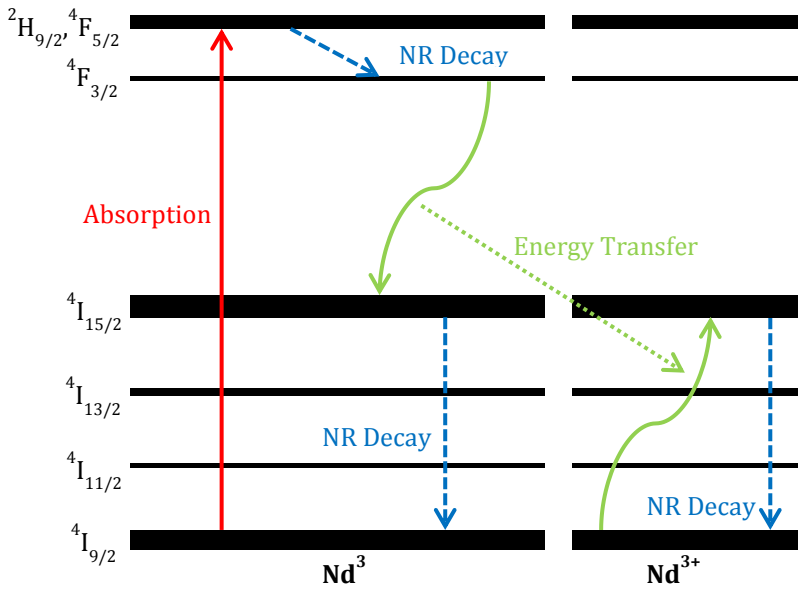

Fig. 2.1 Illustration of cross-relaxation due to energy transfer between interacting neodymium ions.

The effects of charge compensation on the local site geometry in neodymium-doped calcium fluoride have been thoroughly investigated in literature [2]. While the uncompensated active ion sites have a O_h group cubic symmetry, the presence of interstitial fluorine ions causes the appearance of two different configurations. In the case where the fluorine ion takes up a place in a nearest-neighbour site, the centre takes on the C_{4v} symmetry, while if the charge compensation occurs via the next-nearest neighbour interstitial site, the corresponding symmetry belongs to the C_{3v} group. The different symmetries of Nd^{3+} sites appearing in the calcium fluoride structure are illustrated in figure 2.2, from Payne's work.

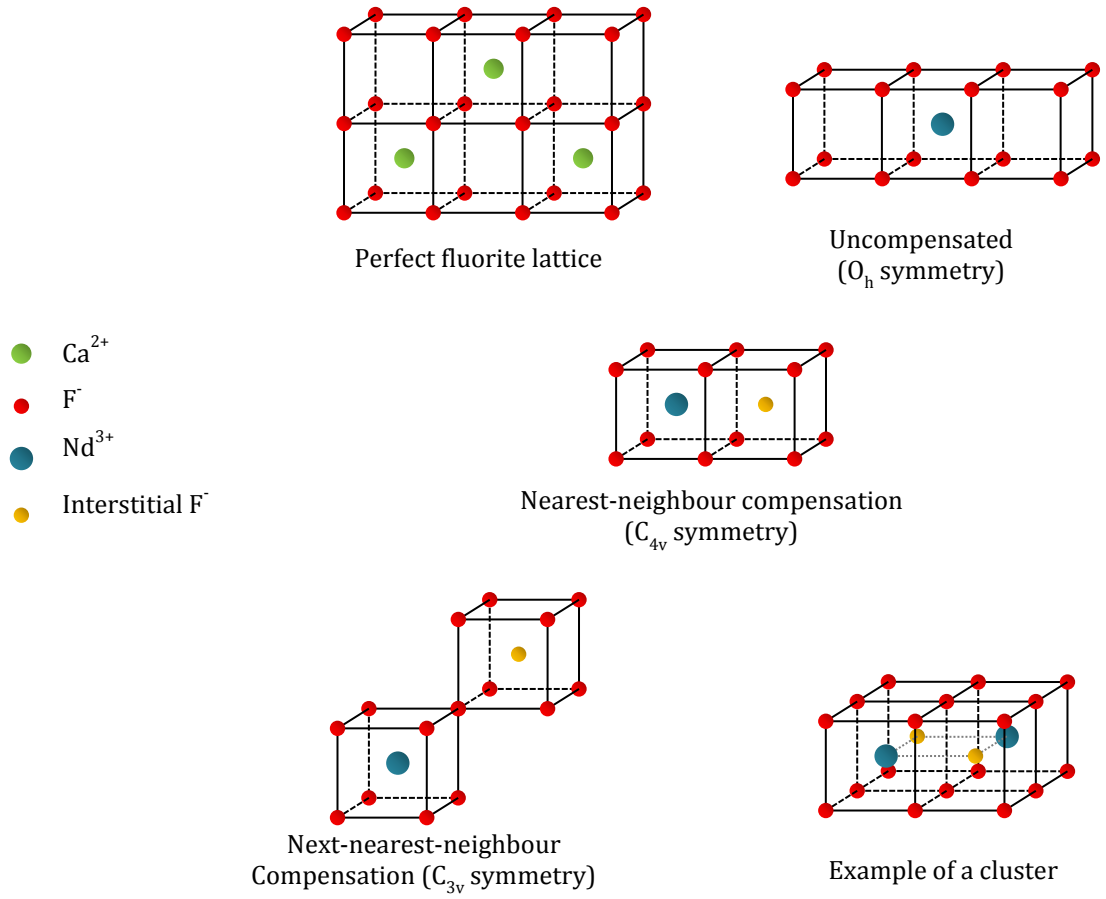

Fig. 2.2 Fluorite lattice structures showing the perfect CaF_2 lattice, the uncompensated Nd^{3+} ion that simply substitutes for a divalent host Ca^{2+} cation, nearest-neighbour and next-nearest-neighbour interstitial fluoride compensation, and an example of a simple Nd^{3+} cluster, from the work of Payne [2].

Although rare earth ion clustering cannot be avoided, a solution to reduce the fluorescence quenching was proposed, consisting in adding a second dopant species with different energy levels to those of the active ion, so that the two may not exchange energy. The principle is to have the inactive codopant ion acting like a buffer to the active dopant within the clusters, by isolating the active centres from one another, and preventing the nonradiative dipole-dipole

energy transfer. For this purpose several ionic species have been taken into consideration as viable candidates for the codoping of neodymium-doped fluorite crystals. Possibly the most notorious codopant investigated in literature is yttrium, which fits the desired characteristics as a buffer. Thus the spectroscopic properties of neodymium- and yttrium-doped fluorites were investigated, as well as their possible application as laser materials, in several works [10,12,13,15,77,84,86], and even scandium was proposed as the buffer ion for neodymium-doped calcium fluoride [15]. Other studies on codoped fluorites for laser applications exist, for instance with CaF_2: Na^+,Yb^{3+} [87,88], used to obtain self-*Q*-switched operation.

Lutetium was also identified as another viable dopant. One of the possible advantages of this element is being closer in ionic radius to the active neodymium ions, which may result in a lesser distortion of the local crystal geometry, and therefore better optical or thermomechanical properties on the macroscopic scale. The use of lutetium as a successful codopant buffer ion was studied by Serrano *et al*. [9] in the case of praseodymium-doped fluoride crystals. Experiments in the CIMAP lab showed that the addition of lutetium was efficient in removing clustered neodymium ions, and enhancing the radiative emission of the doped samples for laser operation [8].

Early experiments reported in literature indicate that three symmetries have been identified for neodymium-doped CaF_2 codoped with either yttrium or lutetium, namely the tetragonal sites labelled L, and the two rhombic sites labelled M and N respectively [73-76]. The presence of similar site geometries was observed also in the case of Nd^{3+}:SrF_2 [18]. While the coexistence of multiple active centre structures was reported, their operational parameters, such as their relative concentration, absorption and emission cross sections, and lifetimes, have not been previously assessed.

Chapter Overview

In this chapter, a thorough spectroscopic investigation of Nd^{3+},Lu^{3+}-doped CaF_2 crystals is presented, highlighting the effects of the gradual increase of buffer concentration. The presence and concentration of different rare-earth clusters are estimated, and their specific optical features are investigated. The properties of Nd^{3+},Lu^{3+}-doped SrF_2 and BaF_2 samples will also be discussed and compared to those of the calcium fluoride samples.

Finally, an optimisation of the spectroscopic features of the investigated materials for ultrashort pulse amplification is discussed within the study of mixed fluoride crystals in order to obtain the broadest and flattest band profile possible. The first investigation of mixed fluorite crystals was performed on CaF_2-SrF_2:Nd^{3+} by Kaminskii [19] and, more recently, Basiev [20], but here is presented a study of the properties of Nd^{3+},Lu^{3+}-codoped SrF_2-BaF_2 crystals by varying the relative concentrations of the two fluorides, in order to estimate the optimal composition for the intended application, i.e. to obtain the broadest and flatter emission band possible.

2.1 Principles and Techniques

The first thing to consider in designing a laser amplifier material is the pumping mechanism. In particular, Nd^{3+} laser operation at 1.05 μm ($^4F_{3/2}\rightarrow{}^4I_{11/2}$ radiative transition) is very well-known for its 4-level system. This radiative transition usually takes place following the non-radiative relaxation from the $^4F_{5/2}$ and $^4H_{9/2}$ levels to the $^4F_{3/2}$ level: the pump wavelength matching the $^4I_{9/2}\rightarrow{}^4F_{5/2},{}^4H_{9/2}$ transition absorption around 800nm (see figure 2.1).

2.2.a Absorption

The ability of a material to absorb light is usually assessed via absorption spectroscopy. Absorption measurements are performed by comparing the intensity of a monochromatic light beam passing through the sample with the intensity of an unabsorbed reference beam of the same wavelength, and gradually tuning the wavelength to cover all the interested spectral range. Absorption spectroscopy can be used to identify the optimal pump wavelength and derive absorption cross sections. It can also provide information about the lattice structure via the distribution of the Stark sublevels observed in the absorption bands. In fact, the shape and width and in some extent the spectral position of rare-earth absorption bands is a product of the coupling between the RE energy levels with the local crystal field in which the ions are embedded [78]. The technique may also be employed to obtain an estimate of the different transition branching ratios and radiative lifetimes using the Judd-Ofelt analysis method [89,90].

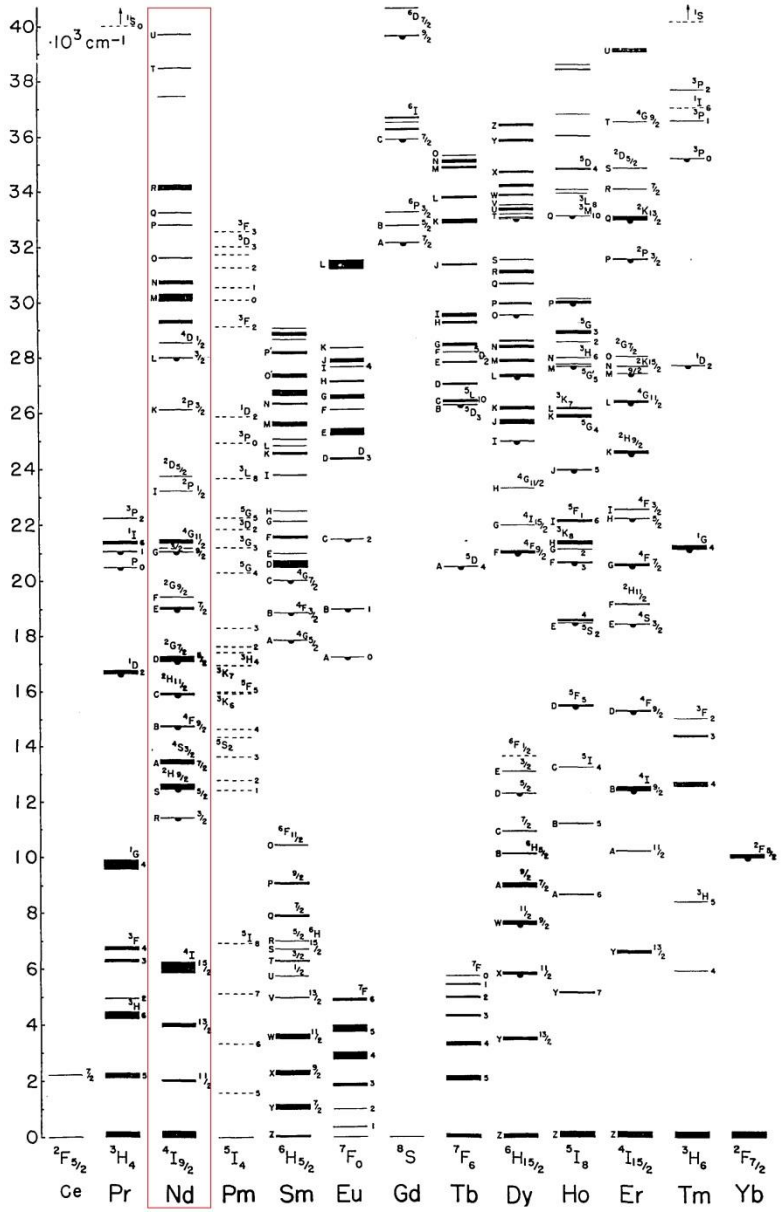

Fig. 2.3 Dieke's diagram; in evidence, the energy levels of the neodymium ion (from Dieke and Crosswhite's work [91]).

The process of optical absorption is governed by the well-known Beer-Lambert law [92,93], which states that the intensity I_{tr} of a light beam transmitted by a uniform sample of thickness l is given by the equation

$$I_{tr} = I_0 \exp(-\alpha \cdot l) \tag{2.01}$$

where I_0 is the beam intensity before absorption, and α is the sample absorption coefficient (or optical density). The absorption coefficient, for a lanthanide-doped material with rare earth ion

concentration N, in the absence of nonlinear effects and ground-state depletion, is defined as follows:

$$\alpha = N \cdot \sigma_{abs} \tag{2.02}$$

Here, σ_{abs} is the RE absorption cross section.

The quantity measured is usually the absorbance (or optical density) of the material, A, defined as:

$$I_{tr} = I_0 \cdot 10^{-A} \tag{2.03}$$

Thus the absorption coefficient is given by:

$$\alpha = \frac{\ln(10)\, A}{l} \tag{2.04}$$

2.2.b Emission

Fluorescent emission can be observed by means of fluorescence spectroscopy. This technique consists in exciting the sample at an absorption wavelength, and collecting the intensity of the spontaneously emitted light. These measurements provide insight on the optimal emission wavelength under a specific pumping wavelength, as well as the width and shape of the observed emission bands. They are also necessary to the estimation of stimulated emission cross sections via the Füchtbauer-Ladenburg equation [94]. Stimulated emission leads to the ion relaxing radiatively to the lower level, and the emission of a second photon, equal in energy and phase to the triggering photon. In this regard, stimulated emission is analogous, albeit opposite in effect, to photon absorption.

Stimulated and spontaneous emission can take place between the very same levels, which means that they are two competing processes. The Füchtbauer-Ladenburg equation is an extension of the relation between Einstein's A and B coefficients [95,96] that links the stimulated transition properties of a system to its spontaneous emission. In particular, it is used to obtain the value of the stimulated emission cross section, σ_{em}. The equation is expressed as:

$$\sigma_{em}(\lambda) = \frac{\beta\lambda^5}{8\pi c n^2 \tau_{rad}} \frac{I(\lambda)}{\int I(\lambda)\lambda \, d\lambda} \tag{2.05}$$

Here, c is the speed of light in vacuum, n is the host refractive index, τ_{rad} is the radiative lifetime, β is the transition branching ratio (i.e. the relative probability of the specific transition taking place over all possible transitions from the excited level), I is the normalised emission intensity, and λ is the photon wavelength, corresponding to an energy hc/λ, h being Planck's constant.

Excitation spectroscopy is another experimental technique which can be performed to obtain information about the excitation spectrum of a specific emission. To this purpose, the sample is pumped by a laser as in the case of fluorescence measurements, but the emission intensity is collected for a fixed emission wavelength, and the pump wavelength is tuned over a determined range. This measurement provides useful spectra to compare to the absorption spectra, allowing to define which absorbed wavelengths concur more or less efficiently to the generation of the emitted photons. In the simplest case, where only one kind of active rare-earth site is present within the material, the excitation spectrum is identical to the absorption spectrum obtained for the same sample. However, if more than one incorporation site coexist within the same sample, the excitation bands shape shows differences with respect to the sample absorption spectrum, depending on the properties and ratios of the different active sites. Moreover, in the latter case, the excitation band shape changes depending on the detected emission wavelength, as different emission line intensities are a result of different combinations of the active sites' excitation.

Emission lifetimes can also be measured, by exciting the sample at an absorbed wavelength with a pulsed laser and collecting the emission intensity decay. The fluorescence decay characteristic time, or fluorescence lifetime thus estimated is a critical parameter to take into account when investigating the sample laser operation.

In the most common case (i.e. in absence of nonlinear effects), the intensity decay $I(t)$ is exponential, so that it can be fitted via the equation

$$I(t) = I_0 \cdot \exp\left(-\frac{t}{\tau_f}\right) \tag{2.06}$$

where I_0 is the fluorescence intensity at $t = 0$. The estimation of the fluorescence lifetime is important to obtain a value of the excited level transition probability, which is by definition the inverse value of τ_f.

When the decay does not follow a single exponential form, however, an effective fluorescence lifetime can be defined as follows:

$$\tau_f = \frac{1}{I_0}\int_0^\infty I(t)\,dt \tag{2.07}$$

In the case of multiple active sites being present in the material, the decay is not described by a single exponential, but rather by a combination of multiple exponentials with different lifetimes, dependent on the different sites local crystal fields. The estimation of such lifetimes in this case provides information on different time windows where the emission of a site prevails upon the others. These data can be used to estimate the spectral properties of the different active centre types by means of time-resolved spectroscopy.

2.2.c Bridgman-Stockbarger Growth of Fluorite Crystals

To fabricate the samples, the Bridgman-Stockbarger technique for crystal growth was employed. The Bridgman-Stockbarger technique is a crystal growth method that includes two similar processes employed in the fabrication of crystal boules and in the solidification of polycrystalline samples via melting and recrystallization. The two different methods are referred to respectively as the Bridgman technique [97] and the Stockbarger technique [98]. The base principle of the crystal growth from melt is to heat the material over its melting temperature, then let it slowly cool down, with enough time for the solidifying mass to rearrange itself into a crystalline structure. It is important to somehow prevent the nucleation of the solid phase in multiple events, which would result in the material to grow into a multi-crystalline structure. The presence of a single crystal grain at the solid-liquid interface ensures that the material will grow into a single-crystal boule [99]. The Bridgman technique applies these principles in two possible configurations, vertical or horizontal growth, employing a crucible with a temperature gradient along the direction of the growth axis. The Stockbarger technique exploits the same principles, but it uses a two-zone furnace, which consists of two separate sections at different set temperatures to control the position of the solid-liquid interface. In particular, the vertical Bridgman crucible was chosen for our samples because fluoride crystals are relatively easy to grow via both techniques and the appropriate Bridgman apparatus is more easily found on the market.

The Bridgman vertical crucible consists of a cylindrical tube with a tapered lower end. In the case of CaF_2, the melting temperature T_m is in between 1360 °C and 1480 °C. As the ampoule

containing the material is lowered in the cylinder, the crystallisation takes place first within the lower, tapering section of the container. This restricted space allows for the single nucleation event that generates a single-crystal grain. The geometry of this grain lattice will act as a seed, defining the growth condition at the phase-transition interface, and thus the entire crystal lattice orientation. Alternatively, single-crystal growth can be achieved with a solid seed setup, in which a previously grown, smaller single-crystal seed is inserted in an appropriate holder in the lower section to provide the initial grain. The two setups are illustrated in figure 2.4. The samples investigated in this work were grown using the seeded Bridgman method into cylindrical barrels several centimetres long and 6 millimetres in diameter.

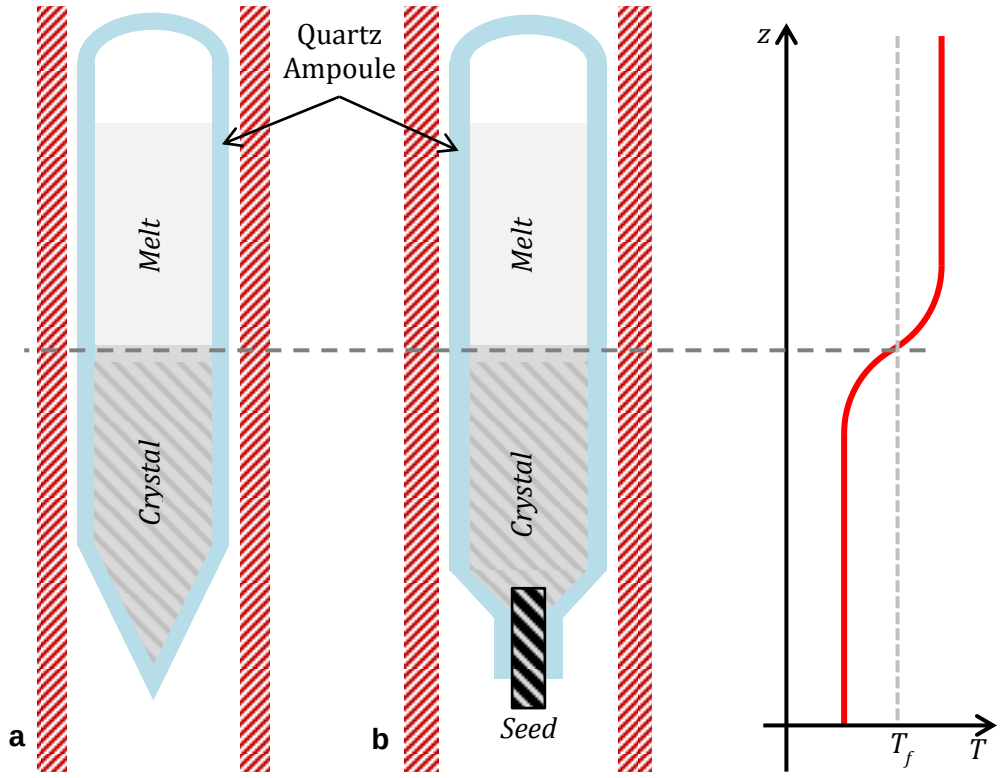

Fig. 2.4 Illustration of the Bridgmann technique crystal growth setup, showing both the tapered-end configuration (a) and the growth from a seed (b).

The use of the Bridgman technique and development of the know-how skills is crucial to the fabrication of high optical quality crystals for the LASCAN project, as it is a very versatile method, which allows fabricating crystals with different cross-section geometries.

2.2.d Experimental Setups for Optical Measurements

In the course of this work, the absorption spectra were recorded with a Perkin-Elmer Lambda1050 spectrophotometer, using a 0.4 nm spectral resolution, recording the spectra from 400 nm to 900 nm.

Emission measurements were performed by exciting the samples with a Coherent 890 tuneable Ti:Sapphire laser, pumped by a Verdi V6 visible laser, and collecting the emitted light with an optical fibre leading to a Leasametric optical spectrum analyser with a 0.2 nm spectral resolution.

Excitation spectra were collected by tuning the Coherent 890 Ti:Sapphire laser wavelength. The emitted light was collected by an ISA Jobin-Yvon monochromator equipped with a photomultiplier tube. The excitation spectra were recorded by keeping fixed the emission wavelength while tuning the pumping wavelength between 765 nm and 825 nm.

Time-resolved emission and excitation spectra were recorded as well with the same setup using an acousto-optic modulator to modulate the pump signal and implementing time windows on the subsequent signal dynamics in order to record time-resolved spectra.

Finally, a Continuum Horizon optical parametric oscillator pumped by a Continuum Surelite Nd^{3+}:YAG pulsed laser tripled in frequency was used to excite the samples in order to collect emission decays after spectral selection by an Oriel monochromator.

2.2 Experimental

2.3.a Crystal Growth and Sample Preparation

A set of nine CaF_2:Nd^{3+},Lu^{3+} crystals was prepared, namely with lutetium content of 0%, 0.1%, 0.5%, 1%, 2%, 5%, 7%, 8%, and 12%. The crystal boules were grown via Bridgman technique; samples were then cut to proper size and shape from the boules, and polished for optical measurements.

The crystal growth was performed within a vacuum chamber at a pressure between 10^{-6} mbar and 10^{-5} mbar. The temperature of the crucible's hot zone was set to about 1450 °C, with a raising speed of the gradient set between 1 mm/h and 2 mm/h. The calcium fluoride crystals

were grown in batches of three at a time in order to save time on the fabrication and maintain the same environmental conditions for multiple samples. Once ready, a disk-shaped section of roughly 5 mm thickness was cut with a wire saw out of each barrel. The disk-like samples were then hand-polished on a rotary lapping machine, using a rough 800-grid abrasive paper, then a 1200-grid, and finishing with an abrasive solution containing micrometre-size diamonds, on both facets. The final thickness of the samples after polishing ranged from 4.2 mm to 4.5 mm.

2.3.b Absorption

Absorption spectra for the different codoped samples (CaF_2:0.5% Nd,*X* % Lu, with *X*=0, 0.5, 5, 12) are shown in figure 2.5. The peak maximum of the $^4I_{9/2} \rightarrow {}^4F_{5/2}$ transition in Nd^{3+} singly doped CaF_2 appears around 792 nm. The integrated absorption spectrum value does not change when adding lutetium ions, as expected since the RE oscillator strengths usually do not change significantly when adding an inactive rare earth as codopant. However, the gradual increase in lutetium concentration is accompanied by the rise of a second peak at 797 nm, which becomes the main absorption feature when the lutetium concentration is higher than 0.5 at%. At the same time, the other peak decreases in intensity and undergoes a shift from 792 nm to 791 nm. This change in the absorption band profile suggests that a structural change of the Nd^{3+} incorporation sites takes place when Lu^{3+} is introduced as a codopant, as the shape of the band is defined by the local crystal field around the lanthanide ion site.

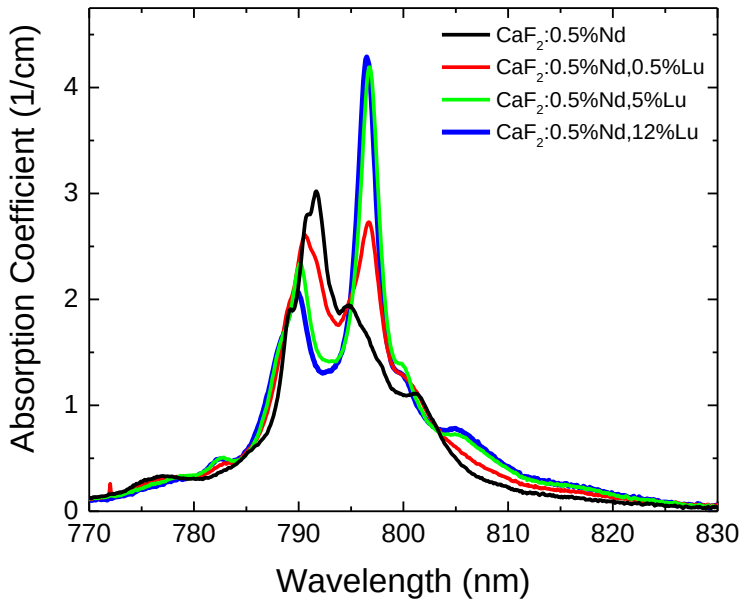

Fig. 2.5 Absorption spectroscopy of CaF_2:Nd^{3+},Lu^{3+} showing the changes in the band shape when increasing Lu^{3+} concentration.

The results are encouraging, since a change in rare earth ion site structure from the singly doped material means a variation in the structure of clusters, which in turn indicates that lutetium ions are in fact incorporated in rare-earth clusters, and may have the desired effect of breaking apart the interacting Nd^{3+} ions.

2.3.c Fluorescence

To assess the effect of Nd^{3+} cluster breaking by Lu^{3+} ions, fluorescence measurements were performed. Figure 2.6 shows the emission spectra for the $^4F_{3/2} \rightarrow {}^4I_{11/2}$ transition recorded for various Nd^{3+},Lu^{3+}-codoped samples under excitation at 797 nm ($^4I_{9/2} \rightarrow {}^4F_{5/2}$ transition). There is an evident increase in fluorescence intensity when increasing the lutetium concentration up to ten times the initial value of the Nd^{3+} singly doped sample. Keeping in mind that the concentration of neodymium remains the same for all samples, this means that more and more Nd^{3+} centres contribute to the emission as the Lu^{3+} concentration increases. This is, thus, a clear evidence for the breaking of Nd^{3+}-Nd^{3+} quenched clusters by the lutetium codoping. These measurements therefore confirm that the Nd^{3+}-Nd^{3+} clusters are gradually replaced by Nd^{3+}-Lu^{3+}

clusters, preventing the onset of cross-relaxation processes, which otherwise quench the Nd^{3+} luminescence.

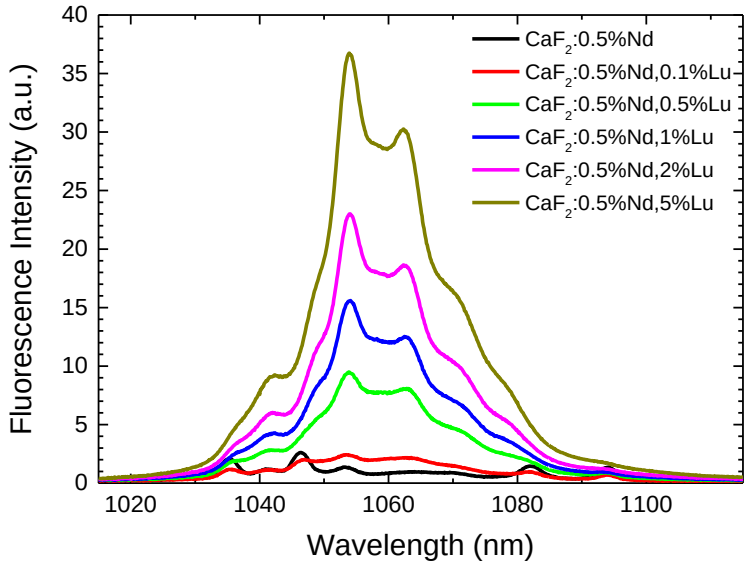

Fig. 2.6 Emission spectra of CaF_2:Nd^{3+},Lu^{3+} under 797 nm excitation showing the increase of intensity when increasing Lu^{3+} concentration.

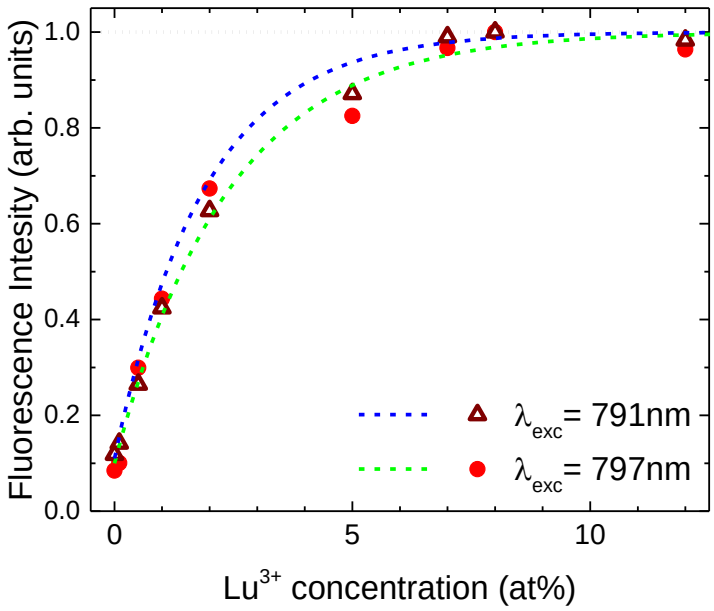

Fig. 2.7 $^4F_{3/2} \rightarrow {}^4I_{11/2}$ integrated emission intensity (for the same absorbed pump power) versus Lu^{3+} codopant concentration.

The integrated emission intensity normalised to the sample absorbance is represented as a function of lutetium concentration in figure 2.7. It shows that the increase follows a cumulative distribution function curve, leading up to an asymptotic value, which indicates that the neodymium clusters are most likely completely removed from the host.

The graph suggests that, roughly above 5 at% Lu^{3+} concentration, the vast majority of quenched Nd^{3+}-Nd^{3+} ions is replaced by Nd^{3+} optically active centres. In addition, the rate of this increase seems to vary when exciting the samples either at 791 nm or at 797nm. This effect is most probably related to the excitation of different structures at the two distinct wavelengths. The analysis of these different structures is discussed in the following paragraphs.

When exciting at 791 nm a Nd^{3+},Lu^{3+}-codoped CaF_2 sample, one can see that the shape of the 1.05 µm emission band is quite different from that under a 797 nm excitation, as shown for CaF_2:0.5% Nd,5% Lu in figure 2.8. This observation suggests the presence of different kinds of optically active Nd^{3+}-Lu^{3+} clusters in the samples. Similarly, the occurrence of different cluster structures has been previously reported in the case of CaF_2:Nd^{3+},Y^{3+} [13] and CaF_2:Pr^{3+},Lu^{3+} [9].

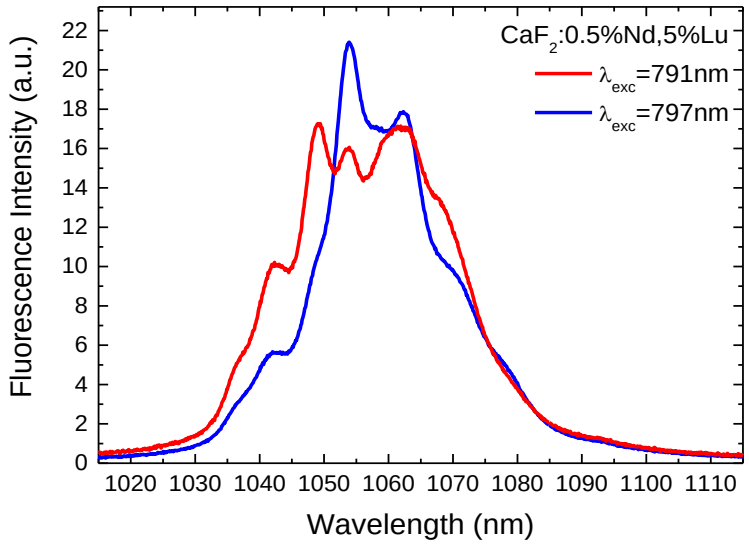

Fig. 2.8 Emission spectra ($^4F_{3/2}\rightarrow{}^4I_{11/2}$ transition) of a CaF_2:0.5% Nd,5% Lu sample after excitation at 791 and 797 nm.

In particular, one can notice from figure 2.8 that under a 791 nm excitation the emission band appears broader with three local maxima of roughly the same intensity, while under the 797 nm excitation the band presents a more pronounced maximum at 1054 nm. The 1054 nm peak can thus be associated to the 797 nm excitation, which is, as a matter of fact, the main absorption

feature that appears when codoping with Lu^{3+} ions (Fig. 2.5). Therefore, it can be concluded that the emission peak at 1054 nm is characteristic of one type of Nd^{3+}-Lu^{3+} centres. This remark is further supported by the various experiments detailed in the rest of this work. On the other hand, the most characteristic feature of the emission spectrum under a 791 nm excitation is the peak at 1049 nm, which is almost non-existent when exciting at 797 nm (Fig. 2.8). From these results, one can identify two pairs of excitation-emission wavelengths, which can be advantageously used to discriminate the corresponding two types of luminescent Nd^{3+}-Lu^{3+} centres, namely 791 nm-1049 nm and 797 nm-1054 nm.

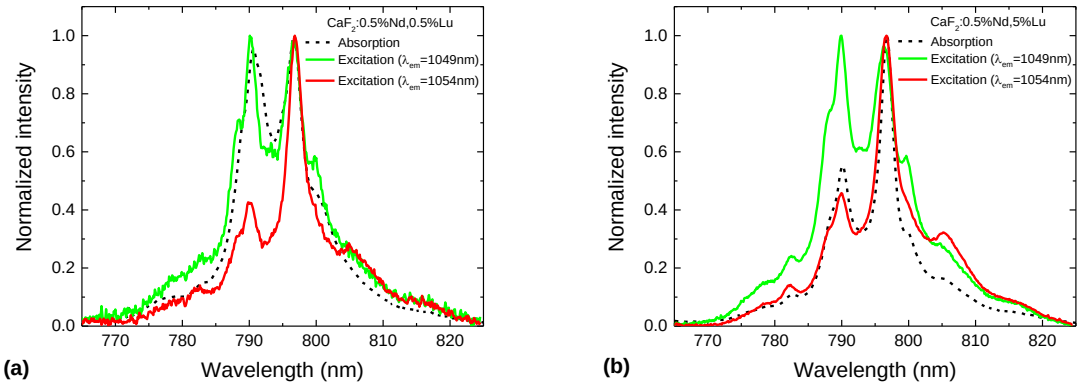

Fig. 2.9 Excitation spectra compared to normalized absorption spectra around 800nm for (a) 0.5% and (b) 5% lutetium-doped samples. Spectra have been normalised for the sake of clarity.

Excitation spectroscopy provides further insight on the differences between specific emission lines. The normalized excitation spectra for the two emission wavelengths of interest (1049 nm and 1054 nm) are shown in figure 2.9, where they are compared to the absorption spectrum recorded for the same samples: CaF_2:0.5% Nd,0.5% Lu (Fig. 2.9(a)) and CaF_2:0.5% Nd,5% Lu (Fig. 2.9(b)). The excitation spectra confirm a correspondence between the 797 nm excitation and the 1054 nm emission, since the excitation peak at 797 nm becomes prominent when recording the emission intensity at 1054 nm in both samples. On the other hand, the excitation peak at 791 nm rises in both samples when monitoring the emission at 1049 nm, again confirming the 791 nm excitation-1049 nm emission correlation suggested by the fluorescence spectra. Now, when comparing absorption and excitation spectra, the absorption spectrum at low Lu^{3+} concentration (CaF_2:0.5% Nd,0.5% Lu, Fig. 2.9(a)) is very similar to the excitation spectrum recorded at 1049 nm. This suggests that the Nd^{3+}-Lu^{3+} centre associated with the 791 nm excitation is the dominant Nd^{3+} centre at low Lu^{3+} concentration. Whereas, at higher Lu^{3+} concentration, the absorption spectrum drastically changes and resembles the excitation spectrum recorded at 1054 nm. The contribution (and therefore, most probably, the

concentration) of the Nd^{3+}-Lu^{3+} centre associated to the 797 nm absorption line becomes more predominant as more Lu^{3+} buffer ions are introduced.

An additional important comment to figure 2.9 is that the excitation spectrum recorded at a specific emission wavelength (either 1049 nm or 1054 nm) is the same in both samples despite the change from 0.5% Lu^{3+} to 5% Lu^{3+}. This result shows uniformity in the spectroscopy of the Nd^{3+},Lu^{3+}-codoped CaF_2 samples indicating that the spectroscopic signatures of each Nd^{3+}-Lu^{3+} emitting centre remain the same when changing the Lu concentration.

2.3.d Lifetimes

Emission decays of the $^4F_{3/2}$ emitting energy level have been recorded with the different Nd^{3+},Lu^{3+} codoped samples. An example is given in figure 2.10. One can see in this figure that in the same sample (here CaF_2:0.5% Nd,5% Lu) the $^4F_{3/2}$ decay time is clearly different depending on the excitation wavelength, further confirming the existence of different Nd^{3+}-Lu^{3+} emitting centres. The largest difference in $^4F_{3/2}$ decay times is observed in all samples between the excitation-emission wavelength couples 797 nm-1054 nm and 791 nm-1049 nm previously mentioned, which are both associated to two different types of Nd^{3+}-Lu^{3+} clusters. Fluorescence lifetimes values for these two excitation-emission wavelength couples are given in figure 2.11 as a function of the Lu^{3+} concentration. Due to the non-exponential character of some decay curves, fluorescence lifetimes τ_f were determined by integrating the entire decay curves according to the expression (2.07):

$$\tau_f = \frac{1}{I_0}\int_0^\infty I(t)dt \qquad (2.07)$$

in which I_0 is the fluorescence intensity at $t = 0$.

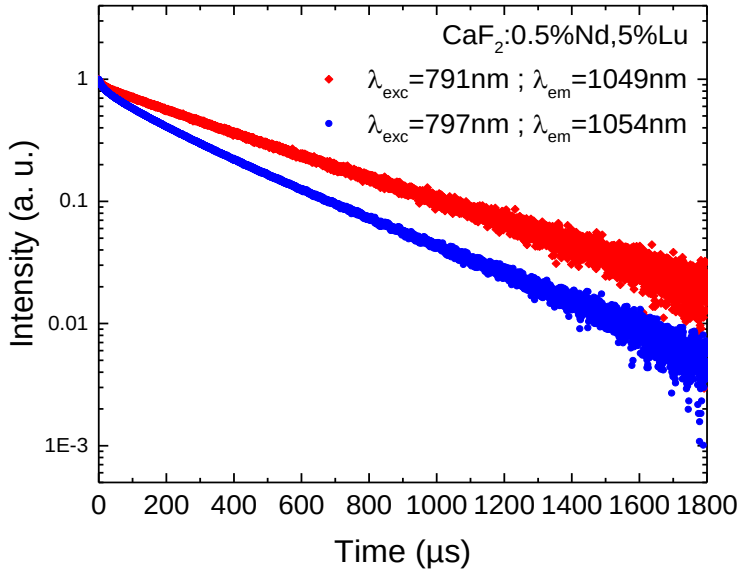

Fig. 2.10 $^4F_{3/2}$ fluorescence decay in CaF_2:0.5% Nd,5% Lu for the excitation-emission wavelength pairs 791 nm-1049 nm and 797 nm-1054 nm.

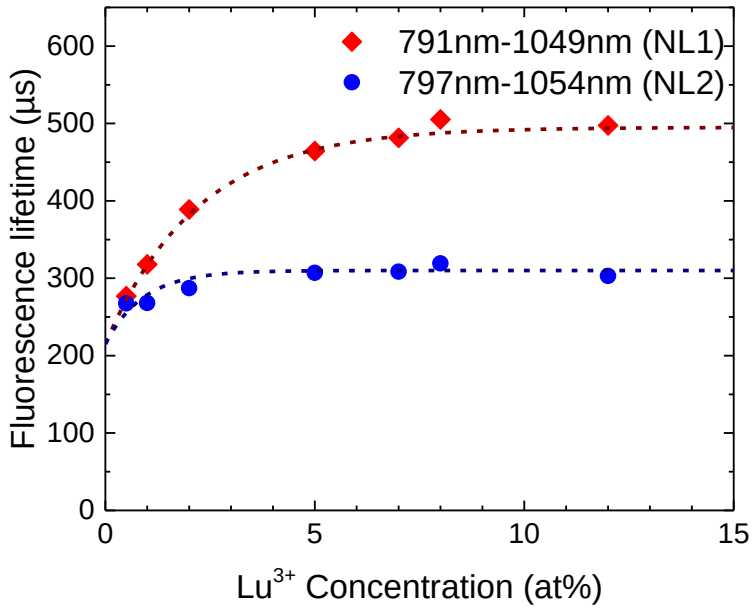

Fig. 2.11 $^4F_{3/2}$ fluorescence lifetimes for the excitation-emission wavelength pairs 791 nm-1049 nm and 797 nm-1054 nm corresponding to NL1 and NL2 centres respectively.

When exciting at 791 nm and recording at 1049 nm, the Nd^{3+}-Lu^{3+} cluster predominant at low Lu^{3+} concentrations, further referred to as NL1, exhibits a $^4F_{3/2}$ lifetime which increases from 280 µs at 0.5% Lu to reach a much longer lifetime with a steady value of 480 µs for Lu^{3+} concentrations equal and above 5% Lu. For the other type of Nd^{3+}-Lu^{3+} clusters labelled as NL2, the $^4F_{3/2}$ lifetimes recorded at 1054 nm while exciting at 797 nm quickly reach a value of about 310 µs. Similarly, the work of Basiev *et al.* [77] identifies two groups of active centres in CaF_2:Nd^{3+},Y^{3+}, which are labelled as I and II. The group I includes the quasi-rhombic M' and N' sites and the group II, corresponds to the quasi-tetragonal L^* sites. Moreover, the quasi-rhombic M' and N' centres usually have a longer emission lifetime, around 500 µs, while the tetragonal L^* centre lifetime is around 300 µs. These results are consistent with the lifetimes measured in this work on Nd^{3+},Lu^{3+} codoping for the NL1 and NL2 centres. Therefore, the NL1 centre is most likely similar to the quasi-rhombic group I of Basiev et al. and the NL2 centre comparable to the quasi-tetragonal group II.

2.3.e Site-Selective Spectroscopy

The fact that both Nd^{3+}-Lu^{3+} emitting centres NL1 and NL2 exhibit different $^4F_{3/2}$ lifetimes enables the use of time-resolved spectroscopy techniques in order to further discriminate the emission spectrum associated to each centre. In fact, the emission spectra displayed in figure 2.8, while being different, have contributions from both Nd^{3+}-Lu^{3+} centres. When exciting the material either at 791 nm or 797 nm, one centre is more efficiently excited than the other, but both centres emit light as they both absorb at 791 nm and 797 nm (Fig. 2.9). Whereas, by carefully choosing the Lu^{3+} concentration, the excitation wavelength and the time window, one can isolate in an efficient manner the "pure" emission spectrum of one specific centre using time-resolved spectroscopy as shown in figure 2.12. In particular, since the lifetime of the NL2 centres is sensibly shorter than for the NL1 centres, the intensity of NL2 emission at a relatively long time is extremely reduced with respect to the NL1 emission.

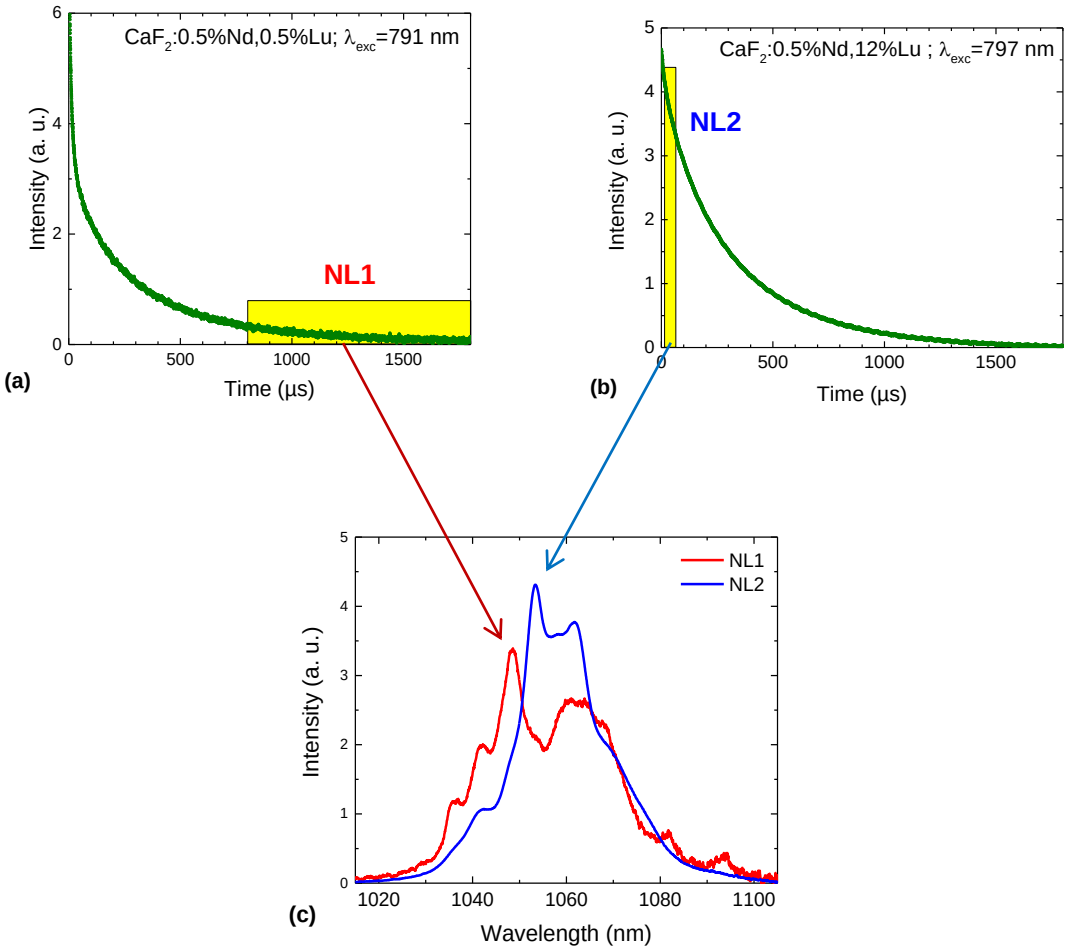

Fig. 2.12 Time-resolved spectroscopy measurements: (a-b) $^4F_{3/2}$ fluorescence decays in CaF_2:0.5% Nd,0.5% Lu excited at 791 nm and in CaF_2:0.5% Nd,12% Lu excited at 797 nm; (c) time-resolved emission spectra recorded for NL1 with decay (a) within a late time window starting at 800 μs and for NL2 with decay (b) within 12 to 60 μs.

In order to first isolate the emission spectrum of NL1 predominant at low Lu^{3+} concentration, which is characterized by a longer decay time, a CaF_2:0.5% Nd,0.5% Lu sample was excited at 791 nm. The corresponding 1.05 μm time-resolved emission spectrum was recorded within a time window starting towards the end of the decay, at 800 μs. The 1.05 μm time-resolved emission spectrum of NL2 was on the contrary obtained by exciting a high-Lu^{3+} concentration sample (CaF_2:0.5% Nd,5% Lu) at 797 nm, and recording the emission spectrum within an early time window (12 μs-60 μs) since that centre displays a shorter decay time than NL1. As shown in figure 2.12(c), the emission spectra of the two sites are quite different, and their emission maxima are positioned at the expected wavelengths of 1049 nm for NL1 and 1054 nm for NL2.

To summarize shortly, to this point it has been shown that NL1 has a slower $^4F_{3/2}$ decay time, an absorption peak at 791 nm, an emission maximum at 1049 nm and is the dominant emitting centre at low Lu^{3+} concentration. Whereas NL2 is associated with a faster decay, the 797 nm absorption line, a maximum of emission at 1054 nm and is the predominant centre at high Lu^{3+} concentration.

Furthermore, NL1 and NL2 have been confirmed to be the only two main emitting centres in CaF_2:Nd^{3+},Lu^{3+}, since a linear combination of the two emission spectra can be used to successfully reproduce any of the emission spectra, regardless of the excitation wavelength and codopant concentration, as illustrated in figure 2.13 for CaF_2:0.5% Nd,5% Lu excited et 797 nm. This excludes the necessity of introducing another site geometry.

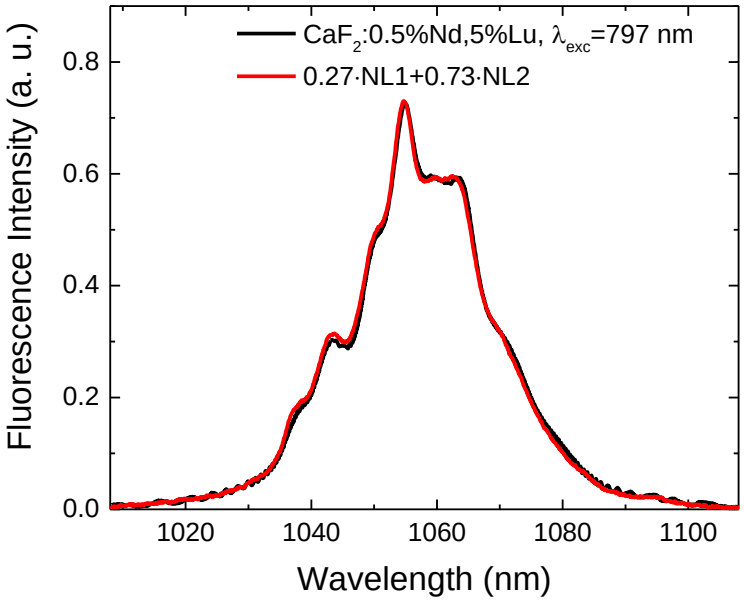

Fig. 2.13 Linear combination of NL1 and NL2 emission spectra compared to the recorded emission spectrum in CaF_2:0.5% Nd, 5% Lu.

Time-resolved excitation spectroscopy was also used in order to isolate the specific excitation spectra of NL1 and NL2 in a similar manner as what was done for the emission spectra since the excitation spectra in figure 2.9 contain contributions from both Nd^{3+}-Lu^{3+} centres. Like in the excitation spectroscopy experiment, a tuneable Ti:sapphire laser was used as the excitation source and tuned between 765 nm and 825 nm. Additionally, the Ti:sapphire was modulated using an acousto-optic modulator. This modulation was used to implement time windows on the collected signal within which the excitation spectrum was recorded. The NL1 excitation

spectrum was recorded by collecting the emission intensity at 1049 nm from a CaF_2:0.5% Nd,0.5% Lu sample within a late time window starting at 800 µs. The NL2 excitation spectrum was obtained by recording the emitted light at 1054 nm from a CaF_2:0.5% Nd,12% Lu sample, within an early time window spanning from 12 µs to 60 µs.

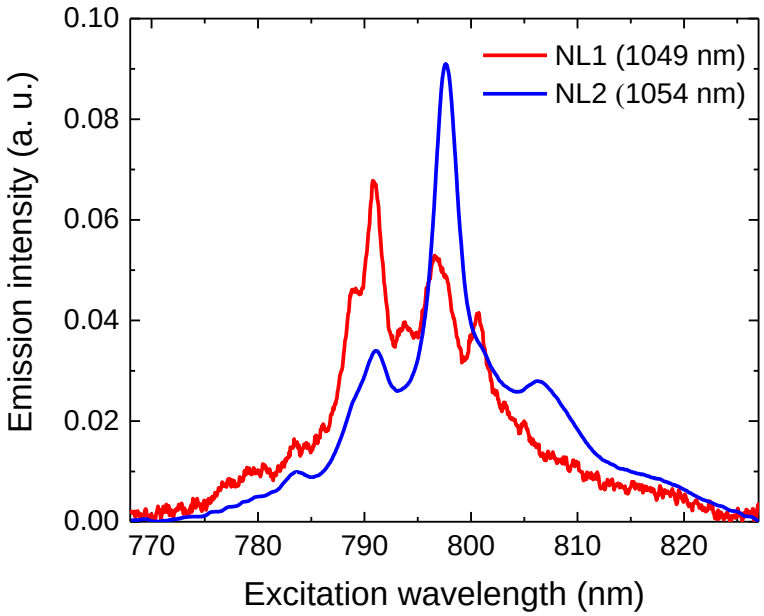

Fig. 2.14 Excitation spectra of NL1 and NL2 sites obtained from time-resolved excitation measurements at 1049 and 1054 nm.

As expected, the excitation maximum is at 791 nm for NL1 while the maximum lies at 797 nm for NL2 (Fig. 2.14). When comparing the time-resolved excitation spectra and the traditional excitation spectra (Fig. 2.9), one can see that the excitation spectrum recorded at 1049 nm (NL1) significantly changes as the peak at 797 nm (NL2 contribution) shrinks sensibly when using time-resolved measurements.

The excitation spectra obtained with these measurements corroborate the observations on the spectroscopic properties of the two main Nd^{3+} active centres. Furthermore it provides the approximate band shape of NL1 and NL2 absorption spectra around 800 nm, which can be used to calculate the NL1 and NL2 absorption cross sections, as discussed in the following subsection.

2.3.f Absorption Cross Sections and Concentrations

The various spectroscopy experiments presented earlier enable one to isolate the decay times, excitation and emission spectra of NL1 and NL2. However, it is important to further assess the absorption and emission cross-sections of each Nd^{3+}-Lu^{3+} centre and to estimate the concentration of each centre as a function of the Lu^{3+} codopant concentration.

The absorption spectra of the different codoped samples are given in absorption coefficient in figure 2.5. It is therefore necessary to discriminate within these absorption spectra the contributions from NL1 and NL2. This discrimination then opens the way to first derive the absorption coefficient and afterwards both the concentration and absorption cross sections of the two different centres in each codoped sample.

In the absence of nonlinear effects, the total absorption coefficient for a given sample can be described by a linear combination of the Nd^{3+} centres absorption coefficients:

$$\alpha(\mathrm{Lu}\%, \lambda) = \sum_i N_i(\mathrm{Lu}\%) \cdot \sigma_{\mathrm{i}}(\lambda) \qquad (2.08)$$

where σ_i is the i-th centre absorption cross section, and N_i is the i-th centre concentration, the sum of all centre concentrations being equal to the total Nd^{3+} ion concentration, N_T. In the case at hand, the centres involved are not just NL1 and NL2. The quenched Nd^{3+}-Nd^{3+} clusters also contribute to the absorption. While the cross-relaxation phenomenon prevents their radiative emission, they do appear in the absorption spectra. Quenched Nd^{3+}-Nd^{3+} clusters are the dominant species in singly Nd^{3+}-doped CaF_2, which explains the very weak luminescence of CaF_2:0.5% Nd^{3+} previously discussed. Therefore, the CaF_2:0.5% Nd^{3+}, absorption spectrum can be considered as the absorption spectrum of Nd^{3+}-Nd^{3+} clusters, further on labelled as NC for simplicity.

The difficulty of this study lies in the fact that most absorption spectra have contributions from the three centres previously mentioned, NL1, NL2 and NC clusters, and neither of the values of the parameters σ_i and N_i to be used in equation (2.08) are known. Fortunately, since virtually all neodymium ions form Nd^{3+}-Nd^{3+} clusters in Nd^{3+} singly-doped CaF_2 crystals, as previously seen and observed in literature [2], the CaF_2:0.5% Nd sample (0% Lu^{3+}) provides the absorption cross section spectrum of the Nd^{3+}-Nd^{3+} clusters (σ_{NC}) via the simple equation:

$$\sigma_{\mathrm{NC}}(\lambda) = \frac{\alpha(\lambda, 0\%\ \mathrm{Lu})}{N_{\mathrm{NC}}(0\%\ \mathrm{Lu})} = \frac{\alpha(\lambda, 0\%\ \mathrm{Lu})}{N_{\mathrm{T}}} \tag{2.09}$$

where N_{NC} indicates the NC centre concentration.

Once σ_{NC} is evaluated, it can be used in the linear reconstruction of the absorption coefficient spectra of different samples. To proceed, then, it is necessary to identify the next sample that can provide the absorption cross section spectrum of a specific centre.

Since, as we know, NL1 is the dominant Nd^{3+}-Lu^{3+} centre at low Lu^{3+} concentrations, the concentration of NL2 centres in CaF_2:0.5% Nd,0.1% Lu can be considered negligible. Therefore, the absorption coefficient in CaF_2:0.5% Nd,0.1% Lu can be written as a linear combination of NC clusters and NL1 absorption coefficients:

$$\alpha(\lambda, 0.1\%\ \mathrm{Lu}) = N_{\mathrm{NC}}(0.1\%\ \mathrm{Lu}) \cdot \sigma_{\mathrm{NC}}(\lambda) + N_{\mathrm{NL1}}(0.1\%\ \mathrm{Lu}) \cdot \sigma_{\mathrm{NL1}}(\lambda) \tag{2.10}$$

Since we know the NC absorption coefficient spectrum and the absorption spectral shape of NL1 centres (see figure 2.14), which can be considered as very similar in shape to the NL1 excitation spectrum (Fig. 2.14), it is possible to first derive the NC clusters concentration (N_{NC}) and then the NL1 concentration and its absorption cross-section spectrum. To do so, eqn. (2.10) can be rewritten:

$$\alpha(\lambda, 0.1\%\ \mathrm{Lu}) - \frac{N_{\mathrm{NC}}(0.1\%\ \mathrm{Lu})}{N_{\mathrm{T}}} \cdot \alpha(\lambda, 0\%\ \mathrm{Lu}) = N_{\mathrm{NL1}}(0.1\%\ \mathrm{Lu}) \cdot \sigma_{\mathrm{NL1}}(\lambda) \tag{2.11}$$

with $N_{\mathrm{NC}}/N_{\mathrm{T}}$ the proportion of NC clusters in the sample.

Following eqn. (2.11), the NC absorption coefficient spectrum (Fig. 2.15(a)) is multiplied by an adjustable factor corresponding to $N_{\mathrm{NC}}/N_{\mathrm{T}}$ the proportion of NC clusters in CaF_2:0.5% Nd,0.1% Lu and then subtracted to the CaF_2:0.5% Nd,0.1% Lu absorption coefficient spectrum so that the resulting absorption spectral shape is as close as possible to the NL1 excitation spectrum (Fig. 2.15(b)). The estimated multiplying factor is 0.75 in figure 2.15(b), which means that 75% of Nd^{3+} centres are NC clusters in CaF_2:0.5% Nd,0.1% Lu. Therefore, the remaining 25% centres in the sample are NL1 centres. It is worth noting that the results obtained using this approach have been successfully confirmed by the reconstruction of absorption spectra and emission spectra which will be detailed later in the text.

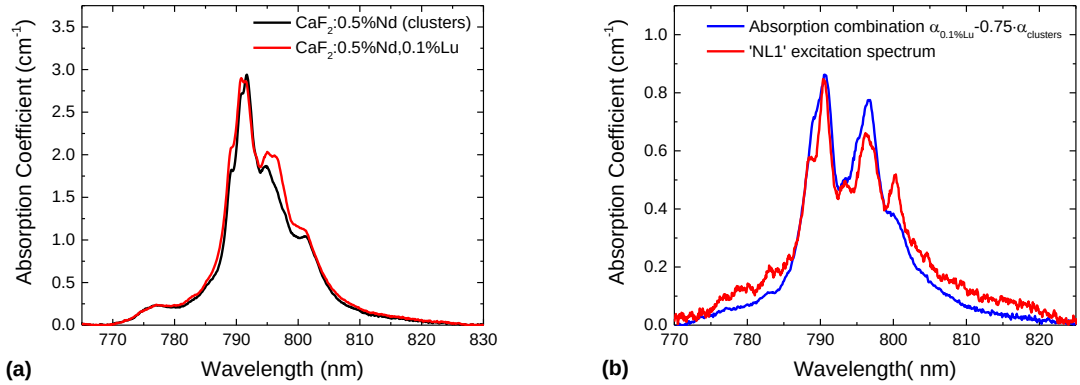

Fig. 2.15 (a) Absorption coefficient spectrum (α) of CaF_2:0.5% Nd (NC only) and CaF_2:0.5% Nd,0.1% Lu (combination of NC and NL1). (b) Comparison between α(0.1%Lu)-0.75·α_{NC} and the NL1 excitation spectrum.

Knowing the NC and NL1 concentrations, the absorption cross section for the NL1 centres can then be derived using eqn. (2.10):

$$\sigma_{\mathrm{NL1}}(\lambda) = \frac{\alpha(\lambda, 0.1\%\ \mathrm{Lu}) - 0.75 \cdot N_{\mathrm{T}} \cdot \sigma_{\mathrm{NC}}(\lambda)}{0.25 \cdot N_{\mathrm{T}}} \qquad (2.12)$$

The corresponding NL1 absorption cross-section spectrum is given in figure 2.16.

In order to now determine the NL2 absorption cross-section spectrum and concentration, σ_{NL2} and N_{NL2} respectively, we followed the same type of procedure. As suggested by figure 2.7, in which the Nd^{3+} intensity reaches a steady-state value at high Lu^{3+} concentration, CaF_2:0.5% Nd,12% Lu can reasonably be assumed to be free of NC clusters and only contains NL1 and NL2 centres. The total absorption coefficient in this sample is therefore written:

$$\alpha(\lambda, 12\%\ \mathrm{Lu}) = N_{\mathrm{NL1}}(12\%\ \mathrm{Lu}) \cdot \sigma_{\mathrm{NL1}}(\lambda) + N_{\mathrm{NL2}}(12\%\ \mathrm{Lu}) \cdot \sigma_{\mathrm{NL2}}(\lambda) \qquad (2.13)$$

The NL1 absorption cross-section spectrum σ_{NL1} multiplied by a factor (= N_{NL1}(12% Lu)) was then subtracted from the total absorption coefficient spectrum so that the result corresponds to the NL2 excitation spectrum. A factor of 0.22·N_{T} was found meaning that N_{NL1}(12% Lu) = 0.22·N_{T} and thus N_{NL2}(12% Lu) = 0.78·N_{T}.

The NL2 centre absorption cross section is then defined as:

$$\sigma_{\mathrm{NL2}}(\lambda) = \frac{\alpha(\lambda, 12\%\ \mathrm{Lu}) - 0.22 \cdot N_{\mathrm{T}} \cdot \sigma_{\mathrm{NL1}}(\lambda)}{0.78 \cdot N_{\mathrm{T}}} \qquad (2.14)$$

The absorption cross sections spectra for NL1, NL2 and NC are shown in figure 2.16, and their characteristic values reported in Table 2.1.

Table 2.1 Peak wavelengths and peak absorption cross sections for the three main Nd^{3+} centres in CaF_2:Nd^{3+},Lu^{3+}.

		NC	**NL1**	**NL2**
$\boldsymbol{\lambda_{max}}$	nm	792	791	797
$\boldsymbol{\sigma_{abs}(\lambda_{max})}$	10^{-20} cm^2	2.4	2.8	3.7

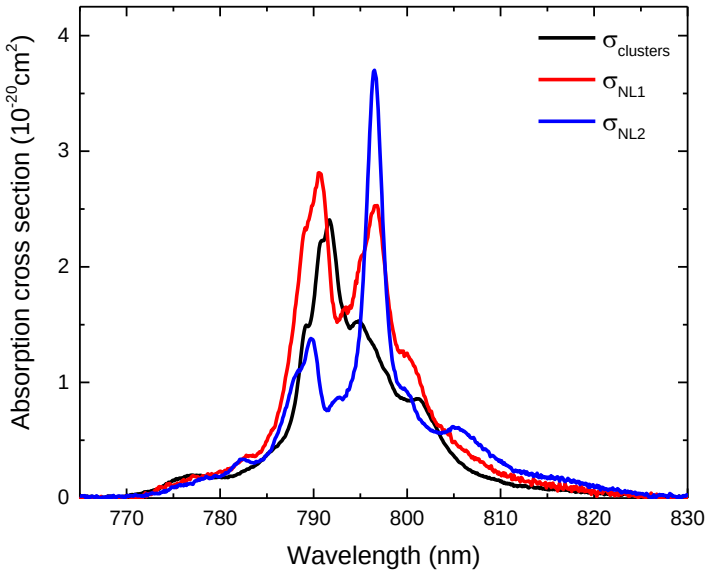

Fig. 2.16 Absorption cross section spectra for N1, NL2, and Nd^{3+}-Nd^{3+} clusters in CaF_2:Nd^{3+},Lu^{3+}.

The association of the 791 nm and 797 nm absorption wavelengths with the NL1 and NL2 centres respectively is consistent with the first spectroscopic observations mentioned earlier in the text. The results of this absorption cross sections estimation provide important parameters for the study and application of these laser materials. However, the validity of these values has to be confirmed before they can be put to use in further calculations.

2.3.g Consistency of the Description

To verify the validity of these absorption cross section spectra, their combination must accurately reproduce the absorption spectra of all CaF_2:Nd^{3+},Lu^{3+} samples. To do so, the absorption spectrum of each sample was compared to a linear combination of the three absorption cross sections, the adjusting coefficients being the respective concentration of each type of centre, as per equation (2.08):

$$\alpha(\lambda) = N_{\mathrm{NC}} \cdot \sigma_{\mathrm{NC}}(\lambda) + N_{\mathrm{NL1}} \cdot \sigma_{\mathrm{NL1}}(\lambda) + N_{\mathrm{NL2}} \cdot \sigma_{\mathrm{NL2}}(\lambda) \qquad (2.15)$$

The absorption cross section spectra have been successfully combined, reproducing the absorption coefficient spectrum of all samples (Fig. 2.17). The reconstruction of these spectra thus validates the calculated absorption cross section spectra (Fig. 2.16).

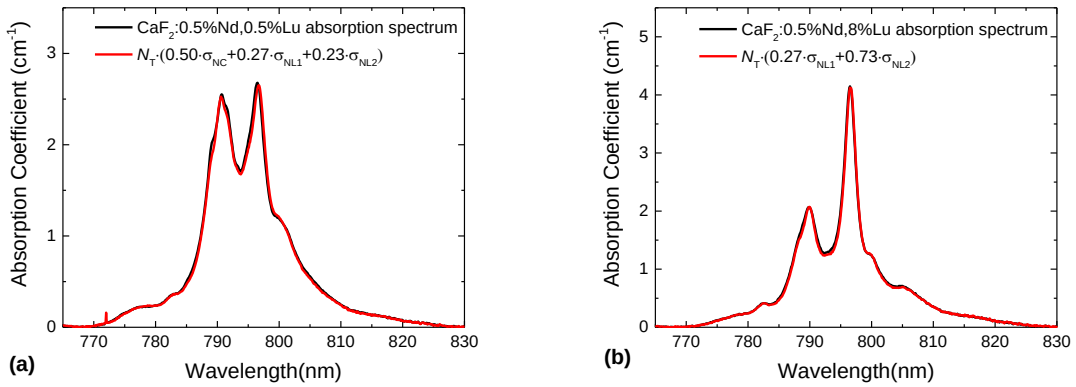

Fig. 2.17 Reconstruction of absorption spectra with linear combinations of the absorption cross sections of clusters, NL1 and NL2 centres for samples (a) CaF_2:0.5% Nd,0.5% Lu and (b) CaF_2:0.5% Nd,8% Lu. Each coefficient corresponds to the fraction of concentration of the relative site.

Moreover, since the optimal coefficients of the linear combinations correspond to the respective concentrations of the different centres in the samples, this procedure allows to trace a plot the centre concentrations as a function of the lutetium concentration, as illustrated by figure 2.18. As expected, NC clusters concentration drastically decreases as Lu^{3+} ions are added into the crystal host becoming negligible at 8% Lu. NL1 centres dominate at low Lu concentration, but are quickly overcome by NL2 centres which become the predominant emitting centres at 2% Lu and beyond (for instance, $N_{\mathrm{NL1}} = 0.34 \cdot 10^{20}$ cm^{-3} and $N_{\mathrm{NL2}} = 0.83 \cdot 10^{20}$ cm^{-3} in CaF_2:0.5% Nd,5% Lu). Interestingly, the NL2/NL1 concentration ratio tends towards a steady value of 4 for high Lu^{3+} concentration.

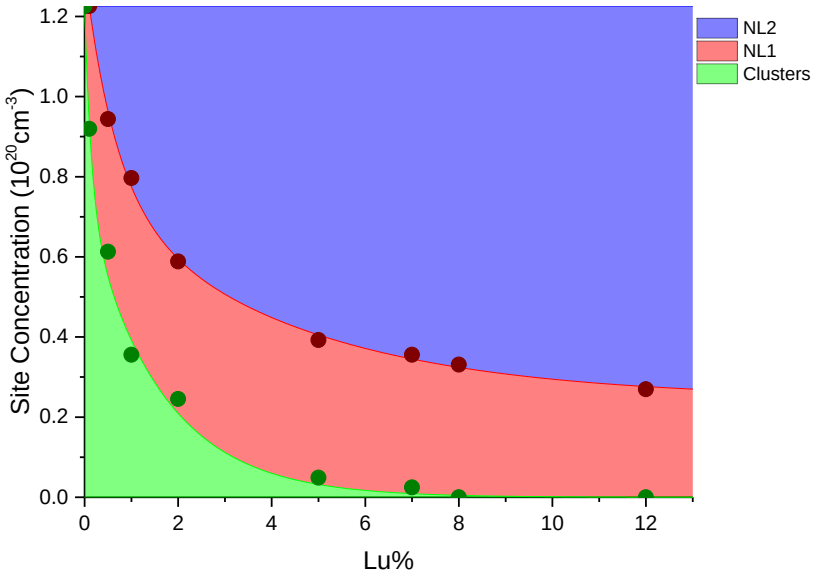

Fig. 2.18 Evolution of Nd^{3+} sites concentration (NL1, NL2 and Nd^{3+}-Nd^{3+} clusters) as a function of lutetium concentration in CaF_2:Nd^{3+},Lu^{3+}.

To further verify the consistency of the overall spectroscopic description, we compared the emission spectra of the different samples with a reconstruction of these spectra based on absorption cross-sections, fluorescence and radiative lifetimes and the different centre concentrations. To do so, we consider that the NC clusters being optically inactive, the fluorescence intensity in any sample is given by $I=I_{NL1}+I_{NL2}$, with

$$I_{\mathrm{NL1,2}} \propto \frac{\beta}{\tau_{\mathrm{rad}}^{\mathrm{NL1,2}}} \cdot N_{\mathrm{NL1,2}}^{*} \tag{2.16}$$

where β is the branching ratio associated with the $^4F_{3/2} \rightarrow {}^4I_{11/2}$ transition and N^* is the excited $^4F_{3/2}$ level population, defined in the steady–state regime as $N^*_{\mathrm{NL1,2}}=N_{\mathrm{NL1,2}} \cdot \phi \cdot \sigma_{abs} \cdot \tau_f$ with ϕ being the pump photon flux. The branching ratio β can be reasonably considered similar for both NL1 and NL2, since it is only very lightly influenced by the crystal field surrounding the Nd^{3+} centres. The pump photon flux ϕ during an experiment is of course the same for NL1 and NL2. Therefore, at a given emission wavelength, the emission intensity becomes:

$$I(\lambda) = I_{NL1}(\lambda) + I_{NL2}(\lambda) \tag{2.17}$$

$$I(\lambda) \propto \frac{N_{\mathrm{NL1}} \cdot \sigma_{\mathrm{abs}}^{\mathrm{NL1}} \cdot \tau_f^{\mathrm{NL1}}}{\tau_{\mathrm{rad}}^{\mathrm{NL1}}} . g_{NL1}(\lambda) + \frac{N_{\mathrm{NL2}} \cdot \sigma_{\mathrm{abs}}^{\mathrm{NL2}} \cdot \tau_f^{\mathrm{NL2}}}{\tau_{\mathrm{rad}}^{\mathrm{NL2}}} . g_{NL2}(\lambda) \quad (2.18)$$

where $g_{NL1}(\lambda)$ and $g_{NL2}(\lambda)$ are NL1 and NL2 normalized lineshape functions (Fig. 2.12), defined as:

$$g_{\mathrm{NL1,2}}(\lambda) = \frac{I_{\mathrm{NL1,2}}(\lambda)}{\int I_{\mathrm{NL1,2}}(\lambda)\, d\lambda} \quad (2.19)$$

Within eqn. (2.18), the absorption cross sections (Fig. 2.16) and Nd^{3+}-Lu^{3+} centre concentrations (Fig. 2.18) are known, along with the fluorescence lifetimes (Fig. 2.11). However, the $^4F_{3/2}$ radiative lifetimes for each Nd^{3+}-Lu^{3+} cluster are not known. Radiative lifetimes are usually derived from Judd-Ofelt analysis which is here difficult to implement since one should isolate for each Nd^{3+}-Lu^{3+} cluster a separate set of absorption cross section spectra to develop two distinct Judd-Ofelt analyses. Provided that energy transfer and multi-phonon relaxation processes are negligible, a reasonable way to assess radiative lifetimes is to consider the longer part of NL1 and NL2 fluorescence decays (after 800 μs) which are single exponential (Fig. 2.10, for instance). In the late part of the decay, direct energy transfer among rare-earth ions or towards impurities can be in fact neglected, since they only affect the early part of fluorescence decays. Migration-assisted energy transfers, which influence the longer part of the decay, can be here reasonably disregarded, as the Nd^{3+} concentration is only 0.5 at% Finally, multi-phonon relaxation processes, which reduce the fluorescence lifetime in comparison with the radiative lifetime, can also convincingly be neglected, since the energy gap between the $^4F_{3/2}$ and its closest lower-energy level $^4I_{15/2}$ is about 6500 cm^{-1} while the maximum phonon energy in CaF_2 is 450 cm^{-1}. As a consequence, the late part of the $^4F_{3/2}$ decay is, for the purpose of this work, a good estimate of the radiative lifetime. Figure 2.19 shows the estimated radiative lifetimes obtained exciting at 791 nm and recording at 1049 nm for NL1 and exciting at 797 nm and recording at 1054 nm for NL2. As expected, the radiative lifetime estimate stays constant with the Lu^{3+} concentration.

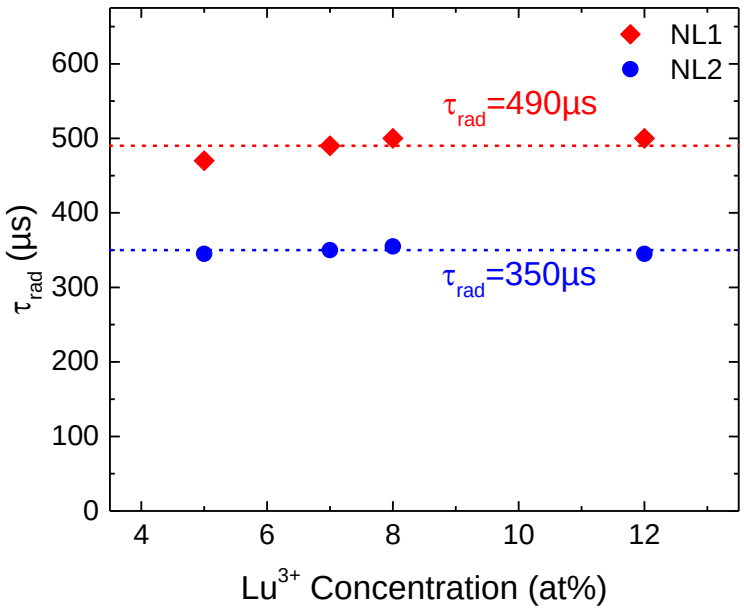

Fig. 2.19 Radiative lifetime estimation for NL1 and NL2 sites, obtained via fitting of the exponential part of the fluorescence decay data.

Emission spectra were then reconstructed using eqn. (2.18) and were compared with the actual fluorescence spectra, showing a successful reproduction both in shape and intensity, as shown for the spectra in figure 2.20 for two different samples using different excitation wavelengths. The very small difference between reconstructed spectra and fluorescence spectra evidences the consistency of the proposed spectroscopic description of CaF_2:Nd^{3+},Lu^{3+}.

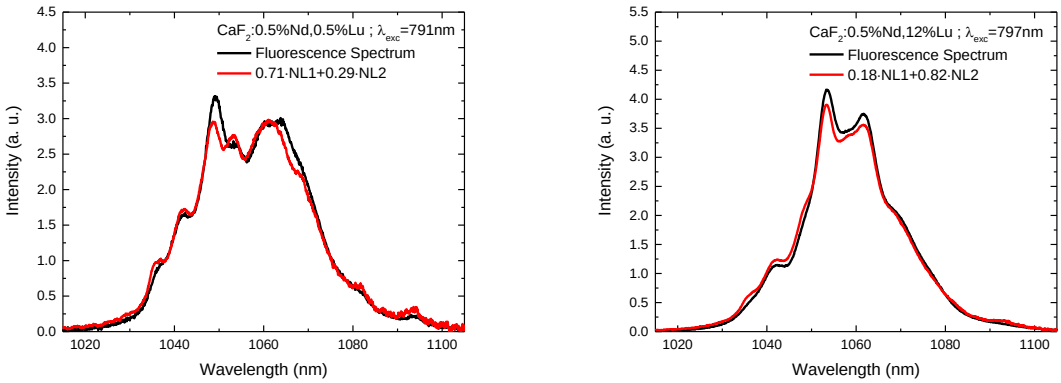

Fig. 2.20 Comparison between fluorescence spectra and spectra reconstructed from pure NL1 and NL2 emission spectra, in CaF_2:0.5% Nd, 0.5% Lu (a) and CaF_2:0.5% Nd, 12% Lu (b).

Eqn. (2.18) can also be used to calculate the evolution of the integrated emission of the $^4F_{3/2}\rightarrow{}^4I_{11/2}$ transition for the different samples and excitation wavelengths. Integrating eqn. (2.18) over the $^4F_{3/2}\rightarrow{}^4I_{11/2}$ emission range, one obtains:

$$I \propto \frac{N_{NL1}\cdot\sigma_{abs}^{NL1}\cdot\tau_f^{NL1}}{\tau_{rad}^{NL1}} + \frac{N_{NL2}\cdot\sigma_{abs}^{NL2}\cdot\tau_f^{NL2}}{\tau_{rad}^{NL2}} \qquad (2.20)$$

These calculated values were compared with the experimental data for excitations at both 791 nm and 797 nm, as shown in figure 2.21. The similarity between the calculated and experimental values once again supports the consistency of the spectroscopic description.

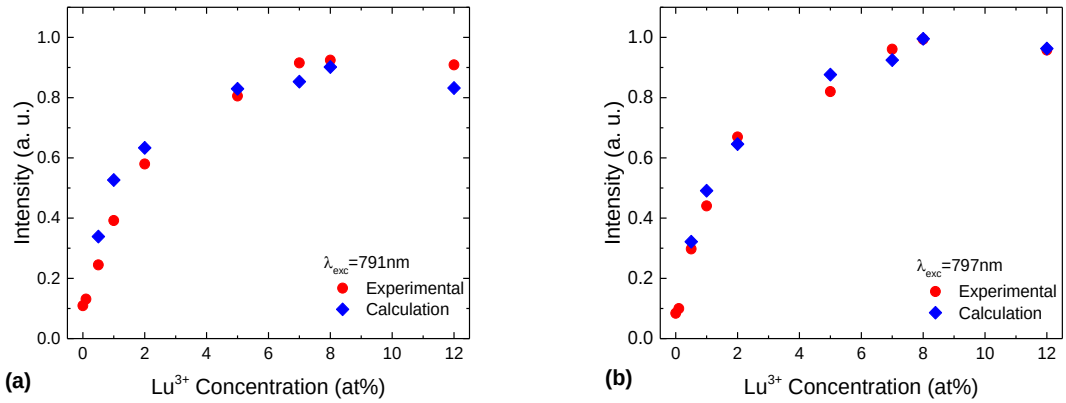

Fig. 2.21 Comparison between the values of integrated intensity obtained from fluorescence spectroscopy measurements and the values of intensity obtained from relation (2.20), for excitation wavelengths (a) 791 nm and (b) 797 nm.

2.3.h Emission Cross Sections

Finally, the NL1 and NL2 emission spectra (Fig. 2.12(c)) were used to calculate the stimulated emission cross sections for the two different Nd^{3+}-Lu^{3+} centres, by applying the Füchtbauer-Ladenburg formula (eqn. (2.05)).

$$\sigma_{em}(\lambda) = \frac{\beta\lambda^5}{8\pi c n^2 \tau_{rad}} \frac{I(\lambda)}{\int I(\lambda)\lambda\, d\lambda} \qquad (2.05)$$

with β ($^4F_{3/2}\rightarrow{}^4I_{11/2}$ transition) equal to 0.45 and n the CaF_2 refractive index, which is 1.42 around 1 μm. The resulting emission cross section spectra are shown in figure 2.22.

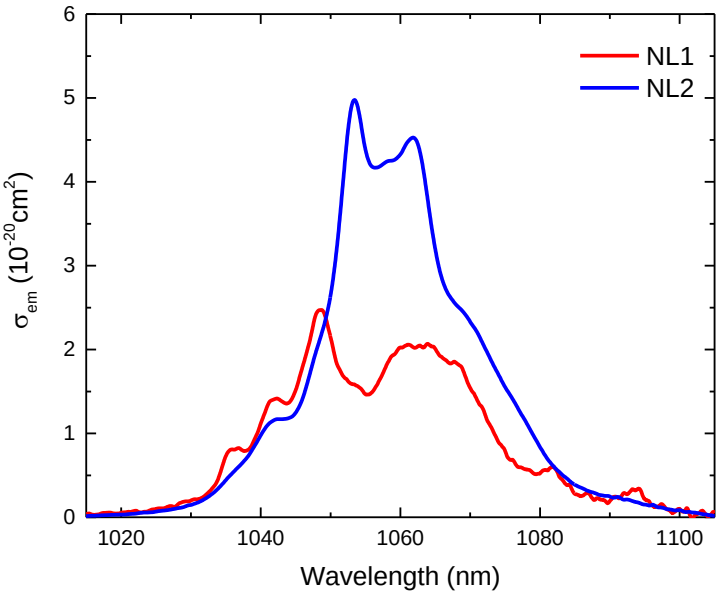

Fig. 2.22 Stimulated emission cross sections for NL1 and NL2 centres, calculated with the Füchtbauer-Ladenburg equation.

This calculation provides a very important set of spectroscopic parameters, since the determination of the emission cross sections is crucial to the estimation of the material laser properties. These results will be further used in chapter 4, presenting laser gain measurements and calculations.

2.3.i Quantum Yield

A sample ability to convert an optical input signal into a different optical signal is described by its quantum yield, or radiative quantum efficiency, which is defined as the ratio between the emitted and absorbed photon fluxes [100]. Quantum yield may be evaluated by measuring the sample total emitted power, and knowing the absorbed power. With a standard photodetector, only relative quantum yield measurements are possible, as fluorescence takes place isotropically. However, absolute quantum yield measurements can be performed by using an integrating sphere, which allows the collection of the entire emitted light.

A quantum yield experiment was set up using an integrating sphere and a tuneable Ti:Sapphire laser as the excitation beam. The spectral response of the integrating sphere and the connected detector was calibrated using a wide-spectrum fluorescence lamp and a set of filters

with known transmittance. The linearity of this response with the pumping power was assessed employing a laser and a set of neutral filters with gradually decreasing transmittance, ensuring that the calibration holds for the power range of the measurements.

The sample excitation beam absorption was measured outside of the apparatus, and a power meter was employed to keep track of the excitation beam power P_e. A long-pass filter was added before the detector to filter out the residual excitation beam light. The beam was then focussed on the sphere entry hole. A silicon photodiode was used as the detector.

Given the electric signal measured via the photodiode, I, and knowing the absorbed power P_{abs}, the quantum yield of the sample, η_q, is given by the following formula:

$$\eta_q = \frac{I}{P_{abs}\,\lambda_{exc}} \left(\int \frac{R(\lambda)\,F(\lambda)\,g(\lambda)}{\lambda} d\lambda \right)^{-1} \tag{2.21}$$

where λ_{exc} is the excitation beam wavelength, $R(\lambda)$ is the system's spectral response, $F(\lambda)$ is the filter's transmission function, $g(\lambda)$ is the sample emission spectral density. The integral is performed over the sample entire emission.

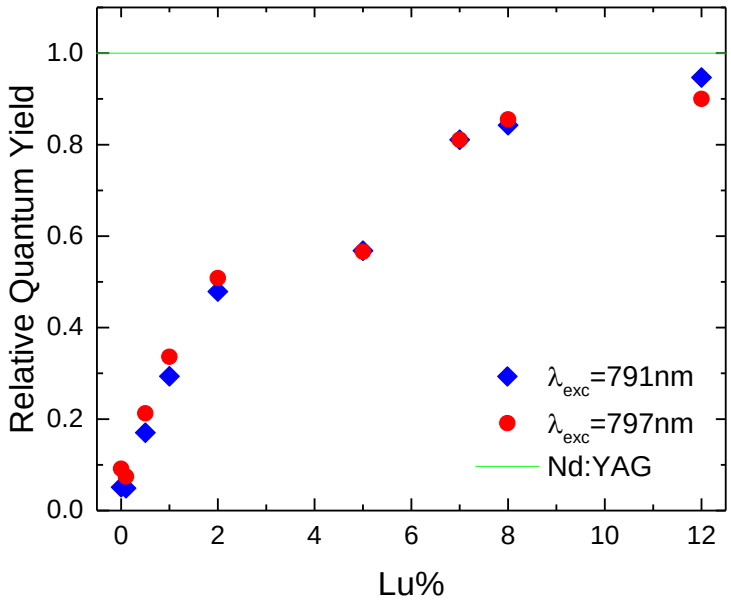

Fig. 2.23 Relative quantum yield results for CaF_2:Nd^{3+},Lu^{3+} samples, normalised and compared to the value of a Nd:YAG sample's quantum yield.

The measurements were performed on all CaF_2 samples, and on a known Nd:YAG sample for comparison purposes. While the measurement of absolute emission values is difficult, an interesting comparison between all the samples was obtained. The relative values (normalised to the reference Nd:YAG sample value) are shown in figure 2.23.

One can see in this evolution that the calcium fluoride samples quantum yield increases monotonously when increasing lutetium concentration, reaching values comparable to those of Nd:YAG above 10% Lu^{3+}. This is an expected behaviour driven by the breaking of the inactive Nd^{3+}-Nd^{3+} clusters in favour of active Nd^{3+}-Lu^{3+} sites. In fact, this behaviour is consistent with that of the integrated intensity discussed earlier in this section and illustrated in figure 2.7. To illustrate the similarity between quantum yield and fluorescence measurements results, they have been plotted together in figure 2.24 for two different excitation wavelengths Results from both approaches show the consistency of both types of measurements regardless of the excitation wavelength.

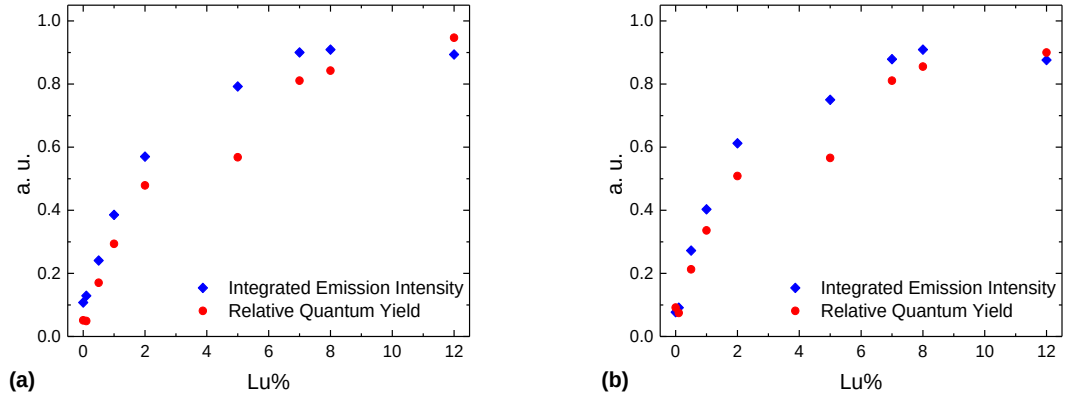

Fig. 2.24 Comparison between integrated emission intensity and relative quantum yield measurements, with excitation upon (a) 791 nm and (b) 797 nm.

2.3 Comparison with SrF_2 and BaF_2

Strontium fluoride (SrF_2) and barium fluoride (BaF_2) are two crystals with a structure similar to CaF_2, and share with it similar properties. In particular, SrF_2 is a well-known laser material, already successfully employed as amplifying media [16-18]. Like in CaF_2, a similar effect of RE cluster forming has been observed in the case of SrF_2:Nd^{3+} samples [18,101], where the appearance of two different Nd^{3+}-Nd^{3+} cluster centres were recognized. In Orlovskii's work [18],

the codoping ion is lanthanum (La^{3+}), and the study shows the appearance of different spectral features as the doping composition is modified. Particularly, the so-labelled L centres are active in Nd^{3+} singly-doped SrF_2 crystals, while M and N centre geometries are observed in Nd^{3+}-La^{3+} codoped samples.

As for barium fluoride, to the best of our knowledge, there is little to none information published about BaF_2-based lasers, although some properties of BaF_2:Nd^{3+} were investigated alongside those of the other fluoride crystals by Payne *et al.* [2].

2.4.a Absorption

A set of SrF_2 and BaF_2 samples doped with 0.5 at% Nd^{3+} and co-doped with a lutetium content ranging from 0 to 20 at% was grown in cylindrical geometry via the Bridgman method, then cut and polished to disk shape.

Absorption spectra were collected in the same manner as for the previous samples, and are shown in figure 2.25.

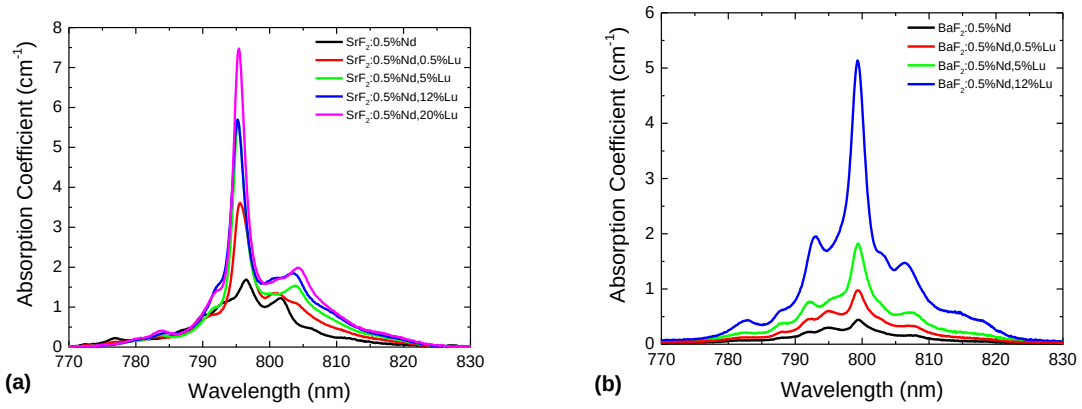

Fig. 2.25 Absorption spectra of (a) SrF_2:Nd^{3+},Lu^{3+} samples and (b) BaF_2:Nd^{3+},Lu^{3+} samples.

The main absorption peak is found at about 795 nm for SrF_2 samples, and 799 nm for BaF_2. One can notice that the absorption coefficient grows sensibly (albeit not monotonously) with the increase in lutetium concentration in both SrF_2 and BaF_2. This suggests that the neodymium site oscillator strength changes as a function of the lutetium concentration in SrF_2:Nd^{3+},Lu^{3+} and BaF_2:Nd^{3+},Lu^{3+}, given that the neodymium concentration is the same in all samples. This

behaviour is peculiar, since the oscillator strength should not strongly depend on the codoping concentration.

Unlike CaF_2, strontium and barium fluoride do not show sensible changes in the shape of their spectral bands, the only exception being the low-lutetium codoped SrF_2 samples. This suggests that one single dominant active site is present in the material, which may facilitate the pumping of the desired emission centres. At high lutetium concentration, one can notice as well that the absorption coefficient peak value is higher than in CaF_2 crystals (compare to figure 2.5), which implies a larger absorption for the same crystal length.

Portions of the $SrF_2:Nd^{3+},Lu^{3+}$ and $BaF_2:Nd^{3+},Lu^{3+}$ crystals were sent to analysed the Laboratoire de Métallographie et d'Analyses Chimiques (LMAC) of the CEA Marcoule for inductively coupled plasma mass spectrometry (ICP-MS) measurements. The results for SrF_2 samples are shown in table 2.2 and those for BaF_2 samples in table 2.3.

Table 2.2 ICP-MS results for $SrF_2:Nd^{3+},Lu^{3+}$ samples.

	Element Concentration (mg/g)					
Sample	**Ba**	**Ca**	**Lu**	**Nd**	**Sr**	**F**
SrF_2:0.5% Nd	7.6	< 0.1	1.2	5.5	661	302
SrF_2:0.5% Nd,0.1% Lu	9.2	1.8	2.4	6.4	673	310
SrF_2:0.5% Nd,0.5% Lu	2.1	1.0	10.0	5.3	663	282
SrF_2:0.5% Nd,1% Lu	0.2	0.7	11.6	8.5	601	259
SrF_2:0.5% Nd,2% Lu	1.9	0.4	33.2	5.1	636	320
SrF_2:0.5% Nd,5% Lu	0.3	0.8	59.7	5.8	594	268
SrF_2:0.5% Nd,6% Lu	1.0	32.3	82.7	5.6	557	292
SrF_2:0.5% Nd,7% Lu	94.5	0.8	75.7	5.5	506	280
SrF_2:0.5% Nd,8% Lu	111.1	0.3	90.9	5.4	505	291
SrF_2:0.5% Nd,10% Lu	2.0	22.6	130.9	6.9	513	299
SrF_2:0.5% Nd,12% Lu	76.0	0.4	122.4	5.3	464	259
SrF_2:0.5% Nd,20% Lu	1.5	38.4	209.5	4.9	364	281

Table 2.3 ICP-MS results for $BaF_2:Nd^{3+},Lu^{3+}$ samples.

	Element Concentration (mg/g)					
Sample	**Ba**	**Ca**	**Lu**	**Nd**	**Sr**	**F**
BaF_2:0.5% Nd	765	< 0.1	4,6	6,1	1,3	212
BaF_2:0.5% Nd,0.1% Lu	773	< 0.1	1,5	6,7	3,4	212
BaF_2:0.5% Nd,0.5% Lu	826	< 0.1	20,0	6,3	4,4	241
BaF_2:0.5% Nd,1% Lu	741	0,2	7,2	6,4	1,8	211
BaF_2:0.5% Nd,2% Lu	755	< 0.1	34,0	6,0	3,7	215
BaF_2:0.5% Nd,5% Lu	764	0,6	35,0	6,0	1,7	214
BaF_2:0.5% Nd,6% Lu	694	0,5	51,8	5,1	2,2	231
BaF_2:0.5% Nd,7% Lu	576	0,5	103,8	5,4	55,4	227
BaF_2:0.5% Nd,8% Lu	559	< 0.1	108,7	6,9	51,7	213
BaF_2:0.5% Nd,10% Lu	481	< 0.1	86,2	5,8	0,5	214
BaF_2:0.5% Nd,12% Lu	544	0,2	176,7	6,5	55,2	223

Most notably, the ICP-MS results show that the Nd^{3+} concentration is approximatively constant for all samples, except for isolated cases such as SrF_2:0.5% Nd,1% Lu, which present a sensible neodymium concentration excess. Therefore, the increase in the samples absorption coefficient as a function of lutetium concentration is not due to an increase in neodymium concentration. This means that the gradual increase in lutetium concentration most likely causes an augmentation in the crystal field intensity on the active centres positions, which in turn increases the Nd^{3+} centres oscillator strengths.

One can also notice that some of the $SrF_2:Nd^{3+},Lu^{3+}$ samples are contaminated with barium (7%, 8% and 12% lutetium-doped) and some present signs of calcium contamination (6%, 10% and 20% lutetium-doped). Some of the $BaF_2:Nd^{3+},Lu^{3+}$ samples also show slight contamination issues, in particular strontium (7%, 8% and 12% lutetium-doped). It is worth pointing out that the samples showing similar contamination issues always belong to the same fabrication set. An excess of Lu^{3+} can also be noticed in the nominally 7%, 8% and 12% lutetium-doped sample set. However, these contaminations do not change drastically the spectroscopic properties of these samples.

2.4.b Fluorescence

The fluorescence spectra were collected while exciting the samples upon their main absorption wavelength; the emission peak wavelength in SrF_2:Nd^{3+},Lu^{3+} is at 1056.5 nm, and in BaF_2:Nd^{3+},Lu^{3+} it is advantageously located at 1053 nm (figure 2.26) in BaF_2:0.5% Nd,12% Lu. In particular, one can see that the SrF_2 samples band shape is much broader around the maximum than in BaF_2, but the peak is not at the optimal wavelength of 1053 nm for the desired application. This suggests the possibility of combining the two materials to achieve a broad emission band as flat as possible around 1053 nm.

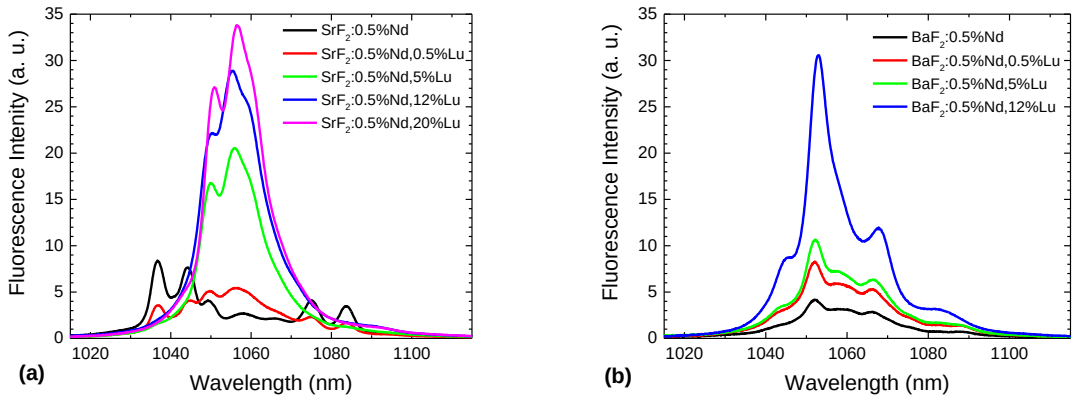

Fig. 2.26 Emission spectra of (a) SrF_2:Nd^{3+},Lu^{3+} samples excited at 795 nm and (b) BaF_2:Nd^{3+},Lu^{3+} samples excited at 799 nm.

Indeed, despite its very broad emission band, the peak maximum position of SrF_2 at 1056.5 nm and the presence of a local minimum precisely at 1052 nm make it less suitable than CaF_2 for the intended application. On the other hand, BaF_2 spectra exhibit the right emission peak, but the sharpness of the peak makes it less appealing than CaF_2, which has a broader band.

2.4.c Lifetimes and Time-Resolved Spectroscopy

Lifetime measurements were also performed, as shown for instance in figure 2.27. The estimated average $^4F_{3/2}$ lifetime in Nd^{3+} and Lu^{3+}-doped SrF_2 and BaF_2 samples are respectively 310 µs and 380 µs. One can see that a single exponential decay function fits accurately the time-dependent behaviour of the fluorescence intensity. This corroborates the hypothesis that one single kind of active centre dominates the spectroscopic properties. This was further confirmed by time-resolved measurements (Fig. 2.28), where early-time window measurements and long-

time window measurements result in very similar emission spectra, with no noticeable change suggesting the presence of different sites contributions.

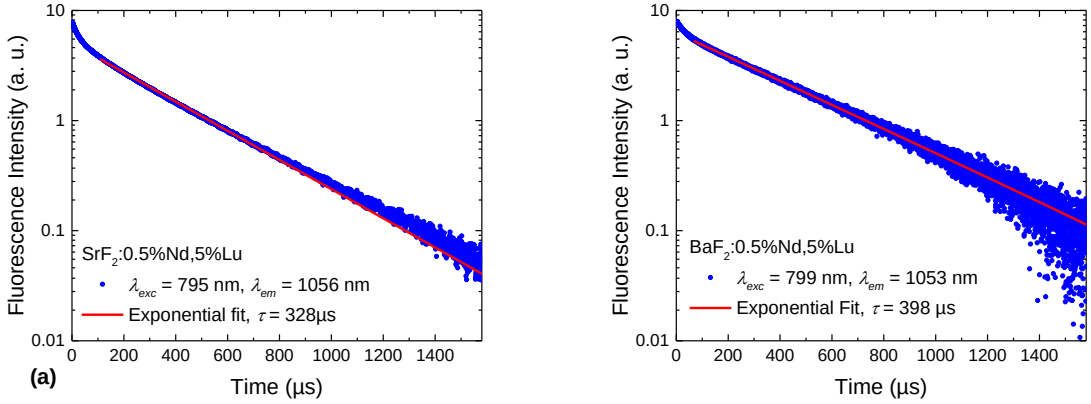

Fig. 2.27 Lifetime measurement of (a) the SrF_2:0.5% Nd,5% Lu sample excited at 795 nm and emitting at 1056 nm, and (b) the BaF_2:0.5% Nd,5% Lu sample excited at 799 nm and emitting at 1053 nm.

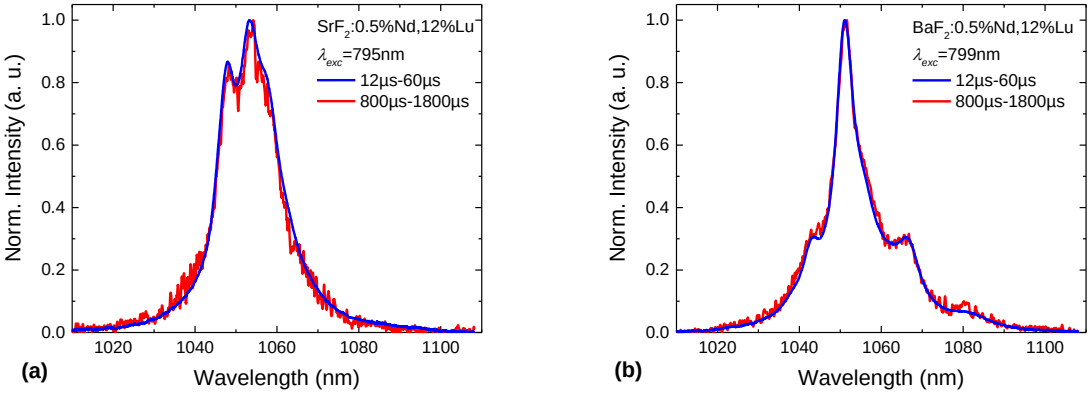

Fig. 2.28 Time-resolved spectra of (a) SrF_2:0.5% Nd,12% Lu and (b) BaF_2:0.5% Nd,12% Lu collected within a 'short' time span (12-60 μs) and a 'long' time span (800-1800 μs).

2.4 Mixed Crystals

As it is possible to see in figure 2.26, the emission bands of SrF_2:Nd^{3+},Lu^{3+} and BaF_2:Nd^{3+},Lu^{3+} around 1.05 μm have complementary traits, first of all the position of local maxima and minima. Figure 2.29(a) shows a direct comparison of the emission band shape for the two crystals doped with 0.5% neodymium and 5% lutetium. The maximum intensity of BaF_2 at 1052nm matches the

local minimum in SrF_2 at the same wavelength. This suggests the possibility of combining the two spectra to obtain an ideal flat band around 1053 nm by growing mixed SrF_2,BaF_2:Nd^{3+},Lu^{3+} crystals, assuming that their spectroscopic properties combine linearly. Figure 2.29(b) shows the optimal result of such a combination, with equal proportions of the two normalised fluorescence spectra.

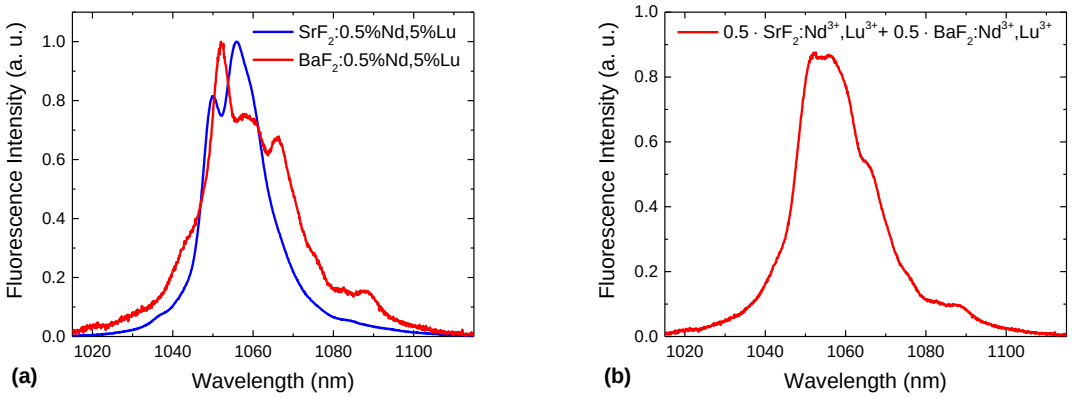

Fig. 2.29 (a) comparison between the SrF_2 and BaF_2 normalised emission spectra; (b) linear combination of the normalised emission spectra in equal proportions, forming a flat and broad band.

The flatness requirement for the LASCAN project consists in obtaining at the output of the amplifier stage an amplified spectral band with a FWHM at least as large as 3 nm around 1053 nm, for a 16 nm wide input Gaussian beam. Considering an input Gaussian beam profile with FWHM $\Delta\lambda_i$:

$$I_i(\lambda) = \exp\left(-4 \cdot ln\,2 \cdot \frac{\lambda^2}{{\Delta\lambda_i}^2}\right) \tag{2.22}$$

and an amplifier medium with a gain profile with FWHM $\Delta\lambda_f$ and effective gain G_{eff}:

$$I_g(\lambda) = \left[\exp\left(-4 \cdot ln\,2 \cdot \frac{\lambda^2}{{\Delta\lambda_f}^2}\right)\right]^{G_{eff}} \tag{2.23}$$

In the case of an active material such as a rare earth-doped crystal, $\Delta\lambda_f$ corresponds to the fluorescence band width (FWHM). The amplified spectrum is then:

$$I_a(\lambda) = \exp\left[-4 \cdot \ln 2 \cdot \frac{\lambda^2}{{\Delta\lambda_i}^2} \cdot \left(1 + G_{eff} \cdot \frac{{\Delta\lambda_i}^2}{{\Delta\lambda_f}^2}\right)\right] = \exp\left(-4 \cdot \ln 2 \cdot \frac{\lambda^2}{{\Delta\lambda_a}^2}\right) \tag{2.24}$$

where the amplified beam profile FWHM, $\Delta\lambda_a$, is defined as:

$$\Delta\lambda_a = \frac{\Delta\lambda_i}{\sqrt{1 + G_{eff} \cdot \frac{\Delta\lambda_i{}^2}{\Delta\lambda_f{}^2}}} \tag{2.25}$$

The intended amplified band FWHM equal or greater than 3 nm, is associated to a 16 nm wide input beam spectrum and an amplifier gain of 10^9 (corresponding to an effective gain G_{eff} = 20.72). With these parameters, a potential amplified spectrum was calculated, using the optimal SrF_2,BaF_2:Nd^{3+},Lu^{3+} fluorescence spectrum as the amplifier gain profile. The resulting band is in fact much broader than the reference 3 nm wide Gaussian, with a FWHM value of 6 nm, as shown in figure 2.30.

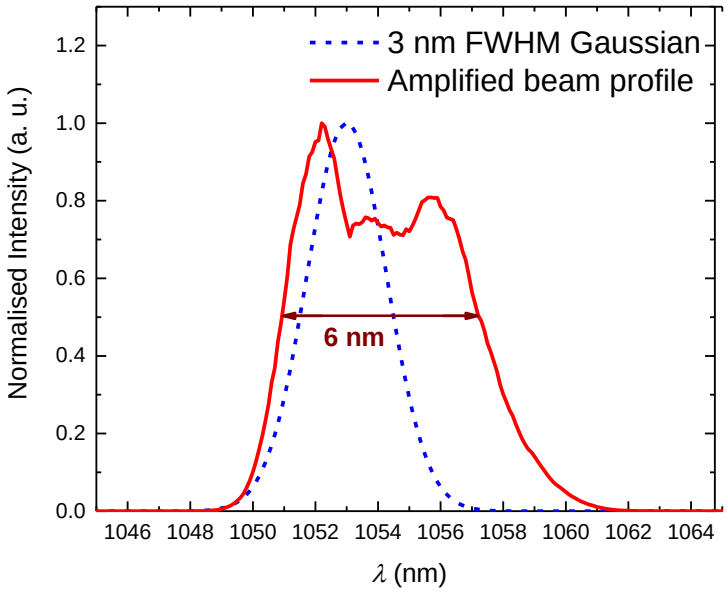

Fig. 2.30 Spectrum obtained from the amplification of a 16 nm Gaussian input beam via a SrF_2,BaF_2:Nd^{3+},Lu^{3+} medium with an effective gain G_{eff} = 20.72, compared to a reference Gaussian peak with 3 nm FWHM.

Three different mixed crystal samples were fabricated via the Bridgman growth method, with different relative concentrations of SrF_2 and BaF_2, namely 50%-50%, 80%-20%, and 90%-10% respectively, and doped with the same rare earth concentrations, i.e. 0.5 at% Nd^{3+} and 5 at% Lu^{3+}. Absorption and emission spectra were both collected for these samples, and are reported in figure 2.31.

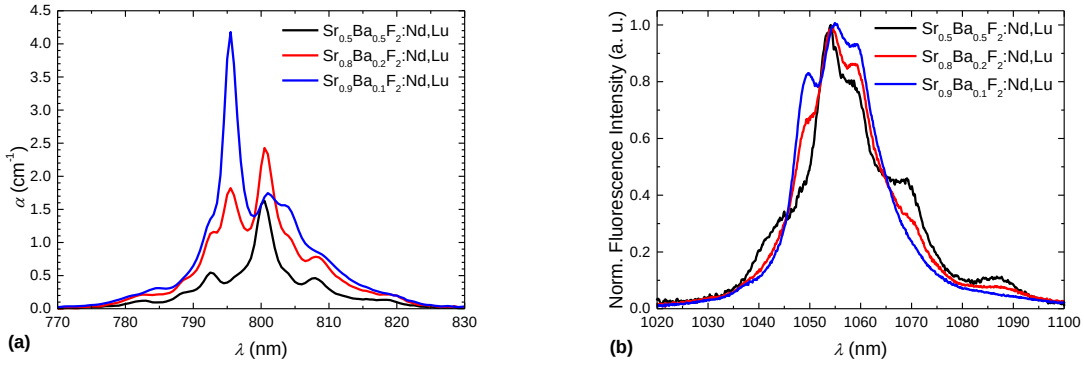

Fig. 2.31 Absorption spectra (a) and normalised emission spectra (b) excited at 795 nm of mixed SrF_2,BaF_2:0.5%Nd^{3+},5%Lu^{3+} crystals, showing the change in shape of the spectral bands as a function of the relative concentration of the two fluorides.

One can notice that the $Sr_{0.5}Ba_{0.5}F_2$:Nd^{3+},Lu^{3+} sample absorption and fluorescence spectra are very similar to those of a BaF_2:Nd^{3+},Lu^{3+} crystal (see figure 2.32). In fact, in the mixed fluoride, there are no discernible contributions associated to SrF_2:Nd^{3+},Lu^{3+}. This suggests that neodymium centres have a tendency to sit in the BaF_2 environment rather than in SrF_2. This is most likely due to the larger ionic radius of barium with respect to strontium, which is therefore closer in size to neodymium, and therefore provides more favourable substitution centres.

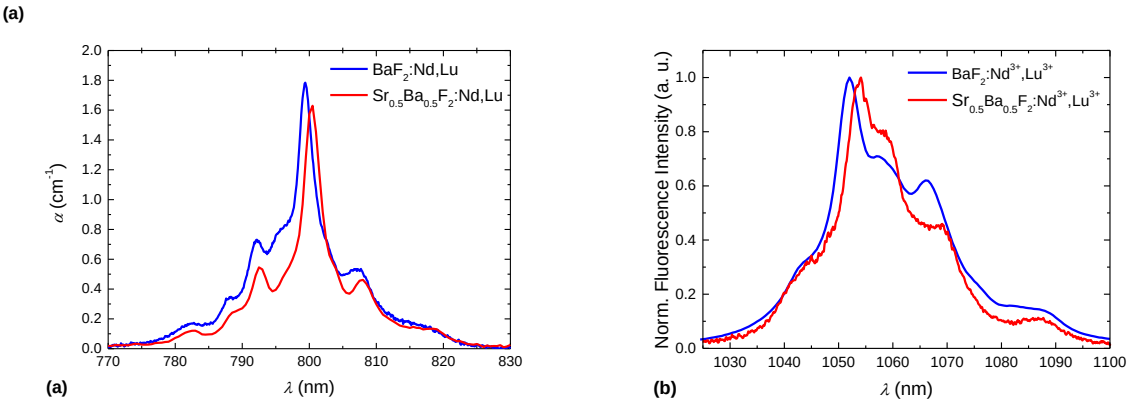

Fig. 2.32 Comparison between the BaF_2:0.5% Nd,5% Lu and the $Sr_{0.5}Ba_{0.5}F_2$:0.5% Nd,5% Lu (a) absorption and (b) emission spectra.

One can see, however, that there are differences between the mixed crystal spectra and those of BaF_2:Nd^{3+},Lu^{3+}. In fact, the $Sr_{0.5}Ba_{0.5}F_2$:Nd^{3+},Lu^{3+} sample absorption and emission peaks are shifted with respect to those of BaF_2:Nd^{3+},Lu^{3+} (Fig. 2.32). This implies that the Ba^{2+} substitution site where Nd^{3+} ions sit is distorted because of the presence of of a large number of Sr^{2+} ions in the vicinity of the Ba^{2+} site.

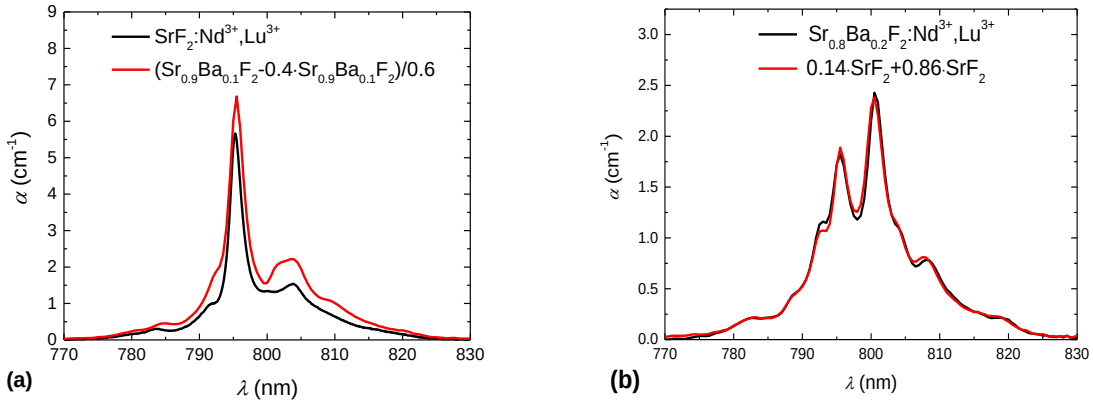

Fig. 2.33 (a) estimation of the "SrF_2-like" Nd^{3+} centre absorption for the $Sr_{0.9}Ba_{0.1}F_2$:0.5%Nd^{3+},5%Lu^{3+} sample; (b) reconstruction of the absorption spectra for the $Sr_{0.8}Ba_{0.2}F_2$:Nd^{3+},Lu^{3+} sample with a combinations of distorted BaF_2:Nd^{3+},Lu^{3+} and SrF_2:Nd^{3+},Lu^{3+} spectra.

Since virtually all neodymium ions are found within the BaF_2 environment in the $Sr_{0.5}Ba_{0.5}F_2$ crystals, one can use the absorption spectrum of that sample to calculate the relative concentration of BaF_2-like and SrF_2-like Nd^{3+} sites. This was done starting by calculating the proportions in the $Sr_{0.9}Ba_{0.1}F_2$ sample. The "distorted" BaF_2-like site absorption spectrum ($Sr_{0.5}Ba_{0.5}F_2$: Nd^{3+},Lu^{3+}), multiplied by a factor <1, was subtracted to the $Sr_{0.9}Ba_{0.1}F_2$ sample spectrum until a band shape as similar as possible to that of SrF_2:Nd^{3+},Lu^{3+} samples was obtained (Fig. 2.33(a)). A combination of the estimated BaF_2-like and SrF_2-like site absorption spectra can then be used to find the site fractions for the $Sr_{0.8}Ba_{0.2}F_2$ sample (Fig. 2.33(b)). The results are shown in figure 2.34.

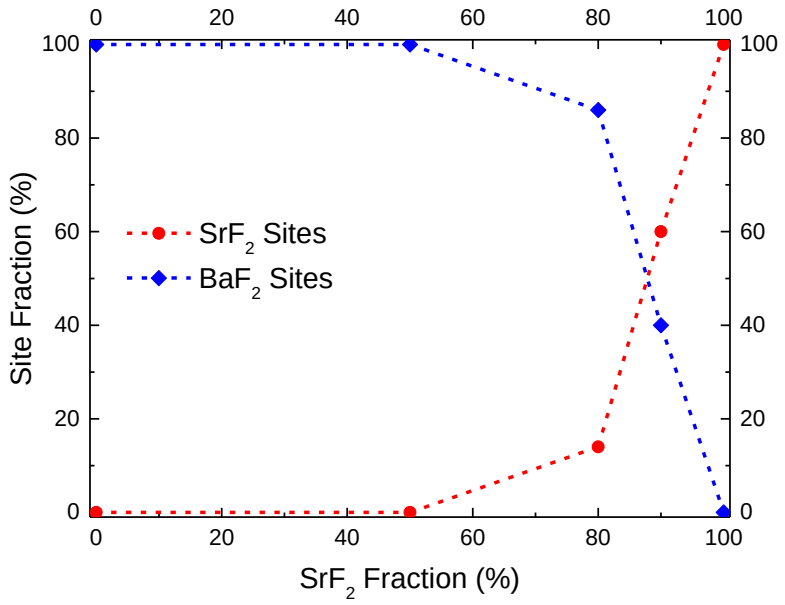

Fig. 2.34 Relative concentration of SrF_2-like and BaF_2-like Nd^{3+} sites in $SrBaF_2:Nd^{3+},Lu^{3+}$ crystals as a function of the SrF_2 fraction. The dotted lines serve as a guide for the eye.

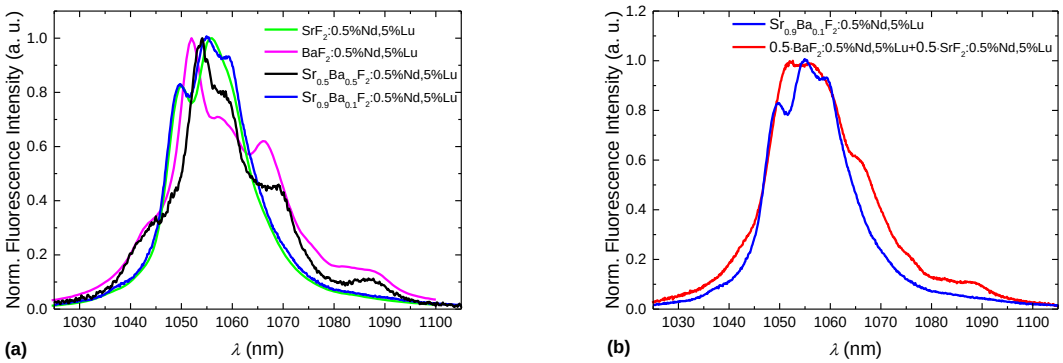

Fig. 2.35 (a) Comparison of the emission spectra of $Sr_{0.5}Ba_{0.5}F_2$:0.5% Nd,5% Lu and $Sr_{0.9}Ba_{0.1}F_2$:0.5% Nd,5% Lu exciting at 795 nm with SrF_2:0.5% Nd,5% Lu and BaF_2:0.5% Nd,5% Lu; (b) comparison between the spectrum of $Sr_{0.9}Ba_{0.1}F_2$:0.5% Nd,5% Lu and the "best-case scenario" linear combination of $SrF_2:Nd^{3+},Lu^{3+}$ and $BaF_2:Nd^{3+},Lu^{3+}$ emission spectra.

In the comparison, one can notice that the distortion of the BaF_2 site contributions causes the 1052 nm peak to shift to 1054 nm. For this reason, the main BaF_2 contribution peak does no longer correspond to the SrF_2 band minimum, which is detrimental to the end of obtaining a flat spectrum, as can be seen in figure 2.35(b). Therefore, because of the BaF_2-like Nd^{3+} sites distortion, it seems difficult to obtain the proper flat profile around 1053 nm with a mixed SrF_2,$BaF_2:Nd^{3+},Lu^{3+}$ crystal.

2.5 Conclusions

The results obtained in this chapter confirm the increase of light yield in Nd^{3+}-doped CaF_2 as a consequence of the introduction of trivalent lutetium buffer ions. The integrated emission intensity for the samples co-doped with 8 at% Lu^{3+} and more is about ten times higher than for the singly-doped crystals. This result is most likely due to the complete removal of optically quenched Nd^{3+}-Nd^{3+} clusters within the crystal lattice. The absorption and emission spectra indicate the existence of two structurally different active Nd^{3+}-Lu^{3+} centres, here labelled NL1 and NL2, which is further confirmed by lifetime measurements revealing two decays and two different radiative lifetimes. These two centres can be reasonably associated with the two types of centres, denoted as I and II for quasi-rhombic and quasi-tetragonal centres, respectively, reported in the literature in the case of Nd^{3+},Y^{3+}:CaF_2 codoping [12].

Time-resolved emission and excitation spectroscopy along with a careful choice of recording time windows, excitation wavelengths and Lu^{3+} codopant concentration allows for the discrimination of NL1 and NL2 emission and absorption spectra. Absorption cross-sections and concentrations for the three main Nd^{3+} centres, i.e. Nd^{3+}-Nd^{3+} clusters, NL1 and NL2, have been estimated using the reconstruction of absorption coefficient spectra in the different co-doped samples. Nd^{3+}-Nd^{3+} clusters are reduced drastically by Lu^{3+} co-doping, effectively disappearing at 8% Lu concentration. NL1 centres tend to dominate at low co-doping concentrations in comparison with NL2. On the other hand, NL2 centres are more and more prominent when the lutetium concentration increases eventually becoming 4 times as abundant as NL1 centres at high Lu^{3+} concentration (12 at% and beyond). The absorption cross-section, centre concentration, and fluorescence and radiative lifetimes have been used to effectively calculate the contribution of each centre in the emission spectra of all the samples under different excitation wavelengths. The subsequent reconstructions of the emission spectra are very similar to the recorded emission spectra in both spectral shape and intensity, which confirms the consistency of the overall spectroscopic description. Finally, the emission cross sections of the two active centres were calculated, leading to a full set of spectroscopic parameters describing the properties of the samples.

SrF_2:Nd^{3+},Lu^{3+} and BaF_2:Nd^{3+},Lu^{3+} samples were fabricated via Bridgman method and their spectroscopic properties were investigated. These crystals seem to possess only one type of dominant active centre, and their spectral band shape does not change when increasing lutetium concentration once the Nd^{3+}-Nd^{3+} clusters are eliminated. These materials are thought to be less appealing than CaF_2:Nd^{3+},Lu^{3+} for the purpose of high-energy laser pulse amplification, as their spectroscopic characteristics are not as well suited to the requirement of the device. A

preliminary spectroscopic study of mixed SrF_2,BaF_2:Nd^{3+},Lu^{3+} crystals suggests the possibility of tailoring and optimising the spectral properties of these materials to match ideal broad and flat emission bands. However, due to the tendency of Nd^{3+} to substitute Ba^{2+} ions rather than Sr^{2+} ions, this result may only be obtained with a high SrF_2 content. As a consequence, the Ba^{2+} substitution sites are distorted by the presence of high strontium quantities, which prevents the achievement of the ideal emission band shape.

A complete table of the spectroscopic parameters obtained for significant CaF_2, SrF_2 and BaF_2 crystals doped with Nd^{3+} and Lu^{3+} is hereby reported, including the corresponding values for LHG-8 and LG-770 neodymium-doped phosphate laser glasses, currently used in high-energy laser pulse amplifiers, for comparison (Table 2.4).

Table 2.4 Spectroscopic parameters of Nd^{3+},Lu^{3+}-doped fluoride crystals, and comparison with those of currently employed laser glasses.

Matrix	%Nd	%Lu	λ_{abs} (nm)	$\Delta\lambda_{abs}$ FWHM (nm)	σ_{abs} α/N_T (10^{-20}cm^2)	λ_{em} (nm)	$\Delta\lambda_{em}$ FWHM (nm)	σ_{em} NL1/NL2 (10^{-20}cm^2)	Quantum Defect * (%)	τ_f (µs)	τ_{rad} NL1/NL2 (µs)	F_{sat} ** NL1/NL2 (J.cm^{-2})
CaF_2	0.5	0.5	796.7	10.7	2.2	1053.9	20	1.6 / 4.9	75.6	270	490/350	12.1 / 3.9
CaF_2	0.5	5	796.8	2.8	3.4	1053.9	18	1.6 / 4.9	75.6	310	490/350	12.1 / 3.9
CaF_2	0.5	8	796.5	2.8	3.4	1053.6	21	1.6 / 5.0	75.6	320	490/350	12.0 / 3.8
CaF_2	0.5	12	796.5	2.8	3.4	1053.3	20	1.6 / 5.0	75.6	300	490/350	11.9 / 3.8
SrF_2	0.5	0.5	795.6	3.5	5.7	1056.2	21	5.5	75.3	270	360	3.4
SrF_2	0.5	5	795.3	2.5	8.6	1055.8	17	5.5	75.3	300	360	3.4
SrF_2	0.5	8	795.1	3.3	5.3	1055.0	17	5.5	75.4	340	360	3.4
SrF_2	0.5	12	795.2	2.8	8.1	1055.5	17	5.6	75.3	340	360	3.4
BaF_2	0.5	0.5	799.4	3.9	1.2	1052.1	21	4.7	76.0	360	440	4.0
BaF_2	0.5	5	799.4	4.4	2.5	1052.2	20	4.8	76.0	400	440	4.0
BaF_2	0.5	8	799.4	3.4	7.1	1052.7	21	5.0	75.9	380	440	3.8
BaF_2	0.5	12	799.3	3.4	7.0	1053.0	20	5.0	75.9	380	440	3.8
LHG-8			801.0	13	2.0	1053.0	26	3.6	76.1	300	365	12
LG-770			802.0	12	2.0	1053.0	25	3.9	76.2	300	350	12

* Quantum defect, $\eta_q = E_{em}/E_{abs} = \lambda_{abs}/\lambda_{em}$

** Saturation flux, $F_{sat} = hc/(\lambda_{abs}(\sigma_{abs} + \sigma_{em}))$

CHAPTER 3

"With five feeble senses we pretend to comprehend the boundlessly complex cosmos, yet other beings with a wider, stronger, or different range of senses might not only see very differently the things we see, but might see and study whole worlds of matter, energy, and life which lie close at hand yet can never be detected with the senses we have."

Thermomechanical Properties

3.1 Thermal Properties of Fluoride Crystals

3.1.a Introduction

One of the major advantages of crystals over glasses for laser applications is their generally higher thermal conductivity provided by their periodical lattice structure. As a consequence, one of the defining properties of crystalline materials is their efficient heat dissipation, a critical ability for an amplifier material subjected to high-energy pulses. The thermomechanical properties of a crystal depend strongly on both its chemical composition and lattice structure, and they are well known for most common crystals. However, the introduction of dopant ions is causes a gradual drop in thermal conductivity. In this chapter, the thermomechanical properties of neodymium-lutetium codoped CaF_2 samples are investigated via mode-mismatched thermal lens measurements and transient-state interferometry. The results are then compared to the predictions of existing models.

Comparison between rare earth-doped laser glasses and crystals can be found in literature: glasses provide a performing material for short-pulse laser emissions thanks to their broad emission bands, but their thermal conductivity is generally lower than 1 $W \cdot m^{-1} \cdot K^{-1}$ [102]. On average, crystals have much higher thermal conductivity values, even reaching over 10 $W \cdot m^{-1} \cdot K^{-1}$. Ytterbium-doped crystals such as $Sr_3Y(BO_3)_3$ (BOYS) [103], $SrY_4(SiO_4)_3O$ (SYS) [104],

$KGd(WO_4)_2$ (KGW) [105], $KY(WO_4)_2$ (KYW) [106] have been employed as laser material for shorter-than-200 fs pulses generation. However, these materials' pulse duration is limited by their narrow emission bands, and the power at which they can operate is limited by their relatively low thermal conductivity, which, in the undoped materials case, is in the order of 2-3 $W \cdot m^{-1} \cdot K^{-1}$.

In addition to their very broad emission bands, calcium fluoride (CaF_2) crystals, are known for possessing a very high thermal conductivity – as high as 9.7 $W \cdot m^{-1} \cdot K^{-1}$ thanks to its cubic lattice geometry. This makes them a very interesting candidate for applications requiring materials with good heat dissipation and thermal shock resistance. Such is the case of high-energy pulsed laser amplifiers, which are subjected to very sudden local thermomechanical strains as a consequence of optical absorption and nonradiative relaxation. For this reason $CaF_2:Yb^{3+}$ crystals and ceramics have been employed successfully in recent years in the realisation of tuneable pulsed laser devices around 1 μm [31,32,107-109], with pulses even shorter than 100 fs [33]. However, in the case of neodymium and lutetium-codoped calcium fluoride crystals, the thermomechanical properties are expected to undergo sensible variations due to the relatively large quantities of dopant ions introduced. Properties such as thermal conductivity can be roughly predicted by calculation via theoretical models, but is otherwise still unknown in these novel materials. This work presents a thorough study of the evolution of the thermal conductivity of $CaF_2:Nd^{3+},Lu^{3+}$ crystals based on optical measurements, and a comparison between the results and the theoretical calculations.

Temperature-dependent components of the optical path within a material such as the thermal expansion and thermo-optic effects cause the transmitted light to focus or defocus. This effect in turn causes a deformation of the transmitted beam wavefront and profile [110], which must be taken into account when choosing laser cavity parameters. In fluoride crystals, these temperature-dependent components are generally higher than in glasses, but their dependency on the doping concentration is not documented. Therefore, in this work, the influence of lutetium concentration on the temperature-related effects are investigated, in order to obtain a comprehensive overview of the impact on the thermomechanical properties of $CaF_2:Nd^{3+},Lu^{3+}$.

As was explained in chapter 2, Nd^{3+}-doped CaF_2 crystals have the tendency to form clusters of trivalent dopant ions because of the charge compensation and the subsequent appearance of interstitial fluorine ions [2,7]. It has been demonstrated that codoping with non-optically active ions such as Y^{3+} and Lu^{3+} is a suitable solution to break apart Nd^{3+}-Nd^{3+} clusters, leading to better emission properties [12].

While the optical properties of such a material are improved by the buffer ions insertion, it is known that a crystal thermal conductivity decreases as more and more dopant centres are inserted. This effect was studied in detail for garnets, particularly in the case of Yb^{3+} or Nd^{3+} doping [3,4,111,112]. The doping ions act as impurities in the crystal structure. As more and more imperfections are introduced, they cause modifications of the local lattice structure [113], which is detrimental to the material thermal properties. This was observed earlier in particular in the case of rare earth-doped crystals for laser amplification such as YAG:Nd^{3+}, YAG:Yb^{3+}, YVO_3:Nd^{3+}, and $GdVO_4$:Nd^{3+} [111,114]. In the particular case of CaF_2, the decrease in the thermomechanical properties of rare earth-doped calcium fluoride has been observed by Popov *et al.* in CaF_2:Yb^{3+} at room temperature [23], where the CaF_2 thermal conductivity decline as a function of Yb^{3+} concentration is shown. The thermal conductivity values are reduced from the original 9.7 $W \cdot m^{-1} \cdot K^{-1}$ in the undoped crystal to about 2 $W \cdot m^{-1} \cdot K^{-1}$ for molar fractions of ytterbium greater than 10%. One can therefore predict a qualitatively similar thermal conductivity behaviour in the case of doubly-doped CaF_2, as the codopant Lu^{3+} concentration increases.

Table 3.1 Main thermo-mechanical parameters discussed in this chapter.

Symbol	Meaning	Units
D	Thermal diffusivity	$cm^2 \cdot K^{-1} \cdot s^{-1}$
K	Thermal conductivity	$W \cdot m^{-1} \cdot K^{-1}$
ds/dT	Thermo-optic path variation	K^{-1}
dn/dT	Thermo-optic coefficient	K^{-1}
$\alpha = l_0^{-1} \cdot dl/dT$	Thermal expansion coefficient	K^{-1}

3.1.b Thermomechanical Properties Assessment

The thermomechanical properties of solid samples may be assessed via traditional calorimetric measurements, which employ electronic systems for heat flow control, thermocouple measurements or infrared radiation collection. These include a range of different techniques for the study of a material response to changes in temperature and heat deposition. One of these techniques, generally employed in the investigation of bulk samples, is for instance, the heat flow methods [71,115,116], which consists of a heater, and a cooling system to keep the sample environment at a set temperature. In particular, the results of Slack's paper that employs

this method [71], are significant for the work presented here, as they provide an estimate for the temperature-dependent behaviour of the CaF_2 thermal conductivity. Slack shows that the CaF_2 thermal conductivity around 300 K (roughly 10 $W \cdot m^{-1} \cdot K^{-1}$) decreases as a function of temperature. The variations in this range are weak (< 1 $W \cdot m^{-1} \cdot K^{-1}$ for temperature changes smaller than 10 K), therefore they can be neglected for small variation in temperature in the course of measurements. Another is the flash method developed by Parker *et al.* [117], and later applied to transparent optical materials by Sato and Taira [114]. In this case, heat deposition is achieved via a short light pulse from a flash lamp or laser, and the sample temperature is probed by observing its infrared emission.

3.1.c Thermo-Optic Techniques

Another useful way of assessing the thermomechanical properties of a sample is via thermo-optic measurements. This kind of measurements takes advantage of the rare earth ions absorption in order to deposit heat within the material. One of the advantages of this method is the level of control it provides over heat deposition, which depends on the absorbed power and therefore on the sample absorbance. Other assets of these techniques are the possibility to perform localised measurements, and the ability to obtain the estimate of different quantities with one measurement. This makes thermo-optic experiments very useful in the study of thermomechanical properties.

The term "thermo-optic experiments" refers to a variety of different techniques, each with its own set of advantages and applications. These measurements have taken the place of calorimetry and other thermomechanical experimental techniques in the field of optical materials, since they can be performed with optical equipment, and may provide both the samples' mechanical and optical properties with a single experiment. Two of these are employed in this chapter, as they provide the relevant information for the study of rare earth-doped materials in the framework of high-energy laser applications. In particular, the techniques chosen in this work are thermal lens spectrometry, which takes advantage of the lensing effect due to the excitation beam profile, and transient-state interferometry, which compares two optical paths through the material, one through a pristine section of the sample and one through a heated portion.

Other thermo-optic techniques include the transient grating diffractometry method, which consists in the first-order diffraction peak measurement for a beam passing through a sample.

The sample is optically pumped to obtain an absorption-induced refractive index phase grating. This technique is used to investigate the thermal and population contributions to refractive index driven by the interfering pump beams absorption [118,119].

Interferometric calorimetry is also a popular technique, which allows for an estimate of both a sample thermal expansion and its thermo-optic coefficient. It provides a relatively easy method for calculating the material quantum efficiency, directly derived from the observation of the interference pattern shifts [30,120].

Another thermo-optic technique that has been employed with interesting results consists in photoreflectance measurements, which allow estimating a sample thermal diffusivity by studying its response in reflectance as a function of temperature. Most interestingly, the work by Petit *et al.* that employs this method provides some additional insight about the rare earth-doped calcium fluoride crystals [121], namely the decreasing behaviour of its thermal conductivity as a function of Yb^{3+} concentration, and a comparison with Klemens theoretical model (which will be discussed further on in this chapter).

3.1.d Thermal Lens Techniques

Thermal lens spectrometry is notoriously considered a very useful tool because it allows for the estimation of a sample quantum efficiency, in addition to its thermal properties such as thermal conductivity and optical path variation. As can be seen in literature, it has been employed reliably in the study of many kinds of samples, in particular rare earth-doped optical glasses [110,122-126]. Multiwavelength thermal lens spectrometry is particularly interesting because it can be used to estimate the absolute quantum efficiency value, without the need for a reference sample [127].

Thermal lens spectrometry principles have been discussed in detail by Osterink *et al.* [128], and thermal lens measurements have been first employed to study the thermomechanical properties of crystals by Koechner in 1970 [25]. The temperature distribution model employed in optically pumped crystalline materials was extensively discussed and refined for the treatment of a top-hat and Gaussian profile pump beam cases [129,130], in particular in the case of YAG. Thermal lens measurement have been successfully used to assess the properties of rare earth-doped materials, notably in the case of Yb^{3+}-doped and Nd^{3+}-doped crystals. Thermal conductivity values were found for YAG:1% Nd crystals ($Y_3Al_5O_{12}$, 12.8 $W \cdot m^{-1} \cdot K^{-1}$ [26]), SNB:0.5

Nd crystals ($Sr_{0.61}Ba_{0.39}Nb_2O_6$, 1.73 $W \cdot m^{-1} \cdot K^{-1}$ [27]), and several other Nd^{3+}- and Yb^{3+}-doped crystals [28].

Thermal lens measurements under lasing conditions have also been developed, and provide a useful means for the estimation of the material thermal properties under laser operation [131]. This technique is particularly useful in the design of profile-correction systems for laser amplifiers.

It is known that the thermal conductivity of CaF_2 crystals follows a monotonous behaviour as a function of temperature, depending on the rare earth doping concentration [23,71]. However, in the thermal lens and interferometry treatment, one may assume the sample thermal conductivity to be independent of the sample temperature. This approximation holds around room temperature, since it has been shown that the thermal conductivity only changes moderately as a function of temperature around 300 K [71,132].

Transient-state interferometry – or Jamin-Lebedev polarization interferometry – on the other hand, allows for the distinction and evaluation of thermal and electronic contributions to the sample optical path variation [133]. The technique consists in dividing a probe laser beam onto two parallel arms with mutually perpendicular polarization. The two beams are then shone on the sample, while exciting the material with a pump beam upon one of the two arms, then measuring the time-resolved phase difference between the two probe beam polarizations. This type of measurements has been successfully employed, notably by Antipov *et al.* [29,30], in the estimation of the Thermo-optic properties of crystals such as YAG, both in the case of neodymium- and ytterbium-doping.

3.1.e Klemens Model for Thermal Conductivity

It is known that low thermal conductivity is a major limitation factor for high-energy pulsed laser operation in the case of laser glasses [134], due to thermal damage to the system. In particular, the modification of thermal properties as a function of dopant concentration has been investigated in the case of rare earth-doped YAG and fluoride laser crystals [24,112]. However, a thorough description of the thermal properties for doubly-doped fluoride crystals is yet to be done.

A theoretical model for the modification of thermal properties was provided by Klemens [42], considering the effect of lattice cell volume modification due to the insertion of doping ions in a

perfect crystal. While this is an approximate model, it gives a good idea of the mechanisms at work in the thermal conductivity changes when doping a crystal with rare earth ions, and has been employed as a reference in the study of both YAG and fluoride crystals doped with Yb^{3+} in different concentrations [24,111,135].

Klemens model [42,136] describing the dependency of a crystal thermal conductivity on the dopant ion concentration starts from the physical properties of the undoped material and the doping ion. The model takes into consideration the crystal lattice modifications introduced by the presence of a dopant and their effect on the thermal conductivity. The calculations start from the definition for thermal conductivity, K:

$$K = \frac{1}{3}\int S_H(\omega)\, v_S^2\, \tau_{rel}(\omega)\, d\omega \tag{3.01}$$

where ω is the phonon frequency, v_S is the velocity of sound in the material, $S_H(\omega)\cdot d\omega$ is the specific heat per unit volume due to lattice modes of frequency ω, and $\tau_{rel}(\omega)$ their effective relaxation time.

One may then assume that the thermal changes introduced by the presence of impurity centres act like phonon scattering centres, with a relaxation time $\tau_{rel} = (A\omega^4)^{-1}$, A being such that:

$$A = \frac{a_0^3}{4\pi}\frac{\delta}{v_S^3} \tag{3.02}$$

where a_0^3 is the atomic volume, δ is the mass variance of the lattice substitution sites, accounting for the mass difference between dopants and lattice atoms average.

Given the masses of the ions present in a single lattice cell, M_i, and their relative concentration, C_i, such that $\sum_i C_i = 1$, we can define the mass variance δ as:

$$\delta = \sum_i C_i \left(\frac{M_i - M}{M}\right)^2 \tag{3.03}$$

where M is the average lattice atom mass, expressed as

$$M = \sum_i C_i \cdot M_i \tag{3.04}$$

Finally, the characteristic cell size a_0 is defined as:

$$a_0 = 2\left(\frac{3}{4\,\pi}\frac{V_m}{Z_m \cdot N_m}\right)^{\frac{1}{3}} \tag{3.05}$$

where V_m is the cell volume, Z_m the number of molecules per cell and N_m the number of atoms per molecule. All these values can be obtained from literature.

In addition to the scattering centres' effect, the material has an intrinsic resistance due to three-phonon processes which do not conserve the total wavevector. Around the Debye temperature, their inverse relaxation time τ_u is in the form:

$$\frac{1}{\tau_u} = B\,\omega^2 \tag{3.06}$$

where $B \propto T$. The combination of scattering centres and three-phonon processes yields a combined relaxation lifetime τ_c:

$$\tau_c(\omega) = \frac{\tau_{rel}\,\tau_u}{\tau_{rel} + \tau_u} \tag{3.07}$$

Using the expression for $S_H(\omega)$ for high temperature:

$$S_H(\omega) = \frac{3\,k_B}{2\,\pi^2}\frac{\omega^2}{v_S^3} \tag{3.08}$$

and with the proper substitutions in eqn. (3.01), the expression for thermal conductivity becomes:

$$K = \frac{k_B}{2\,\pi^2\,v_S\,B}\int_0^{\omega_D} \frac{1}{1 + \omega^2 \cdot A/B}\,d\omega \tag{3.09}$$

where k_B is the Boltzmann constant and ω_D is the sample Debye frequency, which is defined as

$$\omega_D = \left(\frac{3}{4\,\pi} N_n\right)^{\frac{1}{3}} v_S \tag{3.10}$$

where N_n is the crystal number density.

Finally, one may define a frequency ω_0 such that $\tau_{rel}(\omega_0) = \tau_u(\omega_0)$, that is to say, $\omega_0 = \sqrt{B/A}$. This turns (3.09) into the expression:

$$K = \frac{k_B}{2\,\pi^2\,v_S}\frac{\omega_0}{B} \cdot \tan^{-1}\frac{\omega_D}{\omega_0} \tag{3.11}$$

From here, one can see that the thermal conductivity in the absence of scattering centres is:

$$K_0 = \frac{k_B}{2\,\pi^2\,v_S}\frac{\omega_D}{B} \tag{3.12}$$

Thus, after the appropriate substitution, and known the thermal conductivity of the undoped sample K_0, the thermal conductivity K of the doped crystal becomes:

$$K = \frac{K_0}{\pi\,a_0}\sqrt{\frac{2\,k_B\,v_S}{\delta\,K_0}} \cdot \tan^{-1}\left(\pi\,a_0\sqrt{\frac{\delta\,K_0}{2\,k_B\,v_S}}\right) \tag{3.13}$$

One can see that as the mass variance δ increases, the thermal conductivity decreases. In particular, since the gradual introduction of dopant increases the mass variance, the thermal conductivity must follow a decreasing curve as a function of dopant concentration. However, if the substitution ratio increases to the point where the dopant ions become the dominant species, the mass variance δ starts to decrease, and therefore the thermal conductivity increases.

With all of this information at hand, a thorough investigation of the thermal properties of Nd^{3+},Lu^{3+}-doped CaF_2 can be performed, in order to determine the best doping concentrations suitable for high-energy laser pulse amplification. As discussed earlier, the aim of this thesis is to combine both good optical and spectroscopic properties and high thermal shock resistance, i.e. high thermal conductivity.

Mode-mismatched thermal lens technique is an established method to obtain the value of thermal conductivity and temperature-dependent refractive index variation of transparent media [137] and was therefore chosen as the principal means of investigation for the

CaF_2:Nd^{3+},Lu^{3+} crystals thermal properties. Moreover, as a way to double-check the results, a two-beam transient-state interferometry experiment was employed.

3.2 Thermal Lens Technique

3.2.a Thermal Lens Theory

When irradiated with a beam at an absorbed wavelength, a material is generally subject to two main effects, namely thermal lens and population lens. These effects are usually studied by means of pump-probe techniques, where a probe beam is used to investigate an excited region. Thermal lens is caused by the variation in facet shape and refractive index induced by the change in temperature [110]. Population lens is driven by the refractive index modification due to the change in the ground and excited levels population. Jacinto *et al.* [110] have shown that it is possible to distinguish the two phenomena via Z-scan measurements. In particular, the population lens effect being a faster process, it is dominant at high modulation frequencies of the excitation beam, while the thermal lens is generally observed mainly with low-frequency modulation. The work by Anashkina and Antipov [138] studied the contributions of the two effects in relation to the total lensing effect of a sample. They showed that population lens is dominant over thermal lens in the case of a relatively high-frequency pulsed pump beam, because of the electronic transition lifetime being shorter than the thermal diffusion characteristic time. On the contrary, thermal lens becomes dominant under low-frequency modulations or continuous excitation. Moreover, the population lens effect becomes very weak with respect to thermal lens as the sample thickness increases. Under the conditions of the measurements proposed in this work, with quasi-continuous excitation and a sample thickness of several millimetres, population lens is negligible.

To understand the thermal lens phenomenon, one should start by considering the case of an excitation beam with power P_e and a Gaussian profile of waist radius w_{e0}, as is the case of the experiment reported in this work (Fig. 3.1):

$$I_e(r) = \frac{2\,P_e}{\pi\,w_{e0}^2} \cdot \exp\left(\frac{-2\,r^2}{w_{e0}^2}\right) \tag{3.14}$$

In this treatment, the width of the beams is considered constant along the sample portion axis. This approximation holds for samples with thicknesses smaller than the beam Rayleigh

distances. The evolution over time of the temperature profile is then obtained by applying the heat conduction equation:

$$\frac{\partial \Delta T(r,z,t)}{\partial t} = D \cdot \nabla^2 \Delta T(r,z,t) \tag{3.15}$$

D being the sample thermal diffusivity. The solution of this equation in the present case is:

$$\Delta T(r,z,t) = \frac{2\,P_e\,A_e}{\pi\,C_P\,\rho\,w_e^2(z)} \cdot \int_0^t \left[\frac{1}{1+(t'/2t_C)}\right] \cdot \exp\left[\frac{-2\,r^2/w_e^2(z)}{1+(t'/2t_C)}\right] dt' \tag{3.16}$$

where ρ is the density, C_P the specific heat, A_e the optical absorption coefficient at the excitation beam wavelength and t_C is the characteristic thermal time constant defined as:

$$t_C = \frac{w_{e0}^2}{4D} \tag{3.17}$$

In mode-mismatched thermal lens spectrometry, the sample is probed via a non-absorbed laser beam, focussed before the sample, with a Rayleigh length Z_C such that $Z_C \ll Z_2$, where Z_2 is the distance from the sample to the detector. After going through the sample, the probe beam is then passed through a pinhole positioned on the centre of the beam, in order to collect only the beam peak portion. This allows ensuring a linear relationship between the collected signal and the beam peak intensity. The probe beam being larger than the pump beam, and the two beams collinear, the probe signal evolution after the pinhole is approximately proportional to the change of focal distance induced by the pump beam. In this approximation, the temporal evolution of the collected probe signal can therefore be fitted using the following function [28,110,123,137]:

$$I(t) = I(0) \cdot \left[1 - \frac{\vartheta}{2}\tan^{-1}\left(\frac{2mV}{[(1+2m)^2+V^2]\frac{t_C}{2t}+1+2m+V^2}\right)\right]^2 \tag{3.18}$$

Here, m and V are parameters defined by the geometry of the system, namely:

$$m = \left(\frac{w_{p1}}{w_{e0}}\right)^2 \tag{3.19}$$

$$V = \frac{Z_1}{Z_C} \tag{3.20}$$

where w_{p1} is the probe beam radius at the sample position, Z_1 is the distance between the probe beam and pump beam waists (Fig. 3.1), and the Rayleigh length of the probe beam Z_C is defined as:

$$Z_C = \frac{\pi \cdot w_{p0}^2}{\lambda_p} \tag{3.21}$$

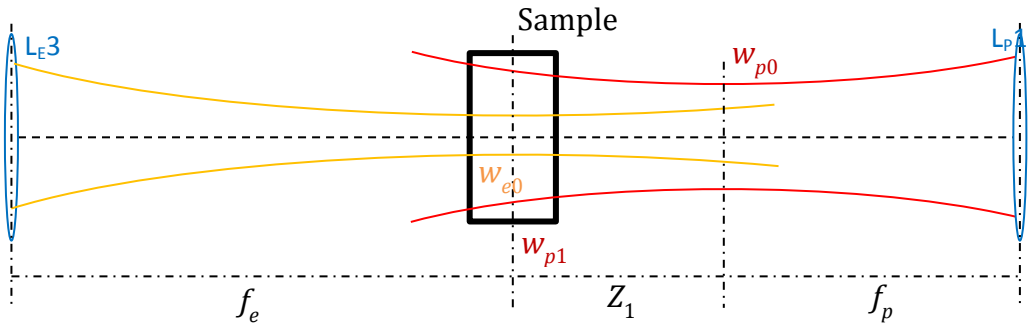

Fig. 3.1 Collinear model of the TL sample setup assumed for the analysis of the data. The probe beam, coming from the right in the picture, is focussed before the sample by a f_p focal lens, and the excitation beam, coming from the left, is focussed upon the sample by a f_e focal lens. The distance between the sample and the probe detector is $Z_2 \gg Z_C$.

In the case of this work, one finds $m = 35$ and $V = 5.3$. According to Shen *et al.* [137], a high m value – that is to say, a high ratio between the probe and excitation beam radii at the sample position (Fig. 3.1) – corresponds to a high sensitivity. However, when increasing m, the excitation beam modulation frequency should be modified accordingly. In particular, high m values require lower frequencies, because the time it takes for a sample to reach a steady state increases as a function of m. Since m represents the ratio between the probed and the excited areas, heat conduction requires a longer time to reach thermal equilibrium from the pumped section throughout a larger area [137]. Therefore, for an m value around 30, the pump beam modulation frequency ν_{exc} should be about:

$$\nu_{exc} \leq \frac{1}{100 \cdot t_C} \tag{3.22}$$

For the samples considered, a characteristic time t_C of about 1 or 2 milliseconds is expected. This means a modulation frequency set to less than 5 Hz ensures valid measurements.

The core of this mode-mismatched thermal lens technique lies in the adjustment of the two fitting parameters ϑ and t_C so as to match the collected probe signal decay (see eqn. (3.18)). These two parameters can indeed be then used to obtain the material thermal properties, in particular the thermal diffusivity D can be obtained from eqn. (3.17):

$$D = \frac{w_{e0}^2}{4\, t_C} \tag{3.23}$$

The thermal conductivity K, can then be calculated via the following relationship [139]:

$$K = \rho \cdot C_P \cdot D \tag{3.24}$$

where ρ and C_P are the material density and specific heat respectively, considered as constant values, regardless of the dopant concentration.

While t_C allows to derive the diffusivity D and subsequently the thermal conductivity K, the other fitting parameter, ϑ, is defined as:

$$\vartheta = -\frac{P_e \cdot A_e \cdot l_{eff}}{K \cdot \lambda_p} \frac{ds}{dT} \tag{3.25}$$

Here, λ_p is the probe beam wavelength, ds/dT is the temperature coefficient of the optical path length change (also called the thermo-optic path variation), and l_{eff} is the sample effective optical length, defined as [126]:

$$l_{eff} = \frac{1 - e^{-A_e l_0}}{A_e} \tag{3.26}$$

l_0 being the thickness of the sample at the room temperature T_0.

Knowing the thermal conductivity K and l_{eff}, the quantity ds/dT can therefore be derived from the fitting parameter ϑ via eqn. (3.25). Moreover, ds/dT can be written as a combination of the

linear thermal expansion coefficient $l_0^{-1} \cdot dl/dT$ (or, for simplicity, α) and the thermo-optic coefficient dn/dT [122]:

$$\frac{ds}{dT} = \frac{n_0 - 1}{l_0}\left(\frac{dl}{dT}\right)_{T_0} + \left(\frac{dn}{dT}\right)_{T_0} = (n_0 - 1)\alpha|_{T_0} + \left(\frac{dn}{dT}\right)_{T_0} \tag{3.27}$$

where n_0 is the room-temperature refractive index of the material. As a consequence, ds/dT can give access to the linear thermal expansion coefficient $l_0^{-1} \cdot dl/dT$, provided dn/dT is known.

3.2.b Thermal Lens Experiment Setup

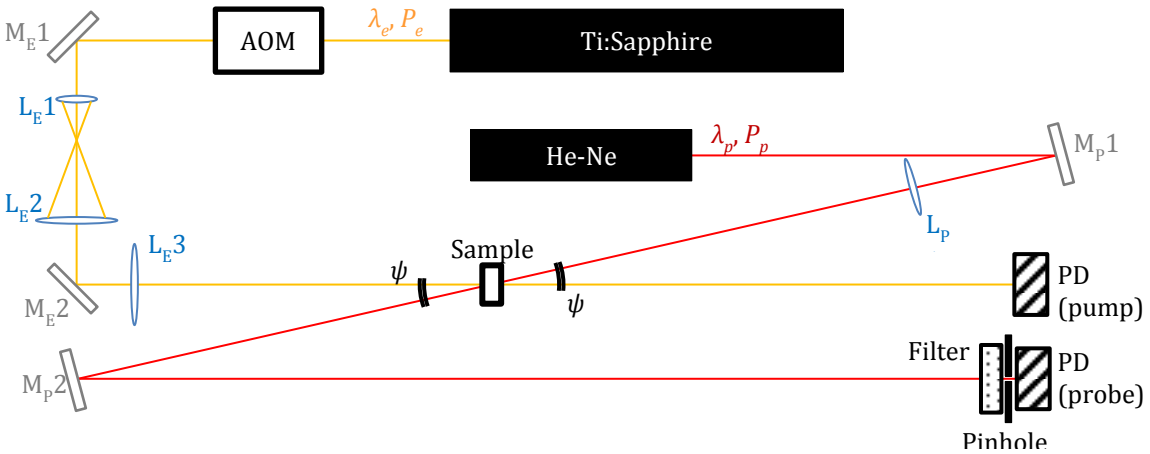

Fig. 3.2 Dual-beam thermal lens setup schematic.

A dual-beam mode-mismatched thermal lens experiment was set up, using a tuneable Ti:sapphire laser for the excitation, and a CW 633 nm He-Ne laser for the probe beam. The entire setup is schematised in figure 3.2. The excitation beam was modulated by a 2.5 Hz frequency (ν_{exc}) square-wave signal using an acousto-optic modulator. A pair of lenses was employed as a telescope to enlarge the excitation beam diameter. The excitation beam was then focused on the sample by a 300 mm focal lens, and collected as trigger by a photodiode. The CW probe beam was focused by a 200 mm focal lens at a distance $Z_1 = 167$ mm before the sample (Fig. 3.1), and the signal at the other end was collected by a photodiode, preceded by a pinhole and a bandpass filter centred around 633 nm to eliminate any residual excitation signal. The excitation and probe beams were superposed within the sample, crossing with an angle ψ smaller than 1.5°, which makes it possible to consider them collinear [122]. The probe signal is then visualised on an oscilloscope, using the residual excitation beam as the trigger. The beam waist radius was

measured for both the excitation (w_{e0}) and the probe beam (w_{p0}) using a *DataRay Inc. BeamScope-P7* beam profiler, and the probe beam radius at the sample position (w_{p1}) was measured as well. The operational parameters of the setup are listed in table 3.2.

Table 3.2 Thermal lens spectrometry setup parameters and geometrical values.

Excitation beam	
P_e	107 mW
λ_e	796.5 nm
w_{e0}	65 μm

Probe beam	
P_p	5 mW
λ_p	632.8 nm
w_{p0}	80 μm
w_{p1}	385 μm

Geometry	
ψ	1.3°
Z_1	167 mm

Excitation Beam modulation	
ν_{exc}	2.5 Hz

The samples used in these measurements are about 2 mm thick, while the Rayleigh distances of the probe and pump beams are, respectively, 16 mm and 32 mm. The approximation of a constant beam radius throughout the sample, as discussed in subsection 3.2.a, is therefore valid.

The position z_0 of the beam waist was measured by using the pinhole technique: the beam of power P is shone through a pinhole of fixed diameter d, as shown in figure 3.3. Granted the pinhole is narrower than the beam ($d \ll w(z)\ \forall z$) and the beam is Gaussian, the transmitted intensity P_{det} is then fitted via the function:

$$P_{det}(z) = \frac{2 \cdot P \cdot d^2}{w(z - z_0)^2} \tag{3.28}$$

An example of the fit via eqn. (3.28) is shown in figure 3.4.

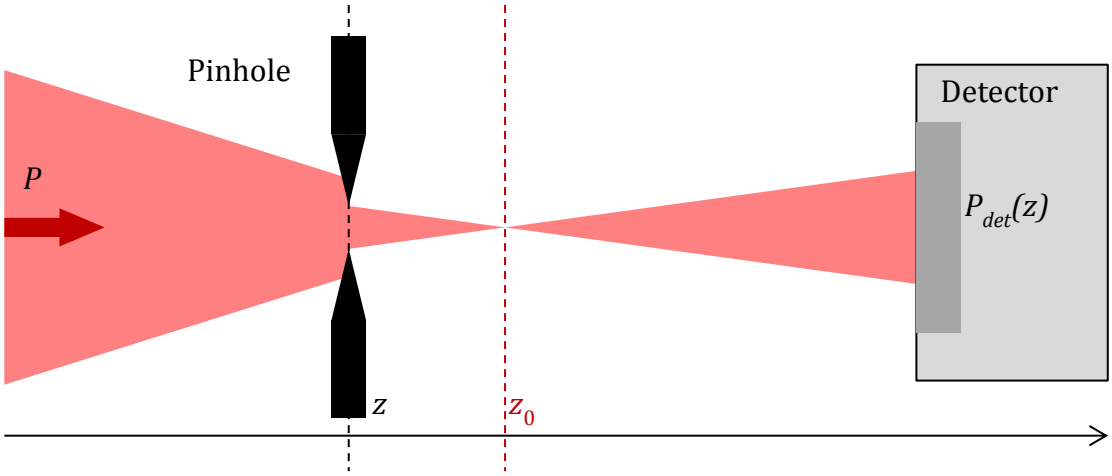

Fig. 3.3 Setup for the beam waist position measurements.

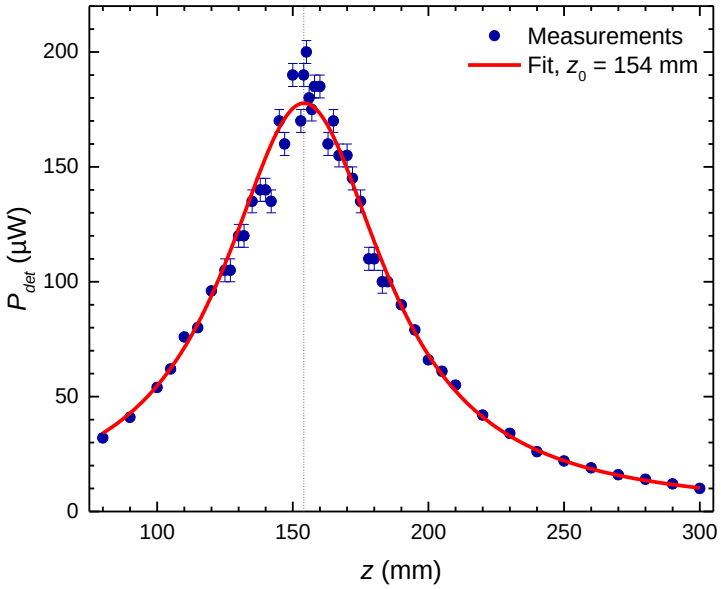

Fig. 3.4 Beam waist position measurements and fit via eqn. (3.28) for the probe beam of the thermal lens experiment.

Figure 3.5 shows the normalised TL measurement for the CaF_2:0.5% Nd,8% Lu sample, obtained by averaging the collected signal 512 times, as well as the fitted curve. The decreasing behaviour of the probe signal indicates a divergent thermal lens effect within the crystal leading to a reduction of the peak probe intensity going through the pinhole (Fig. 3.2).

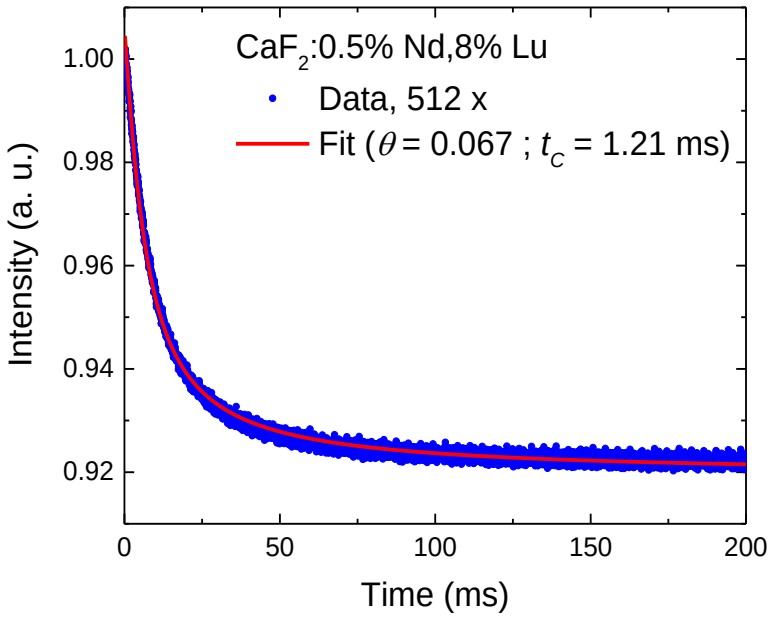

Fig. 3.5 TL measurements and fit of the CaF_2:0.5% Nd,8% Lu sample.

The collected signal reaches a stable regime at the end of each cycle, confirming the validity of the modulation frequency choice. The data were fitted via eqn. (3.18), with amplitude ϑ and characteristic time t_C as fitting parameters, and with the setup parameters presented in table 3.2. The fitting procedure gives amplitude values ϑ of the order of 0.06, and characteristic times t_C in the order of the millisecond. The fact that ϑ is positive is consistent with the divergent thermal lens effect in CaF_2:Nd^{3+},Lu^{3+}, since one can see in eqn. (3.18) that a positive ϑ value corresponds to a decreasing collected signal intensity, and therefore a widening beam profile.

Interestingly, the facet bulging from thermal expansion effect can only produce a converging lens. This implies that it is the refractive index change that causes the diverging lens effect, and this effect is greater than the converging lens due to thermal expansion.

3.2.c Thermal Lens Technique Sensitivity

It was observed that the thermal lens adjusting parameters ϑ and t_C are more sensitive to the uncertainty on the V parameter, than on m. As per their definition shown in eqns. (3.19) and (3.20), m and V correspond respectively to the pump-probe beam area mismatch parameter and the ratio between the pump waist-to-sample distance and its Rayleigh length. While the relationship between the measurement accuracy and the parameter m is well-understood, as explained by Shen *et al.* [137], the effects of the parameter V on the ϑ and t_C values is much less clear. In particular, since both the values describing the thermal properties of the system (the thermal conductivity K and the optical path variation ds/dT) depend on the estimation of t_C, it is important to clearly understand the effect of both parameters m and V on the fit results.

To evaluate and compare the effect of the m and V parameters, one may proceed in a similar manner as in Shen's work: in that paper [137], two so-called steady-state signal functions, S and S', are introduced, defined as follows:

$$S = \frac{I_{t\to\infty} - I_0}{I_0} \tag{3.29}$$

$$S' = \frac{I_0 - I_{t\to\infty}}{I_{t\to\infty}} \tag{3.30}$$

The steady-state signal functions allow evaluating the sensitivity of the signal amplitude to the variations of the geometrical parameters m and V. Since, in the case of our experiment, the signal decreases with time, let us choose S', which is defined from eqn. (3.18) as:

$$S'(m,V) = \frac{I_0 - I_{t\to\infty}(m,V)}{I_{t\to\infty}(m,V)} = \left(1 - \frac{\vartheta}{2}\tan^{-1}\left(\frac{2mV}{1+2m+V^2}\right)\right)^{-2} - 1 \tag{3.31}$$

The plots of the steady-state signal S' as a function of m and V, calculated for the values of the parameters employed in this work (recall table 3.2), are shown in figure 3.6.

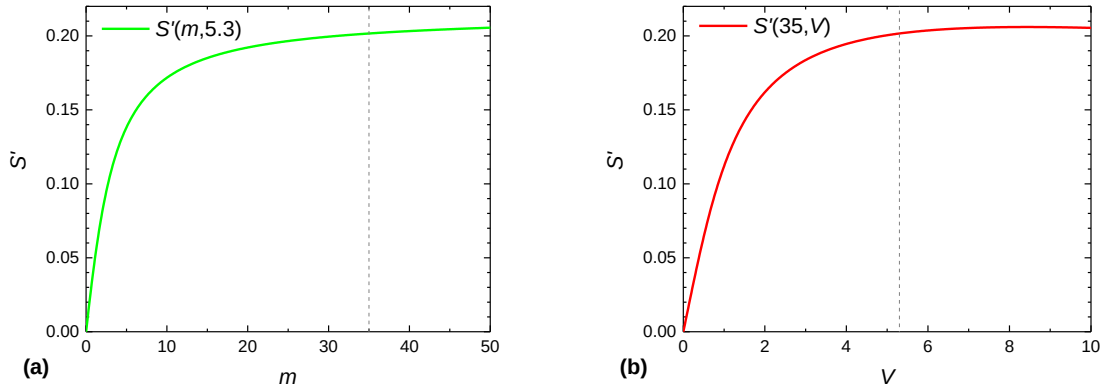

Fig. 3.6 Steady-state signal function S' as a function of geometrical parameters: (a) as a function of m with a fixed V value ($V = 5.3$), and (b) as a function of V at fixed m value ($m = 35$).

The sensitivity $\xi_{S'}$ of the steady-state function to the parameters variations was estimated, given the experimental values m_0 and V_0 (obtained from the geometrical parameters in table 3.2) by calculating the S' function derivative:

$$\xi_{S',m} = \left| \frac{1}{S'(m_0, V_0)} \frac{dS'(m, V_0)}{dm} \right|_{m_0} \tag{3.32}$$

$$\xi_{S',V} = \left| \frac{1}{S'(m_0, V_0)} \frac{dS'(m_0, V)}{dV} \right|_{V_0} \tag{3.33}$$

With eqns. (3.19) and (3.20), the experimental values $m_0 = 35$ and $V_0 = 5.3$ are calculated. Using these values in eqns. (3.32) and (3.33), one obtains that $\xi_{S',m} = 1.7 \cdot 10^{-3}$ and $\xi_{S',V} = 1.7 \cdot 10^{-2}$. The higher sensitivity of S' to variations of V implies that the error on V has a larger impact than the error on m on the estimation of the signal amplitude.

However, while these steady-state signal functions are useful in the study of the signal amplitude, they carry no information on the time-dependent data. For that purpose, here is introduced, for the first time to our knowledge, a transient-state signal function T', defined as:

$$T'(m, V) = \frac{I_0 - I_{t=t_C}(m, V)}{I_{t=t_C}(m, V)} = \left(1 - \frac{\vartheta}{2} \tan^{-1}\left(\frac{4mV}{3 + 8m + 4m^2 + 3V^2}\right)\right)^{-2} - 1 \tag{3.34}$$

A graph of the behaviour of T' as a function of the parameters m and V is also shown in figure 3.7.

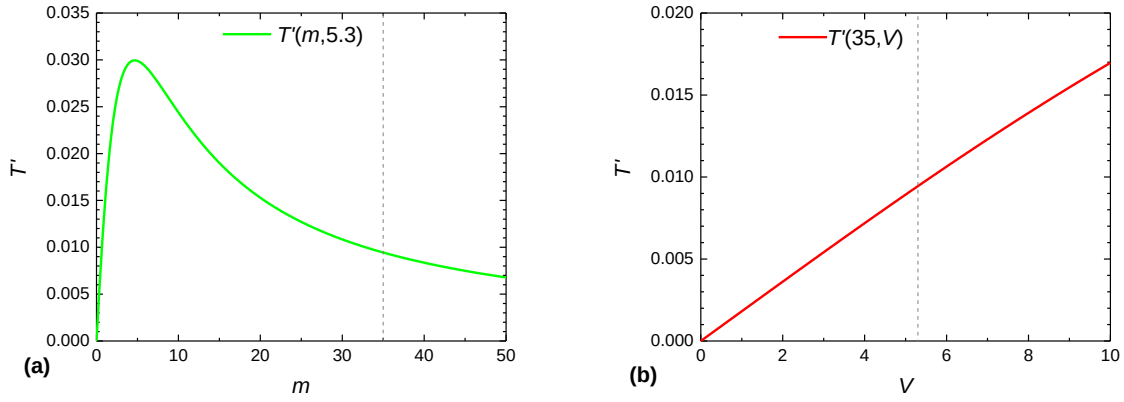

Fig. 3.7 Transient-state signal function T' as a function of geometrical parameters m (a) and V (b).

The transient-state signal function sensitivity $\xi_{T'}$ to the parameters variations was estimated, given the experimental values m_0 and V_0, by calculating the function derivative, in a similar way to what was done for S':

$$\xi_{T',m} = \left| \frac{1}{T'(m_0, V_0)} \frac{dT'(m, V_0)}{dm} \right|_{m_0} \tag{3.35}$$

$$\xi_{T',V} = \left| \frac{1}{T'(m_0, V_0)} \frac{dT'(m_0, V)}{dV} \right|_{V_0} \tag{3.36}$$

In the case considered, with $m_0 = 35$ and $V_0 = 5.3$, one obtains that $\xi_{T',m} = 0.026$ and $\xi_{T',V} = 0.183$. Therefore, the error on the parameter V has a much larger influence in the estimate of the characteristic time t_C than the error on m. This in turn means that the estimated thermal conductivity values are mainly influenced by the fluctuations on V, under the experimental condition reported here.

Let us recall equations (3.20) and (3.21):

$$V = \frac{Z_1}{Z_C} \tag{3.20}$$

$$Z_C = \frac{\pi \cdot w_{p0}^2}{\lambda_p} \tag{3.21}$$

Since the beam waist measurements with the beam profiler are quite accurate, one can safely state that the error on the w_{p0} measurement is very small. On the other hand, the distance Z_1 is much more difficult to determine accurately, because of the larger error on the estimate of beam waist positions (Fig. 3.4). Thus, it represents a critical value in the calculation because of the error on its measurement. Therefore, precise measurements of the position of the beam waists are essential for an accurate fit.

3.2.d Thermal Conductivity

The sample thermal diffusivity is estimated from the thermal lens results by inverting the relationship in eqn. (3.17), as introduced before:

$$D = \frac{w_{e0}^2}{4\, t_C} \tag{3.23}$$

With this value, one can then apply eqn. (3.24) to estimate the thermal conductivity.

$$K = \rho \cdot C_P \cdot D \tag{3.24}$$

In the case of CaF_2:Nd^{3+},Lu^{3+}, the density ρ and specific heat C_P are considered constant and were obtained from manufacturer data (ISP Optics, Crystran). In particular, $\rho = 3.18\ \mathrm{g/cm^3}$ and $C_P = 0.88\ \mathrm{J\ g^{-1}\ K^{-1}}$.

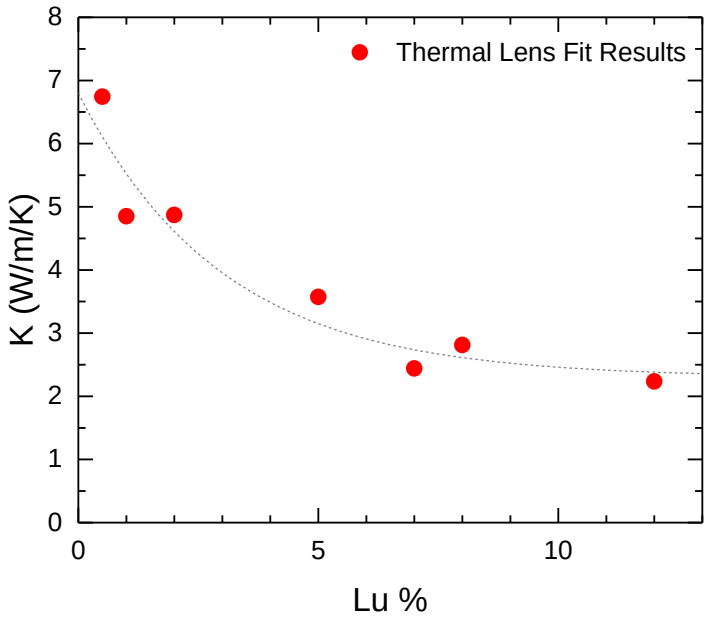

Fig. 3.8 Thermal conductivity values resulting from the thermal lens measurements. The grey dashed line is an indicative monotonous behaviour of thermal conductivity versus lutetium concentration providing a guide for the eye.

The fit results for the thermal conductivity as a function of lutetium concentration are shown in figure 3.8. It is possible to observe a decreasing behaviour of thermal conductivity as the lutetium concentration increases (here indicatively traced by a dashed line), which is to be expected since a higher dopant concentration means a greater number of defects introduced in the crystal lattice. The results for *D* and *K* are reported also in table 3.3.

Table 3.3 Thermal diffusivity D and conductivity K of CaF_2:Nd^{3+},Lu^{3+} crystals and Nd:phosphate laser glasses.

Sample	D (cm²/s)	K (W/m/K)
CaF_2:0.5% Nd,0.5% Lu	0.024	6.7
CaF_2:0.5% Nd,1% Lu	0.017	4.9
CaF_2:0.5% Nd,2% Lu	0.017	4.9
CaF_2:0.5% Nd,5% Lu	0.013	3.6
CaF_2:0.5% Nd,7% Lu	0.009	2.4
CaF_2:0.5% Nd,8% Lu	0.010	2.8
CaF_2:0.5% Nd,12% Lu	0.008	2.2
LHG-8	0.002	0.51
LG-770	0.002	0.46

3.2.e Thermo-Optic Path Variation, ds/dT

From equation (3.25), one can obtain the thermo-optic path variation:

$$\frac{ds}{dT} = -\frac{K \cdot \lambda_p}{P_e \cdot A_e \cdot l_{eff}} \vartheta \tag{3.37}$$

As explained before, A_e and l_{eff} are derived from optical absorption measurements. In particular, let us recall:

$$l_{eff} = \frac{1 - e^{-A_e l_0}}{A_e} \tag{3.26}$$

where l_0 is the initial sample thickness.

K is the thermal conductivity obtained in thermal lens measurements, as seen before, and ϑ is the thermal lens signal amplitude obtained from the fit.

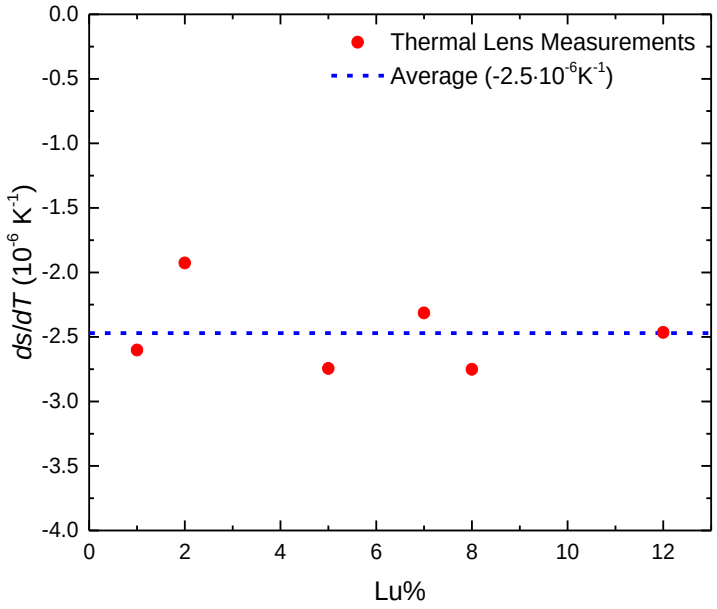

Fig. 3.9 Plot of the thermo-optic path variation as a function of lutetium concentration. The average value of ds/dT is about -2.5·10^{-6} K^{-1}.

The results for ds/dT are shown in figure 3.9, which indicates that there is no sensible variation in the thermo-optic path variation. Moreover, the average value, which was found to be -2.5·10^{-6} K^{-1}, is in very good agreement with the undoped CaF_2 ds/dT value presented in literature and provided by industrial manufacturers (such as Corning and Crystran), estimated around -2.5·10^{-6} K^{-1}.

The thermo-optic path variation is an interesting quantity, because it summarizes the sample optical response to thermal stimuli. In particular, it relates directly to the thermo-optic coefficient dn/dT and the linear thermal expansion coefficient α, which are crucial parameters for the implementation of the medium in a laser amplifier, and they must be taken into consideration when tailoring and optimising the device design.

Recalling eqn. (3.27):

$$\frac{ds}{dT} = (n_0 - 1)\alpha|_{T_0} + \left(\frac{dn}{dT}\right)_{T_0} \qquad (3.27)$$

As seen before, ds/dT is negative in CaF_2:Nd^{3+},Lu^{3+}, meaning the total thermal lens effect is divergent, while the linear thermal expansion coefficient, α, is always positive. Therefore, from

eqn. (3.27) one can see that the material thermo-optic coefficient *dn/dT* has to be negative. This means that *dn/dT* compensates the converging lens effect due to the sample thermal expansion. Moreover, the refractive index effect has to be stronger than the geometrical expansion, thus turning the sample into a diverging lens.

In fact, fluorides are known for having negative thermo-optic coefficient. This is a common feature of halide crystals [140]. This property is a direct consequence of the high thermal expansion coefficient values found in these systems, which causes a sensible expansion in the lattice structure and therefore a reduction of the material number density with temperature.

However, the average absolute value of CaF_2:Nd^{3+},Lu^{3+} crystals ds/dT here obtained is lower than that of Nd^{3+}:YAG laser crystals ($7\text{-}10 \cdot 10^{-6}$ K^{-1}), which means that correcting beam distortions caused by thermo-optic path variations should be easier than in a YAG-based system.

A set of samples was sent to the IRCP of Chimie ParisTech laboratory in Paris for direct linear thermal expansion coefficient measurements, resulting in:

$$\alpha = \frac{1}{l_0}\frac{dl}{dT} = 2.1 \cdot 10^{-5}\ K^{-1} \tag{3.38}$$

The results obtained were used to calculate the thermo-optic coefficient, dn/dT via eqn. (3.27). The final values of these calculations (summarised in table 3.4) were compared to those found in literature [141] (approximately equal to $-12 \cdot 10^{-6}$ K^{-1} at room temperature and at a wavelength of 600 nm).

Table 3.4 Thermomechanical properties of CaF_2:Nd^{3+},Lu^{3+} samples and Nd:phosphate laser glasses obtained via the TLS technique.

Sample	D (cm²/s)	K (W/m/K)	$\frac{ds}{dT}$ $(10^{-6}\ K^{-1})$	$\frac{dn}{dT}$ $(10^{-6}\ K^{-1})$
CaF_2:0.5% Nd,0.5% Lu	0.024	6.7	--	--
CaF_2:0.5% Nd,1% Lu	0.017	4.9	-2.6	-11.6
CaF_2:0.5% Nd,2% Lu	0.017	4.9	-1.9	-11.0
CaF_2:0.5% Nd,5% Lu	0.013	3.6	-2.7	-11.8
CaF_2:0.5% Nd,7% Lu	0.009	2.4	-2.3	-11.3
CaF_2:0.5% Nd,8% Lu	0.010	2.8	-2.7	-11.8
CaF_2:0.5% Nd,12% Lu	0.008	2.2	-2.5	-11.5
LHG-8	0.002	0.51	0.48	-5.4
LG-770	0.002	0.46	0.27	-6.2

The average is around -11.5 10^{-6} K^{-1} for dn/dT, which is close to the value of -12·10^{-6} K^{-1} found in literature, confirming the general validity of the measurements. These results show that the CaF_2:Nd^{3+},Lu^{3+} ds/dT value does not change as more and more rare earth dopants are introduced in the material. As made clear in figure 3.9, while sensible fluctuations of these values appear as a result of the calculations, they do not show any evident dependency on dopant concentration.

On the other hand, the linear thermal expansion coefficient values are higher than that provided for CaF_2 crystals at room temperature by manufacturers such as Corning and Crystran, which is about 1.9·10^{-5} K^{-1}. The difference between the results in this work and those found in

literature in undoped crystals may arise from the rare-earth doping in a manner yet to be clarified.

In general, the values of both thermal expansion coefficient α and thermo-optic coefficient are greater than those of neodymium-doped phosphates LHG-8 and LG-770. This must be obviously taken into account in the application, as it will influence the choice of the operating parameters for a laser amplifier device.

3.3 Transient-State Interferometry

3.3.a Interferometry Theory

When a material absorbs electromagnetic radiation, its properties are affected by both thermal and electronic phenomena introduced with the absorbed energy. These changes translate into a combination of thermally-induced and population-induced refractive index variations. These phenomena, triggered by the pump beam absorption, contribute to change the optical path of a non-absorbed probe beam through the material, which in turn can be measured with a double-probe setup, exploiting the phase shift between two CW probe beams, one passing through the pumped section and another passing through the pristine part of the sample. Moreover, since the thermal and electronic contributions have different characteristic times, they can be separately assessed with a single measurement of the phase shift as a function of time.

In a transient-state interferometry experiment [142], a CW laser probe beam is separated via a Savart plate into two parallel beams with mutually perpendicular polarisations (Fig. 3.10). These parallel beams act as the two arms of the interferometer. The two beams pass through the sample, and are then reflected back by a mirror (M_3), passing a second time through the sample on the same path. They are then recombined via the same Savart plate which separated them. One of the interferometer arms is pumped by a pulsed laser beam at a wavelength absorbed by the sample. The pump beam absorption in turn causes a phase shift of the pumped arm beam. Since the two beams pass twice through the sample as explained before, each pump cycle results in a two-pass phase shift between the two beams at the interferometer end. The recombined probe beam is separated again by a polariser cube, into two beams with mutually perpendicular polarisations. These beams have now each a 45-degree polarization with respect to the interferometer beams. The two beam intensities are collected via photodiodes, and the final

signal measured is the difference between the two signals. A possible configuration for this kind of setup is illustrated in figure 3.10.

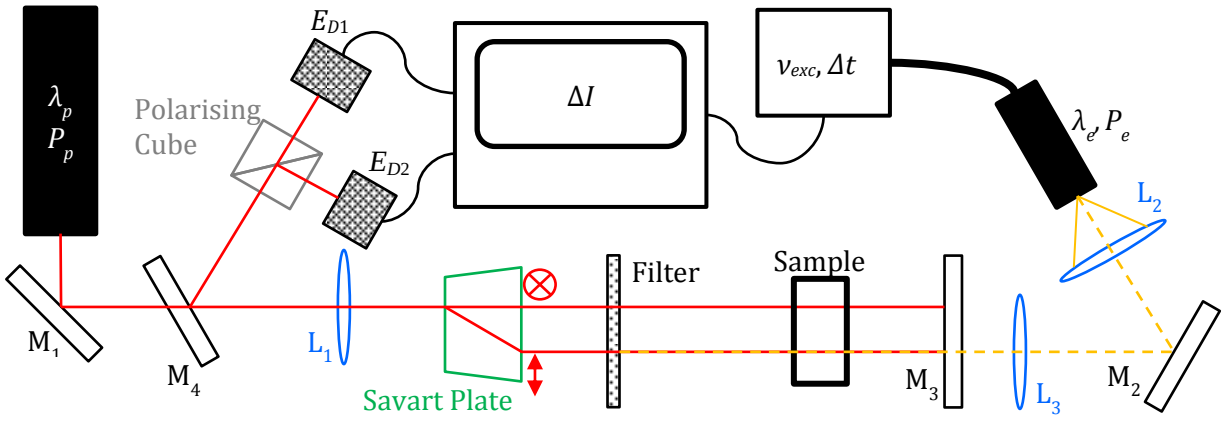

Fig. 3.10 Transient-state interferometry setup schematic.

The signal is recorded as a function of time, starting when the excitation beam is off after each excitation pulse. Therefore, the main difference between the thermal lens experiment and the transient-state interferometry is that the former is a heating process measurement, while the latter is a measurement based on the heat dissipation process.

Let us label the electric field on the pumped arm of the interferometer E_1, and the one along the non-pumped control arm E_2. Then we can rewrite the incoming electric field on the two detectors, E_{D1} and E_{D2} as:

$$E_{D1}(t) = \sqrt{\frac{\Theta_1}{2}}\left(E_1 \cdot e^{\Delta\varphi_p(t)+\Delta\varphi_0} + E_2\right) \tag{3.39}$$

$$E_{D2}(t) = \sqrt{\frac{\Theta_2}{2}}\left(-E_1 \cdot e^{\Delta\varphi_p(t)+\Delta\varphi_0} + E_2\right) \tag{3.40}$$

where Θ_1 and Θ_2 are the polariser transmission values for the two polarisations, and $\Delta\varphi_p$ is the pump-induced phase difference between the pumped and control probe beams, and $\Delta\varphi_0$ is a constant phase shift due to intrinsic optical path differences between the two sections of the material where the probe arms are passing through. The intensity of the two beams is, in turn:

$$I_{D1,2}(t) = \frac{\Theta_{1,2}}{2}\left[I_1 + I_2 \pm 2\sqrt{I_1 \cdot I_2}\cos\left(\Delta\varphi_p(t) + \Delta\varphi_0\right)\right] \tag{3.41}$$

And thus the difference in intensity which makes up the detected signal is, for the optimal condition $\Delta\varphi_0 = \pi/2$:

$$\Delta I(t) = (\Theta_1 - \Theta_2)\frac{I_1 + I_2}{2} + \frac{\Theta_1 + \Theta_2}{2}2\sqrt{I_1 \cdot I_2}\sin\left(\Delta\varphi(t)\right) \tag{3.42}$$

This can be approximated for values of $\Delta\varphi_p(t) \ll \pi/2$ so that the intensity difference is a linear function of the phase difference, or $\Delta I(t) \propto \Delta\varphi(t)$.

Considering the case of a very short excitation pulse (in the order of magnitude of 10 ns FWHM), the deposited heat distribution then takes on the form of a Dirac delta in time at the microsecond scale, which implies an immediate rise in temperature. We can then assume, for a Gaussian pump beam profile with a w_{e0} waist radius, that the temperature distribution within the material is Gaussian at the instant of absorption, $t = 0$.

Let us recall the heat equation:

$$\frac{\partial \Delta T(r,z,t)}{\partial t} = D \cdot \nabla^2 \Delta T(r,z,t) \tag{3.15}$$

The solution to this equation is as follows:

$$\Delta T(r,z,t) = \frac{\Delta T(0,z,0)}{1 + \frac{t}{t_{th}}} \cdot \exp\left(\frac{-2\,r^2}{w_{e0}^2 \cdot \left(1 + \frac{t}{t_{th}}\right)}\right) \tag{3.43}$$

where t_{th} is the characteristic time of thermal diffusion, defined as:

$$t_{th} = \frac{w_{e0}^2}{8\,D} \tag{3.44}$$

This causes a variation in refractive index Δn_{th} with respect to a collinear Gaussian probe beam of wavelength λ_p and with waist radius w_{p0}, defined by the expression:

$$\Delta n_{th}(t) = \frac{\Delta n_{th}(0)}{1 + t/t_{th}} \cdot \frac{w_{e0}^2 \cdot \left(1 + \frac{t}{t_{th}}\right)}{w_{e0}^2 \cdot \left(1 + \frac{t}{t_{th}}\right) + w_{p0}^2} \tag{3.45}$$

The electronic refractive index variation Δn_{el} is driven by the excited level decay, with lifetime t_{el}, which means the total refractive index change can be written as:

$$\Delta n(t) = \Delta n_{el}(0) \cdot \exp\left(-\frac{t}{t_{el}}\right) \cdot \frac{w_{e0}^2}{w_{e0}^2 + w_{p0}^2} + \frac{\Delta n_{th}(0)}{1 + \frac{t}{t_{th}}} \cdot \frac{w_{e0}^2 \cdot \left(1 + \frac{t}{t_{th}}\right)}{w_{e0}^2 \cdot \left(1 + \frac{t}{t_{th}}\right) + w_{p0}^2} \tag{3.46}$$

It is worth pointing out that the electronic lifetime t_{el} corresponds to the excited level fluorescence lifetime, τ_f, discussed in chapter 2.

The two-pass phase change of the probe beam (at the wavelength λ_p) under pump absorption is defined by the variation in optical path for an l_0-long sample:

$$\Delta\varphi(t) = \frac{2\,\pi \cdot \Delta n(t) \cdot 2l_0}{\lambda_p} \tag{3.47}$$

In this case, since the pump power is low and the pump pulse very short, the sample thermal expansion is neglected. In an interferometry experiment, the total phase difference between the pumped and the pristine probe beams is:

$$\Delta\varphi(t) = \Delta\varphi_{el} \cdot \exp\left(-\frac{t}{t_{el}}\right) \cdot \frac{w_{e0}^2}{w_{e0}^2 + w_{p0}^2} + \frac{\Delta\varphi_{th}}{1 + \frac{t}{t_{th}}} \cdot \frac{w_{e0}^2 \cdot \left(1 + \frac{t}{t_{th}}\right)}{w_{e0}^2 \cdot \left(1 + \frac{t}{t_{th}}\right) + w_{p0}^2} + \Delta\varphi_0 \tag{3.48}$$

In this equation, $\Delta\varphi_{th}$ and $\Delta\varphi_{el}$ are the phase shift amplitudes due to thermal and electronic refractive index variations respectively and $\Delta\varphi_0$ is the intrinsic phase difference introduced in eqns. (3.39) and (3.40).

3.3.b Interferometry Experiment Setup

A transient-state interferometry experiment was set up. As explained earlier, this setup is based on the comparison between the optical path lengths traced by a laser beam in two different regions of the sample, one pumped and the other pristine.

A CW He-Ne laser is used as the probe beam source, and a diode-pumped fibre laser with internal modulation was used as the pump beam source. The pump pulse frequency ν_{exc} and pulse duration Δt were chosen so to have a significant heat deposition and give the sample the time to dissipate the heat throughout the sample.

The two beams are then collected by two photodiodes and processed via an oscilloscope, and the difference between the two signals provides the phase difference and thus optical path evolution. The setup follows the schematic illustrated in figure 3.10, and the pump and probe beam geometry in figure 3.11.

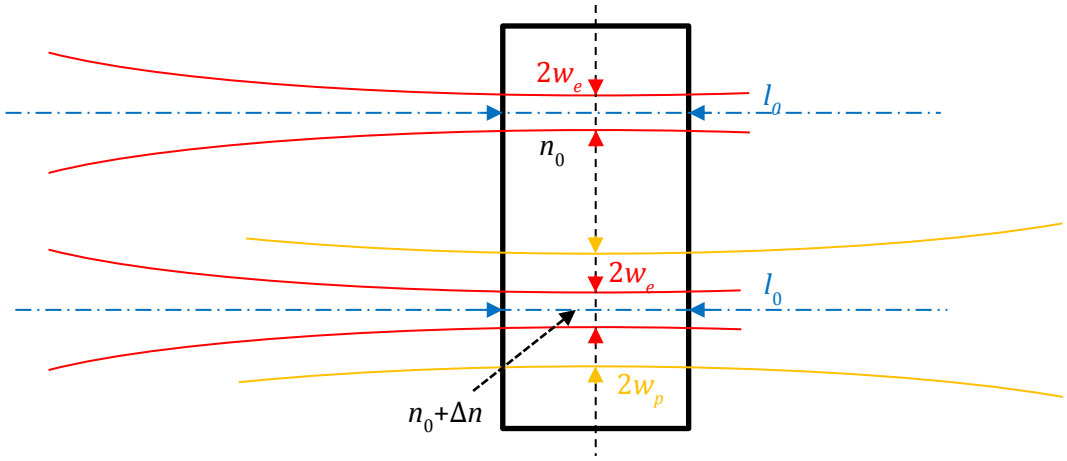

Fig. 3.11 Probe and pump beam geometry at the sample position in the transient-state interferometry setup.

In the case of transient-state interferometry, unlike in thermal lens spectrometry, the pump beam waist is larger than the probe beam waist, so that the pump intensity – and thus the thermal expansion – is approximately constant across the probe beam width. This is done to minimise thermal and population lens effects, and thus unwanted distortion of the pumped-arm probe beam. The beam waist position z_0 was measured via the pinhole technique previously introduced (Fig. 3.3). The beam radii at their waists were measured via a razorblade technique.

In this case, a razorblade is used as a screen to block out a part of the beam, and the total transmitted power beyond it is collected, while gradually moving the edge of the blade along a direction transversal to the beam axis. The detected power P_{det} is then fitted as a function of the transversal position x via a complementary error function for each beam of power P_i:

$$P_{det}(x) = \sum_i \frac{2\,P_i}{\sqrt{\pi}\,w_i} \int_x^{\infty} \exp\left(-\frac{(x' - x_i)^2}{w_i^2}\right) dx' \tag{3.49}$$

where x_i is the beam axis position and w_i is the beam waist radius. An example is shown in figure 3.12. Figure 3.12(a) shows the pump profile measurement, consisting of a single Gaussian beam, while figure 3.12(b) shows the probe profile measurement, which includes the two Gaussian beams corresponding to the two interferometer arms.

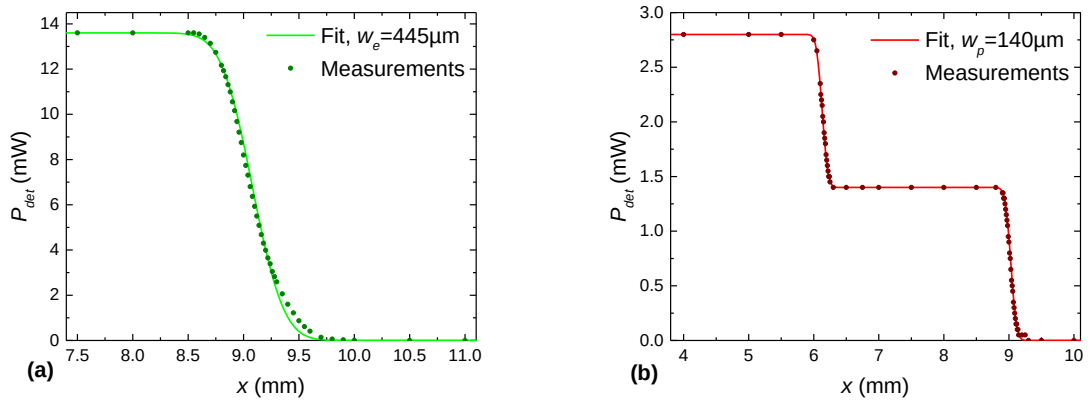

Fig. 3.12 Beam waist width measurement for the pump beam (a) and the two probe beams (b) in the interferometry measurements.

The operational parameters of this setup were measured and are summed up in table 3.5.

Table 3.5 Interferometry setup parameters and geometrical values.

Excitation beam		*Probe beam*	
P_e	30 mW	P_p	5 mW
λ_e	795 nm	λ_p	632.8 nm
w_e	445 µm	w_p	140 µm
Excitation Modulation			
ν_{exc}	4 Hz	Δt	200 µs

3.3.c Interferometry Experiment Results

Interferometry data were collected averaging the signal difference between the two interferometer arms as discussed earlier. The phase difference $\Delta\varphi$ obtained from the interferometry measurements is then fitted via the function (3.48):

$$\Delta\varphi(t) = \Delta\varphi_{el} \cdot \exp\left(-\frac{t}{t_{el}}\right) \cdot \frac{w_{e0}^2}{w_{e0}^2 + w_{p0}^2} + \frac{\Delta\varphi_{th}}{1 + \frac{t}{t_{th}}} \cdot \frac{w_{e0}^2 \cdot \left(1 + \frac{t}{t_{th}}\right)}{w_{e0}^2 \cdot \left(1 + \frac{t}{t_{th}}\right) + w_{p0}^2} + \Delta\varphi_0 \qquad (3.48)$$

In this fit, there are five adjustable parameters, namely $\Delta\varphi_0$, $\Delta\varphi_{el}$, $\Delta\varphi_{th}$, t_{el}, and t_{th}. As introduced before, $\Delta\varphi_0$ is a phase shift due to the intrinsic differences between the two sample sections through which the interferometer arms pass, while $\Delta\varphi_{el}$ and $\Delta\varphi_{th}$ are the electronic and thermal contributions to the phase shift, due to the pump-induced population and thermal refractive index changes, respectively.

The t_{th} value corresponds to the heat diffusion time, describing the temporal spread of the sample temperature profile after the pump beam pulse, and therefore the gradual thermal changes diffusion on the probe beam position. On the other hand, t_{el} is the electronic characteristic time, corresponding to the absorbing centres relaxation time from excited to ground states. This value is therefore related to the excited level fluorescence lifetime.

An example of data and fitting function is shown in figure 3.13.

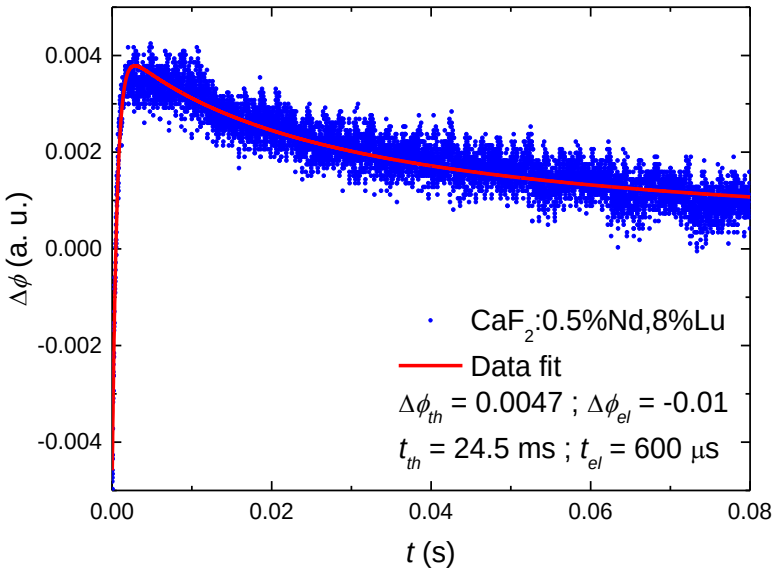

Fig. 3.13 Plot of the interferometry measurement for the sample CaF_2:0.5% Nd,8% Lu, and fit of the data.

As one can see in figure 3.13, the measurements are rather noisy, making the fit more uncertain. One can notice that the electronic contribution is responsible for the rise of the signal at the beginning while the thermal contribution explains the decay of the signal at longer times. The two contributions have thus opposite effects on the total phase shift. Let us recall that as was observed with the TLS measurements (see table 3.4), the thermo-optic coefficient *dn/dT* is negative, and therefore so is the thermal contribution to the phase shift. This implies that, while the thermal contribution decreases the probe beam optical path length *s* through the sample, the electronic contribution increases *s*. The thermal contribution also has a much longer characteristic time than the electronic one, which, as expected, is in the order of magnitude of the fluorescence lifetime.

Knowing the thermal contribution characteristic time value t_{th}, the samples thermal diffusivity D is then obtained by inverting the equation (3.44), very much like what was done in the thermal lens experiment:

$$D = \frac{w_e^2}{8t_{th}} \tag{3.50}$$

Once obtained the thermal diffusivity D, one can again derive the thermal conductivity values K via eqn. (3.24). However, due to the noise observed in most measurements, the signal-to-noise

ratio (SNR) of each measurement was calculated, and only the results corresponding to the highest SNR values were kept and compared to those obtained via thermal lens measurements.

As shown in figure 3.14, the thermal conductivity behaviour as a function of lutetium concentration obtained from the interferometry measurements follows closely the thermal lens results.

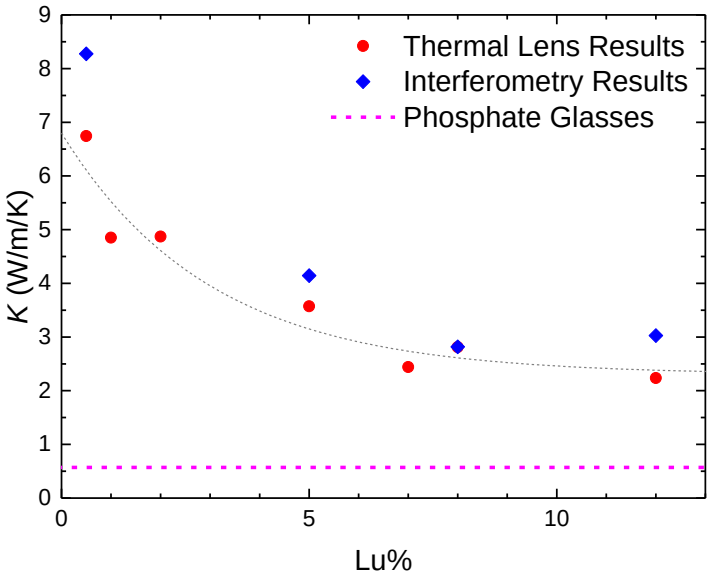

Fig. 3.14 Thermal conductivity of CaF_2:Nd^{3+},Lu^{3+} samples as a function of Lu^{3+} concentration, showing the consistency of results between TLS (red dots) and interferometry (blue diamonds) measurements, and comparison to the thermal conductivity of phosphate glasses (dashed line).

Figure 3.14 also shows the comparison of CaF_2:Nd^{3+},Lu^{3+} thermal conductivity values to the neodymium-doped phosphate glasses LHG-8 and LG-770, currently employed in the MégaJoule laser as amplifying materials. Even at its lowest, the fluoride crystal thermal conductivity is close to four times higher than the phosphate glasses value, which is about 0.6 $W \cdot m^{-1} \cdot K^{-1}$.

This interferometry experiment making use of polarisation-based detections, it is very sensitive to polarisation changes. Therefore, the signal noise observed with some samples is likely due to the samples depolarisation effects. To confirm this hypothesis, a qualitative depolarisation imaging experiment was performed, by placing the samples between crossed polarisers. The samples show some degree of depolarisation regions, recognisable by the bright spots or lines observable through the cross polarisers. The existence of these bright spots means that the polarised light shone on the sample has changed its polarisation, so that it is able to be

transmitted by the second polariser. The main depolarising regions are thought to correspond to interfaces between differently-oriented crystal domains. Examples of these measurements are shown in figure 3.15. Overall, these depolarisation effects are not very strong from a laser application point of view. However, for this particular interferometry experiment they do bring about noise in the signal detection.

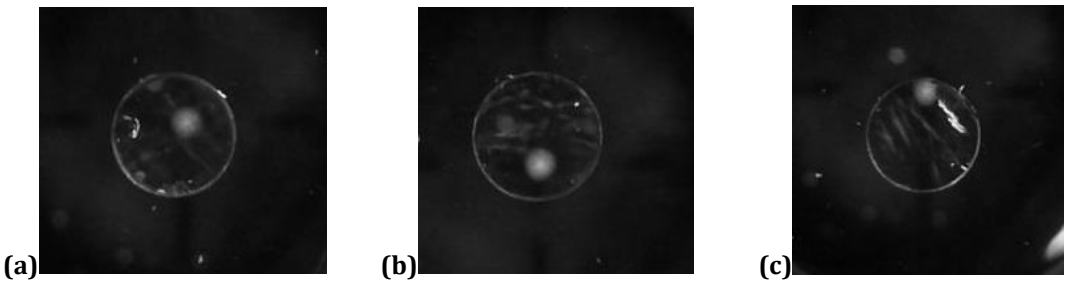

Fig. 3.15 Polarised light imaging showing some depolarisation effects of samples CaF_2:0.5% Nd,1% Lu (a), CaF_2:0.5% Nd,5% Lu (b), and CaF_2:0.5% Nd,12% Lu (c)

3.3.d Comparison to the Theoretical Model

In the specific case of CaF_2:Nd^{3+},Lu^{3+} considered in this work, the only concentration to change is that of Lu^{3+}, while the Nd^{3+} concentration is the same for all samples. Therefore, the thermal conductivity K_1 of the CaF_2:0.5% Nd sample was first calculated. It was then used in the place of K_0 in equation (3.13) of the Klemens model to estimate the evolution of thermal conductivity in the co-doped samples as the Lu^{3+} concentration increases, thus obtaining the curve shown in figure 3.16.

The thermal lens results for the thermal conductivity are consistent, within the uncertainty of the measurements, with the Klemens model for high Lu^{3+} concentration values, but are consistently higher than the theoretical values at low Lu^{3+} concentration. A similar discrepancy between Klemens' calculations and experimental values can be found in the work by Petit *et al.* in the section about CaF_2:Yb^{3+} [121], where one can see that the Klemens curve deviates from the measurements at low dopant concentrations. It can be argued that the model is a tentative theoretical approach of the real thermal conductivity evolution. In particular, the crystal lattice cell size and shape, and the phonon velocity are considered constant, independently of the lattice distortions due to the presence of dopants. In the study of the doubly-doped CaF_2 crystals, another approximation was introduced. The Klemens model was in fact used to calculate the conductivity of the singly-doped CaF_2:0.5% Nd crystal. This was then used as the original value

for the doubly-doped samples, whose thermal conductivity was evaluated by re-applying the model to 0.5% Nd-doped crystals, with Lu^{3+} concentration as the varying quantity. This approximation may be the cause of the discrepancy between experimental and calculated K values.

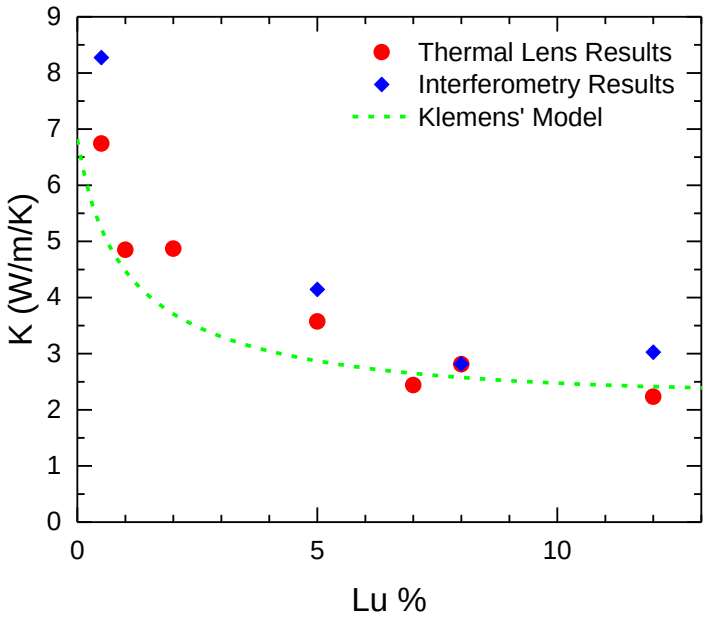

Fig. 3.16 Comparison of the thermal conductivity values obtained from experiments and from Klemens' calculations [42,136].

3.4 Birefringence

Another issue with polarisation-dependent measurements is the induction of birefringence effects by thermal variations in the crystal. To assess the thermally-induced birefringence, CaF_2:Nd^{3+},Lu^{3+} samples were sent to the CESTA laboratory of the CEA in Bordeaux, for birefringence measurements. The measurements were performed both with and without optical pumping, to observe the birefringence effect induced by the pump absorption. These measurements consist in the measurement of a CW probe beam intensity passing through the sample between crossed polarisers. The sample was pumped along a perpendicular direction to the probe light with a pulsed laser diode. The pump-induced birefringence was calculated by subtracting the intrinsic birefringence measurements from the pumped sample measurements. Examples are presented in figure 3.17. It is interesting to notice that the high-birefringence area

corresponding to the pump beam path through the sample is contoured by two “trenches” of low birefringence.

Multiple measurements were performed at different times after the pump pulse to observe the birefringence relaxation dynamics (see figure 3.17). The results showed that the birefringence intensity decreases with time as the sample cools down. However, the birefringence decay follows a non-exponential decay curve, which is not in agreement with the standard heat diffusion model, and therefore is still under investigation.

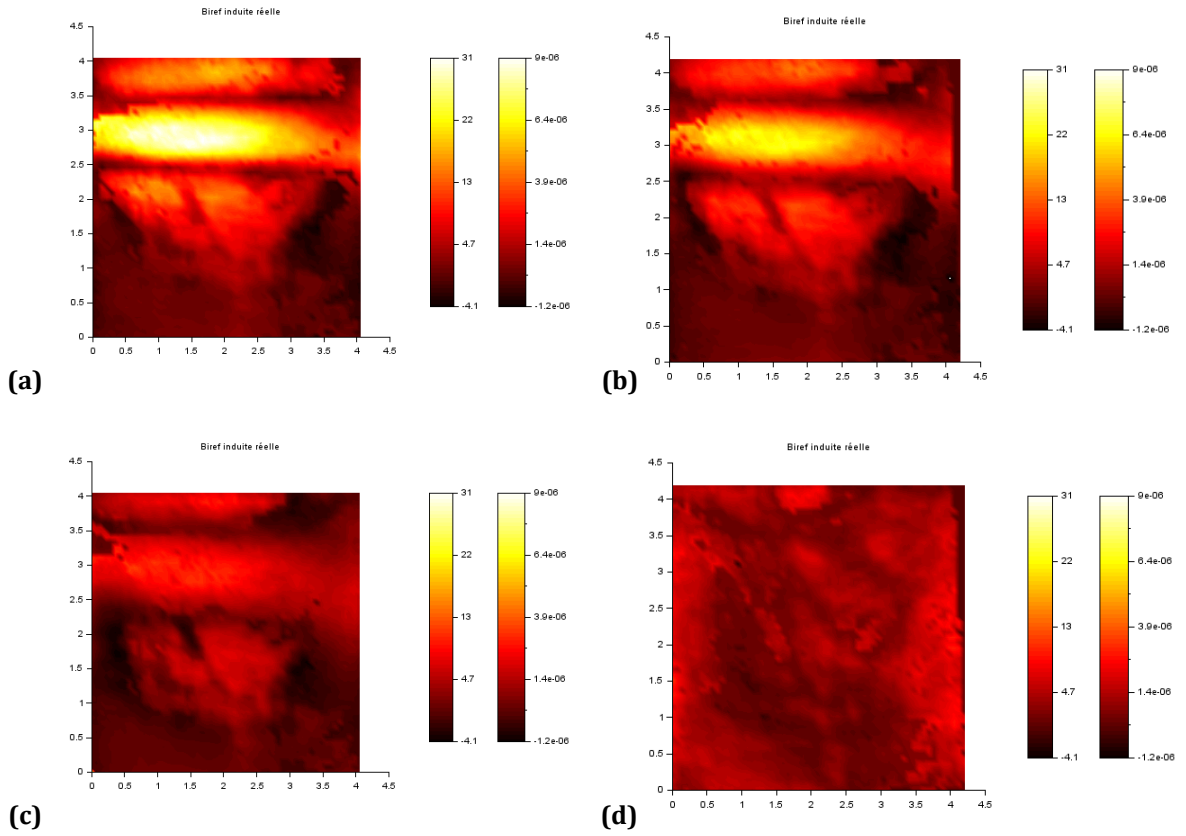

Fig. 3.17 Birefringence measurements for a CaF_2:Nd^{3+},Lu^{3+} sample at 10 ms (a), 30 ms (b), 100 ms (c) and 1 s (d) after the pump pulse.

The induced birefringence profile was measured across the pump beam direction at different times during the sample cooling (Fig. 3.18). As expected, the profile has a peak profile shape corresponding to the pumped region. Interestingly, however, the peak is delimited by two dips in birefringence intensity, corresponding to the trenches mentioned earlier. Moreover, one would expect the profile to spread as the heat diffuses. However, while the measured values decrease, no sensible changes in the profile shape are observed as the sample cools. This effect has not been explained yet, and more thorough investigations are planned in this regard.

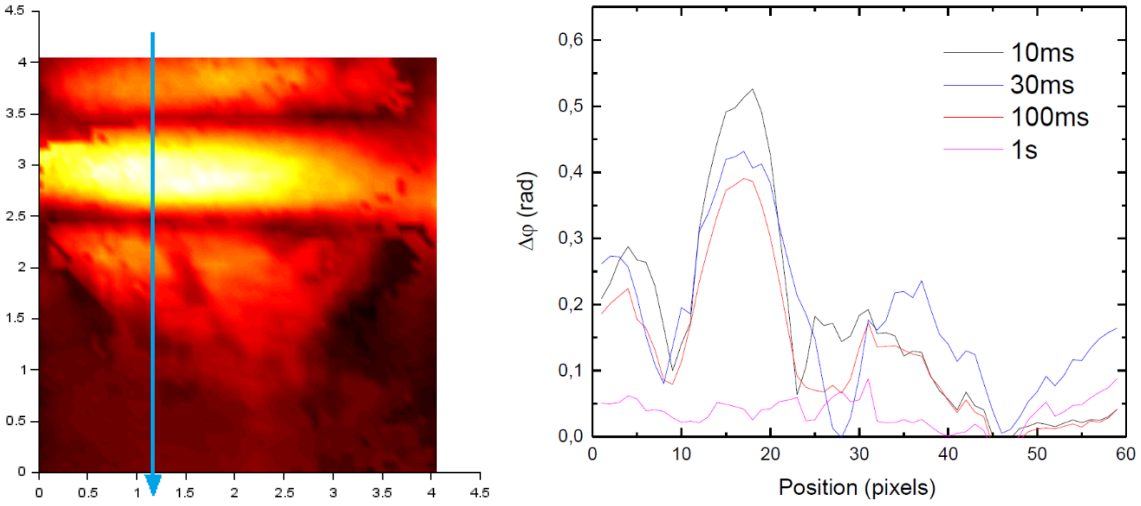

Fig. 3.18 Birefringence profile measurements for a CaF_2:Nd^{3+},Lu^{3+} sample at different times.

Thermally-induced birefringence has then been proven to appear in CaF_2:Nd^{3+},Lu^{3+} samples, with noticeable effects on the polarisation of transmitted light, lasting up to hundreds of milliseconds after the pump beam is off. The measurements are still preliminary, and a more in-depth study of the phenomenon is underway to address the still unexplained effects observed.

3.5 Conclusions

The thermal conductivity of CaF_2:Nd^{3+},Lu^{3+} samples with different Lu^{3+} concentrations was evaluated by using thermal lens spectrometry measurements, showing the evolution of the material thermal properties as the doping increases. The results show that the thermal conductivity decreases as the Lu^{3+} concentration increases, which is consistent with predictions from the theory of phonon scattering. The thermal conductivity drops toward 2 $W \cdot m^{-1} \cdot K^{-1}$ at high Lu^{3+} concentration, which is quite lower than the value of undoped CaF_2 crystals, but still satisfies the requirements for the desired application, as it is several times higher than the value for the Nd^{3+}-doped glasses that the crystals are supposed to replace, which is under 0.6 $W \cdot m^{-1} \cdot K^{-1}$. In fact, the thermal conductivity values obtained for Nd^{3+},Lu^{3+}-doped CaF_2 samples with up to 5 at% Lu^{3+} concentration are still higher than in undoped crystals such as BOYS, SYS, KGW and KYW (typical value of 2-3 $W \cdot m^{-1} \cdot K^{-1}$), which suggests they may offer an all-around better choice for high-energy laser pulse amplification.

The influence of the geometrical parameters on the results of the thermal lens measurements fit was discussed, introducing the steady-state and transient-state signal functions. The results of

the analysis show that the characteristic time t_C of the signal evolution – and therefore the thermal conductivity – is mainly influenced by the V parameter. That is to say, an accurate measurement of the beam waist positions is crucial for a reliable estimate of a sample thermal conductivity, and the error on this measurement is possibly the most important contribution to the uncertainty on thermal conductivity measurements.

Interferometry measurements were also performed on the same samples, yielding results in good agreement with those obtained from thermal lens measurements, which corroborates the observed behaviour of thermal conductivity as a function of lutetium concentration in CaF_2:Nd^{3+},Lu^{3+} samples. However, interferometry measurements have proven quite more delicate than thermal lens spectrometry, and several data points had to be dropped due to their low SNR. The main cause of signal fluctuations in these measurements has been identified with depolarisation effects since this interferometric technique is highly sensitive to polarisations changes.

The thermal conductivity values of CaF_2:Nd^{3+},Lu^{3+} obtained both via thermal lens spectrometry and transient-state interferometry are consistently several times higher than those of currently employed phosphate laser glasses, which is an encouraging result. In fact, it confirms the viability of the investigated materials as replacement for the current glass active medium to improve the properties of the high-energy laser amplifier systems.

The results of the thermal conductivity measurements are overall in agreement with those obtained via a calculation using Klemens model at high Lu^{3+} concentration, though they retain higher values for lower codopant concentrations. The difference in thermal conductivity between experiment and calculations at low lutetium concentration values are likely due to inaccurate approximations in the theoretical calculations in the case of double rare-earth doping at low dopant concentrations. An estimation of the parameters dependency on dopant concentration may yield more accurate theoretical estimates.

The linear thermal expansion coefficient and the thermo-optic coefficient of doubly-doped calcium fluoride crystals were also evaluated. The obtained values are comparable to those presented in literature, but the samples thermal expansion coefficient is higher than the value provided by manufacturers for undoped crystals, suggesting an influence of the rare-earth doping. The average values of the total optical path thermal variation, however, are compatible with those presented in various literature documents, which assesses the validity of the treatment and suggests that there is no sensible variation in their value as a consequence of the introduction of rare earth dopants.

CHAPTER 4

"I have dwelt ever in realms apart from the visible world"

Amplification Properties

4.1 Introduction

In the previous chapters, the spectroscopic and thermomechanical properties of neodymium-lutetium codoped fluoride crystals, in particular CaF_2, have been studied in detail. At this point, it is important to assess the operating qualities of the material as a laser gain medium. In addition, to complete the characterizations, the possibility to obtain both CW and pulsed laser operation can be investigated.

Gain is an extensive quantity for a sample, strictly linked to its gain coefficient, which is dependent on the pump beam profile. Therefore, the gain coefficient can be evaluated as well from the gain measurements, providing a local quantity that can be used in modelling. In particular, knowledge of the material optical gain and gain coefficient are important within the LASCAN project framework for the tailoring and design process for a CaF_2:Nd^{3+},Lu^{3+} crystal-based laser amplifier for the LMJ chain.

The LMJ front-end amplifier has a transversally-pumped setup that employs laser diode arrays exciting the active material from the side, perpendicular to the laser beam axis (Fig. 4.1). However, in order to probe the material gain properties, longitudinal pumping can be used as a way to compare different crystals in order to optimise the composition, and connect the results to the spectroscopic studies. It also allows for an accurate control of the pumped volume and absorbed pump power. Once the gain properties are known, they can be generalised to the transversal pump case. Moreover, since in this work longitudinal pumping will be used to

achieve laser oscillation with in-cavity experiments, single-pass gain measurements are performed in collinear, co-propagating setup geometry.

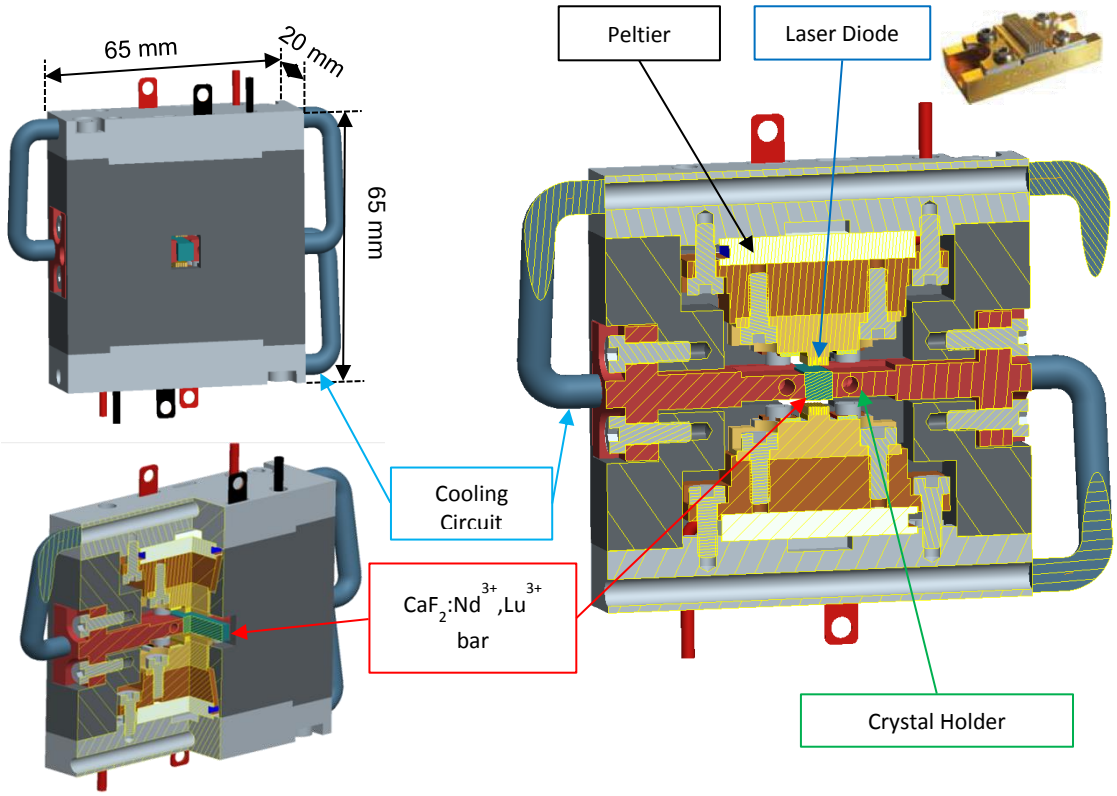

Fig. 4.1 Rendition of the LMJ preamplifier pumping system with the implementation of $CaF_2:Nd^{3+},Lu^{3+}$ crystals.

The material gain is a defining factor for laser operation. A high single-pass gain is very important for the primary amplification of a pulsed laser, in order to provide high power at the front-end output. Laser oscillation properties of the crystals also brings information about the material potential, particularly its short-pulse generation ability, and it can be interesting to look at the laser performances changing, for instance, the pump wavelength in a multisite gain medium like $CaF_2:Nd^{3+},Lu^{3+}$.

One of the most common methods of obtaining ultrashort pulsed laser emission is via CW mode-locking mechanisms. In particular, the mode-locking phenomenon was first described in 1964 by DiDomenico [143] and Hargrove *et al.* [144]. In Hargrove's work [144], mode locking was achieved by active modulation of the internal cavity losses, in what is known as "active" mode-locking. However, it was later shown by Mocker and Collins [145] that mode-locking could be obtained without the need for active modulation in a *Q*-switched dye laser. In particular, it was observed that the *Q*-switched pulses, each many cavity roundtrips long, divided into trains

of much shorter pulses, separated by a timespan equal to the cavity roundtrip period. The studies about these short, high-intensity pulses properties, however, were limited by their accuracy. The precision of mode-locked pulse measurements were impaired by the phenomenon unpredictable nature and reproduction unreliability. However, a successful solution to this drawback was found by Ippen, Shank, and Dienes [146], who achieved passively mode-locked operation in a CW dye laser. This result was obtained by employing a saturable dye as a saturable absorber within the cavity. Since this breakthrough, it has been possible to reliably generate very short, reproducible and predictable pulses using CW mode-locked lasers. For this purpose, a great effort in the design and development of saturable absorber lasers began in the following years, leading soon to the generation of sub-picosecond pulses [147]. In the following years, shorter and shorter CW mode-locked laser pulse generation has been achieved, for a large variety of laser materials [148].

However, fluoride crystals have been considered as interesting femtosecond laser materials only in recent years and, if calcium fluoride is known as one of the first laser host in the history of lasers [149,150], it has been proven relatively recently as a valid candidate for short-pulse laser operation. In particular, ytterbium-doped CaF_2 has been extensively studied as a laser material for laser action at 1 μm. After the first laser operation using this host in 2004 [31], many results have been reported on the subject. A 2009 work by Friebel *et al.* [33] achieved 99 fs pulsed laser operation with a folded cavity setup, using saturable absorber mode-locking. Interestingly, the experiment showed no effects of the thermal lensing effect of CaF_2:Yb^{3+} on the system stability. However, a transition between the mode-locked and *Q*-switched regimes was observed, and a periodic alternation of the two was associated to the thermal effects on the crystal. The periodic alternation between *Q*-switch and mode-locking is consistent with previous observations. In fact, CaF_2:Yb^{3+} mode-locked operation has an additional limitation due to the material tendency to *Q*-switch [151] because of the Yb^{3+} ions $^2F_{5/2}$ metastable state long lifetime.

Neodymium-doped calcium fluoride crystals for laser applications were also investigated with yttrium codoping to avoid quenching. Su *et al.* obtained CW laser action employing CaF_2:Nd^{3+},Y^{3+} in a plano-concave cavity [10], demonstrating the viability of such a material as a broadband laser amplifier, and relating the system slope efficiency to the output coupler transmission. Qin *et al.* [39] used CaF_2:Nd^{3+},Y^{3+} to achieve mode-locked laser operation. They succeeded in obtaining 103 fs pulses with an average output power of 89 mW, and a 100 Hz repetition rate. In a recent work, Zhu *et al.* [152] obtained a mode-locked femtosecond laser device employing a folded cavity setup with a semiconductor saturable absorber mirror

(SESAM). A slope efficiency near to 10% was demonstrated, with a wide tuneability range, from 1042 nm to 1076 nm and 5 nm FWHM pulse spectral peaks.

These works are encouraging, as they open many possibilities for further research about these systems. The results prove that rare earth-doped – and in particular neodymium-doped – calcium fluoride is a promising medium for short-pulse mode-locked laser operation. In fact, it is considered a very interesting material for laser devices, thanks to the possibility of achieving a wide tuneability range (broad bands), and thus very short pulse durations. Moreover the broad absorption features allow for a relatively easy and efficient excitation mechanism via diode pumping. As it was previously introduced, CaF_2 is also relatively easy to grow in large sizes, which is very important for large-scale facilities like LMJ.

In the investigation about the laser operation of samples, the viability of the material as an amplifier must be assessed. For this purpose, the material optical gain has to be quantified. The estimate of optical gain and gain coefficient provides very important parameters for the laser setup design and optimisation. In this context, gain measurements may be performed. These measurements consist in exciting the samples upon the appropriate absorption band, and measuring the amplification of a probe beam of the corresponding emission wavelength. The comparison between the transmitted and incoming probe signals provides an estimate for the sample gain. Various gain measurement configurations can be set up, with different pumping methods and experiment geometries. In this work, in order to recreate the pumping conditions intended for the subsequent laser experiments performed and because of the available equipment, a collinear and co-propagating pump/probe geometry experiment was set up.

As a starting point of this laser study, CW laser operation with $CaF_2:Nd^{3+},Lu^{3+}$ was demonstrated by Doualan *et al.* [8], with a simple plano-concave setup. The work showed that, employing $CaF_2:Nd^{3+},Lu^{3+}$, a higher slope efficiency than in the case of neodymium-yttrium codoping can be obtained. However, a more in-depth study is necessary to assess the crystal viability as a short-pulse laser amplifier.

In this chapter, the opportunity of employing $CaF_2:Nd^{3+},Lu^{3+}$ as an amplifier material will be investigated, both in a single-pass configuration and within in-cavity setups, with CW pumping. First of all, a model for the estimation of stimulated emission and optical gain will be discussed. Measurements of $CaF_2:Nd^{3+},Lu^{3+}$ samples' gain with a collinear-beam setup will be then shown and discussed. Finally, preliminary measurements demonstrating the laser operation of $CaF_2:Nd^{3+},Lu^{3+}$ both in CW operation and in the mode-locked regime will be presented. The

results of the experiments and calculations, and the perspectives for future investigations in the topic will be discussed at the end of the chapter.

4.2 Gain Modelling

Neodymium-based lased materials operate as a 4-level system, as shown in figure 4.2. The atoms in the ground state $^4I_{9/2}$ are pumped to the $^4F_{5/2}$ state, from which they decay nonradiatively to the $^4F_{3/2}$ level. The laser transition then occurs between the levels $^4F_{3/2}$ and $^4I_{11/2}$, and from the latter the atoms relax nonradiatively to the ground state. For our convenience in the modelling of the system, we have labelled the levels $^4I_{9/2}$, $^4I_{11/2}$, $^4F_{3/2}$, and $^4F_{5/2}$ from 1 to 4 in increasing energy order. The ion concentration of each level is labelled N_i, i being the level number.

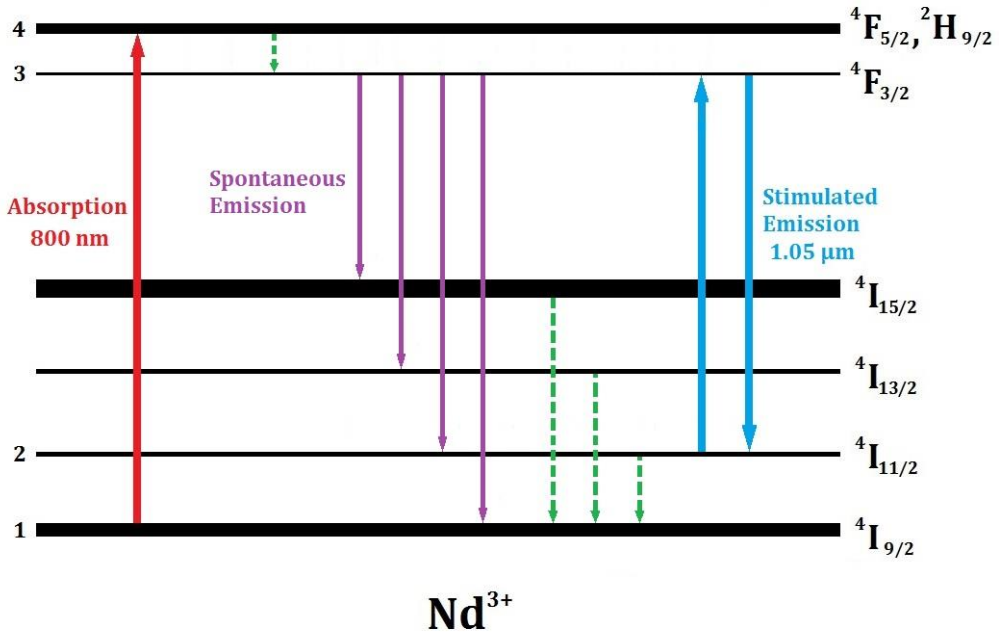

Fig. 4.2 Four-level system diagram of the laser operation at 1.05 µm for Nd^{3+} ions pumped at 800 nm.

In this section the formalism and approach used by Fan, Risk, Laporta and Augé will be employed [153-156]. Thus, the rate equations can be then written by keeping into account the absorption, losses and emission for each level:

$$\frac{dN_1}{dt} = -R_P + W_2 N_2 + W_{31} N_3 + B_{NR} \tag{4.01}$$

$$\frac{dN_2}{dt} = W_{32} N_3 + A_L N_3 - A_L N_2 - W_2 N_2 \tag{4.02}$$

$$\frac{dN_3}{dt} = W_{43} N_4 - W_3 N_3 \tag{4.03}$$

$$\frac{dN_4}{dt} = R_P N_1 - W_4 N_4 \tag{4.04}$$

Here, R_P is the pump ratio, W_{ij} is the transition probability from level *i* to level *j*, W_i is the total emission probability from level *i*, A_L is the stimulated transition probability for laser photons, and the term B_{NR} takes into account the transitions mediated by the $^4I_{15/2}$ and $^4I_{13/2}$ levels. One can therefore rewrite the transition probabilities as:

$$W_{ij} = W_i \beta_{ij} \tag{4.05}$$

where β_{ij} is the branching ratio for the transition from level *i* to level *j*.

In particular, considering the nonradiative transitions as nearly instantaneous, for the spontaneous transitions from level $^4F_{3/2}$ one can write:

$$W_3 N_3 = W_{32} N_3 + W_{31} N_3 + B_{NR} \tag{4.06}$$

In stationary regime, we have that for all levels, it holds that $dN/dt = 0$. Thus, from eqn. (4.02) one obtains:

$$W_2 N_2 = W_{32} N_3 + A_L N_3 - A_L N_2 \tag{4.07}$$

Let us now assume that, since nonradiative transitions are very fast, the population of levels from which nonradiative relaxation takes place is zero, meaning:

$$N_2 \cong N_4 \cong 0 \tag{4.08}$$

With this approximation, substituting eqns. (4.07) and (4.06) in eqn. (4.01), one can see that:

$$\frac{dN_1}{dt} = -R_P N_1 + A_L N_3 + W_3 N_3 \tag{4.09}$$

In the same way, substituting (4.04) into eqn. (4.03), one obtains:

$$\frac{dN_3}{dt} = R_P N_1 - A_L N_3 - W_3 N_3 \tag{4.10}$$

One can see here that $dN_3/dt = -dN_1/dt$, which is consistent with assumption of the total ion density being constant. In particular, since N_2 andN_4 are close to naught, the total ion density N_T is simply given by:

$$N_T = N_1 + N_3 \tag{4.11}$$

Recalling once more the stationary regime case, from equations (4.09), (4.11) and (4.10) one obtains the expression for N_3:

$$N_1 = \frac{A_L N_3 + W_3 N_3}{R_P} = \frac{A_L + W_3}{R_P}(N_T - N_1) \tag{4.12}$$

$$N_1 = \frac{N_T}{1 + \frac{R_P}{W_3 + A_L}} = \frac{N_T}{1 + \frac{\tau_f R_P}{1 + \tau_f A_L}} \tag{4.13}$$

$$N_3 = \frac{N_T}{1 + \frac{1 + \tau_f A_L}{\tau_f R_P}} \tag{4.14}$$

where $\tau_f = W_3^{-1}$ is the fluorescence lifetime of the excited-state ions. With this, we can have an expression for the gain coefficient, g, since, by definition:

$$g = \sigma_{eL} N_3 - \sigma_{aL} N_2 = \frac{\sigma_{eL} N_T}{1 + \frac{1 + \tau_f A_L}{\tau_f R_P}} \tag{4.15}$$

where σ_{eL} and σ_{aL} are the emission and absorption cross sections at the laser wavelength.

Since the pump absorption probability is directly proportional to the incident pump intensity, eqn. (4.15) shows how the gain saturates with increasing pump beam intensity.

Clearly, due to the pump and cavity photon distribution within the device, the gain coefficient is not uniform. One can obtain a description for the gain profile by defining the photon distribution along the crystal. In particular, we can define the profile for both the excitation and laser beam, respectively $s_e(r)$ and $s_p(r)$, where r is the radial position from the centre of the

beam. The profiles must be normalised to the surface of the plane they cross, so that [153,154,157]:

$$\iint s_e(r,z)dS = \iint s_p(r,z)dS = 1 \tag{4.16}$$

Considering a Gaussian beam profile for both pump and probe then:

$$s_e(r,z) = \frac{2}{\pi w_e(z)^2}\exp\left(-\frac{2r^2}{w_e(z)^2}\right) \tag{4.17}$$

$$s_p(r,z) = \frac{2}{\pi w_p(z)^2}exp\left(-\frac{2r^2}{w_p(z)^2}\right) \tag{4.18}$$

Here, $w_e(z)$ and $w_p(z)$ are the excitation and cavity beam waist radii, defined as:

$$w_e(z) = w_{e0}\sqrt{1+\left(\frac{z\,\lambda_P}{\pi\, w_{e0}^2}\right)^2} \tag{4.19}$$

$$w_p(z) = w_{p0}\sqrt{1+\left(\frac{z\,\lambda_L}{\pi\, w_{p0}^2}\right)^2} \tag{4.20}$$

One can then write the expression for the pump rate:

$$R_P(r,z) = \frac{P_e(z)}{h\,\nu_e}\eta_{abs}\,s_e(r,z) = \frac{P_e(z)\,s_e(r,z)(1-\exp(-\alpha\,\Delta z))\lambda_e\,n(\lambda_e)}{h\,c\,\Delta z} \tag{4.21}$$

Here, $P_e(z)$ is the pump beam power at the position z along the crystal, ν_e is the pump photon frequency, λ_e is the pump wavelength, η_{abs} is the absorption efficiency, which is defined as $\eta_{abs} = 1-\exp(-\alpha\cdot\Delta z)$, α is the absorption coefficient, $n(\lambda)$ is the material refractive index as a function of wavelength, and Δz is the beam geometrical path length within the absorbing material.

A similar definition can be applied to obtain the expression for the laser transition probability profile:

$$A_L(r,z) = \sigma_{eL}\frac{P_p(z)}{h\,\nu_p}s_p(r,z) = \frac{P_p(z)\,s_p(r,z)\,\sigma_{eL}\lambda_p\,n(\lambda_p)}{h\,c} \tag{4.22}$$

where $P_p(z)$ is the probe beam power at the position z along the crystal, ν_p is the laser photon frequency, and λ_p is the laser wavelength.

The gain coefficient can therefore be mapped within the crystal volume as:

$$g(r,z) = \frac{\sigma_{eL} N_T}{1 + \frac{1 + \tau_f A_L(r,z)}{\tau_f R_P(r,z)}} \tag{4.23}$$

These equations were employed in the writing of a program for the calculation of gain on Nd^{3+}-doped crystals. The routine divides the sample in thin slices both along the propagation axis of the beam and on the radial direction. This allows to perform a numerical, step-by-step estimation of all the parameters involved, and to apply some approximations, in particular simplifying the exponentials into linear functions. All of this in turn allows both an estimation of the total output power, and therefore the optical gain G, and the mapping of the pump and probe power density, gain coefficient and excited ion distribution within the sample.

4.3 Experimental

In this section, the CaF_2:Nd^{3+},Lu^{3+} samples gain is discussed, first by calculating the gain coefficient ratio between the different emission features, independently of the pump beam flux. This provides an indication of the relation linking lutetium concentration, pumping wavelength and laser emission lines. A gain measurement experiment is then set up, in order to determine the absolute gain values of CaF_2:Nd^{3+},Lu^{3+} samples. The experimental results are compared to the calculations output, via the theoretical model discussed in the previous section.

Finally, the potential of these materials is investigated, using CaF_2:Nd^{3+},Lu^{3+} samples as active material in laser experiment. First, the CW laser operation is assessed in a simple linear plano-concave cavity experiment. Then, the pulsed laser action is investigated in the mode-locked regime, employing a folded cavity setup.

4.3.a Gain Calculations

To calculate the gain of a system, knowledge of an extensive and comprehensive set of quantities is necessary, including absorption and emission spectroscopic parameters, lifetimes

and branching ratios. Therefore, for this purpose, the results of the spectroscopy investigation from chapter 2 will be taken into account as a means to perform the calculations in this section.

Absorption measurements on CaF_2 samples with 0.5% Nd^{3+} doping and various lutetium concentrations show that the absorption band shape substantially changes when increasing the lutetium concentration indicating the existence of different centres comprising Nd^{3+}-Nd^{3+} and Nd^{3+}-Lu^{3+} clusters. Furthermore, fluorescence spectra recorded around 1.05 μm change drastically when pumping at different wavelengths further confirming the presence of two main emitting Nd^{3+}-Lu^{3+} centres, labelled NL1 and NL2.

Time-resolved excitation and emission spectroscopy have been used to distinguish the two main emitting centres by carefully choosing the Lu^{3+} codopant concentration, the recording time window and the emission or excitation wavelength for the excitation and emission spectra respectively. NL1 emission is obtained from low-lutetium concentration samples excited at 791 nm, and recording within a late time window; NL2 emission is obtained from high-lutetium concentration samples excited at 797 nm, and collecting the signal within an early time window. Excitation spectra can be obtained using the same type of method, selecting the emission wavelength (1049 nm for NL1, 1054 nm for NL2) instead of the excitation wavelength.

The "pure" NL1 and NL2 emission spectra, along with the transition ($^4F_{3/2}\rightarrow{}^4I_{11/2}$) radiative lifetimes ($\tau_{rad}$=350 μs and τ_{rad}=490 μs for NL2 and NL1 respectively) allow the calculation of the NL1 and NL2 centres stimulated emission cross-sections, using the well-known Füchtbauer-Ladenburg equation. The results of this calculation were performed in chapter 2, and can be found in figure 2.22.

Recalling once more the calculations presented in chapter 2, the absorption cross section spectra for the different centres in CaF_2:Nd^{3+},Lu^{3+}were discriminated by comparison of the time-resolved excitation spectra with the sample absorption spectra. Furthermore, knowing the absorption cross sections, it was possible to derive the different centres concentrations (see Fig. 2.18).

The centre concentration, absorption and emission cross section values were employed to estimate the laser gain $\gamma(\lambda_{em},\lambda_{exc})$, for various excitation and emission wavelengths. The $^4F_{3/2}\rightarrow{}^4I_{11/2}$ laser transition is well-known to take place within a 4-level system as introduced in section 4.2: we can therefore assume that the nonradiative depopulation of the second level towards the first is instantaneous, which means that at any given instant the population of the

excited level is defined by $N(^4F_{3/2})$-$N(^4I_{11/2})$=$N(^4F_{3/2})$. The small-signal laser gain at a certain emission wavelength is thus given by:

$$\gamma(\lambda_{em},\lambda_{exc}) = \frac{N_{\mathrm{NL1}} \cdot \phi \cdot \beta \cdot \tau_f^{\mathrm{NL1}} \cdot \sigma_{abs}^{\mathrm{NL1}}(\lambda_{exc})}{\tau_{rad}^{\mathrm{NL1}}} \cdot \sigma_{em}^{\mathrm{NL1}}(\lambda_{em}) + \frac{N_{\mathrm{NL2}} \cdot \phi \cdot \beta \cdot \tau_f^{\mathrm{NL2}} \cdot \sigma_{abs}^{\mathrm{NL2}}(\lambda_{exc})}{\tau_{rad}^{\mathrm{NL2}}} \cdot \sigma_{em}^{\mathrm{NL2}}(\lambda_{em}) \tag{4.24}$$

where τ_f is the fluorescence lifetime (obtained from fluorescence decays measurements) and ϕ the excitation photon flux.

Interestingly, eqn. (4.24) shows that depending on the excitation wavelength and the Lu^{3+} concentration the laser gain maximum and thus the actual laser oscillation will be found at different wavelengths. This result is confirmed by laser experiments in which three laser wavelengths values (1049, 1054 and 1062 nm) are observed. The gain ratio $\gamma(\lambda_{em}^1)/\gamma(\lambda_{em}^2)$ between two different emission wavelengths derived from equation (4.24) can give some insight regarding the laser wavelength. The gain ratio between the emission at 1054 nm and that at 1049 nm is given in figure 4.3(a) as a function of the Lu^{3+} concentration showing that the laser emission may occur at 1054 nm shortly above 0.1%Lu^{3+} for a 797 nm excitation and above 0.5%Lu^{3+} for a 791 nm excitation.

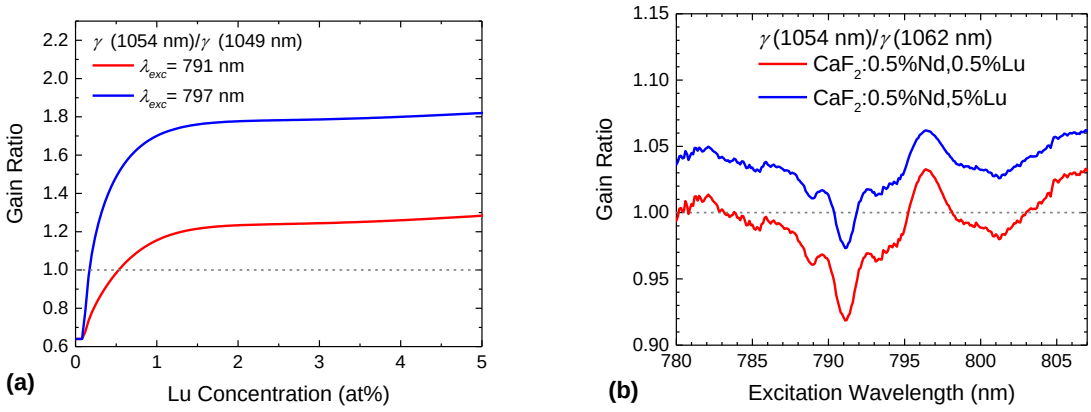

Fig. 4.3 (a) Gain ratio between the 1049 nm and 1054 nm emission peaks, showing the relative increase in laser gain at 1054 nm as lutetium concentration increases; (b) gain ratio between 1054 nm and 1062 nm emission versus excitation wavelength for different samples.

The gain ratio between the emissions at 1054 nm and at 1062 nm was calculated for samples with different concentrations. In particular, figure 4.3(b) shows the calculated gain ratios for the

samples CaF_2:0.5% Nd,0.5% Lu and CaF_2:0.5% Nd,5% Lu. The results show that the 1062 nm laser emission is dominant when exciting at 791 nm in both samples, while the 1054 nm emission is predominant when exciting at 797 nm. The excitation spectral range to achieve laser action at 1054 nm clearly increases with the lutetium concentration as it is broader in CaF_2:0.5%Nd,5%Lu than in CaF_2:0.5%Nd,0.5%Lu.

4.3.b Gain Measurements

Gain measurements can be used to assess the sample amplifying action. Single-pass gain can be estimated by measuring the increase in power through an optically excited sample for a laser beam at the wavelength within the emission spectra. This measurement can be performed with a pump-probe setup, where light of absorbed wavelength is used to pump a section of the sample to the metastable level, and a probe beam is employed to trigger stimulated emission from the excited level. Different setups for the purpose are possible. The sample can be excited evenly throughout the volume, for instance via a lamp, transversely by laser diode stacks or just longitudinally via laser beams. In all cases, it is important to estimate the pump-probe superposition, which defines the total volume contributing to the probe amplification and, consequently, the number of involved emitting centres. The gain values as a function of absorbed pump power can also give an estimate for the absorption saturation threshold, indicating the pump power density at which the system's ground level is depleted and the highest possible metastable level population is achieved.

A gain measurement experiment was set up, employing a CaF_2:Yb^{3+} laser as a probe. This homemade laser was pumped with a diode-pumped fibre laser delivering up to 1.5 W with 4 A pump current at 980 nm (Azur Light Systems/ALS). To pump the CaF_2:Nd^{3+},Lu^{3+} crystals, a tuneable Ti:Sapphire laser was used. The crystal was cleaved along at the Brewster angle from the lattice plane to minimise reflection losses.

The probe laser setup consists of an CaF_2:Yb^{3+} crystal, cleaved at the Brewster angle with respect to the (1 1 1) crystal plane, within an alpha cavity consisting of two concave mirrors with a focal distance of 50 mm, a high-reflection mirror and an output coupler of 2% of transmission. An optical isolator was used to prevent any reflected pump re-entering the fibre laser. Finally a Lyot filter, placed at Brewster angle within the cavity, was used for tuning the output wavelength, as shown in figure 4.4.

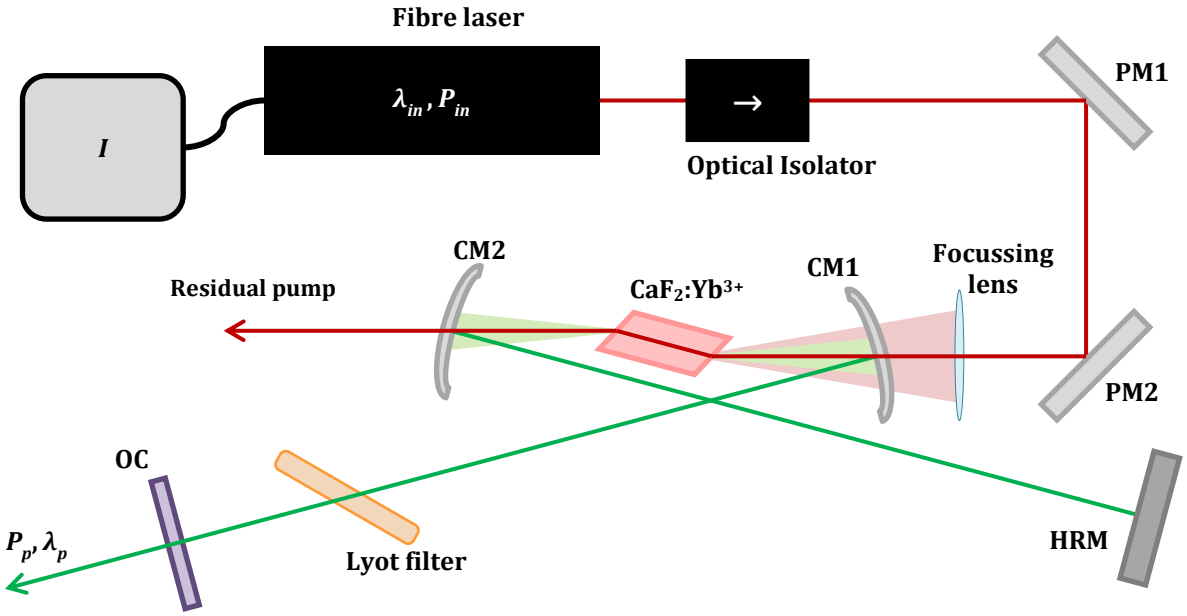

Fig. 4.4 Schematic view of the $CaF_2:Yb^{3+}$ laser probe setup for gain measurements on $CaF_2:Nd^{3+},Lu^{3+}$ samples.

This kind of setup allows for a tuneable laser in the range between 1.03 μm and 1.07 μm. The $CaF_2:Yb^{3+}$ laser was typically pumped with about 850 mW at 980 nm (corresponding to a fibre laser drive current of 2.5 A), yielding an output power about 160 mW at 1060 nm, or 90 mW at 1054 nm. The maximum output power obtained at 1054 nm was about 240 mW with a 4 A fibre laser drive current, and the pump power threshold for $CaF_2:Yb^{3+}$ laser oscillation was found at about 150 mW (corresponding to 0.75 A).

The output wavelengths were calibrated by collecting the output spectrum with an OSA. A measurement of the $CaF_2:Yb^{3+}$ laser output power was performed while turning the Lyot filter, thus obtaining the device calibration curve, as shown in figure 4.5.

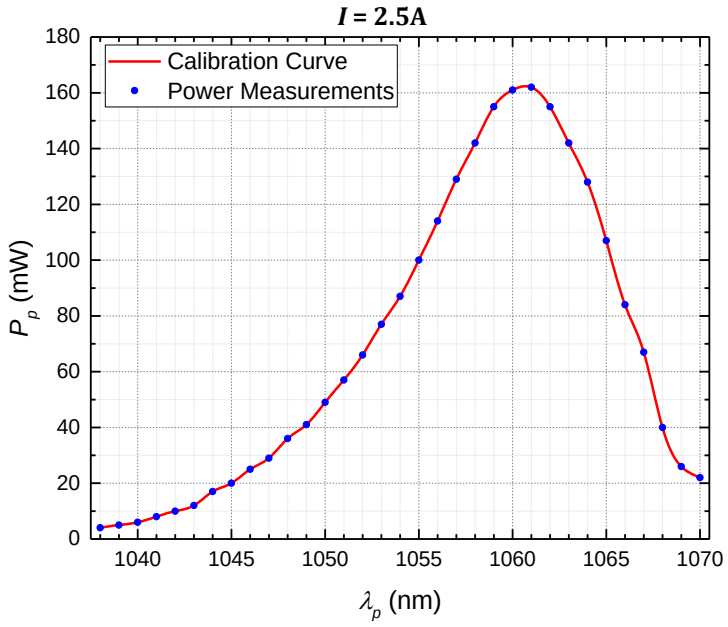

Fig. 4.5 Calibration measurements and extrapolated curve of the $CaF_2:Yb^{3+}$ laser output, with a fibre laser drive current intensity of 2.5 A.

The output of the $CaF_2:Yb^{3+}$ laser was then employed as the probe beam for the gain measurements, combining it with the pump beam coming from a Ti:Sapphire laser through a dichroic mirror. Telescopes were also used, in order to obtain a proper collimation of the two beams and to tailor the waist radii. A fraction of the impinging power was collected for reference before the sample via a beam splitter with 10% reflectivity. The pump beam was then filtered out with the help of a multilayer in order to only detect the final probe power. The gain was then obtained by comparing the probe power ratio between the two detectors P_1/P_0 with and without the pump beam. The entire setup is shown in figure 4.6.

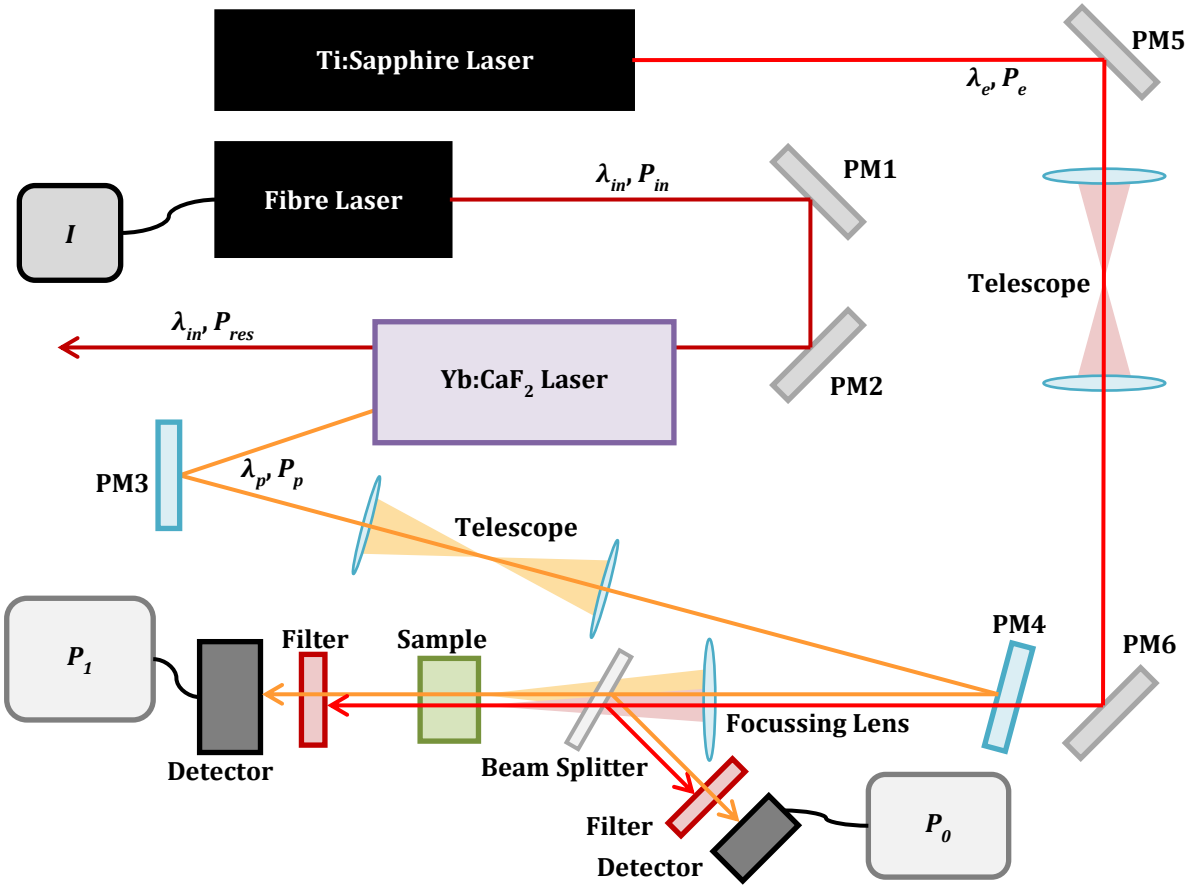

Fig. 4.6 Schematic view of the gain experimental setup.

The beams were superposed and focussed on the sample, so that the width of the beams was approximately constant along the entire thickness of the material.

The gain measurements were performed for different pump power values, and different materials were compared. Measurements of the gain for an appositely cut and polished CaF_2:0.5% Nd,2% Lu with excitation wavelength equal to 797 nm were performed, and the results were compared to those for a LG-770 phosphate laser glass with excitation wavelength 802 nm. In order to keep the probed gain medium at a constant temperature, and to favour heat dissipation during the measurements, each sample under study was placed on a copper holder, water-cooled to 15 °C by a chiller. Because of the low thermal shock resistance and poor heat dissipation of glasses, measurement under higher pump power values were not performed on the LG-770 glass, to avoid cracking the sample. The pump beam waist during these measurements had a 25 μm radius, while the probe beam waist had a 35 μm radius. The measured gain values were plotted as a function of the excitation power, as shown in figure 4.7.

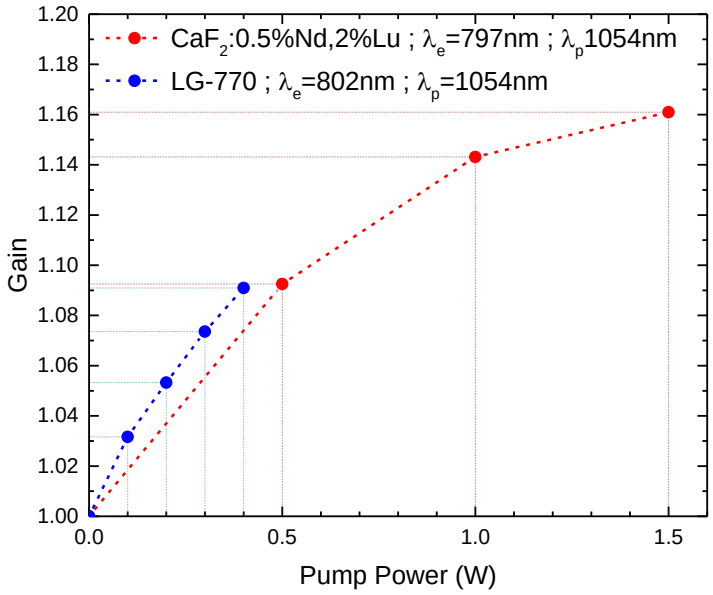

Fig. 4.7 Gain of CaF_2:0.5% Nd,2% Lu and LG-770 glass as a function of excitation power with probe beam at 1054 nm.

From this comparison, one may see that the CaF_2:0.5% Nd,2% Lu crystal has a similar gain value at low pump power to the LG-770 sample. However, the absorption coefficient and thickness of the two samples are different, so the values were plotted as a function of absorbed pump power, calculated by dividing the pump power by its absorbance at the pump wavelength (Fig. 4.8), showing that $CaF_2:Nd^{3+},Lu^{3+}$ has slightly higher gain than neodymium-doped phosphate glasses. The absorbed power is calculated using the sample absorption coefficient obtained via spectroscopic measurements only for incident power values equal to or lesser than 500 mW, because it is apparent from figure 4.7 that absorption saturation takes place as the incident power increases.

However, while the phosphate glass gain follows an approximately linear behaviour, calcium fluoride exhibits a nonlinear curve, which suggests that saturation effects are taking place. In fact, the neodymium concentration within LG-770 is 4.2 cm^{-3}, which is much higher than that of a 0.5 at% neodymium-doped calcium fluoride crystal (1.23 cm^{-3}, see chapter 2), which means that absorption saturation takes place for higher photon flux than in the $CaF_2:Nd^{3+},Lu^{3+}$ samples.

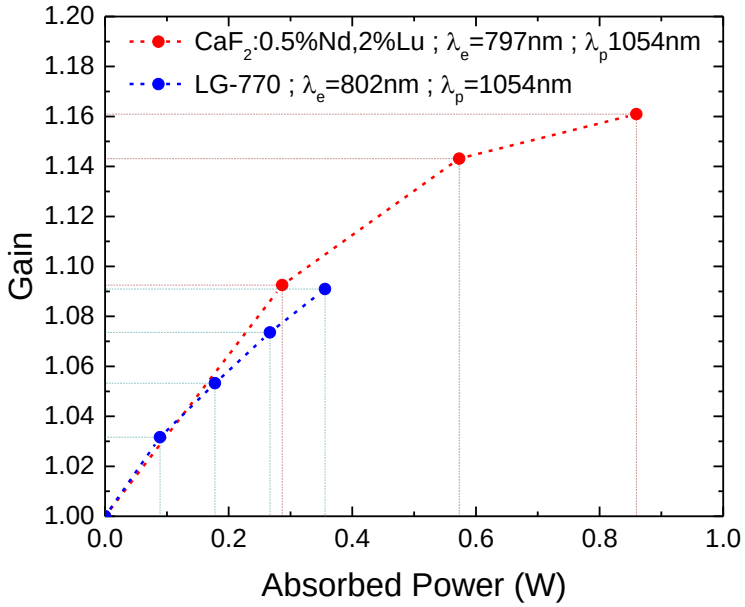

Fig. 4.8 Gain of phosphate glass LG-770 and CaF_2:0.5% Nd,2% Lu as a function of absorbed pump power with probe beam at 1054 nm.

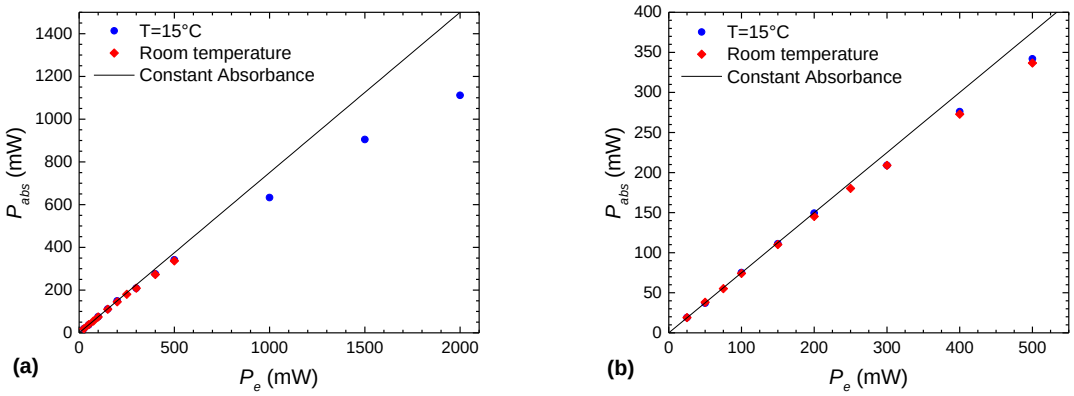

Fig. 4.9 (a) Power absorbed by a 3.7 mm thick CaF_2:0.5% Nd,12% Lu sample versus incoming pump power for a beam with waist radius of 50 µm, without cooling (red diamonds) and with set temperature of 15 °C via chiller (blue dots), and compared to the calculated absorption from absorbance measurements (black line); (b) closeup uf the 0-500 mW range.

With the knowledge that CaF_2:Nd^{3+},Lu^{3+} crystals can withstand CW laser beams of 25 µm radius and powers up to 1.5 W, the experiment was updated, employing a CaF_2:0.5% Nd,12% Lu sample cut and polished for the purpose. Keeping in mind that the thermal conductivity of high-lutetium doping samples is sensibly lower than low-lutetium doping samples, the pump beam was enlarged to a 50 µm radius with a telescope, to distribute the power, reducing the heat

deposition, and to better superpose to the pump and probe beam, ideally increasing overall gain. First, an absorption measurement was performed, to assess the absorption saturation, if any, by simply measuring the incoming and transmitted pump beam powers, and taking into consideration the Fresnel reflection. The results of absorbed versus incoming power are shown in figure 4.9.

The measurements at room temperature and at the fixed temperature of 15 °C show no substantial difference, meaning no thermal effects from the sample cooling impact sensibly the measurements. One can see that the absorbed power values deviate from the constant-absorbance behaviour as the incident excitation power increases beyond 300 mW, meaning that absorbance decreases gradually with increasing pump power. This is due to the gradual depletion of the ground level, and thus the decrease in the number of active absorbers, as the pump power increases.

From these measurements, the crystal absorption coefficient was calculated as a function of incoming pump power, as shown in figure 4.10. It is worth noting that the values of absorbed power are consistent with calculations performed using the model introduced in section 4.2, using the Mathematica code wrote for the purpose of gain calculation, with null probe power (Fig. 4.11).

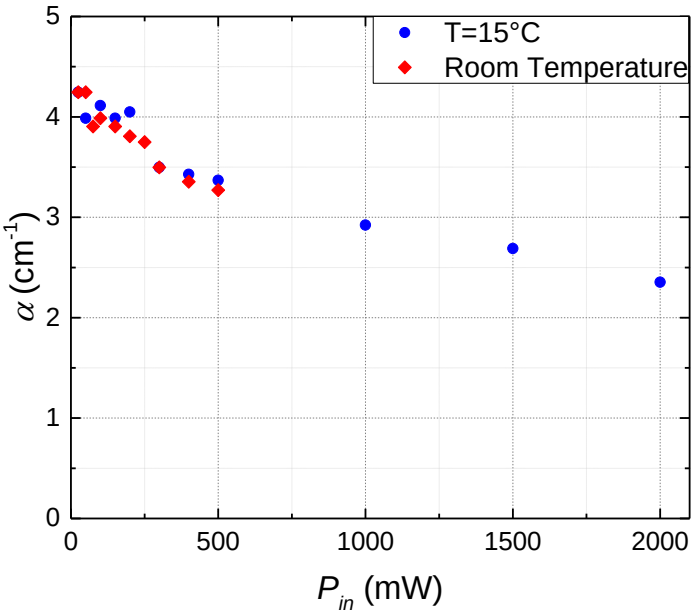

Fig. 4.10 Absorption coefficient of CaF_2:0.5% Nd,12% Lu as a function of excitation power without cooling (red diamonds) and with set temperature of 15 °C via chiller (blue dots).

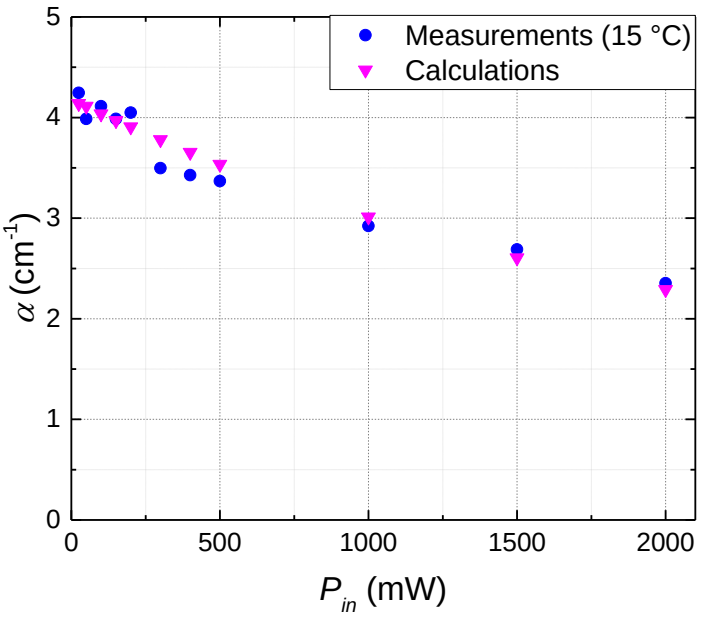

Fig. 4.11 Absorption coefficient of CaF_2:0.5% Nd,12% Lu as a function of excitation power at 15 °C (blue dots) and calculated with *Mathematica* (magenta triangles).

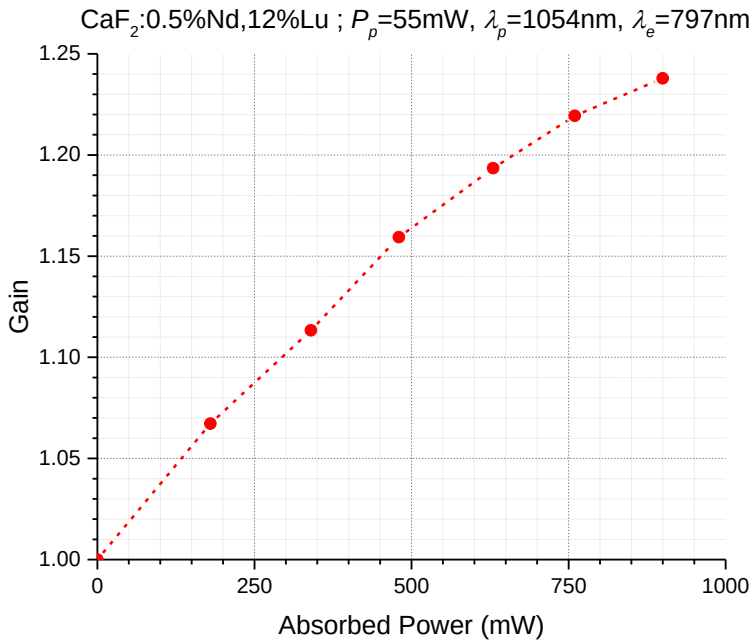

Fig. 4.12 Gain of the CaF_2:0.5% Nd,12% Lu sample versus absorbed pump power. The dashed red lines are a guide for the eye.

These values were used in combination with gain measurements to obtain the actual behaviour of the crystal gain as a function of absorbed pump power. These measurements are shown in figure 4.12.

One can see that the gain follows a linear behaviour as a function of absorbed power, until roughly 500 mW, when it starts to deviate, dropping slightly below the linear function. This suggests the beginning of absorption saturation coming into play as more and more ions are excited and the ground state is gradually depleted.

Since the saturation of absorption takes place starting at approximatively 500 mW absorbed power, with a little calculation one can find the saturation threshold power density. Keeping in mind that the beam is Gaussian, and therefore the saturation starts at the beam centre where intensity is highest, and considering the pump beam radius constant along the sample thickness, the threshold absorbed power density value for saturation, I_{th}, is:

$$I_{th} = \frac{2\,P_p}{\pi \cdot w_0^2} \tag{4.25}$$

which, in the case at hand, means $I_{th} = 13\ \mathrm{kW/cm^2}$. This corresponds to an incident power density threshold roughly equal to 19 kW/cm^2. By multiplying this value by the sample NL2 fluorescence lifetime τ_f, equal to 300 μs, one obtains a saturation flux of about 5.7 J/cm^2. This result, albeit approximated, is roughly consistent with the value F_{sat} calculated from the spectroscopic parameters in chapter 2 (see table 2.4).

To sum up, the doubly-doped CaF_2 crystals gain properties have been demonstrated with a collinear pump-probe setup, and compared to the Nd:phosphate glass LG-770. One can see that CaF_2:Nd^{3+},Lu^{3+} crystals have a similar gain to LG-770 at low absorbed power values, but in addition can reach much higher values by virtue of their better thermomechanical properties. This indicates that calcium fluoride can sustain more intense pump power and therefore provide overall greater amplification than Nd:phosphate glasses.

The possibility of obtaining an optical gain value exceeding 1.2 was demonstrated with a CaF_2:0.5% Nd,12% Lu and an incident pump power of 2 W assessing Nd^{3+},Lu^{3+}-doped fluorite crystals as an effective laser oscillator. The saturation of absorption was observed, and the threshold power density for the saturation was estimated. The saturation behaviour was compared to the proposed model, proving its consistency in the calculation of absorption. However, gain calculations with the model at hand did not yield results consistent with the measured gain values, suggesting that either some part of the model is inaccurate, or some

parameter were estimated with insufficient accuracy. An improvement of the description and of the parameters accuracy for the purpose of obtaining a predictive model is currently under development.

4.3.c CW Laser Operation

To assess the laser generation qualities of CaF_2:Nd^{3+},Lu^{3+} in the CW regime, a simple plano-concave cavity experiment was setup, as shown in figure 4.13. The cavity consisted of a plane mirror with high reflectivity around the 1.05 μm wavelength and high transmittance around the pump wavelength, and a concave mirror with a 100 mm curvature radius. The sample was placed inside the cavity, in contact with the plane mirror. The concave mirror acted as the output coupler, and it focussed the reflected emission upon the plane mirror surface. The system was pumped using a Ti:sapphire laser beam as excitation source, and the beam was focussed onto the sample via a convex lens. The laser beam power P_{out} was collected by a power meter at the cavity output.

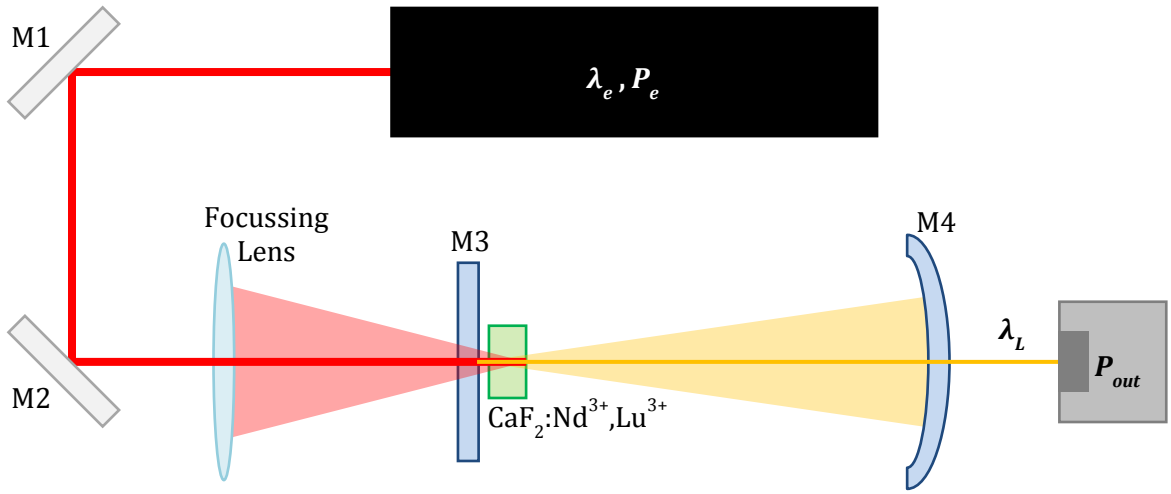

Fig. 4.13 Plano-concave cavity setup for CW laser measurements.

Laser measurements were performed both on a 5.35 mm thick CaF_2:0.5% Nd,5% Lu sample and on a 3.7 mm thick CaF_2:0.5% Nd,8% Lu sample, gradually increasing the pump power, in order to calculate the pump threshold and slope efficiency. The samples were excited with a pump wavelength of 797 nm via a Ti:sapphire laser. The collected laser beam wavelength was 1054 nm. The output coupler chosen had an 8% transmission. The results are shown in figure 4.14, as a function of both incident and absorbed pump power. In this case, the absorbed power was estimated by collecting the transmitted pump beam power through the sample.

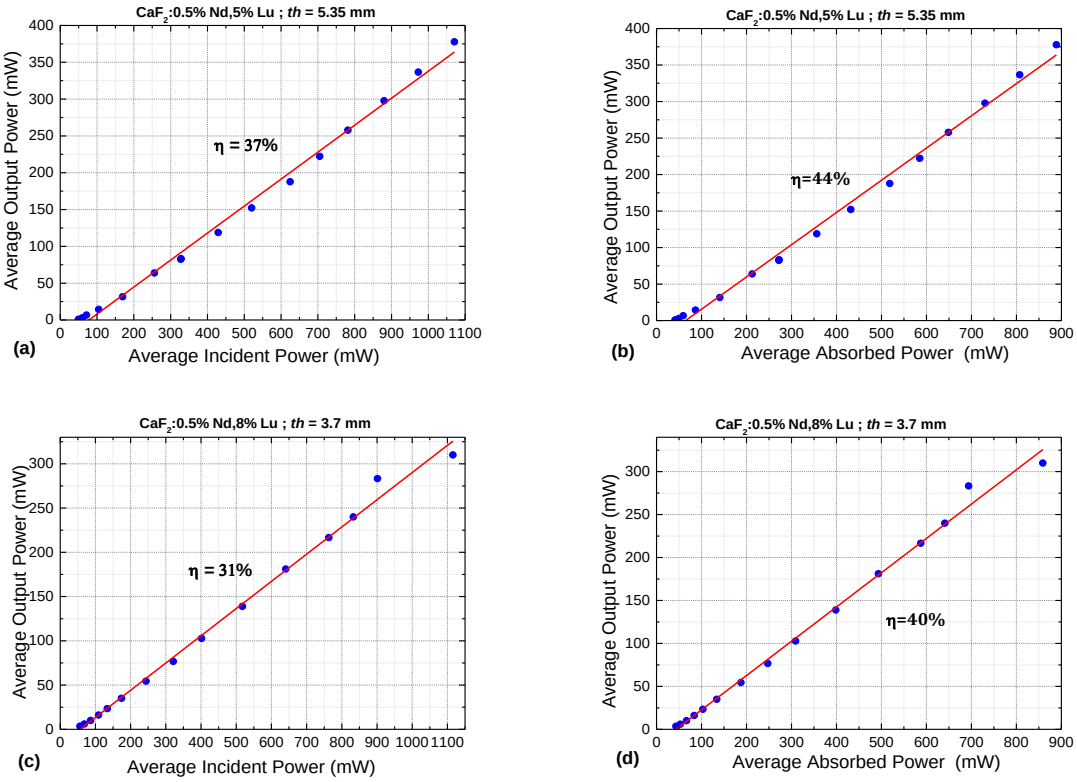

Fig. 4.14 Laser output measurements results for CaF_2:0.5% Nd, 5% Lu (a),(b) and CaF_2:0.5% Nd, 8% Lu (c),(d).

The measurements on the CaF_2:0.5% Nd,5% Lu sample yielded a 37% slope efficiency with respect to incident power, with an incident power threshold of 80 mW. The same measurements resulted in a 44% slope efficiency with respect to absorbed pump power, with an absorbed power threshold of 66 mW. The CaF_2:0.5% Nd,8% Lu sample yielded a 31% slope efficiency with respect to incident power, and a 62 mW threshold. With respect to the absorbed pump power, the CaF_2:0.5% Nd,8% Lu slope efficiency was 40%, with a 46 mW absorbed power threshold.

These measurements are close to the results obtained by Doualan *et al.* on a CaF_2:0.5% Nd,5% Lu sample [8], although they show a lower slope efficiency than those presented in the paper. This is thought to be due to a lesser quality of the sample employed in this experiment with respect to that presented in the literature. However, the slope efficiency obtained is sensibly higher than that observed in the case of CaF_2:Nd^{3+},Y^{3+} [8,10].

4.3.d Mode-Locked Laser Operation

A mode-locked laser operation experiment was prepared to assess the possibility of short-pulse laser oscillation with the CaF_2:Nd^{3+},Lu^{3+} crystals. A CaF_2:0.5% Nd,8% Lu sample was grown via Czochralski method, then cut to the Brewster angle with respect to the [1 1 1] crystal axis, and polished to laser-application quality. A folded laser cavity was set up, as shown in figure 4.15. A set of two concave mirrors with 100 mm curvature radius and high reflectivity in the 1000-1100 nm range was employed to direct the laser beam and focus it upon the sample, and the sample was mounted on a water-cooled copper block and kept at a temperature of 18 °C. Mode locking was achieved via a commercial SESAM saturable absorber (BATOP GmbH). The SESAM employed was designed to operate at 1040 nm and had a modulation depth of 1.2%, a non-saturable loss of 0.8% and a relaxation time of 1 ps. A pair of prisms was used to compensate for the setup intracavity dispersion. Various output couplers were employed in the course of the experiment. The system was pumped using a Ti:sapphire tuneable laser and the pump beam was focussed on a 30 μm diameter spot upon the sample. The pulse trains were detected with a Thorlabs fast photo-detector, together with a Tektronix digital oscilloscope, and the pulse width was measured with an APE commercial autocorrelator.

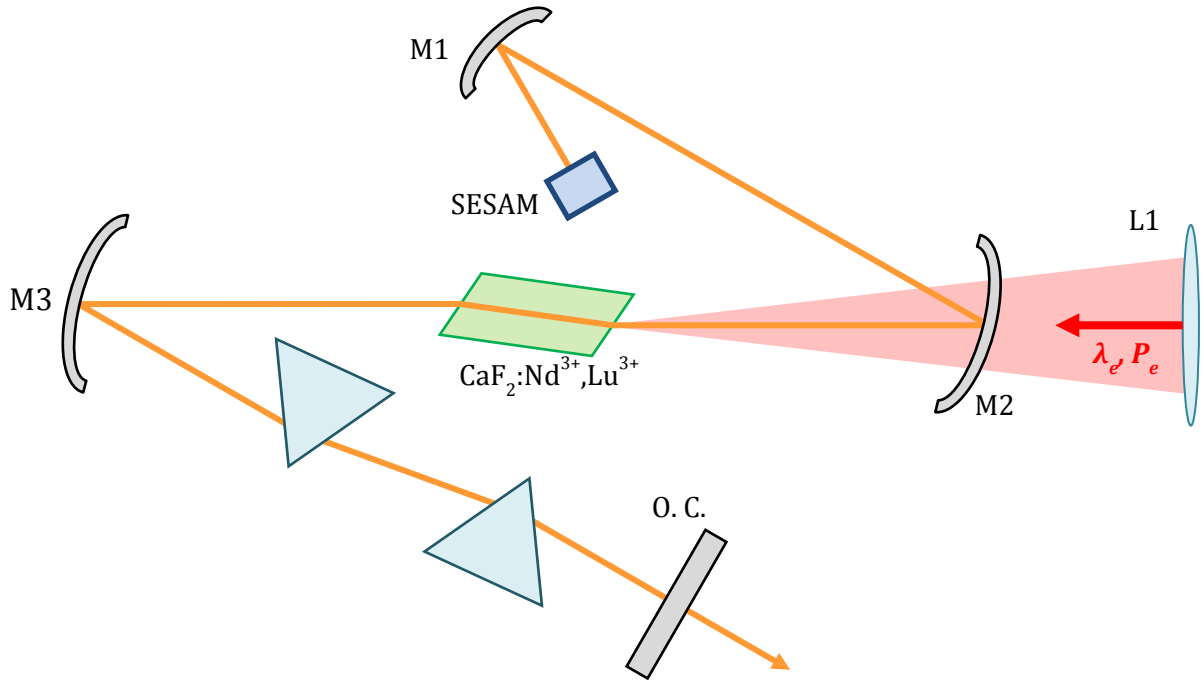

Fig. 4.15 Folded cavity mode-locked laser experiment setup.

Mode-locked laser action was successfully obtained. The possibility of pulsed laser generation via mode-locking with CaF_2:Nd^{3+},Lu^{3+} crystals is therefore assessed. The laser output

power was collected with a 0.5% transmission output coupler under 791 nm excitation. The values were plotted as a function of pump power, in order to assess the threshold pump power and slope efficiency of the device. The results are shown in figure 4.16, showing a threshold of 1350 mW.

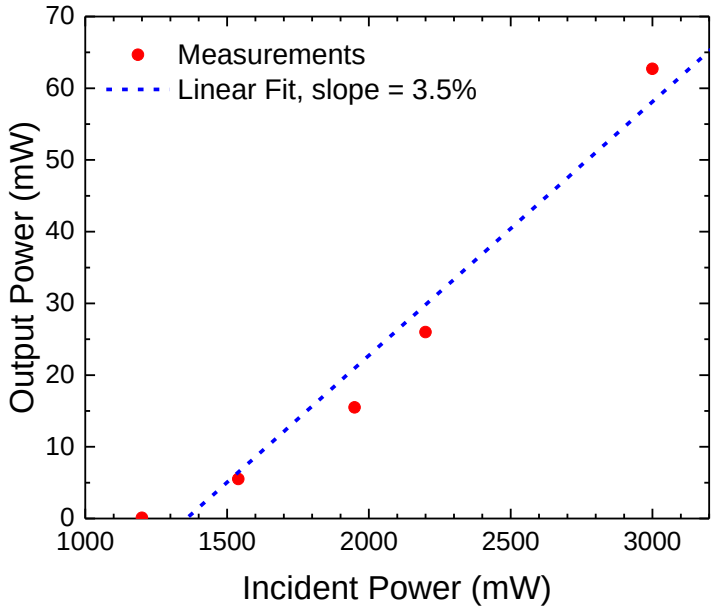

Fig. 4.16 CW mode-locked laser output power versus pump beam power with 791 nm pump wavelength, showing the threshold pump power value and slope efficiency of the laser setup.

The highest power obtained with these measurements was 60 mW, under 3 W pump power. Moreover, stable CW mode-locking is achieved as the incident power increases over 2.2 W.

(a) (b) (c)

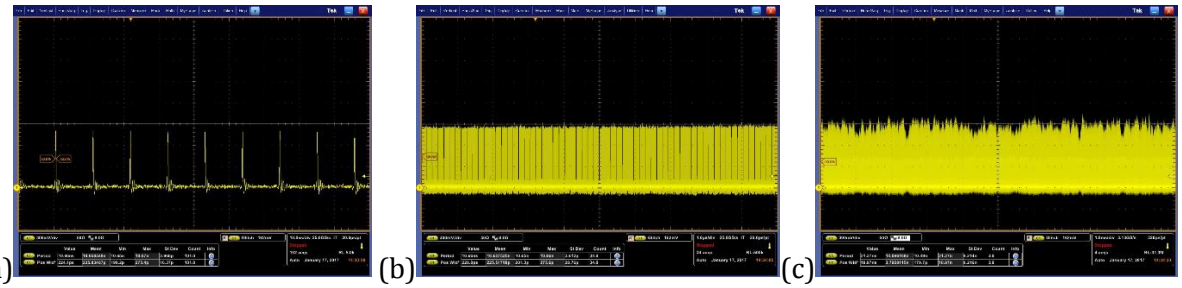

Fig. 4.17 Mode-locked laser pulse trains measured on a 10 ns (a), 1 μs (b) and 1 ms (c) time scale, showing period and stability of the laser pulses.

Figure 4.17 shows the typical mode-locked pulse trains measured under the maximum available pumping. The pulse trains shown in figure 4.17(a), 4.17(b) and 4.17(c) were

respectively recorded with a time scale of 10 ns/div, 1 μs/div and 1 ms/div. It can be seen that the pulses trains were fully modulated with good pulse stability. The pulse repetition rate is 938 MHz, which is in agreement with the cavity length.

The optical spectrum of the mode-locked pulses was collected via an optical fibre leading to a Leasametric optical spectrum analyser. The band shows two distinguishable peaks, located respectively at 1060 nm and 1063 nm, which appear simultaneously in the mode-locking regime. Only one mode-locked pulse was observed in the oscilloscope trace, indicating that the two mode-locked pulses are synchronized and temporally overlapped. The total width of the band is 3.5 nm. The spectrum is shown in figure 4.18(a). The pulses autocorrelation was calculated and is shown in figure 4.18(b): a width of 900 fs was found for the autocorrelation function.

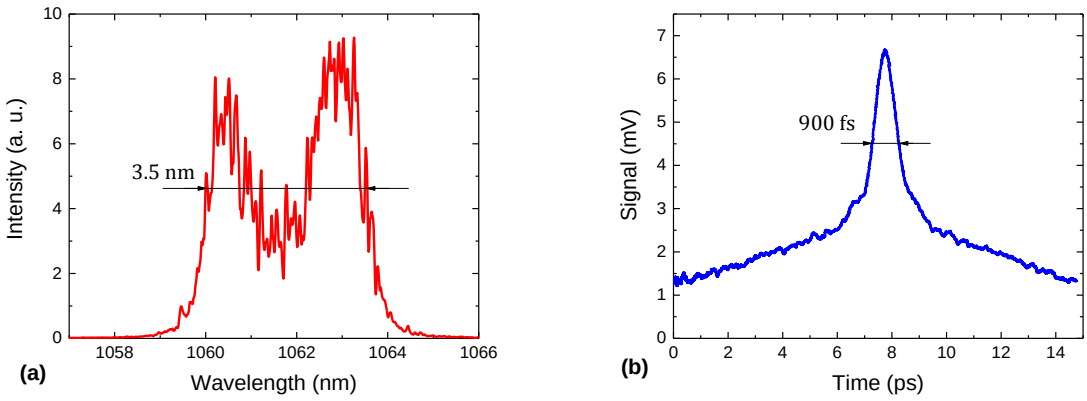

Fig. 4.18 (a) Spectrum of the mode-locked pulses; (b) pulses autocorrelation function.

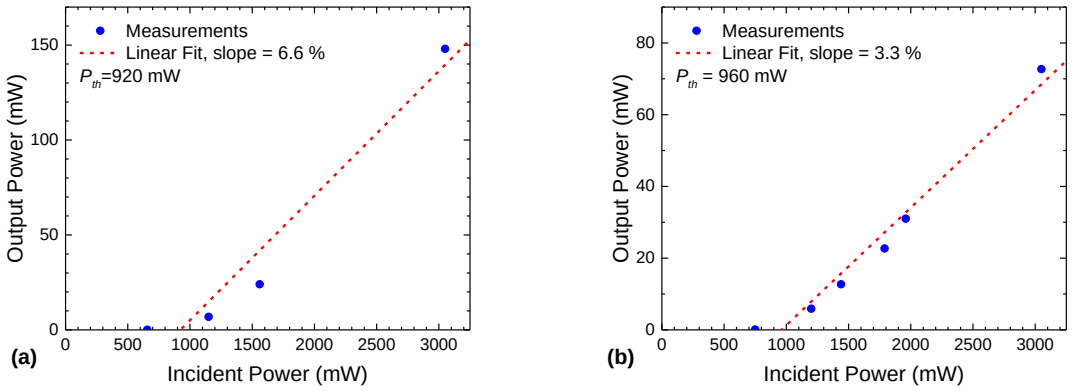

Fig. 4.19 Laser output power versus pump power under 797 nm wavelength excitation, for (a) 1054 nm emission and (b) 1062 nm emission.

The laser operation under a 797 nm excitation wavelength beam was assessed. Two asynchronous pulses were first identified on the oscilloscope, identified as the 1054 nm emission and the 1062 nm emission pulses. The two emission lines were selected by inserting a razorblade as a screen between the output coupler and the diffractive prisms. Figures 4.19(a) and 4.19(b) show the output power as a function of incoming pump power for 797 nm excitation, for the 1054 nm and 1062 nm emission respectively.

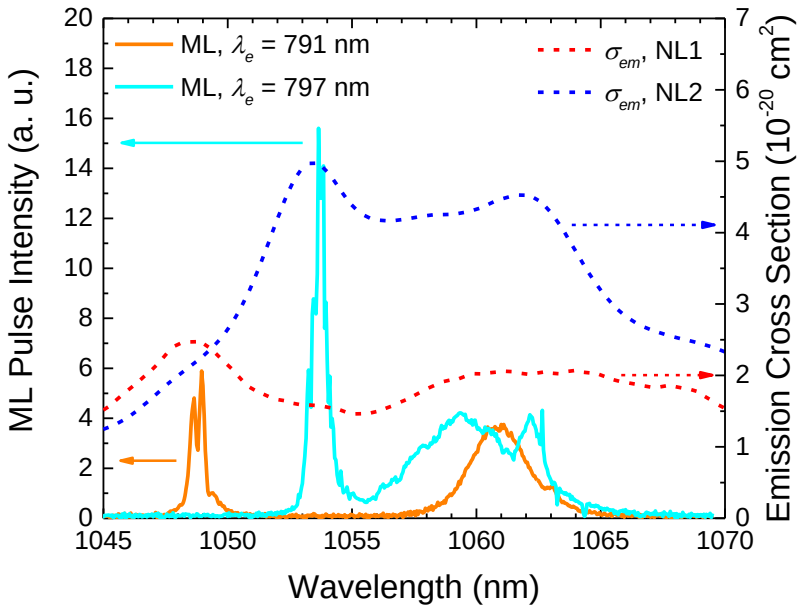

Fig. 4.20 Emission spectra of the mode-locked laser with a CaF_2:0.5% Nd,5% Lu sample, compared to the emission cross section spectra for NL1 and NL2 centres.

In order to synchronise the mode locked pulses at 1054 nm and 1062 nm under 797 nm pump wavelength, a 0.1% output coupler was employed to broaden both emission lines by reducing the spectral gain narrowing and increasing nonlinearities. The spectrum thus obtained is shown in figure 4.20. The output power was about 5 mW. The calculated emission cross section spectrum of a CaF_2:0.5% Nd,5% Lu is also reported on the same figure. However, the emission peaks at 1049 nm and 1061 nm couldn't be synchronised by pumping at 797 nm, and two asynchronous pulse trains were consistently observed. The spectrum of the unfiltered pulses is also shown in figure 4.20.

One can see the laser emission peaks spectral positions obtained in the mode-locking experiment correspond to the main wavelengths of the emission spectra under the corresponding excitation: when exciting at 791 nm, one obtains a sharp laser peak at 1049 nm,

plus a broader peak around 1062 nm, while under 797 nm excitation a sharp 1054 nm emission arises, with a broader, lower feature appearing around 1060 nm. This behaviour is in agreement with the emission results obtained in the spectroscopic study of the material (see chapter 2) and with the gain ratios calculated previously in this chapter (Fig. 4.3), in that the excitation at 791 nm allows for laser emission around 1062 nm, rather than1054 nm, while exciting at 797 nm causes a 1054 nm peak to appear, sensibly more intense than the 1062 nm feature.

It is possible to filter part of the emission to achieve a single-peak mode-locked laser centred at 1062 nm, with very short pulse width. The spectrum and autocorrelation of the emission filtered in this way are reported on figure 4.21, showing the possibility of obtaining 435 fs long pulses with 3 nm emission peak width.

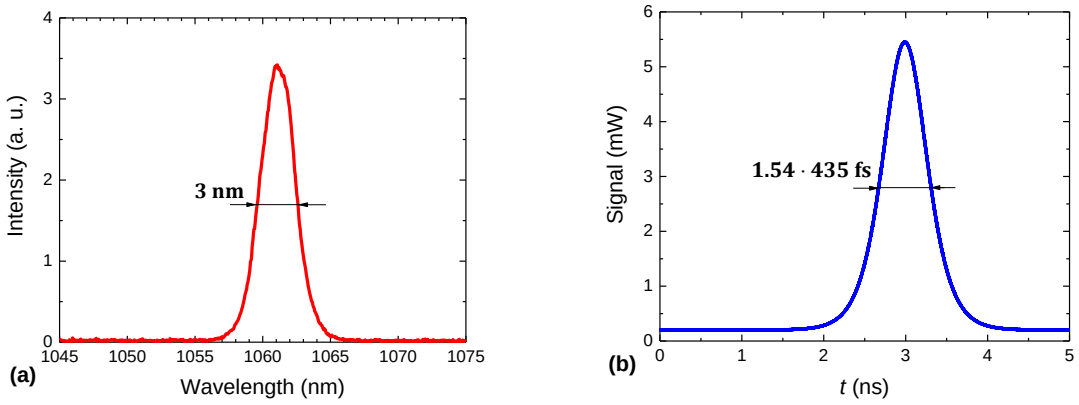

Fig. 4.21 Mode-locked pulse spectrum (a) and autocorrelation (b) for the filtered 1062 nm emission under excitation at 797 nm.

4.4 Conclusions

The potential of CaF_2:Nd^{3+},Lu^{3+} as a gain medium has been investigated in this chapter. The gain coefficient ratio has been computed as a function of excitation wavelength and lutetium concentration. This has shown that gain at the 1054 nm wavelength becomes dominant over the value at 1049 nm, as a result of the NL2 site concentration increase. Furthermore, the calculations suggest that the main gain feature oscillates between the 1054 nm and the 1062 nm emission peaks as the pump wavelength changes between 797 nm and 791 nm. The actual active material gain has been estimated using collinear and co-propagating pump-probe gain measurements. Results show that the material provides a sensible power gain via stimulated

emission on the $^4F_{3/2} \rightarrow {}^4I_{11/2}$ transition. Moreover, a comparison with measurements on a LG-770 sample show that the $CaF_2:Nd^{3+},Lu^{3+}$ crystals have similar, possibly even more efficient gain than the neodymium-doped phosphate glasses currently in use in high-energy laser facilities. However, further measurements and cross-checking are required to confirm this statement and obtain a more in-depth optical gain analysis.

$CaF_2:Nd^{3+},Lu^{3+}$laser operation in the CW regime has been achieved with a plano-concave cavity setup. The experiments yielded slope efficiency and threshold power values higher than the results for other crystal compositions such as $CaF_2:Nd^{3+},Y^{3+}$. Moreover, these results have been obtained with smaller neodymium concentration than in the case of yttrium codoping. This suggests that $CaF_2:Nd^{3+},Lu^{3+}$ is an interesting laser material, and lutetium may be a more efficient codopant to tackle the quenching issues in neodymium-doped calcium fluoride crystals.

Finally, mode-locked laser pulses have been obtained with a $CaF_2:Nd^{3+},Lu^{3+}$ crystal in a folded-cavity setup, employing a SESAM as saturable absorber. The results show the competition between the 1054 nm peak emission and the 1062 nm peak emission predicted by the gain ratio calculations. However, even for high lutetium concentration samples, the 1049 nm emission appears when pumping on the absorption at 791 nm. The main emission pulses are found when pumping at 797 nm, and are centred at 1054 nm.

Laser pulses at the 1062 nm wavelength showed a spectral width of 3 nm, which satisfies the requirements for high-energy laser materials. Pulse durations in the order of hundreds of femtoseconds were measured. These durations clearly are not optimised. The mode-locking set-up (with particular regard to dispersion and nonlinear effects), the pump wavelength and the material itself can be further improved to obtain shorter pulses. The perspectives of the work presented in this section are many, from improvement of the laser operation properties to the refinement of measurements and calculations. In particular, the different Nd^{3+} centres lifetimes and emission cross section need to be evaluated more accurately in order for the theoretical computation to match the optical gain measurements. Furthermore, a more complete set of laser experiments should be performed, assessing the actual effects of lutetium concentration on the material for mode-locked laser operation.

CHAPTER 5

"To the scientist there is the joy in pursuing truth which nearly counteracts the depressing revelations of truth."

Conclusions and Perspectives

The results obtained in this work confirm that the introduction of lutetium buffer ions increases the light yield of Nd^{3+}-doped CaF_2 by breaking up the inactive Nd^{3+}-Nd^{3+} clusters, and demonstrate the viability of this material as a high-energy pulsed laser amplifier medium. The entirety of the presented results is intended as the groundwork for further investigation in the properties of these systems, and for their application in the aforementioned laser amplifier devices.

The integrated emission intensity is enhanced up to tenfold the value found in CaF_2:0.5% Nd in the case of CaF_2:0.5% Nd,8% Lu. One can in fact observe a drastic increase of luminescence as a function of lutetium concentration, as predicted according to the cluster-breaking hypothesis. The emission intensity limit is reached at 8% Lu and above, most likely due to the fact that all optically-inactive Nd^{3+}-Nd^{3+} clusters are removed from the crystal. In addition, the broad emission bands suggest the viability of such crystals as fs pulse amplifiers. In fact, the CaF_2:Nd^{3+},Lu^{3+} emission bands are as broad as those of neodymium-doped phosphate glasses currently in use in the LMJ facility.

Absorption and fluorescence spectra indicate the existence of two separate Nd^{3+}-Lu^{3+} optically active centres, here named NL1 and NL2. This is further confirmed by lifetime measurements, revealing two different decays and radiative lifetimes. These two centres can be reasonably associated to the two centre types I (quasi-rhombic) and II (quasi-tetragonal) respectively, already reported in the literature in the case of the Nd^{3+},Y^{3+}:CaF_2 codoping. Time-resolved emission and excitation spectroscopy along with a careful

choice of excitation wavelength and Lu^{3+} codopant concentration allows for the discrimination of NL1 and NL2 emission and absorption spectra.

Absorption cross sections and concentrations for the three main Nd^{3+} centres (Nd^{3+}-Nd^{3+} clusters, NL1 and NL2) have been estimated by performing a reconstruction of the absorption coefficient spectra in the different codoped samples via a linear combination of the different centres absorption bands. Thus, it was confirmed that Nd^{3+}-Nd^{3+} clusters are reduced drastically by the Lu^{3+} codoping, effectively disappearing at 8% Lu concentration. NL1 centres tend to dominate at low co-doping concentrations in comparison to NL2, while NL2 centres are more and more prominent as the lutetium concentration increase, eventually becoming 4 times as abundant as NL1 centres at high Lu^{3+} concentration (12 at% and beyond).

The subsequent reconstructions of the fluorescence spectra provide results very similar to the experimentally recorded emission, both in spectral shape and in intensity, which confirms the consistency of the spectroscopic description. The inactive clusters disappearance rate is therefore consistent with the integrated emission intensity obtained from fluorescence measurements. Moreover, with relative quantum yield measurements the same behaviour is found, and one can see that the quantum yield for CaF_2:Nd^{3+},Lu^{3+} samples with high codopant concentrations approaches that of YAG:Nd^{3+} laser crystals.

The optical and spectroscopic properties estimated in the whole process have allowed the evaluation of the two CaF_2:Nd^{3+},Lu^{3+} centres emission cross sections, using the Füchtbauer-Ladenburg equation. With this, the complete spectroscopic description for the $^4I_{9/2} \rightarrow {}^4F_{5/2}$ and $^4F_{3/2} \rightarrow {}^4I_{11/2}$ transitions in the doubly-doped fluorite system is obtained.

The samples thermomechanical properties were probed via thermo-optic techniques, i.e. thermal lens spectrometry and Jamin-Lebedev interferometry measurements. The results provide an estimate for the system thermal conductivity evolution as a function of lutetium concentration. The value to which the samples thermal conductivity drops is much lower than that of the pristine CaF_2 crystal, however it is still several times higher than that of neodymium-doped phosphate glasses. This means that, from the thermal point of view, CaF_2 crystals are preferable to phosphate glasses with any Lu^{3+} concentration, for pulsed laser operation. In fact, the measurements prove that even

highly-doped crystals can sustain higher thermal strains and dissipate built-up heat faster, allowing longer operation times and higher output intensities for the device, not to mention higher repetition rates.

The CaF_2:Nd^{3+},Lu^{3+} thermal conductivity values at high lutetium concentrations are approximated by the Klemens model, while the calculated values do not fit well the low-codoping sample data. This is most likely a consequence of Klemens' approximations. One possibility is that the approximations use in the model are not accurate enough in the case of two-rare-earths doping, due to the two species causing different deformations in the crystal lattice geometry. Another possible explanation is given by the fact that the Klemens model does not take into account the formation of clusters, but considers a more even dopant distribution.

Furthermore, crossing the thermal lens fit with the thermal expansion measurement results, the thermo-optic coefficient has been evaluated. The resulting value is approximatively constant with Lu^{3+} concentration. However, both the thermo-optic and the thermal expansion coefficients are greater in absolute value than those of the laser glasses. This means that beam deformation issues due to the beam focussing or defocussing through the sample might be stronger, therefore it might be necessary to consider a stronger wavefront correction in tailoring the device.

Gain measurements in a co-propagating pump-probe setup have shown that CaF_2:Nd^{3+},Lu^{3+} has comparable optical gain to neodymium-doped phosphate glasses. Doubly-doped calcium fluoride crystals have been successfully used as laser amplifiers, obtaining slope efficiencies up to 44% in a plano-concave cavity setup, comparable to the values in literature for the laser medium CaF_2:Nd^{3+},Y^{3+}.

Preliminary mode-locked laser experiments were successfully carried out. CaF_2:Nd^{3+},Lu^{3+} was proved to work as a pulsed laser amplifier in a mode-locking experiment with a folded cavity setup. Interestingly, one may see that it is possible to select the laser output line by tailoring the pumping wavelength, and femtosecond-long pulses were successfully obtained with both pumping laser frequencies. This opens the way for more in-depth investigation, and eventually the application of the crystal in short-pulse lasers.

The absorption and emission spectroscopic features of SrF_2:Nd^{3+},Lu^{3+} and BaF_2:Nd^{3+},Lu^{3+} crystals were recorded as well. Unlike the CaF_2 case, these other two fluorides show a single kind of dominant active site, and their spectral band shape is constant as a function of lutetium concentration. It was observed that the two systems emission maxima and minima are complementary, in that a linear combination of the two spectra provides a very broad and flat band around 1053 nm. The possibility of growing mixed SrF_2-BaF_2:Nd^{3+},Lu^{3+} crystals with different SrF_2/BaF_2 ratios was therefore investigated, and the fabricated samples spectra were collected. Unfortunately a shift in the spectral features appears, attributed to the distortion of the Nd^{3+} sites crystal field symmetry as the result of the two mixed fluoride lattice mutually interacting. This prevents the peaks and valleys of the two spectra to align properly, and thus makes the flat profile virtually unobtainable. The spectral shape evolution as a function of the ratio between the two fluorides shows the general tendency of rare earths clustering in a BaF_2 environment over SrF_2. These results demonstrate the possibility to grow mixed fluorides with Nd^{3+} and Lu^{3+} doping as a possible option for broadband laser amplification at 1.05 μm, but further study is needed for the optimisation of their spectral features.

To sum up, the addition of lutetium greatly improves the spectroscopic properties of neodymium-doped CaF_2 crystals by breaking up the inactive neodymium clusters. Similar performances to neodymium-doped phosphate glasses such as LG-770 and LHG-8, which are currently employed in high-energy laser facilities, are obtained in terms of optical bandwidths, lifetimes and cross sections. In particular, the quasi-tetragonal NL2 centres, become dominant at high Lu^{3+} concentrations, allowing for efficient emission at the appropriate wavelength for LMJ applications, 1054 nm. In addition the NL2 peak absorption cross section value is very close to that of Nd^{3+}-doped phosphates (approximately $4 \cdot 10^{-20}$ cm^2). In particular, the coexistence of two active centres can be an asset in tailoring the spectroscopic features via an appropriate pumping wavelength choice. This possibility was confirmed by preliminary laser operation experiments, where a 1054 nm line was obtained by pumping at 797 nm, and the 1049 nm emission line by pumping at 791 nm.

While high lutetium concentrations allow for better spectroscopic properties, the thermal conductivity of CaF_2 gradually drops with the introduction of dopants. Fortunately, even at high lutetium concentrations, CaF_2 retains a higher thermal conductivity than neodymium-doped phosphate glasses, which corroborates the initial

assumption. This observation, in conjunction with the spectroscopic properties measured, confirms doubly-doped fluorite as a viable option for the improvement of glass-based high-intensity laser amplifiers. The measurements in this work suggest that for 0.5% Nd^{3+} doping the ideal lutetium codoping is around 8 at%, which is the lowest Lu^{3+} percentage with which virtually all inactive Nd^{3+}-Nd^{3+} clusters are removed.

The femtosecond mode-locked laser operation of CaF_2:Nd^{3+},Lu^{3+} opens the way for further investigation on the performances of these samples as short-pulse laser amplifiers. As an added value, the possibility to select the output laser line via an accurate choice of the optical pump was observed, which gives the crystals a further degree of versatility. However, at the same time, it is important to understand the emission choice mechanisms in order to prevent unwanted oscillation between the two output wavelengths.

Finally, the possibility of combining doubly-doped SrF_2 and BaF_2 spectra to obtain the broadest and flattest bands possible has shown that the spectroscopic features of composite SrF_2-BaF_2:Nd^{3+},Lu^{3+} suffer from modifications due to lattice distortions, which prevents the achievement of the best-case calculated spectrum. Further study on these hybrid systems is necessary to better understand the mechanics at play in these materials, and possibly manipulate their spectroscopic features into the desired shape.

In short, one can conclude that lutetium-codoping is an effective method for improving the spectroscopic properties of neodymium-doped fluorite-type crystals, while retaining favourable thermal properties, in particular high thermal conductivity and diffusivity. Moreover, CaF_2 proved to be versatile, as they allow the selection of emission wavelength, and therefore the output line in a laser oscillator setup. As femtosecond pulsed laser emission was proven using CaF_2:Nd^{3+},Lu^{3+} in CW-pumped, mode-locked experiments, the crystal was confirmed as a viable replacement for neodymium-doped glasses in high-energy and short-pulse laser amplifiers. The improvement of laser performance is granted by the better thermal properties of doubly-doped CaF_2 with respect to phosphate glasses, while retaining the appropriate spectroscopic features.

However, these systems are complex and further research is required to fully understand their properties and for their practical application in high-energy laser amplifier chains. First of all, a more thorough understanding of the crystals thermal properties is needed, particularly regarding the thermally-induced birefringence, which has only been briefly discussed here. Moreover, it is very important to evaluate the samples properties under the stimuli to which they will be subjected to in their operating

environment. In particular, it is necessary to assess the extraction of 1 J energy pulses from CaF_2:Nd^{3+},Lu^{3+}-based amplifiers, and the possibility of obtaining a 10 Hz repetition rate under these conditions.

The next steps in the study of these systems shall therefore focus, in general, on their thermo-optic properties, and the optimisation of their laser operation. In particular, short-pulse laser oscillation of CaF_2:Nd^{3+},Lu^{3+} has to be investigated more in depth, in order to identify the ideal setup parameters for both ultrashort pulse generation and high-energy output. A fine-structure investigation of the samples energy levels may help in the optimisation of these parameters, therefore low-temperature spectroscopy experiments can already be predicted.

Thus, thanks to an appropriate way of cluster engineering, with the help of buffer ions, one can consider that, as for CaF_2:Yb^{3+}, Nd^{3+}-doped calcium fluoride crystals may become a suitable gain medium for pulsed high-energy laser amplifier chains. Once characterised more in depth in all their optic and thermomechanical properties, and optimised, they may take the place of neodymium-doped glasses in laser chains for plasma physics experiment and ICF in the near future. As the LASCAN project advances, CaF_2:Nd^{3+},Lu^{3+} crystals are predicted to enhance the performances of high-energy and ultrashort lasers at the LMJ facility, and possibly eventually in other projects around the globe, leading to significant advances in high-energy density science research and nuclear fusion applications.

A more thorough study on composite crystals may also be carried out, with the aim of optimising their spectroscopic properties. Circling the active site geometry deformation issue that results from the two fluorides mixing and prevents the hybrid crystal from achieving the ideal band shapes, is another challenge. If solved, it could lead to the achievement of a high-performance short-pulse laser amplifier medium, thanks to the breadth and flatness of its emission bands, as calculated via the linear composition of its single-crystal component spectra.

References

[1] R. Hull, G. Liu, B. Jacquier, *Spectroscopic Properties of Rare Earths in Optical Materials*, Springer (2005)

[2] S. A. Payne, J. A. Caird, L. L. Chase, L. K. Smith, N. D. Nielsen, and W. F. Krupke, J. Opt. Soc. Am. B 8 (4) pp 726-740 (1991)

[3] G. A. Slack and D. W. Olivier, Phys. Rev. B 4 (1971) 592

[4] S. Chénais, F. Druon, F. Balembois, P. Georges, A. Brenier, G. Boulon, Opt. Mater. 22, 2 (2003) pp. 99–106

[5] J. H Campbell and T. I Suratwala, J. Non-Cryst. Sol. 263-264 (2000) 318-341

[6] L. Hu, S. Chen, J. Tang, B. Wang, T Meng, W. Chen, L. Wen, J. Hu, S. Li, Y. Xu, Y. Jiang, J. Zhang, and Z. Jiang, High Power Laser Science and Engineering 2, e1 (2014)

[7] Yu. K. Voron'ko, and V. V. Osiko, JETP Letters 10, 357-360 (1967)

[8] J. L. Doualan, L. B. Su, G. Brasse, A. Benayad, V. Ménard, Y. Y. Zhan, A. Braud, P. Camy, J. Xu, and R. Moncorgé, J. Opt. Soc. Am. B 30 (11), pp 3018-3021 (2013)

[9] D. Serrano, A. Braud, J. L. Doualan, P. Camy, and R. Moncorgé, J. Opt. Soc. Am. B 29 (8) pp 1854-1862 (2012)

[10] L B Su, Q G Wang, H J Li, G Brasse, P Camy, J L Doualan, Braud, R Moncorgé, Y Y Zhan, L H Zheng, X B Qian and J Xu, Laser Phys. Lett. 10, 035804 (4pp) (2013)

[11] M. Jelínek, V. Kubeček, L. B. Su, D. P. Jiang, F. K. Ma, Q. Zhang, Y. X. Cao and J. Xu, Laser Phys. Lett. 11, 055001 (4pp) (2014)

[12] T.T. Basiev, A.Ya.Karasik, R.L. Shubochkin, Journal of Luminescence 64 (1995) 259-265

[13] J.L. Doualan, L. Su, G. Brasse, A. Benayad, V. Ménard, Q. Wang, A. Braud, P. Camy, J. Xu, and R. Moncorgé, ASSL 2013

[14] I. Iparraguirre, J. Azkargorta, J. Ferna´ndez, R. Balda, A. Oleaga, and A. A. Kaminskii, J. Opt. Soc. Am. B 16 (9) pp 1439-1466 (1999)

[15] A. A. Kaminskii, Z. I. Zhmurwa, V. A. Lomonov, and S. E. Sarkisw, Phys. Stat. Sol. (a) 84 (1984)

[16] O. K. Alimov, T. T. Basiev, M. E. Doroshenko, P. P. Fedorov, V. A. Konyushkin, A. N. Nakladov, and V. V. Osiko, Opt. Mater. 34 (2012), 799–802

[17] T. T. Basiev, M. E. Doroshenko, V. A. Konyushkin, and V. V. Osiko, Opt. Lett. 35, 23 (2010), 4009-4011

[18] Yu. V. Orlovskii, T. T. Basiev, I. N. Vorob'ev, V. V. Osiko, A. G. Papashvili, and A. M. Prokhorov, Laser Phys. 6, 3 (1996) pp. 448-455

[19] A. A. Kaminskii, R. G. Mikaelyan, and I. N. Zygler, Phys. Stat. Sol. 33, K85 (1969)

[20] T.T. Basiev, V.B. Sigachev, M.E. Doroshenko, A.G. Papashvili, V.V. Osiko, Proceedings of SPIE 2498 (1995)

[21] W. Hayes, M. C. K. Wiltshire, R. Berman, and P. R. W. Hudson, J. Phys. C: Solid State Phys., Vol. 6 (1973)

[22]S. Palchoudhuri and G. K. Bichile, Solid State Commun. 70, 4 (1989), 475-478

[23] P. A. Popov, P. P. Fedorov, S. V. Kuznetsov, V. A. Konyushkin, V. V. Osiko, and T. T. Basiev, Doklady Physics 53, 4 (2008), 198-200

[24] F.Druon, S. Ricaud, D. N. Papadopoulos, A. Pellegrina, P. Camy, J. L. Doualan, R. Moncorgé, A.Courjaud, E. Mottay, and P. Georges, Opt. Mater. Express 1, 3 (2011), 489-502

[25] W. Koechner, Applied Optics 9, 6 (1970) 1429–1434

[26] C. Jacinto, T. Catunda, D. Jaque, L. E. Bausá, and J. García-Solé, Opt.Express 16,9 (2008)

[27] L. R. Freitas, C. Jacinto, A. Ródenas, D. Jaque, and T. Catunda, J. Lumin. 128 (2008) 1013–1015

[28] V. M. Martins, G. Brasse, J. L. Doualan, A. Braud, P. Camy, D. N. Messias, T. Catunda, and R. Moncorgé, Opt. Mater. 37 (2014) 211-213

[29] O. L. Antipov, O. N. Eremeykin, A. P. Savikin, V. A. Vorob'ev, D. V. Bredikhin, and M. S. Kuznetsov, IEEE J. Quantum Electron. 39, 7 (2003)

[30] O. L. Antipov, D. V. Bredikhin, O. N. Eremeykin, A. P. Savikin, E. V. Ivakin, and A. V. Sukhadolau, Opt. Lett. 31, 6 (2006) 763-765

[31] V. Petit, J. L. Doualan, P. Camy, V. Ménard, and R. Moncorgé, Appl. Phys. B 78 (2004) 681–684

[32] D. N. Papadopoulos, F.Friebel, A.Pellegrina, M. Hanna, P.Camy, J. L.Doualan, R.Moncorgé, P. Georges and F.Druon, IEEE J. Sel. Top.Quantum Electron. 21, 1 (2014) pp. 3100211

[33] F. Friebel, F. Druon, J. Boudeile, D. N. Papadopoulos, M. Hanna, P. Georges, P. Camy, J. L. Doualan, A. Benayad, R. Moncorgé, C. Cassagne, and G. Boudebs, Opt. Lett. 34, 9 (2009) 1474-1476

[34] M. Siebold, F. Roeser, M. Loeser, D. Albach, and U. Schramm, Proc. of SPIE 8780 (2013) 878005-1

[35] M.Hornung, H.Liebetrau, S.Keppler, A. Kessler, M.Hellwing, F.Schorcht, G. A. Becker, M. Reuter, J.Polz, J.Körner, J. Hein, and M. C. Kaluza, Opt. Lett. 41, 22 (2016) pp. 5413-5416

[36] D. N. Papadopoulos J. P. Zou, C. Le Blanc, G. Chériaux, P. Georges, F. Druon, G. Mennerat, P. Ramirez, L. Martin, A. Fréneaux, A. Beluze, N. Lebas, P.Monot, F.Mathieu, and P.Audebert

[37] W. B. Xu, L. Chai, J. K. Shi, M. L. Hu, C. Y. Wang, L. B. Su, D. P. Jiang, and J. Xu, Laser Phys. Lett. 11 (2014) 115816

[38] J. Fernandez, A. Oleaga, J. Azkargorta, I. Iparraguirre, R. Balda, M. Voda, and A.A. Kaminskii, Opt. Mater. 13 (1999) 9-16

[39] Z. P. Qin, G. Q. Xie, J. Ma, W. Y. Ge, P. Yuan, L. J. Qian, L. B. Su, D. P. Jiang, F. K. Ma, Q. Zhang, Y. X. Cao, and J. Xu, Opt. Lett. 39 (7) 1737-1739 (2014)

[40] J. F. Zhu, L. Wei, W. L. Tian, J. X. Liu, Z. H. Wang, L. B. Su, J. Xu, and Z. Y. Wei, Laser Phys. Lett. 13, 5 (2016) 055804

[41] J. Liu, M. W. Fan, L. B. Su, D. P. Jiang, F. K. Ma, Q. Zhang and J. Xu, Laser Phys. 24 (2014) 035802

[42] P. G. Klemens, Phys. Rev. 119, 507 (1960)

[43] J.-C. Chanteloup and D.Albach, IEEE Photonics Journal 3, 2 (2011)

[44] M. Dunne, BA high-power laser fusion facility for Europe, Nat. Phys. 2, 1 (2006) pp. 2–5

[45] J.-C. Chanteloup, D. Albach, A. Lucianetti, K. Ertel, S. Banerjee, P. D. Mason, C. Hernandez-Gomez, J. L. Collier, J. Hein, M. Wolf, J. Körner, and B. J. Le Garrec, J. Phys.: Conf. Ser., 244,. 1 (2010) p. 012010

[46] B. J. Le Garrec, C. Hernandez-Gomez, T. Winstone, and J. Collier, J. Phys.: Conf. Ser. 244, 3 (2010) p. 032020

[47] A. J. Bayramian, R. W. Campbell, C. A. Ebbers, B. L. Freitas, J. Latkowski, W. A. Molander, S. B. Sutton, S. Telford, and J. A. Caird, J. Phys.: Conf. Ser. 244, 3 (2010) p. 032016

[48] C. Yamanaka, Y. Kato, T. Mochizuki, M. Nakatsuka, T. Yamanaka, K. Yoshida, and S. Nakai, *Gekko XII system for laser fusion research*, in Conference on Lasers and Electro-Optics, D. Hodges, W. Silfvast, G. Bjorklund, and E. Hinkley, eds., OSA Technical Digest (Optical Society of America, 1984), paper FP1.

[49] N. C. Holmes, *High Energy Laser Facilities at Lawrence Livermore National Laboratory*, AIP Conference Proceedings 78, 648 (1982)

[50] P. J. Wisoff, M. W. Bowers, G. V. Erbert, D. F. Browning, D. R. Jedlovec, *NIF Injection Laser System*, Proc. SPIE 5341 (2004) 146–155

[51] J. Kawanaka, K. Yamakawa, K. Tsubakimoto, T. Kanabe, T. Kawashima, H. Nakano, M. Yoshida, T. Yanagitani, F. Yamamura, M. Fujita, Y. Suzuki, N. Miyanaga, and Y. Izawa, Rev. Laser Eng. Supplemental Volume (2008) 1056-1058

[52] H. Furuse, Y. Takeuchi, T. Nakanishi, A. Yoshida, R. Yasuhara, T. Kawashima, H. Kan, N. Miyanaga, and J. Kawanaka, *Recent progress in GENBU laser*, Proc. 6th Int. Workshop HEC-DPSSL, Versailles, France, Sep. 8–10, 2010.

[53] L. J. Perkins, R. Betti, K. N. LaFortune, and W. H. Williams, Phys. Rev. Lett. 103 (2009) 045004

[54] R. Betti, C. D. Zhou, K. S. Anderson, L. J. Perkins, W. Theobald, and A. A. Solodov, Phys. Rev. Lett. 98

(2007) 155001

[55] N. Hopps, K. Oades, J. Andrew, C. Brown, G. Cooper, C. Danson, S. Daykin, S. Duffield, R. Edwards, D. Egan, S. Elsmere, S. Gales, M. Girling, E. Gumbrell, E. Harvey, D. Hillier, D. Hoarty, C. Horsfield, S. James, A. Leatherland, S. Masoero, A. Meadowcroft, M. Norman, S. Parker, S. Rothman, M. Rubery, P. Treadwell, D. Winter, and T. Bett, Plasma Phys. Control. Fusion, 57, 6 (2015)

[56] K. Jungwirtha, J. Ullschmied, K. Rohlena, and B. Rus, *Prague Asterix Laser System-a new high power facility*, Pulsed Power Conference, 1999. Digest of Technical Papers. 12th IEEE International, Volume 2

[57] C. Danson, D. Hillier, N. Hopps, and D. Neely, High Power Laser Science and Engineering 3, 3 (2015) 14 pages

[58] M. Tabak, J. Hammer, M. E. Glinsky, W. L. Kruer, S. C. Wilks, J. Woodworth, E. M. Campbell, and M. D. Perry, Phys. Plasmas 1 (1994) 1626

[59] G. Sarri, W. Schumaker, A. Di Piazza, M. Vargas, B. Dromey, M. E. Dieckmann, V. Chvykov, A. Maksimchuk, V. Yanovsky, Z. H. He, B. X. Hou, J. A. Nees, A. G. R. Thomas, C. H. Keitel, M. Zepf, and K. Krushelnick, Phys. Rev. Lett. 110 (2013) 255002

[60] C. Danson, D. Neely, and D. Hillier, High Power Laser Sci. Eng., 2, e34 (2014) 12 pages

[61] C. Hernandez-Gomez, P.A. Brummitt, D.J. Canny, R.J. Clarke, J. Collier, C.N. Danson, A.M. Dunne, B. Fell, A.J. Frackiewicz, S. Hancock, S. Hawkes, R. Heathcote, P. Holligan, M.H.R. Hutchinson, A. Kidd, W.J. Lester, I.O. Musgrave, D. Neely, D.R. Neville, P.A. Norreys, D.A. Pepler, C.J. Reason, W. Shaikh, T.B. Winstone, and B.E. Wyborn, J. Phys. IV France 133 (2006) 555-559

[62] R. Kodama, H. Shiraga, K. Shigemori, Y. Toyama, S. Fujioka, H. Azechi, H. Fujita, H. Habara, T. Hall, Y. Izawa, T. Jitsuno, Y. Kitagawa, K. M. Krushelnick, K. L. Lancaster, K. Mima, K. Nagai, M. Nakai, H. Nishimura, T. Norimatsu, P. A. Norreys, S. Sakabe, K. A. Tanaka, A. Youssef, M. Zepf, and T. Yamanaka, Nature 418 (2002) 933-934

[63] G. L. Bourdet, J.-C. Chanteloup, A. Fulop, Y. Julien, and A. Migus, *The LUCIA project: a high average power ytterbium diode pumped solid state laser chain*, Laser Optics 2003: Solid State Lasers and Nonlinear Frequency Conversion, edited by Vladimir I. Ustugov, Proceedings of SPIE Vol. 5478 (SPIE, Bellingham, WA, 2004)

[64] A Lucianetti, V Jambunathan, M Divoky, O Slezak, M Sawicka, J Pilar, S Bonora , P D Mason, P J Phillips, K Ertel, S Banerjee, C Hernandez Gomez, J L Collier, C Edwards, M Tyldesley, and T Mocek, *HiLASE: a scalable option for Laser Inertial Fusion Energy*, 8th International Conference on Inertial Fusion Sciences and Applications (IFSA 2013)

[65] A. Bayramian, P. Armstrong, E. Ault, R. Beach, C. Bibeau, J. Caird, R. Campbell, B. Chai, J. Dawson, C. Ebbers, A. Erlandson, Y. Fei, B. Freitas, R. Kent, Z. Liao, T. Ladran, J. Menapace, B. Molander, S. Payne, N. Peterson, M. Randles, K. Schaffers, S. Sutton, J. Tassano, S. Telford, and E. Utterback, Fusion Sci. Technol. 52, 3 (2007) 383-387

[66] J. D. Sethian, F. Hegeler, M. Myers, M. Friedman, S. Obenschain, R. Lehmberg, J. Giuliani, P. Kepple, S. Swanekamp, I. Smith, D. Weidenheimer, D. Morton, L. Schlitt, R. Smilgys, and S. Searles, *The Electra KrF Laser Program*, 13th IEEE Pulsed Power Conference, Las Vegas, NV, June 17-22, 2001. IEEE, New York, NY p 232 (2002)

[67] R. Yasuhara, T. Kawashima, T. Sekine, T. Kurita, T. Ikegawa, O. Matsumoto, M. Miyamoto, H. Kan, H. Yoshida, J. Kawanaka, M. Nakatsuka, N. Miyanaga, Y. Izawa, and T. Kanabe, Opt. Lett. 33, 15 (2008) 1711-1713

[68] A. Casner, T. Caillaud, S. Darbon, A. Duval, I. Thfouin, J. P. Jadaud, J. P. LeBreton, C. Reverdin, B. Rosse, R. Rosch, N. Blanchot, B. Villette, R. Wrobel, and J. L. Miquel, High Ener. Dens. Phys. xxx (2014) 1-10

[69] J.-L. Miquel and E. Volant, *Overview of the Laser Megajoule First Experiments*, 26th IAEA Fusion Energy Conference - IAEA CN-23 (2016)

[70] E. d'Humières, J. Caron, C. Perego, D. Raffestin, J.-L. Dubois, J. Baggio, A. Compant La Fontaine, S. Hulin, J.-E. Ducret, F. Lubrano, J.C. Gommé, J. Gazave, J. Ribolzi, J.-L. Feugeas, P. Nicolai, E. Lefebvre, V. T. Tikhonchuk, and D. Batani, J. Phys.: Conf. Series 688 (2016) 012012

[71] G. A. Slack, Phys. Rev. 112, 5 (1961) 1451-1464

[72] H. G. Danielmeyer and M. Blätte, Appl. Phys. 1, 269-274 (1973)

[73] T. P. J. Han, G. D. Jones, and R. W. G. Syme, Phys. Rev. B 7, 22 (1993)

[74] V. V. Fedorov, W. Beck, T. T. Basiev, A. Ya. Karasik, and C. Flytzanis, Chem. Phys. 257 (2000) 275-281

[75] F. K. Ma, Q. Zhang, D. P. Jiang, L. B. Su, Y. J. Shao, J. Y. Wang, F. Tang, J. Xu, P. Solarz, W. Ryba-Romanowski, R. Lisiecki and B. Macalik, Laser Phys. 24 (2014) 105703 (7pp)

[76] Kh. S. Bagdasarov, Yu. K. Voron'ko, A. A. Kaminskii, L. V. Krotova, and V. V. Osiko, Phys. Status Solidi 12, 905 (1965)

[77] T. T. Basiev, Yu. K. Voron'ko, A. Ya. Karasik, V. V. Osiko, and I. A. Shcherbakov, Zh. Eksp. Teor. Fiz. 75, 66-74 (July 1978)

[78] J. Stark, Annalen der Physik, vol. 43, pp. 965–983 (1914).

[79] A. Smakula, Z. Phys. 134, 279 (1953)

[80] A. Smakula, Phys. Rev. 91, 1570 (1953)

[81] S. Minomura and H. G. Drickamer, J. Chem. Phys. 34, 2 (1960)

[82] J. Arends, Phys. Stat. Sol. 7, 805 (1964)

[83] A. S. Shcheulin, A. V. Veniaminov, Yu. L. Korzinin, A. E. Angervaks, and A. I. Ryskin, Opt. and Spectr. 103, 4 (2006)

[84] A. A. Kaminskii, V. V. Osiko, A. M. Prochorov, and Yu. K. Voronko, Phys. Lett. 22, 4 (1966), 419-421

[85] A. A. Kaminskii, Phys. Status Solidi 20, (1967), K51-K54

[86] D. Jiang, Y. Zhan, Q. Zhang, F. Ma, L. Su, F. Tang, X. Qiana, and J. Xu, Cryst. Eng. Comm. 2015, 17, 7398-7405

[87] L. B. Su, J. Xu, Y. H. Xue, C. Y. Wang, L. Chai, X. D. Xu, and G. J. Zhao, Opt. Lett. 30 (2005) 1003-1005

[88] J. Du, X. Y. Lian, Opt. Express 13, 20 (2005) 7970-7975

[89] B. R. Judd, Phys. Rev. 127 (1962), 750-761

[90] G. S. Ofelt, J. Chem. Phys. 37 (1962), 511-520

[91] G. H. Dieke and H. M. Crosswhite, Appl. Opt. 2, 7, pp. 675-686 (1963)

[92] J. H. Lambert, *Photometria sive de mensura et gradibus luminis, colorum et umbrae*, Eberhardt Klett, (1760)

[93] A. Beer, Annalen der Physik und Chemie. 86 (1852) 78–88

[94] P. M. Becker A. A. Olsson J. R. Simpson, *Erbium-Doped Fiber Amplifiers: Fundamentals and Technology*, Academic Press (1999)

[95] A. Einstein, Verhandlungen der Deutschen Physikalischen Gesellschaft 18 (1916), 318–323

[96]A. Einstein, Phys. Z. 18 (1917), 121-128

[97] P. W. Bridgman, Proc. Am. Acad. Arts Sci., 60, 6 (1925) 305.

[98] D. C. Stockbarger, Rev. Sci. Instrum. 7, 3 (1936)

[99] C. H. L. Goodman, *Crystal Growth: Theory and Techniques, Volume 1*, Springer (1974)

[100] J. R. Lakowicz, *Principles of Fluorescence Spectroscopy*, Kluwer Academic / Plenum Publishers (1999) p.10

[101] Yu. V. Orlovskii, V. V. Fedorov, T. T. Basiev, M. Altwein, B. Leu, J. Heber, and S. Mirov, J. Lum. 83-84 (1999), 361-366

[102] C. Hönninger, R. Paschotta, M. Graf, F. Morier-Genoud, G. Zhang, M. Moser, S. Biswal, J. Nees, A. Braun, G.A. Mourou, I. Johannsen, A. Giesen, W. Seeber, and U. Keller, Appl. Phys. B 69, 3–17 (1999)

[103] F. Druon, S. Chénais, P. Raybaut, F. Balembois, P. Georges, R. Gaumé, G. Aka, B. Viana, S. Mohr, and D. Kopf, Opt. Lett. 27, 197 (2002)

[104] F. Druon, F. Balembois, and P. Georges, Opt. Express 12, 20 (2004)

[105] F. Brunner, G. J. Sphler, J. Aus der Au, L. Krainer, F. Morier-Genoud, R. Paschotta, N. Lichtenstein, S. Weiss, C. Harder, A. A. Lagatsky, A. Abdolvand, N. V. Kuleshov, and U. Keller, Opt. Lett., 25, 1119 (2000)

[106] H. Liu, J. Nees, and G. Mourou, Opt. Lett., 26, 1723 (2001)

[107] A. Lucca, G. Debourg, M. Jacquemet, F. Druon, F. Balembois, P. Georges, P. Camy, J. L. Doualan, and R. Moncorgé, Opt. Lett. 29,23 (2004)

[108] M. Siebold, M. Hornung, S. Bock, J. Hein, M. C. Kaluza, J. Wemans, and R. Uecker, Appl. Phys. B 89, 543–547 (2007)

[109] P. Aballea, A. Suganuma, F. Druon, J. Hostalrich, P. Georges, P. Gredin, and M. Mortier, Optica (OSA), 2 (4), pp. 288-291 (2015)

[110] C. Jacinto, D. N. Messias, A. A. Andrade, S. M. Lima, M. L. Baesso, and T. Catunda, J. Non-Cryst. Solids 352 (2006) 3582–3597

[111] R. Gaumé, B. Viana, D. Vivien, J. P. Roger, and D. Fournier, Appl. Phys. Lett. 83, 7 (2003) 1355-1357

[112] Y. Sato, J. Akiyama, and T. Taira, Opt. Mater. 31 (2009) 720-724

[113] J. Callaway and H. C. von Baeyer, Phys Rev. 120, 4 (1960), pp. 1149-1154

[114] Y. Sato, T. Taira, Opt. Express 14 (2006) 10528

[115] G. A. Slack, Phys. Rev. 126, 2 (1962) 427-441

[116] N. N. Sirota, P. A. Popov, and I. A. Ivanov, Cryst. Res. Technol. 27, 4 (1992) 535

[117] W. J. Parker, R. J. Jenkins, C. P. Butler, and G. L. Abbott, J. Appl. Phys. 32 (1961) 1679

[118] T.Y. Fan, IEEE J. Quant. Electron. 29, 6 (1993) 1457–1459

[119] E. V. Ivakin, A. V. Sukhadolau, O. L. Antipov, and N. V. Kuleshov, Appl. Phys. B 86, 315-318 (2007)

[120] P. Devor, L.G. DeShazer, Nd :YAG quantum efficency and related radiative properties, IEEE J. Quant. Elect., 25, 8 (1989) 1863-1873

[121] J. Petit, B. Viana, Ph. Goldner, J.P. Roger, and D. Fournier, J. Appl. Phys. 108 (2010) 123108

[122] M. L. Baesso, J. Shen, and R. D. Snook, J. Appl. Phys. 75 (1994) 3732

[123] M. L. Baesso, A. C. Bento, A. A. Andrade, J. A. Sampaio, E. Pecoraro, L. A. O. Nunes, T. Catunda, and S. Gama, Phys. Rev. B. 57, 17 (1998)

[124] S. M. Lima, A. A. Andrade, R. Lebullenger, A. C. Hernandes, T. Catunda, and M. L. Baesso, Appl. Phys. Lett. 78, 21 (2001) 3220-3222

[125] S. M. Lima, A. S. S. de Camargo, L. A. O. Nunes, T. Catunda, and D. W. Hewak, Appl. Phys. Lett. 81, 4 (2002) 589-591

[126] A. A. Andrade, S. M. Lima, V. Pilla, J. A. Sampaio, T. Catunda, and M. L. Baesso, Rev. Sci. Instrum. 74, 1 (2003), pp 857-860

[127] N. G. C. Astrath, J. H. Rohling, A. C. Bento, M. L. Baesso, C. Jacinto, S. M. Lima, L. A. O. Nunes, and T. Catunda, J. Phys. IV France 125 (2005) 185-187

[128] L. M. Osterink and J. D. Foster, Appl. Phys. Lett. 12, 4 (1968) 128-131

[129] U. O. Farrukh, A. M. Buoncristiani, and C. E. Byvik, IEEE J. Quant.. Electron. 24, 11 (1988)

[130] M. E. Innocenzi, H. T. Yura, C. L. Fincher, and R. A. Fields, Appl. Phys. Lett. 56, 19 (1990)

[131] S. Chénais, F. Balembois, F. Druon, G. Lucas-Leclin, and P. Georges, IEEE J. Quant. Electron. 40 (9) (2004) 1217–1234.

[132] D. C. Brown, IEEE J. Quantum Electron. 33, 5 (1997) 861-873

[133] R. C. Powel, *Physics of Solid-State Laser Materials*, Springer-Verlag (1998).

[134] J. F. Philipps,T. Töpfer, H. Ebendorff-Heidepriem, D. Ehrt, and R. Sauerbrey, Appl. Phys. B 72, 399-405 (2001)

[135] R. Gaumé, *Relations structures-propriétés dans les lasers solides de puissance à l'ytterbium. Elaboration et caractérisation de nouveaux matériaux et de cristaux composites soudés par diffusion*, PhD Dissertation, Université Pierre et Marie Curie – Paris VI (2006)

[136] J. Callaway and H. C. von Baeyer, Phys. Rev. 120, 4 (1960)

[137] J. Shen, R. D. Lowe, and R. D. Snook, Chem. Phys. 165 (1992) 385-396

[138] E. Anashkina and O. Antipov, J. Opt. Soc. Am. B 27 (3) pp 363-369 (2010)

[139] R. Byron Bird, W. E. Stewart, and E. N. Lightfoot, *Transport Phenomena*, John Wiley and Sons (1960)

[140] G. Ghosh, *Handbook of Thermo-Optic Coefficients of Optical Materials with Applications*, Academic Press (1998)

[141] D. B. Leviton, B. J. Frey, T. J. Madison, Proceedings of SPIE - The International Society for Optical Engineering 6692 (2008)

[142] R. Soulard, A. Zinoviev, J.L. Doualan, E. Ivakin, O. Antipov, and R. Moncorgé, Opt. Express 18, 2 (2010)

[143] M. DiDomenico, J. Appl. Phys. 35 (1964) 2870–2876

[144] L. E. Hargrove, R. L. Fork, and M. A. Pollack, Appl. Phys. Lett. 5 (1964) 4–6

[145] H.W. Mocker and R. J. Collins, Appl. Phys. Lett. 7 (1965) 270–272

[146] E. P. Ippen, C. V. Shank, and A. Dienes, Appl. Phys. Lett. 21 (1972) 348–350

[147] C. V. Shank and E. P. Ippen, Appl. Phys. Lett. 24 (1974) 373–375

[148] H. A. Haus, IEEE J. Sel. Topics Quantum Electron. 6, 6 (2000)

[149] P. P. Sorokin and M. J. Stevenson, IBM J. Res. Dev. 5, 56 (1961)

[150] A. Kaminskii, L. Kornienko, L. Makarenko, A. Prokhorov, and M. Fursikov, Sov. Phys. JETP 19, 262 (1964)

[151]C. Hönninger, R. Paschotta, F. Morier-Genoud, M. Moser, and U. Keller, J. Opt. Soc. Am. B 16, 46 (1999)

[152] J. Zhu, L. Zhang, Z.Gao, J. Wang, Z. Wang,L. Su, L. Zheng, J. Wang, J. Xu, and Z. Wei, Laser Phys. Lett 12 (2015)

[153] T. Y. Fan and R. L. Byer, IEEE J. Quant. Electron. 23, 5 (1987)

[154] W. P. Risk, J. Opt. Soc. Am. B 5, 7 (1988)

[155] P. Laporta, S. Longhi, S. Taccheo and O. Svelto, Opt. Commun. 100 (1993) 311-321

[156] F. Augé, F. Druon, F. Balembois, P. Georges, A. Brun, F. Mougel, G. Aka, and D. Vivien, IEEE J. Quant. Electron. 36, 5 (2000)

[157] T. Taira, W. M. Tulloch, and R. L. Byer, Appl. Opt. 36, 9 (1997) 1867-1874

Français

Mots clés

CaF_2; néodyme; laser; fluorures; terres rares; spectroscopie; LMJ; lentille thermique

Résumé

La possibilité d'obtenir une émission laser efficace sur une large bande spectrale autour de 1.05 µm a été démontrée récemment en utilisant des monocristaux CaF_2 and SrF_2 dopés Nd^{3+}. Cette émission, éteinte du fait de la relaxation croisée entre ions dans les matériaux de type fluorite, peut être exaltée avec l'insertion d'ions "tampons" comme Y^{3+} ou Lu^{3+}. Une émission laser accordable sur une large bande spectrale et la génération d'impulsions ultracourtes sont donc possibles. De plus, ce type de matériau est particulièrement intéressant pour des amplificateurs de forte puissance pompés par diodes. Une étude complète des propriétés spectrales et thermomécaniques de cristaux de CaF_2:Nd^{3+} co-dopés avec des concentrations variables de Lu3+ a été menée en collaboration avec le CEA CESTA au sein du projet LASCAN pour de futurs développements au sein du Laser MégaJoule (LMJ) avec pour but l'amélioration des performances des amplificateurs pilotes. L'effet d'élimination des clusters de Nd^{3+} par le co-dopage avec le Lu^{3+} et l'apparition de deux sites actifs différents a été mise en évidence et caractérisée en détail. Ce travail présente ainsi une spectroscopie complète des centres actifs dans CaF_2:Nd^{3+},Lu^{3+}, une étude des propriétés thermomécaniques, ainsi que des propriétés d'amplification optique des matériaux étudiés.

English

Keywords

CaF_2; neodymium; laser; fluorides; rare earths; spectroscopy; LMJ; thermal lens

Summary

It was recently demonstrated that efficient and broadband laser emission was possible with Nd-doped CaF_2 and SrF_2 single crystals around 1.05 µm. Such laser emission, known as completely quenched because of cross-relaxation in the singly doped fluorites, increases spectacularly by co-doping with non-optically active "buffer" ions like Y^{3+} or Lu^{3+}. Broadband laser emission and ultra-short laser operation are therefore possible. The material is particularly appealing for large scale high peak power diode-pumped amplifiers. A deep investigation of the spectral properties of CaF_2:Nd^{3+} crystals co-doped with various amounts of Lu^{3+} was performed. The cluster breaking effect of Lu^{3+} codoping has as a side-effect the appearance of two different contributions, identified as two different active sites, which is in agreement with recent observations. In this work, we investigate in depth the different centres' spectroscopic properties and operational parameters for laser applications,their evolution as the lutetium concentration increases, and the thermomechanical properties of said samples. A preliminary investigation on the amplification properties and laser operation of said materials is performed as well.